

DEVELOPMENT OF A SUBSURFACE HEATER TECHNOLOGY FOR
IN-SITU HEATING

by

Fatemeh Babazadeh Shareh

A dissertation submitted to the faculty of
The University of Utah
in partial fulfillment of the requirements for the degree of

Doctor of Philosophy

Department of Chemical Engineering

The University of Utah

May 2018

Copyright © Fatemeh Babazadeh Shareh 2018

All Rights Reserved

The University of Utah Graduate School

STATEMENT OF DISSERTATION APPROVAL

The dissertation of Fatemeh Babazadeh Shareh
has been approved by the following supervisory committee members:

<u>Eric G. Eddings</u>	, Chair	<u>07/28/2017</u> Date Approved
<u>Geoffrey Silcox</u>	, Member	<u>07/28/2017</u> Date Approved
<u>Milind Deo</u>	, Member	<u>07/28/2017</u> Date Approved
<u>John David McLennan</u>	, Member	<u>07/28/2017</u> Date Approved
<u>Leonard Switzer</u>	, Member	<u>07/28/2017</u> Date Approved

and by Milind Deo, Chair/Dean of
the Department/College/School of Chemical Engineering

and by David B. Kieda, Dean of The Graduate School.

ABSTRACT

The primary objective of this project was to develop a downhole heater to raise oil shale to a specified temperature in-situ, and to recover energy-rich liquids and gasses. The project had two main phases. Phase I was a preliminary study investigating several different burner concepts for generating heat at great depth and over significant horizontal lengths. In Phase II, a unique configuration of a downhole heater was proposed that eliminates some of the issues regarding previously-considered configurations. The feasibility and applicability of the proposed heater were investigated by looking at key issues that have not been completely addressed in the literature by other researchers. First, calculations were performed to determine appropriate sizes for feeder pipes and nozzles, as well as the pressure distributions in different sections of the heater, so that a uniform flow distribution is maintained along the 2000 ft length of the heater. Then, the overall heat transfer coefficient in the heater and the required gas mixture temperature were determined based on design specifications. The average overall heat transfer coefficients of the outer annulus and the reaction chamber were estimated as $15 \text{ W}/(\text{m}^2 \cdot \text{K})$ and $3.5 \text{ W}/(\text{m}^2 \cdot \text{K})$. The average flue gas temperature was determined to be equal to 939 K. Second, a cold-flow study was performed to investigate the effect of nozzle spacing and orientation on the mixing behavior inside the heater. It was concluded the radial orientations of the nozzles have a more significant role in the mixing behavior than the axial positions. Finally, the effects of the diluents N_2 , CO_2 , and H_2O on the oxidation behavior of methane-oxygen mixtures were

investigated by CHEMKIN modeling studies and reaction sensitivity analysis. These studies concluded that at low gas inlet temperatures, the flame temperature is mainly controlled by the thermal properties of the diluents, and the chemical effect of the diluents is almost negligible. As the heat capacity of the mixture increases, the reaction temperature and the flame speed drop, while the ignition delay time increases. Water vapor addition at a low initial temperature (800-900 K) and 30 atm promotes methane oxidation and decreases the ignition delay time.

To those who devoted their lives to achieving and expressing values

CONTENTS

ABSTRACT.....	iii
ACKNOWLEDGMENTS.....	x
Chapters	
1. INTRODUCTION	1
1.1. Overview	1
1.2. Introduction	2
1.2.1. Permeable membrane heater.....	3
1.2.2. Segregated zone catalytic oxidation heater	4
1.2.3. Homogenous heater configuration	6
1.3. Research objectives	6
1.4. Summary	9
1.5. References	10
2. LITERATURE REVIEW	14
2.1. Overview	14
2.2. Section I: Proposed configuration for homogeneous underground heater and associated literature on homogenous combustion.....	14
2.2.1. Overview	14
2.2.2. Heater configuration.....	15
2.2.3. Flammability limits	16
2.2.3.1. Definition of flammability limits.....	16
2.2.3.2. Correlations to estimate the flammability properties.....	16
2.2.3.3. Effect of oxygen concentration on flammability limits	19
2.2.3.4. Effect of inert gases on flammability limits	19
2.2.3.5. Effect of turbulence on flammability limits.....	20
2.2.4. Autoignition.....	20
2.2.4.1. Definition of autoignition	20
2.2.4.2. Effect of pressure and fuel concentration on autoignition temperature	21
2.2.4.3. Effects of other gases on autoignition	22
2.2.4.4. Shock tube tests	25
2.2.4.5. Flow reactor tests.....	28
2.2.5. Flame Stability.....	29
2.2.5.1. Definition of flame stability.....	29
2.2.5.2. Correlations to predict lift-off height and blow-out velocity.....	29
2.2.5.3. Effect of oxygen concentration on flame stability.....	31
2.2.5.4. Effect of flue gas on flame stability.....	33

2.3. Section II: Heterogeneous (catalytic) underground heater approach and associated literature on heterogeneous combustion	34
2.3.1. Overview	34
2.3.2. Heater configuration.....	34
2.3.3. Nobel metal catalysts.....	35
2.3.4. Transition metal catalysts.....	36
2.3.5. Summary.....	37
2.4. References	39
3. ENGINEERING CALCULATION	59
3.1. Overview	59
3.2. Section I: Determining the appropriate sizes for feeder pipes, nozzles/holes	59
3.2.1. Overview	59
3.2.2. Introduction	60
3.2.3. Case 1: The cross-sectional area of the perforated pipe (A) and the discharge flowrate (q) are known; the diameter of the holes (d) or their spacing (L_n) will be calculated.....	62
3.2.3.1. Case 1, approach 1.....	63
3.2.3.2. Case 1, approach 2.....	65
3.2.3.3. Case 1, approach 3.....	66
3.2.3.3.1. Developing an equation for the pressure of the perforated pipe (P) as a function of the perforated pipe length (x).....	67
3.2.3.3.2. Generating an equation for the hole diameter (d) as a function of the perforated pipe length (x).....	69
3.2.4. Case 2: Discharge flow rate (q), hole diameter (d), and their spacing (L_n) are known; the diameter of the perforated pipe (A) will be calculated as a function of the distance to the inlet end (x)	70
3.2.5. Summary.....	72
3.3. Section II: Heat transfer calculation.....	73
3.3.1. Overview	73
3.3.2. Geometry.....	73
3.3.3. Determining gas and oil properties.....	74
3.3.4. Determining the convection heat transfer coefficient of the outer annulus.....	76
3.3.5. Calculating the convection heat transfer coefficient for the reaction chamber	78
3.3.6. Calculating the boiling heat transfer coefficient ⁷	79
3.3.7. Calculation of metals thermal conductivities	82
3.3.8. Calculating the overall heat transfer coefficient of the heater.....	83
3.3.9. Determining the overall heat transfer coefficient of the annulus.....	84
3.3.10. Determining the overall heat transfer coefficient in the reaction chamber.....	86
3.3.11. Summary.....	87
3.4. References	88
4. EXPERIMENTAL WORK	94
4.1. Overview	94
4.2. Section I - Experimental and modeling study of catalytic oxidation of methane on several materials	95
4.2.1. Introduction	96
4.2.2. Experimental setup	96
4.2.2.1. Bench-scale apparatus	96
4.2.3. Experimental parameters and operating conditions.....	98

4.2.3.1. Fixed parameters.....	98
4.2.3.2. Materials tested.....	98
4.2.3.3. Bed depth and residence time.....	99
4.2.3.4. Pressure.....	99
4.2.3.5. Furnace temperatures.....	99
4.2.4. Experimental procedure.....	100
4.2.4.1. Micro GC calibration.....	100
4.2.4.2. Measurement of temperature profiles.....	101
4.2.5. Results and discussion.....	101
4.2.5.1. Experimental results.....	101
4.2.5.2. CHEMKIN modeling results.....	103
4.2.6. Summary.....	105
4.3. Section II: Cold-flow mixing study.....	105
4.3.1. Experimental setup.....	106
4.3.1.1. Bench-scale apparatus.....	106
4.3.1.2. Experimental parameters and operating conditions.....	106
4.3.1.3. Gas flowrates.....	107
4.3.2. Experimental procedure.....	107
4.3.2.1. Orientations and positions of holes.....	107
4.3.2.2. Mixing measurement methodology.....	108
4.3.2.3. GC calibration.....	109
4.3.2.4. Calibration of mass flow controllers.....	109
4.3.3. Results and discussion.....	109
4.3.4. Uncertainty analysis.....	111
4.3.4.1. Sealing of the system.....	111
4.3.4.2. Uncertainty of the inlet flows.....	112
4.3.4.3. Uncertainty in sampling and data collection.....	112
4.3.4.4. Uncertainty in data analysis.....	113
4.3.5. Summary.....	114
4.4. References.....	115
5. MODELING.....	138
5.1. Overview.....	138
5.2. Section I: Calculated impacts of diluents on flame temperature, ignition delay and flame speed of methane-oxygen mixtures at high pressure and low to moderate temperatures.....	139
5.2.1. Overview.....	139
5.2.2. Introduction.....	140
5.2.3. Chemical kinetic models, mechanisms and validation.....	142
5.2.4. Results and discussion.....	143
5.2.4.1. The effect of diluents on adiabatic flame temperature.....	143
5.2.4.2. The effect of diluents on ignition-delay time.....	145
5.2.4.3. The effect of diluents on flame speed.....	149
5.2.5. Summary.....	153
5.3. Section II: Determination of ignition bounds when including heat transfer considerations.....	155
5.3.1. Introduction.....	155
5.3.2. Modeling.....	155
5.3.3. Results and discussion.....	157
5.4. References.....	158

6. SUMMARY AND CONCLUSION.....	173
6.1. Overview	173
6.2. Introduction	173
6.3. Summary and conclusions.....	174
6.4. Recommendations for future work.....	180
6.5. References	181
Appendices	
A: CHEMKIN CALCULATION TO FIND GAS PROPERTIES	182
B: DETERMINING THE EXHAUST GAS INITIAL PROPERTIES	187
C: DETERMINING THE EXHAUST GAS FINAL PROPERTIES	191
D: DETERMINING THE PROPERTIES OF THE BOILING OIL	194
E: DETERMINING THE GAS PHYSICAL PROPERTIES	198
F: CATALYTIC EXPERIMENTAL STUDY CATALYTIC MATERIALS PROPERTIES.....	205

ACKNOWLEDGEMENTS

I begin by expressing my most sincere gratitude and appreciation to Dr. Eddings and Dr. Silcox for their encouragement and support throughout my graduate studies. They allowed me the freedom to initiate new ideas, and were always there to lend a listening ear and provide constructive feedback. Their technical and editorial advice was invaluable to the completion of this dissertation.

I also express my heartfelt appreciation to my advisory committee, Dr. Deo, Dr. MacLennan, and Dr. Switzer, for their critical comments and guidance on my research.

I would like to express my gratitude to Dr. Ignacio Preciado, who helped me with the experiment in the lab, and also for her invaluable advice during the research. I would also like to thank Dana Overaker for his assistance in ordering and buying lab materials, equipment repair and maintenance.

I would like to appreciate my husband, Hossein, and my daughter, Lenna, for their support, encouragement, patience, and companionship that have turned my journey through graduate school into a pleasure. I am deeply thankful to my parents, my brother, and my sisters for their faith in me and for encouraging me to be ambitious. Their love and continuous encouragement has always given me the strength to tackle challenges.

I would like to appreciate the American Shale Oil, LLC (AMSO) for their financial support in this project.

CHAPTER 1

INTRODUCTION

1.1. Overview

The primary objective of this project is to develop a downhole heater to raise oil shale to a specified temperature in order to recover energy-rich liquids and gasses. The project has two main phases. Phase One was a preliminary study investigating several different heater concepts for generating heat at great depth and over significant horizontal lengths. That preliminary study included engineering calculations of overall energy balances, heat transfer, and pressure drop. Two heater concepts, based on homogenous oxidation and flameless catalytic oxidation, were then investigated. In Phase Two, a unique configuration of a downhole heater was proposed which eliminates some of the issues regarding the existing configurations. The feasibility and applicability of the proposed heater were explored by addressing some key issues that have not been completely addressed in the literature by other researchers. The questions addressed in Phase Two are:

- 1- Do some inexpensive and widely available metals have reasonable catalytic activity and durability such that they can be considered as a catalyst for methane oxidation in our application?
- 2- How to design heater nozzles for a 2000-ft-long heater so that the fuel/oxidizer distribution, and thus heat release, remains uniform.

- 3- How does nozzle orientation and position in the heater affect mixing of fuel and oxidizer?
- 4- How does the presence of exhaust gas in the heater affect the performance of the heater?
- 5- How do the chemical and thermodynamic properties of the components of exhaust gases N_2 , CO_2 or H_2O , affect the ignition-delay time of methane?
- 6- Which specific methane oxidation reactions are affected by diluents such as N_2 , CO_2 or H_2O ?

1.2. Introduction

There are large underground oil shale deposits in the U.S. and around the world. Heating oil shale deposits to about 300 °C results in shale oil and natural-gas-like production via pyrolysis of kerogen within the rock. There are two ways to heat the oil shale and extract the hydrocarbons: surface retorting and in-situ retorting. The first method has three steps: 1) mining the oil shale, 2) thermal processing to obtain a refinery feedstock and 3) disposal of the spent shale. The second method involves heating the oil shale underground to extract the hydrocarbons directly. There has been increasing attention given to the second method, in-situ retorting, especially for deep formations or other situations where mining is less suitable. In particular, in-situ retorting doesn't have many of the disadvantages of surface retorting, and it provides the opportunity to recover deeply-deposited oil shale.¹ The Conduction, Convection, Reflux (CCRTM) retorting process is one of the in-situ heating and extraction processes proposed by AMSO, LLC.² Figure 1.1 is a schematic of the CCR process. There is a boiling pool of shale oil in the bottom of the

retort, in contact with a heat source. Hot vapors from the boiling pool recirculate through the retort by natural convection and heat the surrounding oil shale. It is hypothesized that heating the shale may cause it to fracture and further enhance the effective permeability of the retort. Thus, more oil shale is exposed to the hot vapors. The hot vapors condense on recently exposed oil shale and drain to the boiling pool. As the oil shale reaches temperatures between 300 °C and 350 °C, the pyrolysis rate of the kerogen becomes high enough to yield oil and gas in a reasonable time frame.

A downhole heater is proposed as an efficient way to provide the heat required to boil the pool. A schematic of the heater is shown in Figure 1.2. Fuel and oxidizer pass through the 2000-ft vertical well to the mostly horizontal borehole where the boiling pool is distributed. The downhole heater is placed in the horizontal section where there is a counter-current heat exchange between the incoming fuel/oxidizer and the outgoing flue gas. AMSO, LLC, who was a financial sponsor of this project, was interested in developing a downhole heater technology for in-situ processing of oil shale.

Two preliminary heater configurations were proposed by AMSO, LLC.³ Under a research agreement, the University of Utah initiated a preliminary study investigating the feasibility of the proposed heaters. A brief explanation of the configurations is presented in the following section.

1.2.1. Permeable membrane heater

The permeable membrane heater shown in Figure 1.3 was the first heater configuration proposed and patented by AMSO, LLC.³ It is based on regions of heterogeneous and homogeneous combustion. It has one open end that provides both gas inflow and outflow.

There is a permeable membrane acting as a flow restriction medium that divides the interior volume of the heater housing into an inner flow pathway and an outer flow pathway. The permeable membrane is made from catalytic material that has a permeability to provide a controlled transverse flow from the inner to the outer pathway. Premixed fuel and oxidizer flows through the inner pathway towards the closed end.

As the premixed gases flow through the heater, they permeate the catalytic material and catalytically combust. The flue gases return to the surface in the outer annulus and flow countercurrent to the premixed fuel and oxidant. The flue gases preheat the fuel and oxidizer. There are number of concerns regarding the permeable membrane configuration;

- Safely handling the combustible premixed gases
- Deactivation and poisoning of the catalytic membrane, which would cause a problem in long-term operation
- Difficulty in achieving the desired flowrate of fuel and oxidant along the heater
- Difficulty in obtaining a uniform temperature along the heater
- Unknown type of permeable membrane

1.2.2. Segregated zone catalytic oxidation heater

The second configuration proposed by AMSO was a segregated zone catalytic heater, which would be based on a hybrid heterogeneous/homogeneous reaction.³ This section provides a brief explanation of the heater configuration and feasibility study.

A schematic of the catalytic heater is presented in Figure 1.4. The heater has an inner annulus for the flow of oxidant and outer flow of exhaust gases. A separate line injects the fuel. The inner annulus has several reaction zones. Each has a mixing section where the

oxidizer and the fuel mix, and a thin catalytic bed where the oxidation occurs. The flue gases pass through the outer annulus, preheat the fuel and oxidizer, and return to the surface. Although the flameless catalytic oxidation concept can provide the desired temperature and the heat needed to retort the oil shale, there are some concerns regarding this design:

- Dilution of the oxygen along the length of the heater
- Ensuring sufficient mixing of fuel and oxidizer
- Preventing ignition of the fuel/oxidizer mixture before reaching the catalyst bed
- Preventing channeling of the gas mixture in the catalytic beds
- Excessive pressure drop in catalytic beds
- Finding a catalyst with a reasonable lifetime and thermal stability for long-term operation

To address some of the concerns, we performed detailed bench-scale experiments to examine the catalytic activity of several metals, as well as a Pd-coated catalyst, for dilute methane oxidation. Commercial chemical kinetics software⁴ was also used to model homogenous methane oxidation under a range of conditions. In addition, kinetic parameters were derived from the experimental data to start engineering calculations for heater design. Additional details and results of these analyses are presented in Chapter 4.

Based on the results obtained in these preliminary studies, we proposed a new heater configuration that is based on homogenous oxidation. The new design can eliminate some of the issues regarding the two configurations discussed above. A brief explanation of the new heater configuration is presented in the following.

1.2.3. Homogenous heater configuration

The new configuration is shown in Figure 1.5. The heater includes an outer annulus to convey the flue gas and an inner annulus containing two separate pipes for fuel and oxidizer. Each pipe has multiple holes acting as small nozzles to introduce nonpremixed fuel and oxidizer along the length of the heater. The fuel and oxidizer would be injected into the reaction chamber, or inner annulus, in a manner that would create sufficient mixing. The mixing would also be controlled by the relative locations of the nozzles to produce a dilute combustion environment to control peak temperatures and NO_x formation. Flue gas may also be used as a diluent to help control temperatures, assist with mixing, and control the rate of the combustion reactions and thus keep the flame temperatures in the desired range.

The fuel and oxidizer mix and autoignite under the high-pressure conditions inside the heater. Combustion of fuel and oxidizer takes place in the reaction chamber that has holes to allow flue gas to escape into an annular exhaust pathway. The length of the heater can be divided into a series of separate reaction chambers or mixing zones, to prevent accumulation of combustion products. The ideal situation is to have a complete reaction within each mixing zone so that there would not be a significant amount of unburned fuel within the chamber.

1.3. Research objectives

The main objective of this project is to develop a downhole heater to heat oil shale to a specified temperature in order to recover energy-rich liquids and gasses.

The project has two main phases. Phase One was a preliminary study that included

overall energy balances, heat transfer and pressure drop calculations and some catalytic performance testing, which helped to identify the optimum heater configuration that could eliminate some of the issues regarding the initially-proposed configurations. Phase Two focused on addressing some of the key scientific issues related to the new downhole heater configuration, or any other homogenous oxidation heaters, that have not entirely been addressed by other researchers in the literature and that will affect the design of gas-fired downhole heaters. The key issues and questions addressed in Phase Two are listed below.

1. Having a uniform gas distribution along the 2000-ft heater is one of the key parameters to maintain a uniform heat release inside the heater. Therefore, the first issue to be addressed in designing the heater is to develop a procedure to calculate the size of the injector nozzles so that there is a uniform distribution of fuel/oxidizer along the 2000-ft length of the heater. Most of the calculation procedures developed in the past have been based on the assumption that the gas is injected through a nozzle into an environment with a constant pressure. In addition, the procedures aren't applicable to a very long manifold.⁵⁻⁸ In this project, a calculation procedure was developed to determine the size of the holes for a very long manifold (2000 ft). The developed method is also applicable to a situation where gas is injected from the nozzle to a nonconstant pressure environment. The details of these procedures will be presented in Chapter 3.

2. As explained in Section 1.2.3, in the proposed heater configuration, the fuel and oxidizer are injected through nozzles in the feeder pipes and into the reaction chamber. Gases mix and react in the chamber. Mixing plays an important role in determining ignition behavior, local temperature, and pollutant formation. Therefore, it is critical

to choose the position and orientation of the nozzles so that appropriate mixing occurs in each section of the reaction chamber. As a result, the second question to be addressed in this phase of the project is how the nozzle orientation and position within the heater affect the fuel and oxidizer mixing and subsequent combustion behavior. The answer to this question is critical for the design of either a downhole heater, or any other flameless heater, oxy-fuel combustor or homogenous oxidation device. Most of the available studies in this area have focused on two impinging jets.⁹⁻¹⁹ Some of them also investigate the effect of the shape of the nozzle on gas mixing behavior.^{20,21} However, to our knowledge, data are not available to analyze the effect of nozzle position and orientation in a configuration similar to that shown in Figure 1.5. Cold flow experiments were performed to understand the mixing of gases inside such a chamber and these results are presented in Chapter 4.

3. It is also important to look at the reactions occurring inside the chamber and investigate how the presence of exhaust gas species in the reaction chamber affect ignition and oxidation behavior. In the proposed downhole heater, as well as in many oxy-fuel combustors and gas turbines, part of the exhaust gas is recirculated to lower the temperature and control pollutant formation. The exhaust gas in oxy-fuel combustion mainly consists of CO_2 and H_2O . The effect of CO_2 on the oxidation of the methane or natural gas has been well-studied by other researchers. There are also some experimental and modeling data available on the effect of water addition on methane oxidation (please refer to Chapter 2 for references). However, few studies have performed sensitivity analysis to determine the effect of water addition on reaction rates. This study used CHEMKIN to provide a fundamental understanding of

how chemical and thermodynamic properties of diluents inhibit or promote the reactivity of the gas mixture of interest. In Chapter 5, we address these fundamental questions.

1.4. Summary

The dissertation consists of five chapters: (1) Introduction, (2) Literature review, (3) Engineering calculations, (4) Experimental work, and (5) Modeling and reaction analysis.

Chapter 1 introduces the project. It includes the motivations and objectives, as well as a brief summary. Chapter 2 reviews the literature on homogenous oxidation and autoignition of methane and oxygen mixtures at high pressure and low to moderate temperatures ($P=10-30$ atm, $T=800-1800K$). The effects of the temperature, pressure, diluents (N_2 , CO_2 , and H_2O) and other components (lighter hydrocarbons and H_2) on flammability limit, autoignition, and flame stability of methane/oxygen mixture are explored. Chapter 3 presents engineering calculations to evaluate the feasibility of the new heater configuration. The calculations included:

- Pressure drop calculations to determine the range of operating pressures.
- Macroscopic mass, momentum and energy balance calculations to determine appropriate sizes for feeder pipes and nozzles.
- Overall energy balance and heat transfer calculations to estimate the required gas mixture temperature.

Chapter 4 is a summary of the experimental work. The experiments consisted of two parts: (1) tests to explore the catalytic activity of metals used in heater construction and (2) cold flow studies to determine the effect of nozzle orientation and spacing on the mixing

of gases. Chapter 5 consists of the modeling studies and reaction analysis. This chapter has two main objectives: First is to perform thermodynamic calculation of fuel/oxidizer mixtures with varying levels of dilution over a range of temperatures and pressures to determine the approximate adiabatic flame temperature. Second is to perform CHEMKIN simulations to determine the bound of ignition (autoignition) and understand the chemical and thermodynamic effects of water on methane oxidation. In Chapter 5, the effect of diluents, especially water dilution, on methane ignition delay time, flame speed, and flame temperature is also studied. The sensitivity analyses and reaction pathway analyses are performed to determine which of the elementary reactions inhibits reactivity and which one promotes it in the presence of diluents.

1.5. References

- (1) AMSO, Oil Shale Extraction Methods, <http://amso.net/about-oil-shale/oil-shale-extraction-methods>.
- (2) A.K.Burnha; R.L.Day; P.H.Wallman; J.R.McConaghy; H.G.Harris; P.Lerwick, et al. In situ method and system for extraction of oil from shale. US 8,162,043 B2 US patent, **2010**.
- (3) L.Furman; Z.Stegowski. *Chem. Eng. Process.* **2011**, *50*, 300-304.
- (4) V.Patkar; A.Patwardhan. *Chem. Eng. Res. Des.* **2011**, *89*, 904-920.
- (5) Ph.Wood; A.Hrymak; R.Yeo; D.Johnson; A.Tyagi. *Physics of Fluids A*, **1991**, *3*, 1362-1368.
- (6) M.Bouaifi; M.Mortensen; R.Andersson; W.Orciuch; B.A.Andersson; F.Chopard; T.Noren. *Chem. Eng. Res. Des.* **2004**, *82*, 274-283.
- (7) W.F.Li; Y.Wei; G.Tu; Z.Shi; H.Liu. *Chem. Eng. Sci.* **2016**, *144*, 116-125.
- (8) A.Orfanotis; C.Fonade; M.Lalane; N.Doubrovine. *Can. J. Chem. Eng.* **1996**, *74*, 203-212.
- (9) X.Song; J.R.Grace; H.Bi; J.Lim; E.Chan; B.Knapper; C.A.MvKnight. *Ind. Eng. Chem.*

Res. **2005**, *44*, 6067-6067.

- (10) J.Holman; D.S.Liscinsky; V.L.Oechsle; G.S.Samuelsen; C.E.Smith. Birmingham, UK : s.n., **1996**. *41s Gas Turbine and Aeroengine Congress*.
- (11) J.Holdeman; D.S.Liscinsky; D.B.Bain. Orlando, Florida : s.n., **1997**. *42nd Gas Turbine and Aeroengine Congress*.
- (12) J.Holdeman. Sacramento, California : s.n., **1991**. *27th Joint Propulsion Conference*.
- (13) M.Boutazakhti; M.J.Thomson; M.Lightstone. *Combust. Sci. Technol.* **2001**, *163*, 211-228.
- (14) D.S.Conochi; N.B.Gray. *Miner. Process. Extr. Metall*, **1979**, *88*, 14-18.
- (15) A.S.Larsson; S. P. Johansson; T.Lundstrom; B.Marjavaara. *Exp. Fluids*, **2015**, *56*, 1-12.
- (16) M.Blomeyer; B.Krautkremer; D.K.Hennecke. *J. Propul. Power*, **1999**, *15*, 288-295.
- (17) N.Donohoe; K.A.Heufer; C.J.Aul, E.L.Petersen; G.Bourque; R.Gordon; H.J.Curran. *Combust. Flame*, **2015**, *162*, 1126-1135.
- (18) T.L.Cong; P.Dagaut. *Energy & Fuel*, **2009**, *23*, 725-734.
- (19) A.Goy; J.Moran; G.O.Thomas. *ASME*, **2001**, *2*, 1-7.

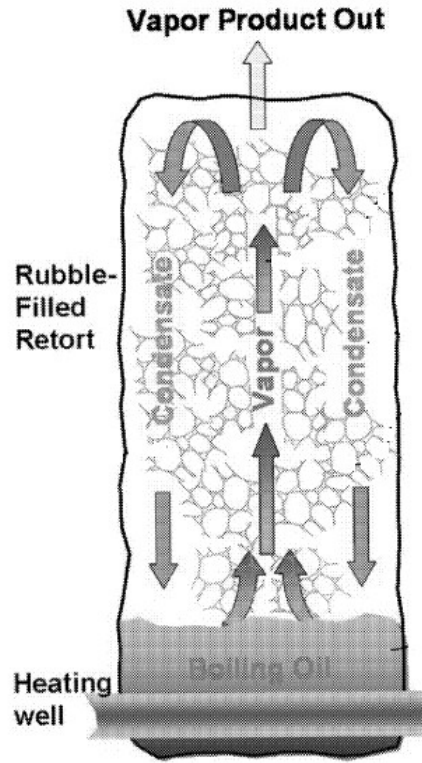


Figure 1.1: Schematic of the CCR™ process²

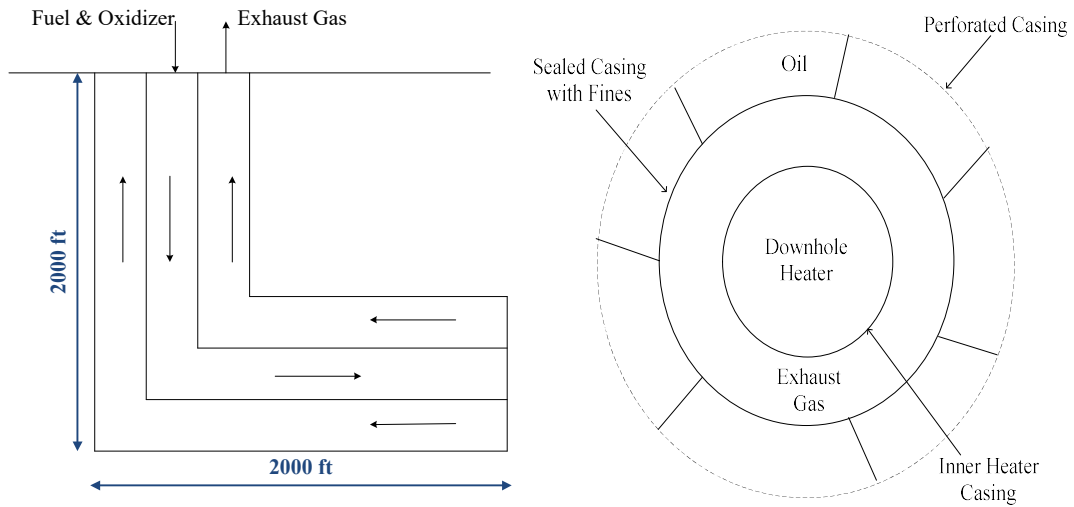


Figure 1.2 : Schematic of a generalized downhole heater

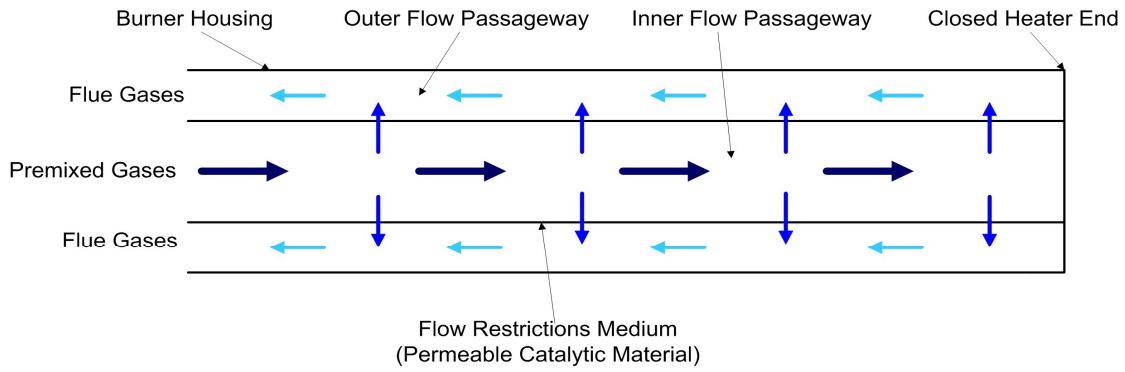


Figure 1.3: Permeable membrane heater configuration³

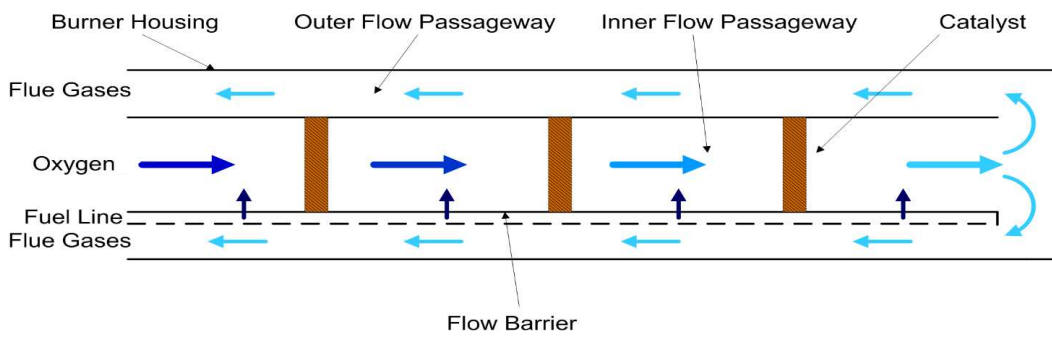


Figure 1.4: Segregated zone catalytic oxidation heater configuration³

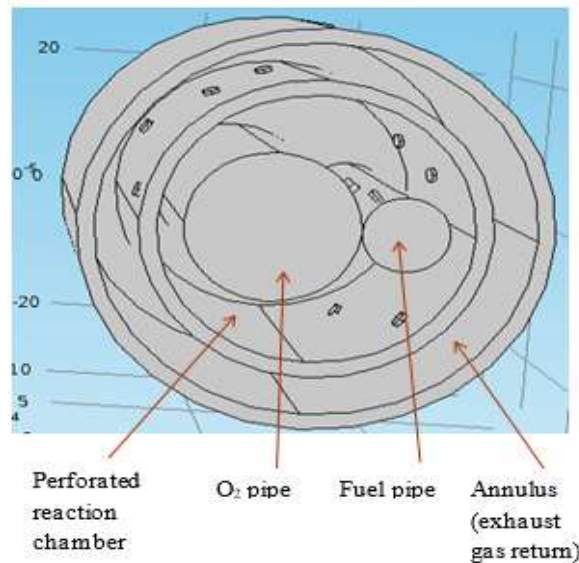


Figure 1.5: Heater configuration based on the homogenous reaction concept

CHAPTER 2

LITERATURE REVIEW

2.1. Overview

Chapter 2 consists of two sections focusing on two heater concepts: Section I covers homogeneous oxidation and Section II covers catalytic oxidation. Section I provides a brief explanation of the proposed heater configuration and then addresses autoignition, flammability limits and flame stability of the fuel/oxidizer mixture at the heater operating conditions. Section II examines catalysts used in methane oxidation. Research results for two categories of catalyst, noble metal and transition metal, are explored and brief results for the alumina – supported Pd catalyst used by the University of Utah are also presented. A brief summary is provided at the end of each section.

2.2. Section I: Proposed configuration for homogeneous underground heater and associated literature on homogenous combustion

2.2.1. Overview

The purpose of the project is to develop a heater for in-situ heating of oil shale to recover energy-rich liquids and gases. The heater will heat the shale to a specified temperature along a horizontal length of about 2000 ft. To fulfill this purpose, the

University of Utah proposed a new heater configuration that is described briefly in this section. This section goes on to review the literature on homogeneous combustion, particularly regarding ignition, flammability properties, and flame stability.

2.2.2. Heater configuration

The heater configuration is shown in Figure 2.1. The heater includes two separate pipes carrying fuel and oxidizer. Each pipe has several holes acting as small nozzles to introduce the nonpremixed fuel and oxidizer along the length of the heater. The fuel and oxidizer would be injected into the reaction chamber in a manner that would create sufficient mixing. The mixing would also be controlled by the relative locations of the fuel and oxidizer nozzles to produce a dilute combustion environment so as to control peak temperatures and NO_x formation. Flue gas or CO₂ may also be used as a diluent to assist with mixing, to control the rate of the combustion reactions and thus keep the flame temperatures low.

The fuel and oxidizer mix and autoignite under the high-pressure conditions inside the heater. Combustion of fuel and oxidizer takes place in the reaction chamber that has holes to allow for flue gas to escape into an annular exhaust pathway. The ideal situation would be to have complete reaction within each mixing zone so that there would be insignificant amounts of unburned fuel. One of the concerns about the underground heater is how to initiate the reaction. The goal is to mix the fuel and oxidizer under conditions such that autoignition can occur. Therefore, it is important to know the autoignition and flammability properties of the fuel/oxidizer mixture for the range of operating conditions anticipated. It

is also beneficial to know the effects of hydrogen and higher alkanes in the fuel, as well as combustion products, on the reaction kinetics. The following is a literature review that addresses these concerns.

2.2.3. Flammability limits

2.2.3.1. Definition of flammability limits

Flammability limits are defined as the concentration range in which a flammable substance can produce a fire or explosion when an ignition source (such as a spark or open flame) is present. The concentration in air is generally expressed as percentage fuel by volume in the vapor phase. Additionally, flammability limits are divided into two types: (i) the upper flammable limit (UFL) above which the fuel concentration is too rich (deficient in oxygen) to burn and (ii) the lower flammability limit (LFL) below which the fuel concentration becomes too lean (excess oxygen) to be ignited.¹

Crowl and Louvar defined the limiting oxygen concentration (LOC) as the lowest oxygen concentration where combustion can occur. The lower oxygen limit (LOL) is the lowest fuel concentration in pure oxygen that combusts and the upper oxygen limit (UOL) is the maximum fuel concentration in pure oxygen that combusts.

2.2.3.2. Correlations to estimate the flammability properties

There are several correlations to estimate the flammability properties. Some of them are discussed in this section.²

1- Jones 1938 proposed a simple relationship to evaluate these properties.

$$y_{LFL} = \frac{5.50 C_{st}}{100} \quad (2.1)$$

$$y_{UFL} = \frac{3.50 C_{st}}{100} \quad (2.2)$$

where C_{st} is the stoichiometric volume % fuel in air

2- Suzuki 1994 related the heat of combustion (ΔH_c) of the fuel to the UFL and LFL.

$$y_{LFL} = \left(\frac{-3.42}{\Delta H_c} + 0.569 \Delta H_c^2 + 1.80 \right) \frac{1}{100} \quad (2.3)$$

$$y_{UFL} = \left(6.30 \Delta H_c + 0.567 \Delta H_c^2 + 23.5 \right) \frac{1}{100} \quad (2.4)$$

where ΔH_c is the heat of combustion ($\frac{kJ}{mol}$). Scott suggested the Burgess-Wheeler law, for the effect of temperature on the LFL and UFL of hydrocarbons in the absence of cool flames, which is expressed by Equation (2.5) and Equation (2.6)¹ where ΔH_c is the net heat of combustion (kcal/mole) and T is in °C.

$$LFL_T = LFL_{25} - \frac{0.75}{\Delta H_c} (T - 25) \quad (2.5)$$

where

LFL_T =lower flammability limit at temperature T

LFL_{25} =lower flammability limit at temperature 25°C

ΔH_c =Heat of combustion (kcal/mol)

T=Temperature (°C)

$$UFL_T = UFL_{25} + \frac{0.75}{\Delta H_c} (T - 25) \quad (2.6)$$

UFL_T =upper flammability limit at temperature T

UFL_{25} =upper flammability limit at temperature 25°C

ΔH_c =Heat of combustion (kcal/mol)

T=Temperature (°C)

V. Babrauskas also proposed equations showing the dependence of LFL and UFL on pressure.¹

$$LFL_p = LFL_{1atm} - 0.31 \ln P \quad (2.7)$$

$$UFL_p = UFL_{1atm} + 0.89 \ln P \quad (2.8)$$

Vanderstraeten et al.³ determined the upper flammability limit of methane / air mixtures at pressures up to 54.3 atm and temperatures up to 473K. They correlated their data by one correlation for the pressure-dependence of the UFL and one correlation for the temperature-dependence of the UFL.

$$UFL(P_1) = UFL(P_0) \left[1 + a \left(\frac{P_1}{P_0} - 1 \right) + b \left(\frac{P_1}{P_0} - 1 \right)^2 \right] \quad (2.9)$$

$$UFL(T_1) = UFL(T_0) \left[1 + c \left(\frac{T_1 - T_0}{100} \right) \right] \quad (2.10)$$

The coefficients a , b and c are given in Table 2.1 and Table 2.2. F. Van den Schoor et al. proposed four different methods to calculate the flammability limits.⁴⁻⁷ They used two of those methods to calculate LFL of a methane / air mixture at initial pressures in the range of 1– 30 atm and initial temperatures in the range of 298 -473K. They showed that at around 20 atm and 473K, the LFL of the methane / air mixture would be about 4.1 mole % and the UFL would be about 39 vol%. However, M. Caron et al.⁸ found a wider range for the flammability limits. Please refer to reference 5 for more information. In summary, pressure has only a slight effect on the LFL except at low pressure (<50 mmHg absolute), where flames do not propagate, while the UFL increases considerably as the pressure

increases.¹ The LFL decreases slightly with increasing pressure while the UFL is highly sensitive to pressure. Pressure and temperature are not the only factors that affect the flammability conditions. For underground heaters, it is helpful to use oxygen instead of air to avoid handling large flowrates of N₂. It may also be useful to use flue gas to control temperature. Therefore, it is worthwhile to discuss the effects of diluents and higher oxygen levels on flammability limits.

2.2.3.3. Effect of oxygen concentration on flammability limits

Upper flammability limits are sensitive to oxygen concentration while LFLs are not. Since the LFL is a fuel-lean condition, any additional excess oxygen acts as a diluent. In addition, the molar heat capacities of oxygen and nitrogen are similar, so the LFL value is not changed by going to a 100% oxygen atmosphere.¹ However, the UFLs increase sharply with increasing oxygen concentrations.

As mentioned before, if we dilute the oxygen concentration in the air continuously, the LFL and UFL converge at one point which is called the limiting oxygen concentration (LOC), below which the fuel-air mixtures cannot support sustained combustion no matter how large the ignition energy.

2.2.3.4. Effect of inert gases on flammability limits

Generally, inert gases decrease the flammability limits or lead to the mixture being entirely outside the range of flammability. The presence of inert gas mostly affects the UFL, and some gases such as CO₂ affect LFL, too. Studies show that gases with higher

heat capacities (such as CO₂) have a higher LFL than gases with lower heat capacities (such as N₂). Thus, the heat capacity of the inert gas and combustion products can have a great effect on the flammability limits.¹

2.2.3.5. Effect of turbulence on flammability limits

There is a limited amount of data suggesting that turbulence can narrow the flammability range for pure fuel gases/vapors. It has been observed that “The narrowing effect on observed flammability limits has been interpreted as being an MIE (minimum ignition energy) impact: if the experiments are conducted at the same ignition energy and it requires more energy to ignite mixtures that are either turbulent or have an equivalence ratio far away from stoichiometric conditions, then turbulent mixtures will be observed as having a smaller flammability range”.¹

There are other conditions such as experimental apparatus sizing which can affect flammability limits. For more information, please refer to reference 1.

2.2.4. *Autoignition*

2.2.4.1. Definition of autoignition

The autoignition temperature (AIT) is defined as the lowest temperature to which a given mixture of a fuel and an oxidant must be heated to combust spontaneously in the absence of an ignition source. The ignitability of a flammable gas is characterized by its minimum ignition energy (MIE) and its autoignition temperature (AIT). The MIE is the lowest energy content of a point ignition source which ignites the most ignitable mixture

of a fuel and an oxidant.⁹ Like the flammability limit, the AIT of a given mixture is not constant. It depends on the fuel concentration, flow condition, initial pressure and volume of the mixture, as well as the geometry of the explosion vessel. In the following, the effect of pressure and fuel concentration on autoignition temperature is discussed.

2.2.4.2. Effect of pressure and fuel concentration on autoignition temperature

The initial pressure of mixtures affects the autoignition temperature (AIT). Therefore, the AIT values obtained at atmospheric pressure should not be used at high pressures. Higher initial pressures lead to a lower AIT in a given oxidant. For example, the AIT of natural gas in air at 1atm is about 803K, whereas at 610 atm (9,000 psig) the AIT is about 513K.¹⁰

Semenov's equation can be used over a limited pressure range to predict the AIT's of several hydrocarbons.¹⁰

$$\log \frac{P}{T} = \frac{A}{T} + B \quad (2.11)$$

where T is the AIT at an initial pressure P, and A and B are constants.

M. Caron et al.¹¹ investigated the effect of pressure and methane concentration on the autoignition temperature of methane/air mixtures. The initial temperature of the mixture was about 683K in their experiment.

Before discussing the result, it is worthwhile to clarify the definition of autoignition and cool flame used in Caron's paper. The classification criteria for autoignition and cool flame are presented in Table 2.3. It was shown that both fuel concentration and initial

pressure have a significant effect on the autoignition condition of the methane/air mixture. The concentration showing the highest ignitability is found to be about 40 vol. % in terms of the autoignition and the corresponding initial pressures is 7atm. Please note that the results are for a methane/air mixture; the corresponding initial pressure for a methane/oxygen mixture would be less than this amount. Additionally, this experiment was running at considerably high methane concentrations, but the methane concentration in an underground heater would be less than this amount, and there would be flue gases present in the mixture of the methane/oxidizer. As a result, it would be worthwhile to analyze the effect of other gases on AIT.

2.2.4.3. Effects of other gases on autoignition

In addition to what was explained before about the effect of different inert gases on the flammability limit of methane, several studies have been done on the effect of fuel additives. As mentioned before, autoignition is defined as spontaneous and homogeneous ignition of the reactive mixture that results in chemical reactions and hot gases in premixing sections. It is not only a function of pressure and temperature but also fuel, oxidizer, and diluent composition.

Although natural gas mainly consists of methane, its specific make-up can change drastically depending on the geographical location and the season in which it is obtained.^{12,13} Because of the importance of ethane and other alkanes as trace species in natural gas, several studies have been performed since 1963 to study combustion behavior of natural gas and related fuel blends. The experimental work includes mainly shock-tube,

flow reactor, stirred reactor, model combustors and engine studies. An excellent summary of the experimental work up to 1994 is given by Spadaccini et al.¹² The results mainly show that the addition of higher-order hydrocarbons to the methane-based fuel has significant effects on the autoignition behavior of methane at high temperatures ($T > 1300$ K). It reduces the ignition-delay time of the fuel blend.^{12,14}

Many studies also investigate the effect of the most common diluents, N_2 , H_2O , and CO_2 , on methane autoignition. Diluents normally have three impacts on a reaction:

- Change mixture specific heat and adiabatic flame temperature,
- Change chemical kinetic rates,
- Change radiative heat transfer.

The addition of N_2 only changes the mixture specific heat and the adiabatic flame temperature, which can be determined with equilibrium calculations. However, CO_2 has a relatively high specific heat capacity as compared to N_2 . Thus, more fractional energy is taken by CO_2 and would result in lower temperature increases for the same amount of energy release, which means that the temperature rise, the reaction rate, and the flame speed would all be lower. CO_2 also contributes to longer ignition delays and narrower flammability limits than the corresponding values for methane–air mixtures.

In addition, CO_2 absorbs and emits radiation more effectively than O_2 or N_2 . Thus, it enhances the level of radiation and emission and helps to control the temperature in oxy-fuel reaction. Also, unlike N_2 , CO_2 is not chemically inert but directly participates in the reaction through $CO + OH \leftrightarrow CO_2 + H$ ¹⁵ which reduces the concentration of important radicals (H, O, OH) in the combustion chamber and decreases the burning velocity.

Table 2.4 to Table 2.11 show selected summaries of the studies. Some of the more relevant data from shock tube studies and flow reactor studies will be discussed later in this chapter. For more information regarding each of those studies, please refer to the references presented in the tables. Note that most of these studies were conducted at pressures below 10 atm and in the high-temperature regime ($T > 1200\text{K}$). Some of them cover pressures up to 480 atm.^{16–20}

Further analyses were done by Krishnan et al.,²¹ Zellner et al.,²² Frenklach, Bornside,²³ Gardiner et al.,^{22,24} Lamoureux Paillard,¹³ Huang and Bushe,²⁰ and Petersen et al.^{9,14,17–19,25–34} All these attempts led to the development of the GRI-Mechanism,³⁵ which can predict methane chemistry under high-temperature, low-pressure conditions very well. Li and Williams subsequently created a methane reaction mechanism that covers temperatures from 1000 to 2000 K and pressures up to 150 atm.³⁶

Petersen et al.^{9,14,17–19,25–34} also validated models of methane combustion at intermediate temperatures and higher pressures by using their fuel-rich data. Kozubková et al.³⁷ tested the performance of global (one-step and two-step) chemical kinetics models for conditions of argon- and nitrogen-diluted flames. Two configurations, premixed flat flames and nonpremixed counter flow (opposed-jet) flame were considered. They showed that the reliability of global chemistry models was highly dependent on the level of dilution. The one-step predictions were satisfactory for a moderate level of dilution with non-premixed flames. The two-step chemical kinetics also predicted the temperature and concentration of the primary species in premixed flames adequately. Please note that the study was for dilution by argon and nitrogen. There is still doubt if the predictions would be reliable at

high levels of CO₂.

2.2.4.4. Shock tube tests

Goy et al.⁴³ determined the autoignition characteristics of methane over a range of temperatures, pressures, stoichiometric ratios, gas additives, and humidity levels. To assess the suitability of available mechanisms and correlations to predict the autoignition delay times at high pressure and low/moderate temperature, they compared experimental results against predictions using GRI – Mech³⁵ and mechanisms from Spadaccini et al.¹² and correlations from Li and Williams.³⁶ They showed that if the temperature or the pressure increases, the autoignition delay time decreases. However, the dependency of the delay time on temperature is greater than that on pressure. Other researchers, such as Spadaccini et al.,¹² Burcat et al.,⁴¹ and Petersen et al.,¹⁸ reached the same conclusion but under a different range of conditions. There is excellent agreement between Goy's experimental data at high temperature and Burcat's.⁴¹ Since GRI-Mech 3.0 is validated for temperatures above 1350 K, there is also good agreement between the predictions of GRI-Mech and the shock tube data at $T > 1300\text{K}$. However, Goy et al. believe that GRI-Mech over-predicts the delay time at $T < 1300\text{K}$ because it cannot predict the observed changes in activation energy. Therefore, if GRI-Mech is used at lower temperatures, there is a risk of significantly over-predicting the autoignition delay time.⁶⁵ Since there are no other shock tube data available for lower temperature, the authors compared GRI-Mech to the low-temperature, flow reactor data. They showed that there was a remarkable difference between the two experimental techniques at these conditions. In fact, the fuel / air mixing time is embedded

in the flow reactor tests and the autoignition time observed by this technique is longer than the shock tube technique. Three factors contribute to the overall autoignition delay:

- Time for fuel and air to mix
- Time for the fuel and oxidizer temperature to rise
- Chemical kinetic time for the autoignition reactions to initiate

The shock tube technique measures only the delay due to chemical kinetics. Since there was good agreement between data from a flow reactor and the GRI-Mech predictions, they concluded that GRI-Mech takes into account all three delays and can be a reliable mechanism to predict the methane autoignition behavior at low to moderate temperatures and high pressure.⁴³ Please note that the data presented were only for methane / air mixtures and the effect of CO₂ dilution is not considered.

Koroglu et al.³³ also investigated the effects of CO₂ dilution on the ignition of methane in a shock tube experiment. The summary of their experimental conditions is available in Table 2.4. Their data are of interest because they studied the relatively high level of CO₂ dilution (over 30 %) for methane combustion. They compared the experimental results with the predictions of two different natural gas mechanisms: GRI-Mech 3.0 and Aramco Mech 1.3. Both mechanism predictions are in good agreement with the data. However, the Aramco Mech 1.3 predictions are in better agreement. Empirical correlations were also developed for methane ignition at different levels of CO₂ dilution.

They also performed sensitivity analyses to understand the influences of chemistry, collision efficiencies, and heat capacity of CO₂ addition to the gas mixtures. The effects of chemistry and global collision efficiency were negligible for those particular experimental

conditions.

Peterson¹⁷ performed over 80 experiments of the CH₄/O₂ mixture from 1410 to 2040 K at pressures from 10 to 90 atm and equivalence ratios from 0.5 to 4. Table 2.9 shows the mixture compositions used in his experiments. Peterson's correlation for the methane/oxygen ignition delay is presented in Equation (2.12) where τ_{ig} is in seconds, the activation energy (E) is 51.8 kcal/mol, T is in kelvin and concentrations are in mol/cm³.

$$\tau_{ig} = 4.05 * 10^{-15} [CH_4]^{0.33} [O_2]^{-1.05} \exp\left(\frac{E}{RT}\right) \quad (2.12)$$

This correlation is valid for T=1400-2050 K, $\varphi = 0.5 - 2$, and concentrations up to [CH₄]= 3.6*10⁻⁵ mole/cm³, [O₂]= 3.6*10⁻⁵ mole/cm³. In a separate study, Peterson et al.²⁴ studied the ignition behavior of different methane/hydrocarbon and methane/hydrogen mixtures. They used two CH₄-only blends, two CH₄/H₂ blends (80/20 and 60/40), two CH₄/C₂H₆ blends (90/10 and 70/30) and one CH₄/C₃H₈ blend (80/20). The initial temperatures in the experiments ranged mainly from 1090 to 2001 K and pressures were from 0.5 to 25.3 atm. The equivalence ratio was 0.5 ($\varphi = 0.5$). They demonstrated that hydrogen and higher-order hydrocarbons decrease the methane ignition delay time and accelerate methane ignition.

As mentioned before, their observations were at initial temperature equal to 1090 to 2001K which is higher than our desired design condition for the underground heater. Therefore, it is not possible to totally rely on their observations for our case.

Other studies were performed at higher pressures and lower temperatures. For example, J. de Vries et al.⁹ studied the ignition behavior of methane/HC blends covering alkanes through n-pentane at P=20atm, T_{initial}=800K and equivalence ratio of 0.5 ($\varphi = 0.5$). They

studied 21 different fuel mixtures, and Table 2.11 shows that the average ignition time of methane- hydrocarbon blends is about 7.9 ms with a standard deviation of 1.9 ms. This is a relatively small variation compared to the larger impact of hydrocarbons on methane ignition at temperatures greater than 1200 K, as seen in Petersen et al.¹⁴ J. de Vries also showed when the initial temperature is not high, in this special case $T_{\text{initial}}=800\text{K}$, specific hydrocarbons did not seem to have a great impact on the autoignition.

2.2.4.5. Flow reactor tests

Holton et al.⁴⁷ conducted ignition delay time measurements, including methane and ethane mixtures, with small amounts of CO_2 (5 and 10%). They found that ignition-delay in a blend at $\phi=0.5$ and $T=1137\text{K}$, when diluted with 5% CO_2 , increased by only 2%. On the other hand, an addition of 10% CO_2 to the same mixture resulted in longer times by 46%. They related this observation to the third-body collision efficiencies of CO_2 , which is an order of magnitude greater than those of N_2 .

Glarborg et al.^{45,46,66} studied the effect of the CO_2 dilution on the methane oxidation in a flow reactor. They also developed a kinetic model for methane oxidation at a low/moderate temperature and high pressure. The details of their kinetic model will be discussed further in Chapter 5.

In conclusion, there is little autoignition data available in the range of initial temperatures and pressures applicable to the proposed downhole heater designs. Many researchers have studied the autoignition characteristics of natural gas in shock tubes at high temperatures, typically above 1200 K, which is significantly above the inlet

temperature range applicable to the proposed heater. Much work has also been performed in flow reactors at moderate temperatures, but not at high pressure. To our knowledge, there is still a gap over the range of initial temperature from 800 to 1000 K, pressure from 10 to 40 atm, and CO₂ mole fraction more than 30%. Data in this region would help validate combustion reaction mechanisms.

2.2.5. Flame Stability

2.2.5.1. Definition of flame stability

The other important concern related to heater design is flame stability. Flame stability results from a balance of local flame speed and local flow velocity. It is usually characterized by lift-off velocity, lift-off height and blow-out velocity. Conditions for lift-off and blow-out are important in developing a heater with stable flames. Thus, a brief literature review regarding the effect of heater diameter, O₂ concentration and flue gas concentration on flame stability is provided.

2.2.5.2. Correlations to predict lift-off height and blow-out velocity

Several studies have modeled flame stability, lift-off and blow-out phenomena. In general, the models are classified into three categories:⁶⁷

- 1- premixed flame propagation models
- 2- laminar flamelet models
- 3- large-scale turbulent structural mixing models

The premixed flame propagation models assume sufficient premixing ahead of the

lifted flame. The laminar flamelet treat flame lift-off as the quenching of laminar flamelets. Finally, large-scale turbulent structural mixing models consider large-scale turbulent eddies as the controlling stability mechanism. One of the earliest correlations for lift-off height was derived by Kalghatgi.⁶⁸ He conducted several experiments for H₂, CH₄, C₂H₄, and C₃H₆ with a wide range of jet exit diameters and concluded that the lift-off height increases linearly with the jet exit velocity and it is not dependent on jet diameter. He also derived a correlation for lift-off height which is shown in Equation (2.13):

$$h = C_h \left(\frac{v_0}{S_{Lmax}^2} \right) \left(\frac{\rho_{jet}}{\rho_\infty} \right)^{1.5} U_0 \quad (2.13)$$

h : lift-off height (m)

v_0 : fuel kinematic viscosity (m²/s)

S_{Lmax} : maximum laminar flame speed

U_0 : average jet velocity at the nozzle outlet (m/s)

ρ_{jet} : density at the jet exit (kg/m³)

ρ_∞ : air density (kg/m³)

$C_h \sim 50$

He also proposed an empirical equation for the blow-out velocity ($U_{blow\ out}$) for CH₄-air, CH₄-CO₂, C₃H₆-air and C₃H₆-CO₂ at various jet diameters:

$$U_{blow\ out} = S_{Lmax} \left(\frac{\rho_\infty}{\rho_{jet}} \right)^{1.5} (0.017 Re_H) (1 - 3.5 * 10^{-6} Re_H) \quad (2.14)$$

where Re_H is Reynolds number based on dimensionless height, H , which is obtained from

Equation (2.15).

$$H = \left[4 \frac{Y_0}{Y_{st}} \left(\frac{\rho_{jet}}{\rho_\infty} \right)^{0.5} + 5.8 \right] d_0 \quad (2.15)$$

Y_0 : fuel mass fraction at the jet exit

Y_{st} : stoichiometric mass fraction

d_0 : jet exit diameter (m)

Broadwell et al.⁶⁹ also developed a model for blow-out velocity as a function of diameter and maximum flame speed. They showed that the blow-out velocity increased linearly with the fuel nozzle diameter:

$$\varepsilon_B = \frac{d_0 S_L^2 \psi^2 \left(\frac{\rho_0}{\rho_\infty} \right)^{0.5}}{\chi U_{blow\ out}} \quad (2.16)$$

where, ψ is the stoichiometric air-to-fuel ratio, and χ is the diffusivity. ε_B is the ratio of large scale mixing time, τ_d , versus the chemical reaction time, τ_c . Table 2.12 shows the values of ε_B for some fuels.

2.2.5.3. Effect of oxygen concentration on flame stability

Because we will likely use oxygen-enriched gases instead of air as the oxidizer in the system, this section reviews the effect of oxygen concentration on flame stability. Dearden et al.⁷⁰ performed experiments and identified regimes of flame stabilization, lift-off and blow-out of turbulent methane flames with an oxygen enriched co-flowing oxidant stream (oxygen concentration between 21% and 32.5%). It showed that as oxygen concentration increases, the stability region became wider. For example, at 21% O₂, the jet velocity should be less than 5m/s in order to have a stable flame, but at 31% O₂% the stability extends to 20 m/s. Amato et al.⁷¹ observed similar results when they tested the effect of

equivalence ratio on stability of N_2/O_2 oxyfuel flames. They performed the measurements in a premixed swirl combustor; the fuel is injected into the oxidizer stream 150 cm upstream of the combustor to achieve fully premixed conditions. Reactant mixtures were preheated to 500°F (590 K) before reaching the combustor inlet.

Blow-off measurements were obtained with baseline CH_4 -air mixtures, and with $CH_4/O_2/CO_2$ and $CH_4/O_2/N_2$ mixtures. For the CH_4 /air mixtures, blow-off data were obtained by fixing the air flowrate and fuel/air ratio at some stable value. Then, the fuel flowrate was slowly turned down until the blow-off event. As such, blow-off was obtained by decreasing flame temperature and fuel/air ratio at a nearly constant nozzle exit velocity. For the oxygen system, blow-off data were obtained by fixing overall flowrates at some nominal velocity and the fuel/oxygen ratio at the desired stoichiometry. Then, the CO_2 flowrate was increased until the blow-off event. As such, blow-off was obtained at a fixed stoichiometry, a decreasing flame temperature and increasing nozzle exit velocity. A similar procedure was used to obtain a data set with an N_2/O_2 system. It was shown that the mixture with an equivalence ratio equal to 0.9 blows off at lower temperatures, compared to the mixture at equivalence ratio equal to 1, due to the fact that the stoichiometric conditions are associated with slower chemistry.⁷¹

The above results are for N_2/O_2 mixtures, but if we have flue gases such as CO_2 in the system the results would be slightly different as discussed in Section 2.2.5.4, “Effect of flue gas on flame stability.”

Other researchers showed that at any fixed average jet exit velocity, increasing the oxygen concentration reduces the lift-off height. On the other hand, the increase in lift-off

heights with relative average jet exit velocity weakly depends on the oxygen concentration.⁷⁰ They also concluded that the lift-off height increases almost linearly with average jet exit velocity.

2.2.5.4. Effect of flue gas on flame stability

Studies show that $\text{CH}_4/\text{O}_2/\text{CO}_2$ flames have slower chemical kinetics than CH_4/air flames. Thus, they are easier to blow off. This issue was investigated by A. Amato et al.⁷¹ by characterizing the stability boundaries of a swirl-stabilized combustor. They compared near-stoichiometric CO_2 -diluted methane / O_2 flames with lean CH_4/air flames. The blow-off points for CO_2 -diluted systems at different equivalence ratios were studied. Unlike the $\text{CH}_4/\text{N}_2/\text{O}_2$ systems discussed in the previous section, conditions with equivalence ratios closer to stoichiometric are easier to blow off for $\text{CH}_4/\text{CO}_2/\text{O}_2$ mixtures. Thus, if we have excess O_2 in the system, we may be able to improve the stability of the flame. These results were obtained at one atmosphere pressure. The authors also compared the results for $P=1$ atm with the results at $P=15$ atm and showed that as pressure increases, the $\text{CH}_4/\text{O}_2/\text{CO}_2$ flame becomes more difficult to blow off, and thus is more stable.

2.3. Section II: Heterogeneous (catalytic) underground

heater approach and associated literature on

heterogeneous combustion

2.3.1. Overview

A second approach to designing an underground heater is a flameless catalytic heater, which would be based on either a fully heterogeneous reaction or a hybrid heterogeneous/homogeneous reaction. A brief explanation of the heater configuration, as well as some of the concerns regarding this approach, is presented. Then, a brief literature review regarding catalysts used for methane oxidation is presented.

2.3.2. Heater configuration

A schematic of the second heater approach is presented in Figure 2.2. The heater has two main pathways, the inner flow passageway and the outer flow passageway. The inner flow passageway comprises several reaction zones. Each zone has a mixing section for the oxidizer and fuel and a catalytic reaction section. The flue gases pass through the outer flow passageway, preheat the fuel and oxidizer and then return to the surface. In addition to the configuration explained above, there would be another approach, the hybrid approach. A hybrid concept includes a thin disk of catalyst material, mainly for starting up the reaction, followed by an open zone to allow the homogeneous oxidation of the premixed fuel/oxidizer stream. Like the other catalytic approach, the length of the heater would be divided up into a number of reaction zones, which would be hybrid heterogeneous/homogeneous oxidation zones. In both of these approaches, one of the main

concerns would be finding a catalyst with reasonable activity and stability for long-term operation. The focus of this section is mainly on this concern. Several studies have been performed to evaluate catalysts for methane oxidation. They focus on improving the activity, as well as the life-time and stability of the catalyst. The following is a brief literature review of the catalysts proposed for methane oxidation.

2.3.3. Nobel metal catalysts

A major requirement for the catalyst for underground heater purposes is that it must light off the methane/oxidizer mixture at a temperature around 800K and at high pressure.

The catalysts mainly suggested and employed for catalytic flameless combustion are supported noble metals. Noble metals (Pt, Pd, Rh, and Ir) have been widely used for low temperature methane oxidation. Among them, Pt and Pd are used most widely due to their high activities. Pd is even more active than Pt.⁷³ Palladium oxide (PdO) supported catalysts have been shown to initiate the oxidation of methane at about 700K; however, they become deactivated at atmospheric pressure and about 1100K through conversion to Pd and sintering.⁷⁴ There are several factors such as catalyst pretreatment, calcination temperature, precursors, catalyst support, and reaction conditions, which affect the catalyst activity and stability.

In terms of catalyst supports, most studies have focused on alumina as a support for Pd. Li et al.⁷³ summarized these studies, as presented in Table 2.13.

The University of Utah has also performed experiments on complete methane oxidation with an alumina-supported Pd catalyst with the properties in Table 2.14. The experimental

results showed that the catalyst had good activity for methane oxidation. The stability of the catalyst was not tested, however. Additional details of the experiment and the results obtained are provided in Chapter 4.

2.3.4. *Transition metal catalysts*

Apart from noble metals, some other catalysts that are less expensive have been synthesized for methane oxidation. Perovskite-type transition metal oxide mixtures are suggested as replacements for noble metals.⁷⁵⁻⁷⁷ These types of catalysts are generally mixed oxides of general formula $ABO_{3\pm\delta}$, where A is usually a lanthanide ion and B is a transition metal ion like Co, Fe, Mn, or Ni.⁷⁸ For this type of catalyst, most of the tests for activity have been carried out at temperatures around 600°C.⁷⁵⁻⁷⁸

The preparation method determines if a catalyst is active and durable. The procedures mostly proposed cannot readily provide both high surface area and thermal resistance to sintering. Forni et al.⁷⁵ found that flame-hydrolysis (FH) provides perovskitic catalysts with high crystallinity, high surface area, high thermal resistance and high activity for flameless combustion of methane.

In general, these types of catalysts are still not suitable for long-term industrial operation, and research is still going on to improve them. Some companies such as Fast Engineering Ltd.⁷⁹ have claimed that they have developed a hydrocarbon oxidation catalyst which has been operated for 4-5 years at temperatures around 1300–1600 K. This catalyst consists of an alumina carrier coated with nickel oxide, NiO. Additional characteristics are given in Table 2.15.

2.3.5. Summary

Chapter 2 consists of two sections. In Section I, the proposed heater concept is for the homogeneous oxidation of diluted natural gas /oxygen mixtures at high pressures and low temperatures ($P \sim 10\text{-}30$ atm and $T \sim 700\text{-}1000\text{K}$). The main focus of Section I was to study the combustion behavior of that mixture at appropriate heater operating conditions, and investigate the effects of pressure, temperature and diluent on flammability, ignition and stability. The first part of Section I focused on the effects of pressure and temperature on flammability limits. It is demonstrated that both temperature and pressure have a notable effect on flammability limits, such that it is not possible to use flammability data at ambient condition for heater calculations. It was shown that pressure has a more significant effect on UFL than LFL. Generally, we can say that higher pressure tends to keep the fuel mixture in the flammable range. The highest temperature was 473K, which is below our desired operating temperature. If we extrapolate the data to higher temperatures, we can expect to have LFL ~ 3.5 mole % and UFL ~ 47 vol % at 773K and 20 atm. Please note that these numbers are only based on extrapolation and are not accurate enough to be used in critical design calculations.

The above information is all for CH_4 /air mixtures; however, fuel/ O_2 mixtures will likely be used in the proposed heater, and there will likely be flue gas to dilute the system and control the temperature. In addition, we will be using natural gas instead of pure CH_4 in the system; therefore, there will be traces of higher hydrocarbons. Thus, it is important to understand how combustion behavior will change when we have O_2 , flue gas, H_2 and higher hydrocarbons. Table 2.4 to 2.11 summarize the studies performed to investigate

these effects. Two different experimental methods were compared. Experimental data obtained by flow reactors were discussed and shown to be generally more representative of the ignition behavior of the gas mixtures in actual applications. It was also shown that at low or moderate temperature, predictions based on the GRI-Mech kinetic mechanism is more compatible with data obtained from a flow reactor. There are currently little autoignition data available in the range of temperatures from 800 to 1000 K, pressures from 10 to 40 atm, and CO₂ mole fractions greater than 30%. The effect of flue gas as a diluent in the system may push the fuel-oxygen mixture outside the limits of flammability. Thus, it is still necessary to collect data at the desired operating conditions for our proposed heater configuration.

In addition, the effect of higher hydrocarbons and hydrogen on ignition behavior of the fuel/oxidizer mixture was discussed in this section. Research shows that although the presence of higher hydrocarbons and hydrogen can accelerate methane ignition at high initial temperatures (1200-2000K), it doesn't have any significant effect on methane ignition at lower temperatures (T~800K). Please note that those studies were done mostly at high pressure (P~20 atm), and the effect of pressure was also considered in the results. We can conclude that there would be a minor effect of higher hydrocarbons and hydrogen on ignition properties of methane at our desired operating conditions.

Finally, flame stability was reviewed. There are several factors, such as pressure, nozzle diameter, gas exit velocity, O₂ concentration, and flue gas species concentration that affect flame stability. The data show that the presence of flue gas species such as CO₂ decrease flame stability. On the other hand, increasing the pressure or O₂ concentration

help to improve flame stability.

In Section II, a brief explanation of the catalytic heater configuration was provided. This section was mostly focused on studies carried out to find a suitable catalyst for methane oxidation. Methane oxidation catalysts are divided into two categories, noble metal catalysts and transition metal catalysts.

Noble metal oxide-supported catalysts usually show good activity, but they can be sintered and deactivated at higher temperatures. The University of Utah also performed an experimental study and investigated the activity of an alumina-supported Pd catalyst on methane oxidation. The catalyst showed very good activity towards methane oxidation but the long-term stability of the catalyst was not tested. For more information regarding this experiment, please refer to Chapter 4.

Several studies have been done so far to investigate the effect of different transition metals, precursors, catalyst supports as well as synthesis methods on the activity and stability of the catalysts. Fast Engineering Ltd. has claimed⁷⁹ that they developed a transition-metal-type catalyst for hydrocarbon oxidation that worked for 4-5 years at temperatures in the range of 1300–1600 K. This catalyst consists of an alumina carrier coated with nickel oxide, NiO. Some specifications of this catalyst were provided in Table 2.15. No additional information has been found for this catalyst to date.

2.4. References

- (1) Zhao, F. Experimental measurements and modeling prediction of flammability limits of binary hydrocarbon mixtures, Texas A&M University, **2008**.
- (2) Hansen, T. Estimation of the flammability zone boundaries with thermodynamic and

empirical equations, Michigan Technological University, **2009**.

(3) Berghmans, J. J. *Hazard. Mater.* **1997**, *56*, 237–246.

(4) Van den Schoor, F.; Verplaetsen, F.; Berghmans, J. *Int. J. Hydrogen Energy* **2008**, *33*, 1399–1406.

(5) Schoor, F. Van Den; Norman, F.; Vandebroek, L.; Verplaetsen, F.; Berghmans, J. J. *Hazard. Mater.* **2009**, *164*, 1164–1170.

(6) Van den Schoor, F.; Hermanns, R. T. E.; van Oijen, J. A.; Verplaetsen, F.; de Goey, L. P. H. J. *Hazard. Mater.* **2008**, *150* (3), 573–581.

(7) Van den Schoor, F.; Verplaetsen, F.; Berghmans, J. J. *Hazard. Mater.* **2008**, *153* (3), 1301–1307.

(8) Caron, M.; Goethals, M.; Smedt, G. De; Berghmans, J. J. *Hazard. Mater.* **1999**, *A65*, 0–11.

(9) Vries, J. De; Petersen, E. L. In *Proceedings Combustion Institute*; **2007**, *31*, 3163–3171.

(10) Zabetakis, M. G. *Bur. Mines Bull.* **1965**, *627*, 1–129.

(11) Caron, M.; Goethals, M.; De Smedt, G.; Berghmans, J.; Vliegen, S.; Van't Oost, E.; van den Aarssen, A. J. *Hazard. Mater.* **1999**, *65* (3), 233–244.

(12) Spadaccini, L. J.; Colket, M. B. I. I. I. *Prog. Energy Combust. Sci.* **1994**, *20* (5), 431–460.

(13) N. Lamoureux, C.E. P. *Shock Waves* **2003**, *13*, 57–68.

(14) de Vries, J.; Petersen, E. L. In *Energy Convers. Resour., ASME Int. Mech. Eng. Congr. Expo.*; American Society of Mechanical Engineers, **2005**; 209–219.

(15) Heil, P.; Toporov, D.; Fo, M.; Kneer, R. In *Proceedings Combustion Institute*; **2011**, *33*, 3407–3413.

(16) Tsuboi, T.; Wagner, H. G. In *Proceedings Combustion Institute*; **1975**, *15*, 883–890.

(17) Davidson, D. F.; Hanson, R. K.; Petersen, E. L.; Ro, M.; Bowman, C. T. In *Twenty-sixth Symposium on Combustion/The Combustion Institute*; **1996**; 799–806.

(18) Petersen, E. L.; Davidson, D. F.; Hanson, R. K. *Combust. Flame* **1999**, *290*, 272–290.

(19) Zhukov, V. P.; Sechenov, V. A. *Combust. Explos. Shock Waves* **2003**, *39* (5), 487–495.

- (20) Huang, J.; Bushe, W. K. *Combust. Flame* **2006**, *144* (1/2), 74–88.
- (21) Krishnan, K. S.; Ravikumar, R.; Bhaskaran, K. A. *Combust. Flame* **1983**, *49* (1–3), 41–50.
- (22) Zellner, R.; Niemitz, K. J.; Warnatz, J.; Gardiner Jr., W. C.; Eubank, C. S.; Simmie, J. M. *Prog. Astronaut. Aeronaut.* **1983**, *88* (Flames, Lasers, React. Syst.), 252–272.
- (23) Frenklach, M.; Bornside, D. E. *Combust. Flame* **1984**, *56* (1), 1–27.
- (24) Yang, H.; Lissianski, V.; Okoroanyanwu, J. U.; Gardiner Jr., W. C.; Shin, K. S. *Chem. Phys. Process. Combust.* **1993**, 117–120.
- (25) Mcdonell, V.; Petersen, E. *J. Eng. Gas Turbines Power* **2008**, *130* (January), 1–10.
- (26) de Vries, J.; Petersen, E. L. *Proc. Combust. Inst.* **2007**, *31* (Pt. 2), 3163–3171.
- (27) Mcdonell, V. G. *J. Eng. Gas Turbines Power* **2016**, *130* (September 2008), 1–8.
- (28) Norman, F. Influence of Process Conditions on the Autoignition Temperature of Gas Mixture, Katholieke Universiteit Leuven, **2008**.
- (29) ԴՅ, C. A. O. Z.; Tong, Z. H. U. *Chinese J. Chem. Eng.* **2012**, *20* (4), 701–709.
- (30) Zhang, J.; Mi, J.; Li, P.; Wang, F.; Dally, B. B. *Energy & Fuels* **2015**, *28* (2), 1524–1535
- (31) Horning, D. C. A Study of the High-Temperature Autoignition and Thermal Decomposition of Hydrocarbons, Report No . TSD-135 by, **2001**.
- (32) Beerer, D. J.; Mcdonell, V. G. *Proc. Combust. Inst.* **2011**, *33* (1), 301–307.
- (33) Koroglu, B.; Pryor, O. M.; Lopez, J.; Nash, L.; Vasu, S. S. *Combust. Flame* **2016**, *164*, 152–163.
- (34) Fleck, J. M.; Griebel, P.; Steinberg, A. M.; Arndt, C. M.; Aigner, M. *Int. J. Hydrogen Energy* **2013**, *38* (36), 16441–16452.
- (35) Smith, G. P.; Golden, D. M.; Frenklach, M.; Moriarty, N. W.; Eiteneer, B.; Goldenberg, M.; Bowman, C. T.; Hanson, R. K.; Song, S.; William C. Gardiner, J.; Lissianski, V. V.; Qin, Z. GRI-Mech 3.0 http://www.me.berkeley.edu/gri_mech/.
- (36) Li, S. C.; Williams, F. A. *J. Eng. Gas Turbines Power* **2002**, *124* (3), 471–480.
- (37) Kozubkova, M.; Kozubek, E.; Nevrlý, V.; Bitala, P.; Stepanek, O.; Dlabka, J.; Vasinek, M.; Bojko, M.; Zelinger, Z.; Kubat, P.; Grigorova, E. *Procedia Eng.* **2012**, *42*,

2001–2017.

(38) Umi, C. *Proc. Combust. Inst.* **1969**, *12*, 579–590.

(39) Burcat, A.; Scheller, K.; Lifshitz, A. *Combust. Flame* **1971**, *16* (1), 29–33.

(40) Lifshitz, A.; Scheller, K.; Burcat, A.; Skinner, G. B. *Combust. Flame* **1971**, *16* (3), 311–321.

(41) Crossley, R. W.; Dorko, E. A.; Scheller, K.; Burcat, A. *Combust. Flame* **1972**, *19* (3), 373–378.

(42) Cheng, R. K.; Oppenheim, A. K. *Combust. Flame* **1984**, *58* (2), 125–139.

(43) C. J. Goy. *ASME* **2001**, *2*, 1–7.

(44) Bakali, A. El; Dagaut, P.; Pillier, L.; Desgroux, P.; Pauwels, J. *Combust. Flame* **2004**, *137*, 109–128.

(45) Glarborg, P.; Bentzen, L. L. B. *Energy & Fuels* **2008**, *22* (20), 291–296.

(46) Mendiara, T.; Glarborg, P. *Energy & Fuels* **2009**, *23* (17), 3565–3572.

(47) Holton, M. M, P. Gokulakrishnan, M. S. Klassen, R. J. Roby, G. S. J. *J. Eng. Gas Turbines Power* **2010**, *132*.

(48) Liu, F.; Guo, H.; Smallwood, G. J. *Combust. Flame* **2003**, *133*, 495–497.

(49) Pekalski, A. A.; Zevenbergen, J. F.; Braithwaite, M.; Lemkowitz, S. M.; Pasman, H. *J. J. Hazard. Mater.* **2005**, *118*, 19–34.

(50) Di Benedetto, A.; Cammarota, F.; Di Sarli, V.; Salzano, E.; Russo, G. *Chem. Eng. Sci.* **2012**, *84*, 142–147.

(51) J.F.Griffiths, P.Gray, K. K. *Combust. Flame* **1974**, *22*, 197–207.

(52) Cavaliere, A.; Joannon, M. De. *Mild Combustion, Prog. Energy Combust. Sci.* **2004**, *30*, 329-366.

(53) Dagaut, P.; Dayma, G. *Combust. Flame* **2005**, *143* (1–2), 135–137.

(54) Abd-Alla, G. H.; Soliman, H. A.; Badr, O. A.; Abd-Rabbo, M. F. *Energy Convers. Manag.* **2001**, *42* (8), 1033–1045.

(55) Konnov, A. A.; Dyakov, I. V. *Exp. Therm. Fluid Sci.* **2005**, *29*, 901–907.

(56) Mi, J.; Li, P.; Dally, B. B.; Craig, R. A. *Energy & Fuels* **2009**, *13*, 5349–5356.

- (57) Li, P.; Mi, J.; Dally, B. B.; Craig, R. A.; Wang, F. *Energy & Fuels* **2011**, 2782–2793.
- (58) Persis, S. De; Foucher, F.; Pillier, L.; Osorio, V. *Energy* **2013**, 55, 1055–1066.
- (59) Yossefi, D.; Ashcroft, S. J.; Hacoheh, J.; Belmont, M. R.; Thorpe, I. *Fuel* **1995**, 74 (7), 1061–1071.
- (60) Safta, C.; Madnia, C. K. *Combust. Flame* **2006**, 144 (1-2), 64–73.
- (61) Chen, J.; McDonnell, V.; Samuelsen, S. *J. Propuls. Power* **2007**, 23 (3), 585–592.
- (62) Thiessen, S.; Khalil, E.; Karim, G. *Int. J. Hydrogen Energy* **2010**, 35 (18), 10013–10017.
- (63) Knizley, A. A.; Srinivasan, K. K.; Krishnan, S. R.; Ciatti, S. A. *Energy* **2012**, 43 (1), 315–328.
- (64) Kozubková, M.; Kozubek, E.; Nevrlý, V.; Bitala, P.; Št, O.; Dlabka, J. *Procedia Eng.* **2012**, 42, 1826–1839.
- (65) Masri, A. R.; Dibble, R. W.; Barlow, R. S. *Combust. Flame* **1992**, 91 (3–4), 285–309.
- (66) Christian Lund Rasmussen, Jon Geest Jakobsen, P. G. *Int. J. Chem. Kinet.* **2008**, 40 (12), 778–807.
- (67) W. Yajue. *Handb. Combust.* **2010**, 3, 121–140.
- (68) Kalghatgi, G. T. *Combust. Sci. Technol.* **1984**, 41 (1–2), 17–29.
- (69) Broadwell, J. E.; Dahm, W. J. A.; Mungal, M. G. *Symp. Combust. Proceedings* **1985**, 20th, 303–310.
- (70) Dearden, L. M.; Howard, L. M.; Pourkashanian, M.; Williams, A.; Yetter, R. A.; Yap, L. T. *Proc. Int. Gas Res. Conf.* **1998**, 5, 78–87.
- (71) Amato, a; Hudak, B.; D'Carlo, P.; Noble, D.; Scarborough, D.; Seitzman, J.; Lieuwen, T. *J. Eng. Gas Turbines Power* **2011**, 133 (6).
- (72) Burnham, A. K.; Day, R. L.; Wallman, P. H.; McConaghy, J. R.; Harris, H. G.; Lerwick, P.; Vawter, R. G. In-situ method and system for extraction of oil from shale., November 18, **2010**, US7921907B2.
- (73) Li, Z.; Hoflund, G. B. *J. Nat. Gas Chem.* **2003**, 12 (3), 153–160.
- (74) Farrauto, R. J. *Sci. (Washington, DC, United States)* **2012**, 337 (6095), 659–660.
- (75) Forni, L.; Rossetti, I. *Appl. Catal. B Environ.* **2002**, 38 (1), 29–37.

(76) Buchneva, O.; Rossetti, I.; Biffi, C.; Allieta, M.; Kryukov, A.; Lebedeva, N. *Appl. Catal. A Gen.* **2009**, *370* (1–2), 24–33.

(77) Leanza, R.; Rossetti, I.; Fabbrini, L.; Oliva, C.; Forni, L. *Appl. Catal. B Environ.* **2000**, *28* (1), 55–64.

(78) Tretyakov, V. F.; Sadykov, V. A.; Chernyshov, K. A. *Pet. Coal* **2004**, *46* (3), 95–99.

(79) Astanovsky, D. L.; Astanovsky, L. Z.; Kustov, P. V. *Catal. Ind.* **2013**, *5* (2), 148–155.

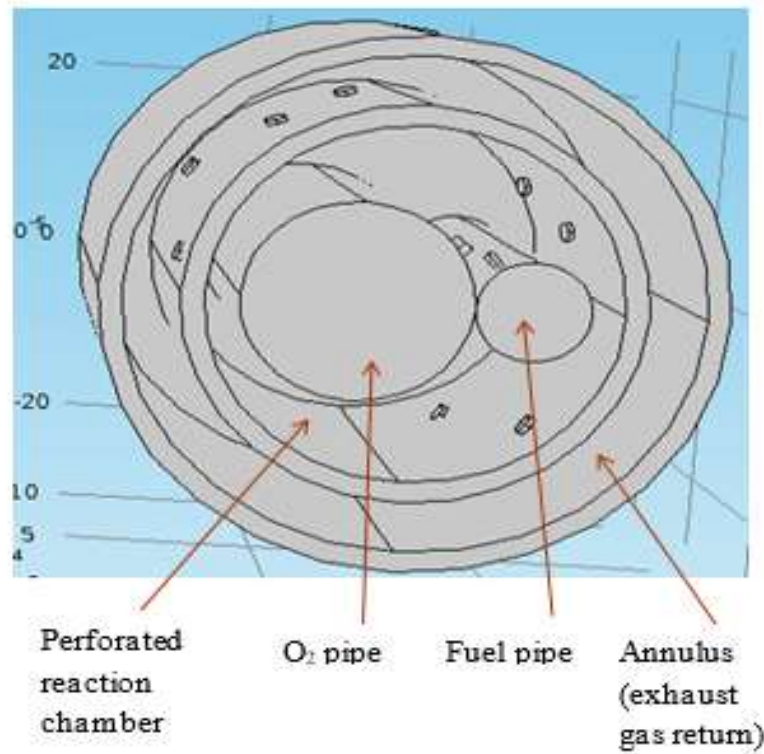


Figure 2.1: Heater configuration (homogenous reaction concept)

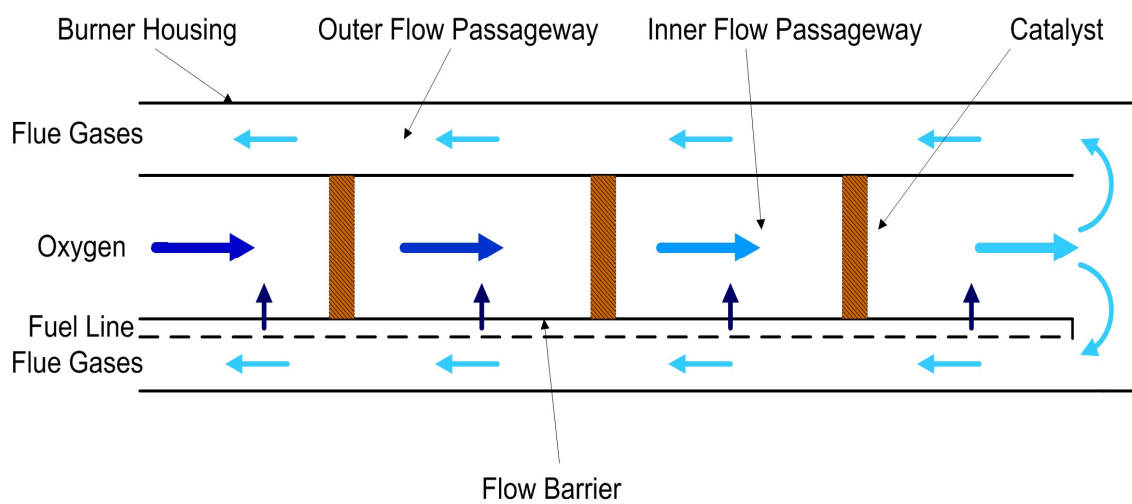


Figure 2.2: Catalytic bed heater configuration⁷²

Table 2.1: Coefficients of Equation (2.9)³

T_1 [°C]	UFL(p_0) [vol.%]	a [-]	b [-]
20	15.7	0.0466	-0.000269
100	16.8	0.0552	-0.000357
200	18.1	0.0683	-0.000541
410	20.8	0.0782	-0.000691

Table 2.2: Coefficients of Equation (2.10)³

p_1 / p_0 [-]	UFL(T_0) [vol.%]	c [1/K]
1	15.7	0.0854
3	16.1	0.1157
6	16.6	0.1494
10	18.6	0.1530
20	25.6	0.1968
35	32.5	0.2033
55	37.8	0.1769

Table 2.3: Classification criteria⁸

Type of reaction	Temperature rise	Maximum pressure ratio
No reaction	Very small	=1
Autoignition	>200 °C	> 1
Cool flame	< 200 °C	< 2

Table 2.4: Summary of shock-tube studies with methane-based fuel blends

Authors	Fuel	Oxidizers	Additives	T (K)	P (atm)	Equivalence ratio	Mechanism used in the Model
Higgin and Williams, 1969 ³⁸	CH ₄	-	C ₄	1800 - 2500	0.2- 0.4	0.5	Not Applicable
Burcat et al., 1971 ³⁹	CH ₄	O ₂ -Ar		1476 - 1900	11.2- 15.3	-	Not Applicable
Lifshitz et al., 1971 ⁴⁰	CH ₄	O ₂ -Ar	H ₂ , C ₃	1500 - 2150	2-10	0.5-2	Not Applicable
Crossley et al., 1972 ⁴¹	CH ₄	O ₂ -Ar	C ₂ -C ₅	1400 - 2000	0.2	1	Not Applicable
Tsuboi, T , Wanger, 1974 ¹⁶	CH ₄	O ₂ -Ar	-	1200 - 2100	0-300	0.2-2	Not Applicable
Zellner et al., 1983 ²²	CH ₄	air	C ₂ -C ₄	1400 - 2000	3	0.2	Not Applicable
Eubank et al., 1983 ²⁴	CH ₄	air	C ₂ -C ₄	1200 - 1850	4	0.2-0.4	Not Applicable
Krishnan et al., 1983 ²¹	CH ₄	O ₂ -Ar	C ₂ H ₂	1700 - 1900	1-4	0.5-2	Not Applicable

Table 2.4: Continued

Authors	Fuel	Oxidizers	Additives	T (K)	P (atm)	Equivalence ratio	Mechanism used in the Model
Spadaccini and Colket, 1984 ¹²	CH ₄	-	C ₂ -C ₄	1300 - 2000	3-15	0.45-1.25	Not Applicable
Cheng and Oppenheim, 1984 ⁴²	CH ₄	O ₂ -Ar	H ₂	800-2400	1-3	0.5-1.25	Not Applicable
Frenklach and Bornside, 1984 ²³	CH ₄	-	C ₃	1300 - 1600	2.5	1	Not Applicable
Petersen et al., 1996 ¹⁷	CH ₄	O ₂ -Ar or O ₂ -N ₂		1410 - 2040	9-480	0.5-4	GRI mech 1.2
Spadaccini et al., 1999 ¹²	CH ₄	-	C ₂ -C ₄	1300 - 2000	3-15	0.45-1.25	Not Applicable
Petersen et al., 1999 ¹⁸	CH ₄	O ₂ -Ar	-	1040 - 1500	40-260	0.4-6	developed a detailed kinetic mech predict the ignition characteristics of their shock tube experiments, compared to GRI mech
Goy et al., 2001 ⁴³	CH ₄	air	C ₂ -C ₃ , H ₂ O	900-1700	5-20	0.5-1	GRI mech, Spadaccini et al. ¹² correlation and one correlation from Li & Williams
Lamoureux and Paillard., 2002 ¹³	CH ₄	-	C ₂ -C ₃	1485 - 1900	3-13	0.5-2	Not Applicable

Table 2.4: Continued

Authors	Fuel	Oxidizers	Additives	T (K)	P (atm)	Equivalence ratio	Mechanism used in the Model
Zhukov et al, 2003 ¹⁹	CH ₄	air		1200 - 1700	30-450	0.5	GRI mech 3.0
Bakali et al, 2004 ⁴⁴	CH ₄	O ₂ -Ar	C ₂ -C ₆	1300 - 1800	0.1	0.75-1.5	developed a model, 671 reactions, 99 species
Huang and Bushe, 2005 ²⁰	CH ₄		C ₂ -C ₆	900-1400	16-40	1	Not Applicable
Petersen et al, 2005 ¹⁴	CH ₄	air	C ₂ -C ₆ , H ₂	1200 - 2000	0.54 - 25	0.5	GRI mech 3.0
Petersen et al, 2007 ⁹	CH ₄	O ₂ -Ar	C ₂ -C ₅ , H ₂	800-1100	15.5-27.5	0.5	Curran et al., GRI mech, Konnov et al, EXGAS, Williams et al
Koroglu et al, 2016 ³³	CH ₄	O ₂ -Ar-CO ₂ and O ₂ -N ₂ -CO ₂		1577 - 2144	0.53-4.4	0.5-2	GRI mech 3.0 / Aramco Mech 1.3

Table 2.5: Summary of flow reactor autoignition studies with methane-based fuel blends

Authors	Fuel	Oxidizers	Additives	T (K)	P (atm)	Equivalence ratio	Mechanism Used in the Model
Glarborg et al., 2008 ⁴⁵	CH ₄	O ₂ -N ₂ , O ₂ -CO ₂		1200-1800	1	0.5-2	detailed Mech (60species, 424 reactions)
Glarborg et al., 2009 ⁴⁶	CH ₄ + NO	N ₂ - CO ₂		1173-1773			detailed Mech (97species, 779 reactions)
McDonnell et al., 2010 ³²	CH ₄	air	C ₂ -C ₃	785-935	7-15	0.6	Not Applicable
Holton et al., 2010 ⁴⁷	CH ₄	O ₂ -N ₂ / O ₂ -CO ₂	C ₂ -C ₃	930-1140	1	0.5-1.25	developed a correlation

Table 2.6: Summary of autoignition studies with methane-based fuel blends in spherical vessels

Authors	Fuel	Oxidizers	Additives	T (K)	P (atm)	Mechanism Used in the Model	Setup
Berghmans et al., 1997 ³	CH ₄	air	-	293-473	1-55	Not Applicable	vessel (8 dm ³)
Berghmans et al., 1999 ¹¹	CH ₄ (30-84%)	air	-	683	2-47	Not Applicable	vessel (8 dm ³)

Table 2.6: Continued

Authors	Fuel	Oxidizers	Additives	T (K)	P (atm)	Mechanism Used in the Model	Set up
HONG et al., 2002 ⁴⁸	CH ₄	air	-	1200 - 1500	density: 20.4 kg/m ³	reduced GRI mech 1.2 (24 species and 104 elementary reactions), developed a correlation	vessel
Pekalskia et al., 2005 ⁴⁹	ethylen	-	-	-	-	Not Applicable	vessel (20 L)
Berghmans et al., 2008 ⁵	CH ₄	air	C ₃ -C ₄	-	1-30	Fluent (GRI Mech 3.0)	vessel (8 dm ³)
Di Benedetto , 2012 ⁵⁰	CH ₄	O ₂ -N ₂ , O ₂ -CO ₂	-	300	1	study the flammability limit	vessel (5 dm ³)

Table 2.7: Summary of autoignition studies with methane-based fuel blends in stirred reactor

Authors	Fuel	Oxidizers	Additives	T (K)	P (atm)	Equivalence ratio	mechanism used in the model	Setup
Bakali et al., 2004 ⁴⁴	CH ₄	O ₂ -Ar	C ₆	1300 - 1800	0.1	0.75-1.5	developed a model, 671 reactions, 99 species	jet-stirred reactor
Dagaut et al., 2005 ⁵³	CH ₄	O ₂ -Ar, O ₂ -N ₂	C ₂	1000 - 1350	10	-	Not Applicable	jet-stirred reactor

Table 2.8: Summary of autoignition studies with methane-based fuel blends in heaters

Authors	Fuel	Oxidizers	T (K)	P (atm)	Equivalence ratio	modeling	Set up
Rabbo et al., 2001 ⁵⁴	NG	Air-CO ₂ , air-N ₂	-	-	-	Not Applicable	high speed indirect injection dual fuel engine
Konnov et al., 2005 ⁵⁵	CH ₄	O ₂ -CO ₂	323-338	-	0.5-1.5	Not Applicable	heater
Jianchun et al., 2009 ⁵⁶	CH ₄	air	-	-	-	CFD simulation with fluent	furnace
Kneer et al., 2010 ¹⁵	CH ₄	O ₂ -CO ₂ , O ₂ -N ₂	900	-	O ₂ /fuel=1.15	Not Applicable	furnace (flameless combustion heater)
Mi et al., 2011 ³⁰	NG	air	-	1	0.5-1	CFD simulation with fluent	furnace
Mi et al., 2011 ⁵⁷	NG	O ₂ -CO ₂ , O ₂ -N ₂	-	-	-	Not Applicable	simulation (furnace)
de Persis et al., 2013 ⁵⁸	-	-	-	-	-	Not Applicable	4 lit combustion chamber
Zhang et al., 2015 ³⁰	NG, LPG	O ₂ -CO ₂ , O ₂ -N ₂	300	-	-	well stirred reactor (CHEMKIN, GRI mech 3.0)	Furnace

Table 2.9: Summary of simulations to study the autoignition of methane-based fuel blend

Authors	Fuel	Oxidizers	Additives	T (K)	P (atm)	Equivalence ratio	Mechanisms
Yoseffi et al., 1995 ⁵⁹	CH ₄	O ₂ -N ₂ , O ₂ -CO ₂	C ₂	1300 - 1700	9, 16	-	Not Applicable
Liu et al., 2003 ⁴⁸	CH ₄ , H ₂	O ₂ -N ₂ , O ₂ -CO ₂	-	-	-	-	CHEMKIN, GRI Mech 3.0
Madnia et al., 2005 ⁶⁰	CH ₄ , H ₂	O ₂ -N ₂	-	-	-	-	GRI-Mech 3.0 and two augmented reduced mechanisms (11- step and 12-step).
Samuelsen et al., 2007 ⁶¹	CH ₄	-	C ₂ -C ₃	773- 1573	1-15	0.4-1	Not Applicable
Thiessen et al., 2007 ⁶²	CH ₄	O ₂ -N ₂ , O ₂ -CO ₂ (0-90%)	-	800- 1200	1, 10	1	GRI Mech 3.0
Petersen et al., 2008 ⁹	CH ₄	air	H ₂ , CO ₂	300- 460	1,4.4, 15	0.4	GRI Mech 3.0

Table 2.9. Continued

Authors	Fuel	Oxidizers	Additives	T (K)	P (atm)	Equivalence ratio	Mechanisms
Van den Schoor et al., 2009 ⁵	Amonia/CH ₄	air	-	723	1	-	Not Applicable
Karim et al., 2010 ⁶²	CH ₄	air	H ₂	1000	1-100	-	Not Applicable
Krishnan et al., 2012 ⁶³	H ₂	CO ₂ , H ₂ O, N ₂ , and O ₂	CH ₄ , C ₂ H ₅ OH, C ₈ H ₁₈	300-1200	1-10	0.3-1.5	Not Applicable
Kozubková et al., 2012 ⁶⁴	CH ₄	O ₂ -Ar-N ₂	-	300	1	1	One-step ZC model/ One-step PS model/ Two-step WD model/Two-step CM model/ GRI Mech 3.0
ZHU Tong et al., 2012 ²⁹	CH ₄	Air-CO ₂	-	1200 - 1600	1	0.2-2	GRI Mech 3.0
Liu et al., 2016 ⁴⁸	NG	O ₂ -N ₂ , O ₂ -CO ₂	-	-	-	-	GRI Mech 2.11

Table 2.10: Gas mixture compositions used in Peterson's experiments¹⁷

Mixture	%CH ₄	% O ₂	% Ar	%N ₂	Ø
1	0.25	1.00	98.75	-	0.5
2	0.5	2.00	97.50	-	0.5
2N	0.52	2.02	-	97.46	0.5
3	1.00	4.00	95.00	-	0.5
4	0.25	0.56	99.16	-	1.0
5	0.56	1.14	98.30	-	1.0
6	1.02	2.04	96.94	-	1.0
7	3.40	6.70	89.90	-	1.0
8	0.25	0.25	99.50	-	2.0
9	0.50	0.50	99.00	-	2.0
10	5.00	5.00	90.00	-	2.0
11	0.25	0.14	99.61	-	3.6
12	0.50	0.25	99.25	-	4.0

Table 2.11: Mixture table with experimental results on the right column⁹

L21	T (K)	P (atm)	CH ₄	C ₂ H ₆	C ₃ H ₈	C ₄ H ₁₀	C ₅ H ₁₂	H ₂	τ_{ign} (ms)
1	849	20.1	1.000	0	0	0	0	0	7.00
1	1107	20.2	1.000	0	0	0	0	0	2.35
1 ^a	1007	27.2	1.000	0	0	0	0	0	4.56
1 ^a	1043	24.9	1.000	0	0	0	0	0	3.39
1 ^a	1099	27.5	1.000	0	0	0	0	0	2.62
2	811	20.3	0.750	0.250	0	0	0	0	7.72
3	817	20.2	0.751	0	0.249	0	0	0	10.79
3	1100	20.3	0.751	0	0.249	0	0	0	1.45
4	881	18.7	0.750	0	0	0.250	0	0	5.07
4	976	18.5	0.750	0	0	0.250	0	0	4.24
5	876	15.7	0.750	0	0	0	0.250	0	5.42
5	925	18.2	0.750	0	0	0	0.250	0.000	4.58
6	816	20.7	0.750	0	0	0	0	0.250	8.10
7	827	19.7	0.500	0.500	0	0	0	0	9.69
8	815	20.5	0.500	0.250	0.250	0	0	0	6.92
9	792	18.4	0.493	0.257	0	0.250	0	0	11.96
10	794	20.8	0.497	0.255	0	0	0.248	0	7.90
11	802	20.6	0.500	0.251	0	0	0	0.249	7.80
13	797	20.3	0.498	0.000	0.251	0.251	0	0	9.32
14	791	20.8	0.497	0	0.256	0	0.248	0	8.36
15	786	20.0	0.489	0	0.252	0	0	0.259	8.58
16	914	18.1	0.500	0	0	0.500	0	0	4.00
17	807	20.1	0.500	0	0	0.251	0.250	0	5.34
18	797	18.7	0.501	0	0	0.245	0	0.254	10.38
19	934	15.5	0.500	0	0	0	0.500	0	3.69
19	803	19.2	0.500	0	0	0	0.500	0	6.04
20	798	20.0	0.505	0	0	0	0.248	0.248	5.98
21	803	20.1	0.503	0	0	0	0	0.497	7.70

The numbers for each fuel species represent the mole fraction of that fuel in the blend.

Each mixture was mixed with O₂-Ar “air” at $\phi=0.5$.

^a Specifies mixtures that were created using N₂ as a bath gas.

Table 2.12: Values of ϵ_B ⁶⁹

Gas	ϵ_B
Methane	4.6
Propane	5.6
Ethylene	5.3
Acetylene	3.9
Hydrogen	4.4
Butane	4.8
Average value	4.8

Table 2.13: Summary of selected data on complete methane oxidation over alumina-supported Pd catalysts⁷³

Catalyst composition	Reactant mixture	Particle size (nm)	Temperature range (°C)	Turnover frequency (s ⁻¹)		Activation energy (kJ/mol)	
				Low	High	Low	High
5%Pd/ γ -Al ₂ O ₃	1%CH ₄ /air	2–70	270–470	0.428	3.4	78.2	158.9
5%Pd/ δ -Al ₂ O ₃	1%CH ₄ /air	5–75	270–470	7.02	67.7	69.6	96.2
5%Pd/ γ -Al ₂ O ₃	1%CH ₄ /air	5.4	270–470	17.5	—	80.9	—
5%Pd/ γ -Al ₂ O ₃	1%CH ₄ /air	8.8	270–470	41.3	—	80.4	—
5%Pd/ γ -Al ₂ O ₃	1%CH ₄ /air	2.1	270–470	0.466	—	120.6	—
4.03%Pd/ γ -Al ₂ O ₃ ^a	1%CH ₄ /air	1.6–4.1	275–450	1.19	4.54	80.4	107.8
0.88%–4.03%Pd/ γ -Al ₂ O ₃ ^b	1%CH ₄ /air	—	275–450	—	—	71.3	80.3
3.19%Pd/SiO ₂	1%CH ₄ /air	9.4–20	275–450	2.37	19.7	100.9	132.1
2.7%Pd/TiO ₂	O ₂ : CH ₄ = 0.4:1	2–32	230–530	—	—	35	83
2.7%Pd/ γ -Al ₂ O ₃	O ₂ : CH ₄ = 0.6:1	2–32	230–530	—	—	23	84
2.7%Pd/ α -Al ₂ O ₃	O ₂ : CH ₄ = 0.4:1	—	230–530	—	—	45	89
2.7%Pd/ThO ₂	O ₂ : CH ₄ = 0.4:1	—	230–530	—	—	34	85
0.5%Pd/Al ₂ O ₃	CH ₄ :O ₂ =0.66:40 not diluted	—	300–450	—	—	91.2	—
0.2%–0.5%Pd/Al ₂ O ₃	CH ₄ :O ₂ :He=1:2.2:18	1–17	260–370	0.02	0.06	107.5	118.0
0.5%–2.3%Pd/Al ₂ O ₃	$p_t=1.41 \times 10^5$ Pa	1–3.3	260–370	1.2	5.6	113.0	121.3
0.038%Pd/Al ₂ O ₃	CH ₄ :O ₂ :He=1:0.1:98.9	1.6–6.4	250–500	0.012	0.31	71.1	83.7
Pd wire	CH ₄ :O ₂ =1:4	—	350–500	5.4	—	71.7	—
1%–10%Pd/Al ₂ O ₃	2%CH ₄ /Air	2–110	240–400	—	—	75.3	92.0
1%–10%Pd/ZrO ₂	—	—	—	0.02	0.08	—	—
4%Pd/ γ -Al ₂ O ₃	1%CH ₄ /air	—	300–800	—	—	—	—
1.95%Pd/ γ , δ -Al ₂ O ₃	CH ₄ :O ₂ :N ₂ =1:4:95	6–16	200–500	Increase 20 times		74.0	100.4

a: The catalyst was prepared by PdCl₂, b: it was prepared by Pd(NO₃)₂, c: it was prepared by Pd(NO₃)₂

Table 2.14: Specification of the alumina-supported Pd catalyst used by the University of Utah

Alumina – supported Pd catalyst (BASF PuriStar, Ro-20/47)	
Pd (% wt)	0.5
Particle shape	Beads
Diameter (mm)	2-4
Surface area (m ² /g)	250-300
Max. Temperature (°C)	600
Price	\$250/500gr

Table 2.15: Characteristics of hydrocarbon oxidation catalyst developed by Fast Engineering Ltd.⁷⁹

Nickel oxide fraction (wt %)	9.0
Specific granule surface, cm ² /cm ³	31.8
Bulk density (gr/cm ³)	1.46
Granule diameter (mm)	1.3
Granule height (mm)	2.0 – 6.0
Mechanical strength (kg/mm ²)	2.8

CHAPTER 3

ENGINEERING CALCULATIONS

3.1. Overview

Chapter 3 summarizes preliminary engineering calculations to support design of a new heater configuration. It consists of two sections. In Section I, macroscopic mass, momentum, and energy balance calculations are performed to determine appropriate sizes for feeder pipes and nozzles, as well as the pressure distributions in different sections of the heater. In Section II, overall energy balance and heat transfer calculations are used to determine the required gas mixture temperature to meet design specifications. The results of this chapter are the input for future calculations.

3.2. Section I: Determining the appropriate sizes for feeder pipes,

nozzles/holes

3.2.1. Overview

As shown in Figures 3.1 to 3.3, the homogeneous burner approach consists of two perforated pipes that inject the fuel and oxidizer into the perforated reaction chamber. It is critical to design a system appropriately so that the fuel and oxidizer are provided in a controlled way along the length of the burner. Section I summarizes the engineering calculations to determine the appropriate size of feeder pipes, and the size and spacing of

the holes in the pipes, so that a uniform distribution of fuel and oxidant is obtained. Two different scenarios were considered. First, the size of the feeder pipes (manifolds) was held constant, and the hole sizes change along the length of the system. Second, the size of the holes was held constant, and the pipe diameter was varied along the system.

In the first scenario, the calculation was based on three different approaches, starting with a basic approach that used a number of simplifying assumptions. Ultimately, a more sophisticated approach was utilized to more accurately determine the appropriate size of the holes.

For the second scenario, the axial pressure of the volume surrounding the fuel and oxidant pipes (P_{chamber}) was assumed constant as a design constraint. It was assumed that the gases were injected through the feeder pipe holes into a chamber where the pressure was constant along the length of chamber. Then, the cross-sectional area of the feeder pipe (manifold) was determined as a function of the distance from the pipe inlet (x), such that the pressure could be maintained constant. A summary of the results from these two different scenarios is presented and discussed below.

3.2.2. Introduction

As shown in Figure 3.2, the heater consists of two closed lengths of pipes having a row of holes along the length. The gases are introduced into the open end. Despite its physical simplicity, it is challenging to understand the gas flows and to develop a system to provide a uniform flow and combustion rate throughout the 2000 ft of the heater.

Dow et al.¹ set up and solved a system of ordinary differential equations for the case of

constant discharge along the length of a manifold (perforated pipe). That solution became the basis for our design calculations of a pipe burner having uniform heating along its length. The model assumed that the static pressure remained constant along the length of the perforated pipe, which ensures a uniform flow passing through the holes. The assumption also implies that the pressure drop due to friction losses in the perforated pipe should be equal to pressure increase due to the deceleration of the flow that occurs as the gas escapes through the holes.

The general manifold problem seeks the relation between pressure head, nozzle and manifold velocities, fluid friction, length and diameter of manifold, nozzle spacing, and diameters.² In particular,

- For a required discharge, what is the required pressure at the manifold inlet?
- What is the distribution of discharge along the manifold length?
- What conditions provide uniform distribution along the manifold?

The requirement of having a uniform discharge per unit of length (L) facilitates the determination one of the below parameters;

- Holes diameter, d , where manifold diameter (D) and number of holes (n) are uniform
- Holes spacing, L_n , where the manifold diameter (D) and the hole diameter (d) are uniform
- Perforated pipe diameter, D , where the hole diameter (d) and number of holes (n) are uniform.

The manifold problem can be classified into two cases:

Case 1: The cross-sectional area of the manifold (A) and the discharge flowrate (q) are known; the diameter of the holes (d) or their spacing (L_n) will be calculated.

Case 2: The discharge rate (q), hole diameters (d), and their spacing (L_n) are known; the cross-sectional area of the manifold (A) as a function of the distance to the inlet end (x) will be calculated.

There are three approaches to solve Case 1. In the first two, it is assumed that the flow is passing through the holes into a constant pressure environment. However, the third approach is more sophisticated and does not assume constant pressure for the chamber surrounding the perforated pipes (manifold). The results obtained from each approach will be presented and compared in the following section.

In Case 2, it was assumed that the pipe diameter was changing so that there was no pressure drop in the perforated pipe ($dP/dx=0$). In all calculations, CH_4 was the fuel and O_2 was the oxidizer. The inlet gas temperature and pressure were 900 K and 10 bar. The reaction was not considered in the calculation and the gas was assumed to be ideal.

3.2.3. Case 1: the cross-sectional area of the perforated pipe (A) and the discharge flowrate (q) are known; the diameter of the holes (d) or their spacing (L_n) will be calculated

It was assumed that the cross-sectional area of the perforated feeder pipe (A) and the discharge flowrate (q) were known. The diameter of the holes (d) or the spacing (L_n) were determined by three different approaches, as explained in the following.

3.2.3.1. Case 1, approach 1

D. S. Miller^{3,4} proposed an engineering estimation to reach a uniform discharge along the length of a manifold (perforated pipe). He defined the loss ratio (LR) as the ratio between the entire cross-sectional area of the holes, to the perforated pipe cross-sectional area. He suggested that the loss ratio should be less than 0.5 to have a uniform flow across the holes.

Equation (3-1) shows the definition of the Loss Ratio (LR). Equation (3-2) shows the relation between the perforated pipe diameter (D) and the maximum hole diameter (d) to maintain a uniform discharge along the perforated feeder pipe.

$$\text{Loss ratio} = \left(\frac{\text{Total hole cross-sectional area}}{\text{feeder pipe cross-sectional area}} \right)^2 = \left(\frac{nA_b}{A} \right)^2 = \left(\frac{nd^2}{D^2} \right)^2 \quad (3-1)$$

where

A_b : a hole cross-sectional area

A: perforated feeder pipe cross-sectional area

n: numbers of holes

d: hole diameter

D: perforated pipe diameter

The loss ratio should be less than 0.5 to have a uniform flow.

$$\left(\frac{nd^2}{D^2} \right)^2 < 0.5 \rightarrow d^2 < \frac{\sqrt{0.5} D^2}{n} \quad (3-2)$$

Assuming there is a uniform discharge through all the holes, a mass balance provides the relationship between velocity in the holes (u) and the feeder pipe inlet velocity (V_0).

$$\begin{aligned}
 u &= \frac{q}{A_b} = \frac{\left(\frac{Q_i}{n}\right)}{A_b} = \frac{\left(\frac{Q_i}{n}\right)}{\left(\frac{\pi d^2}{4}\right)} = \frac{\left(\frac{Q_i}{n}\right)}{\left(\frac{\pi \sqrt{0.5} D^2}{4}\right)} = \frac{Q_i}{\sqrt{0.5} \left(\frac{\pi D^2}{4}\right)} = \frac{V_0}{\sqrt{0.5}} \rightarrow u \\
 &= \frac{V_0}{\sqrt{(\text{loss ratio})}}
 \end{aligned}
 \tag{3-3}$$

where

n : number of holes

A_b : cross-sectional area of a hole

u : minimum hole velocity which can provide a uniform discharge

V_0 : feeder pipe inlet velocity

Q_i : feeder pipe inlet flowrate

q : flowrate through a hole ($q = \frac{Q_i}{n}$)

For 3-inch diameter feeder pipes, the total fuel and oxidizer inlet flowrates are $2.61 \cdot 10^3$ ft³/hr and $5.24 \cdot 10^3$ ft³/hr at 10 bar and 900 K. Based on this analysis, the hole diameter in the feeder pipes should be equal to or less than $\frac{1}{2}$ inches so that the flow discharge along the perforated pipe remains uniform. If the feeder pipe diameters and the hole spacing increase, the size of the holes also increases. For example, for 4-inch diameter pipe the hole size will be $\frac{3}{4}$ in and for a 5-inch pipe the hole size will be 1 in. This approach results in an approximate maldistribution of 10%. The maldistribution is defined as the percentage variation in flow between the first and last holes. It may be estimated reasonably well for small maldistribution by Equation (3-4).⁵ The pressure drop across the holes (ΔP_0) is 5.2 times the pressure drop over the perforated feeder pipe (ΔP).

$$\text{Percent maldistribution} = 100 \left(1 - \sqrt{\frac{\Delta P_o - \Delta P}{\Delta P_o}} \right) = 10$$

$$\rightarrow \Delta P_o \sim 5.2 \Delta P \quad (3-4)$$

3.2.3.2. Case 1, approach 2

Perry's Chemical Engineering Handbook⁵ states that to obtain a uniform flow discharge, the average pressure drop across the holes (ΔP_o) should be ten times larger than the pressure variation over the length of the perforated pipe (ΔP). Thus, the relative difference in pressure drop across the various holes becomes small, and so does the change in flow passing through the holes.

$$\rightarrow \frac{(\text{pressure drop across the holes})}{(\text{pressure drop over the length of the pipe})} = 10 \quad (3-5)$$

When the area of an individual hole is small compare to the cross-sectional area of the perforated pipe, the hole pressure drop (ΔP_o) is expressed by Equation (3-6).

$$\Delta P_o = \frac{1}{C_o^2} \frac{\rho u^2}{2} \quad (3-6)$$

where

C_o : discharge coefficient (taken to be 0.62 for all holes²)

u : hole velocity ($u = \frac{4q}{\pi d^2}$)

d : hole diameter

q : hole flowrate

To determine the appropriate size of the holes, first, the pressure drop over the length of the perforated pipe (ΔP) was calculated, and then the pressure drop across the holes

(ΔP_0) was determined by Equation (3-5). Substituting ΔP_0 in Equation (3-6), we estimated the velocity in the holes. Then, the diameter of a hole was calculated based on the volumetric flowrate and the gas velocity.

The flowrate and the velocity of the gas in the perforated pipe decreases as the gas is injected into the reaction chamber. Thus, the flow pattern eventually changes from turbulent to laminar. Depending on the flow regime, the friction factor (f) changes along the perforated pipe. Therefore, the perforated pipe was divided into short sections where a constant friction factor, f , was assumed in each. For a 3-inch diameter pipe, the feeder pipe hole diameter changes from approximately 1/4 inch to 1/2 inch along the 2000 ft pipe. For a 4-inch diameter feeder pipe, the hole size changes from approximately 1/4 inch to 3/4 inch. The hole size for a 5-inch diameter feeder pipe varies from approximately 1/2 inch to 1 inch.

3.2.3.3. Case 1, approach 3

In the first two approaches, it was assumed that the pressure in the reaction chamber (where the perforated feeder pipes are located) is constant. However, as illustrated in Figure 3.2, the perforated feeder pipes are located inside a chamber where the pressure is not constant along the length of it. It was assumed that the perforated pipe diameter (D) and the inlet gas flowrate were known. Some steps were followed to calculate the diameter of the holes and their spacing;

1. Develop an equation for the pressure inside the perforated pipe (P) as a function of the length of the perforated pipe (x)
2. Develop an equation for the pressure inside the perforated pipe (P) as a function of

the hole diameter (d) and the pressure in the reaction chamber, P_{chamber}

3. Couple the two equations to generate an equation for the hole diameter (d) as a function of the length of the perforated pipe (x).

Each of these steps are discussed in more detail in the following. To have a uniform discharge distribution from a perforated pipe into the chamber, the pressure drop due to friction losses in the perforated pipe should be balanced by the pressure increase due to deceleration of the flow.¹ “In general, the pressure loss due to friction is related to the surface of the pipe, while the pressure gain due to deceleration is related to the cross-sectional area of the pipe. Therefore, it is possible to control the pressure by adjusting the ratio of these two areas.”¹

3.2.3.3.1. Developing an equation for the pressure of the perforated pipe (P) as a function of the perforated pipe length (x). Equation (3-7) is the general equation of motion for a flow in a pipe with a constant cross-sectional area. The underlying assumptions for the calculation are: an isothermal condition, the flow is steady state and on a streamline, and the gas density is constant along the pipe.

$$\rightarrow \frac{d(P + \frac{\rho}{2}V^2)}{dx} = -\frac{\lambda\rho V^2}{2D} \rightarrow \frac{dP}{dx} = -\frac{\rho}{2}2V\frac{dV}{dx} - \frac{\lambda\rho}{2D}V^2 \quad (3-7)$$

where

D: perforated pipe diameter.

P: pressure along the perforated pipe

V_0 : perforated pipe inlet velocity

V: gas velocity inside the perforated pipe

λ : Coefficient of fluid friction

We assumed the equations for fluid friction in nonperforated pipes also hold for perforated pipes. Blasius's law was used to calculate the friction factor for turbulent flow inside the perforated pipe.

$$\lambda = 0.316 \text{ Re}^{-\frac{1}{4}} \quad (3-8)$$

Blasius's law is good for smooth pipe of uniform diameter where $3 \cdot 10^3 < \text{Re} < 1 \cdot 10^5$. Since the Blasius's law requirements were not satisfied for the entire length of the pipe, the problem was solved section by section. For the end section of the heater where the flow is laminar, we can use $\lambda = \frac{64}{\text{Re}}$. The gas velocity changed linearly through the perforated feeder pipe as Equation (3-9), where V is the gas velocity in the perforated pipe, and V_0 is the inlet gas velocity in the perforated pipe. The pressure head in the perforated pipe was calculated by substituting.

$$V = V_0 \left(1 - \frac{x}{L}\right) \rightarrow \frac{dV}{dx} = -\frac{V_0}{L} \quad (3-9)$$

λ and V from Equations (3-8) and (3-9) into Equation (3-7) to yield:

$$\text{When flow is turbulent: } \frac{dP}{dx} = \frac{\rho V_0^2}{L} \left(1 - \frac{x}{L}\right) - \frac{0.158 \rho \theta^{\frac{1}{4}} V_0^{\frac{7}{4}}}{D^{\frac{5}{4}}} \left(1 - \frac{x}{L}\right)^{\frac{7}{4}} \quad (3-10)$$

$$\text{When flow is laminar: } \frac{dP}{dx} = \left(1 - \frac{x}{L}\right) \left(\frac{\rho V_0^2}{L} - \frac{32\mu V_0}{D^2}\right)$$

$$\text{When flow is laminar: } \frac{dP}{dx} = \left(1 - \frac{x}{L}\right) \left(\frac{\rho V_0^2}{L} - \frac{32\mu V_0}{D^2}\right) \text{3.2.3.2.2.}$$

The hole flowrate is proportional to the perforated pipe inlet flowrate (Q_0) and the number of the holes (n), provided that there is a uniform flow discharge along the

perforated pipe.

$$\Delta P_{\text{hole}} = \frac{1}{C_0^2} \frac{\rho u^2}{2} \rightarrow P - P_{\text{chamber}} = \frac{1}{C_0^2} \frac{\rho u^2}{2} \rightarrow P = \frac{1}{C_0^2} \frac{\rho u^2}{2} + P_{\text{chamber}} \quad (3-11)$$

$$q = \frac{Q_0}{n} = \frac{u \pi d^2}{4} \rightarrow u = \frac{4Q_0}{\pi n d^2} \quad (3-12)$$

where

q: hole flowrate

Q₀: pipe inlet flowrate

u: hole velocity

d: hole diameter

3.2.3.3.2. *Generating an equation for the hole diameter (d) as a function of the perforated pipe length (x).* Substituting the hole velocity (u) from Equation (3-12) into Equation (3-11), we can define the perforated pipe pressure (P) as a function of perforated pipe inlet flowrate (Q₀), the hole diameter (d), and number of the holes (n), as shown in Equation (3-13).

$$P = P_{\text{chamber}} + \frac{8\rho Q_0^2}{C_0^2 \pi^2 n^2} d^{-4} \quad (3-13)$$

The axial pressure distribution in the perforated feeder pipes (P) and the outer annulus (P_{outer annulus}), which contains the whole system, can be determined by Equation (3-13). However, to find the hole diameter, we still need to estimate P_{chamber}. One approach is to assume P_{chamber} is the average of P_{outer annulus} and P_{perforated pipe}.

The gas inlet pressure (P₀) and the hole diameters (d) are determined by an iterative procedure. Figure 3.4 shows the Reynold's number in the feeder pipes. For a 3-inch CH₄ pipe, the hole sizes are approximately 1/8 in. For a 3-inch O₂ pipe, the hole sizes are

approximately 1/4 in.

3.2.4. Case 2: Discharge flowrate (q), hole diameter (d), and their spacing (L_n) are known; the diameter of the perforated pipe

(A) will be calculated as a function of the distance to the inlet end (x)

In Case 2, it was assumed that diameter of the holes (d) and the spacing between the holes (L_n) were constant. The flowrate in the perforated pipe decreases as the gas escapes through the holes to the reaction chamber. Therefore, the cross-sectional area of the perforated pipe should decrease so that we have uniform discharge along it. In this section, an equation was developed to define the cross-sectional area of the perforated pipe (A) as a function of the length (x). It was assumed that the pressure of the chamber (into which the gases are discharged) was constant.

First, the perforated pipe velocity, V , was defined as a function of the perforated pipe cross-sectional area, A (cross-sectional area is a function of pipe length (x)).²

$$V = \frac{Q_0}{A} \left(1 - \frac{x}{L}\right) \rightarrow \frac{dV}{dx} = -\frac{Q_0}{AL} \left\{1 + \left(1 - \frac{x}{L}\right) \frac{L}{A} \frac{dA}{dx}\right\} \quad (3-14)$$

where

V : velocity of the perforated pipe

Q_0 : gas inlet flowrate

A : cross-sectional area of the perforated pipe

x : distance from the pipe inlet

Substituting the velocity, V , from Equation (3-14) into the general equation of motion,

Equation (3-7), we generated a relation between the pressure drop along the perforated pipe ($\frac{dP}{dx}$), the pipe cross-sectional area (A), and the pipe length (L).

$$\frac{dP}{dx} - \frac{\rho Q_0^2}{LA^2} \left(1 - \frac{x}{L}\right) \left\{1 + \frac{L}{A} \left(1 - \frac{x}{L}\right) \frac{dA}{dx}\right\} = - \frac{0.158 \rho \vartheta^{0.25} Q_0^{\frac{7}{4}}}{A^{\frac{7}{4}} D^{\frac{5}{4}}} \left(1 - \frac{x}{L}\right)^{\frac{7}{4}} \quad (3-15)$$

$$\text{We know that } A = \frac{\pi D^2}{4} \rightarrow D^{\frac{5}{4}} = 1.16 A^{\frac{5}{8}} \quad (3-16)$$

$$\begin{aligned} \rightarrow \frac{dP}{dx} - \frac{\rho Q_0^2}{LA^2} \left(1 - \frac{x}{L}\right) \left\{1 + \frac{L}{A} \left(1 - \frac{x}{L}\right) \frac{dA}{dx}\right\} \\ = - \frac{0.136 \rho \vartheta^{0.25} Q_0^{\frac{7}{4}}}{A^{\frac{19}{8}}} \left(1 - \frac{x}{L}\right)^{\frac{7}{4}} \end{aligned} \quad (3-17)$$

Because the hole diameters and spacing are constant, uniform discharge is only possible if $\frac{dP}{dx} = 0$. Equation (3.18) shows the pipe cross-sectional area, A, as a function of inlet Reynolds number and the pipe length. where A_0 and Re_0 are the inlet cross-sectional area and the inlet Reynolds number, respectively. There is also another approach proposed by Dow et al.⁶ Starting from the general equation of motion, Equation (3-7), and with the assumption of $\frac{dP}{dx} = 0$, we can determine the pipe sizes (D) as a function of distance from the pipe inlet (x).

$$\frac{A}{A_0} = [1 + 0.158 Re_0^{-0.25} \left\{1 - \left(1 - \frac{x}{L}\right)^{\frac{3}{8}}\right\}]^{\frac{8}{3}} \left(1 - \frac{x}{L}\right) \quad (3-18)$$

$$\frac{dD}{dy} = \frac{D}{2y} - \gamma \left(\frac{D}{y}\right)^n \quad (3-19)$$

where $\gamma = \frac{b}{\left(\frac{4Q_0}{\pi \vartheta L}\right)^n}$, y: distance from the pipe close end ($y = L - x$), and L: pipe length.

The results indicated that the pipes diameter starts with a constant 3 inches and gradually decreases to less than 1 inch. Since it is not practically possible to decrease the pipes diameters linearly, the whole length of the pipes is divided into three sections in which the diameters are assumed to be constant. The pipes diameter starts with a constant 3 inches for the first 300 meters, and then decreases to 2 inches diameter for the next 250 meters. Then, for the last 50 meters, the pipe diameter becomes 1 inch.

3.2.5. *Summary*

As discussed in Chapter 1 and Chapter 2, the homogeneous heater approach consists of two perforated pipes that inject the fuel and oxidizer into the perforated reaction chamber. The main objective of this section was to design a system so that a uniform flow distribution is maintained along the 2000 ft of the heater. An engineering calculation was performed to determine the appropriate size of the feeder pipes and the hole sizes and locations on the pipes. Two different cases were considered:

Case 1: the pipe sizes are constant, and the hole sizes change

Case 2: the hole sizes are constant, and the pipe sizes change

In both cases, the gas inlet temperatures and pressure in the feeder pipes were 900 K and 10 atm. It was assumed that there was no reaction occurring in the chamber, and that the gas properties were constant along the system.

Three different approaches were evaluated in Case 1. In the first two approaches, it was assumed that the gases were injected into a chamber, which had a constant pressure. In the third approach, the axial pressure distribution in the chamber was also taken into account.

In Case 2, it was assumed the hole diameters and the hole spacing were constant and uniform along the length of the pipe. The O₂ and the CH₄ pipes were divided into three sections. The pipes diameter starts with a constant 3 inches for the first 300 meters, and then decreases to a 2 inches diameter for next 250 meters. Then, for the last 50 meters, the pipe diameter becomes 1 inch. Note that all the results were based on the assumption that the fuel was pure methane and the oxidizer was pure oxygen. However, in the downhole heater, natural gas probably will be used as the fuel, and there may be some diluents such as N₂, CO₂, or H₂O present in the O₂ stream in the oxidizer pipe. Thus, the results may change based on the gas composition and properties.

3.3. Section II: Heat transfer calculation

3.3.1. Overview

Preliminary heat transfer calculations were performed to determine the overall heat transfer coefficient in the heater. The results of this section are the input for future CHEMKIN calculations in Chapter 5. As discussed in Section I, the gas properties and the Re number change along the length of the heater. Thus, the calculation was performed for a 1-meter section of the heater, with average gas properties and Re number.

3.3.2. Geometry

The heater consists of two 3-inch perforated feeder pipes, which are within an 8-inch perforated chamber. The whole system is located inside a 10-inch annulus. The length of the heater is 2000 ft. The Re number plays a significant role in the heat transfer calculations.

Since the Re number changes along the heater length, a 1-meter section of the heater, which is positioned 1000 ft from the gas inlet, is considered for the heat transfer calculations. It was assumed that the pipes all have Schedule 40 wall thickness. Table 3.1 listed the outer diameter, inner diameter, and the nominal sizes of the pipes used in these calculations.

3.3.3. Determining gas and oil properties

It was necessary to estimate the gas properties inside the system as well as the properties of the surrounding oil for the heat transfer calculations. Aspen HYSYS modeling was used to determine the properties of boiling oil at 650 K and about 64 bar. More information regarding the oil property estimation will be presented later in this chapter. At beginning, there were many unknown parameters, such as the gas initial T and P, required level of diluent in the system, and average gas temperature in the heater. We fixed some of the parameters and performed a preliminary CHEMKIN calculation to determine initial guesses for the properties of the flue gas in the reaction chamber and the annulus (the gas mixture produced at each reaction zone that escapes to the annulus). As the heat transfer calculation was completed and the approximate gas temperature inside the heater was determined, all the calculations were repeated considering the updated gas temperature. The preliminary CHEMKIN calculation was performed for a methane/oxygen mixture at $P_{\text{initail}} = 10$ bar and $T_{\text{initial}} = 800\text{K}$, $\phi = 1$. 50 mole % CO_2 was also added to the mixture as a diluent. Figure 3.5 is a schematic of the system. The hydraulic diameters of the reaction chamber for the initial CHEMKIN calculation were based on nominal Schedule 40 pipe sizes; however, the heat transfer calculations were based on the actual pipe sizes listed in

Table 3.1.

The details of the CHEMKIN and Aspen HYSYS modeling are available in Appendices A, B, C, and D. The thermo-physical properties for the gas mixture, which is produced in the reaction chamber and escapes to the annulus, are summarized below. This information was used in calculation of the heat transfer coefficients in the chamber and outer annulus.

$$m_{out-chambe} = 0.991 * 10^{-3} kg/s$$

$$M_{w,ave} = 34.6 * 10^{-3} \frac{kg}{mol}$$

$$\rho_{ave} = 2.23 \frac{kg}{m^3}$$

$$C_{p,ave} = 1.61 * 10^3 \frac{J}{kg.K}$$

$$\mu_{ave} = 71.57 * 10^{-6} \frac{kg}{m.s}$$

$$K_{ave} = 62.69 * 10^{-3} \frac{W}{m.K}$$

First, the convection heat transfer coefficients inside the annulus and the chamber were calculated. Then, the boiling heat transfer coefficient for the surrounding oil was estimated. Finally, the overall heat transfer coefficient of the system and the average gas temperature inside the heater were determined. Then, all the calculation steps were repeated with the updated gas temperature.

3.3.4. Determining the convection heat transfer coefficient of the outer annulus

The annulus Reynold's number is calculated based on the cross-sectional area of the annulus ($A_{annulus}$), gas average flowrate ($m_{out_chamber}$), and the average gas properties obtained from the initial CHEMKIN calculation,

$$D_{h\ annulus} = (ID_{outer\ pipe} - OD_{chamb}) = 1.4\ in = 0.035m$$

$$D_{h\ chamb} = \frac{ID_{chamber}^2 - 2 * OD_{pipe}^2}{(ID_{chamb} + 2 * OD_{pipe})} = 2.6in = 0.07m$$

$$A_{annulus} = \frac{\pi}{4} (ID_{outer\ pipe}^2 - OD_{chamb}^2) = 0.0132\ m^2$$

$$U_{annulus}^* = \frac{m_{out-chamber}}{\rho_{ave} \cdot A_{annulus}} = \frac{0.991 * 10^{-3}}{2.23 * 0.0132} = 0.034\ m/s$$

$$(Re_{annulus})_{laminar} = \frac{\rho_{ave} \cdot U_{annulus}^* \cdot D_{h-annulus}}{\mu_{ave}} = \frac{2.23 * 0.034 * 0.035}{71.57 * 10^{-6}} = 37.2$$

The Re number calculated is based on the estimated gas flowrates injected from a 1-meter section of the reaction chamber into the annulus. In reality, unlike the reaction chamber, the sections in the annulus are not isolated from each other; a 1-meter section in the annulus receives gases from upstream of that section, as shown in Figure 3.5. For simplicity, a 1-meter length section in the middle of the system was considered for further calculation. The total flowrate of gases passing through the outer annulus of that section is the summation of the upstream flowrates and the outlet of the chamber in that region. Since the section is in the middle of the system, there would be 300 meters (about 1000 ft.) upstream of that particular section. Thus, the average gas flowrate is multiplied by 300 to

give us an estimation of the total gas flowrate in a 1-meter section of the annulus, which is located in the middle of the system.

$$m_{annulus} = 300 * m_{out-chambe} = 300 * 0.991 * 10^{-3} = 0.297 \frac{kg}{s}$$

$$U_{annulus} = \frac{m_{annulus}}{\rho_{ave} \cdot A_{annulus}} = \frac{0.297}{2.23 * 0.0132} = 10.1 \text{ m/s}$$

$$Re_{annulus} = \frac{\rho_{ave} \cdot U_{annulus} \cdot D_{h-annulus}}{\mu_{ave}} = \frac{2.23 * 10.1 * 0.035}{71.57e-6} = 1.11 * 10^4$$

$$Pr = \frac{\mu_{ave} C_{p,ave}}{K_{ave}} = \frac{71.57 * 10^{-6} * 1.61 * 10^3}{62.69 * 10^{-3}} = 1.84$$

The flow regime is different at different positions of the system. However, in the middle section of the annulus, the flow regime is turbulent ($Re=1.11 * 10^4$). Therefore, the heat transfer correlation for turbulent flow was used to calculate the heat transfer coefficient in the annulus.

The convection heat transfer coefficient of the outer annulus was determined based on the Dittus and Boelter correlation:⁷

$$Nu_d = 0.023 Re_d^{0.8} Pr^n \quad (3-20)$$

$$\left. \begin{array}{l} \{n = 0.4 \text{ for heating}\} \\ \{n = 0.3 \text{ for cooling}\} \end{array} \right\}$$

This equation is good for a fully developed and turbulent flow ($Re_D > 10^4$), where there is a moderate temperature difference between wall and fluid, and $0.6 < Pr < 100$, $\frac{L}{D} \geq 10$. The Nu number and the average convection heat transfer coefficient of a 1-meter section of the annulus, which is located in the middle of the system, was determined as follows:

$$(Nu_{annulus})_{turbulent} = 0.023 (1.11 * 10^4)^{0.8} (1.84)^{0.3} = 47.8$$

$$\begin{aligned}
 (h_{annulus})_{Turbulent} &= \frac{K_{ave}}{D_{h-annulus}} (Nu_{annulus})_{turbulent} = \frac{62.69 * 10^{-3}}{0.035} 47.8 \\
 &= 84.56 \frac{W}{m^2 \cdot K}
 \end{aligned}$$

3.3.5. Calculating the convection heat transfer coefficient for the reaction chamber

In the proposed heater configuration, it is assumed that a reaction zone at each section, unlike the annulus, is isolated from the other sections. This assumption eliminates adding the flue gas from one reaction zone to other reaction zones; otherwise, combustion flue gases from an upstream reaction zone may prevent oxidation in that zone due to excessive dilution.

The average gas velocity and the Re number are calculated based on the cross-sectional area of the chamber ($A_{chamber}$), the estimated gas flowrate ($m_{out-chamber}$), and the average gas properties obtained from the initial CHEMKIN and HYSYS calculations.

The cross-sectional area of the chamber is

$$A_{chamber} = \frac{\pi}{4} (ID_{chamb}^2 - 2 * OD_{pipe}^2) = 0.02 \text{ m}^2$$

The gas velocity is

$$U_{chamber} = \frac{m_{out-chambe}}{\rho_{ave} \cdot A_{chamber}} = \frac{0.991 * 10^{-3}}{2.23 * 0.02} = 0.022 \text{ m/s}$$

The Reynolds number is

$$Re_{chamb} = \frac{\rho_{ave} \cdot U_{chamb} \cdot D_{h-chamber}}{\mu_{ave}} = \frac{2.23 * 0.022 * 0.07}{71.57e-6} = 46.4$$

The flow regime in the reaction chamber is laminar. The Nu number is calculated by

Equation (3-22);⁷

$$(Nu_d)_{cha} = 3.66 + \frac{0.0668 \left(\frac{D_{h-chamber}}{L_{chamber}} \right) Re_{chamber} Pr}{1 + 0.04 \left[\left(\frac{D_{h-chamber}}{L_{chamber}} \right) Re_{chamber} Pr \right]^{\frac{2}{3}}} \quad (3-21)$$

$$(Nu_d)_{chamb} = 3.66 + \frac{0.0668 * \left(\frac{0.07}{1} \right) * 46.4 * 1.84}{1 + 0.04 \left[\left(\frac{0.07}{1} \right) * 46.4 * 1.84 \right]^{2/3}} = 4.0$$

Determining the Nu number in a 1-meter section of the reaction chamber, we calculated the convection heat transfer coefficient in a 1-meter zone of the reaction chamber;

$$h_{chamb} = \frac{K_{ave}}{D_{h-chamber}} (Nu_d)_{chamber} = \frac{62.69 * 10^{-3}}{0.07} 4.0 = 3.8 \frac{W}{m^2.K}$$

3.3.6. Calculating the boiling heat transfer coefficient ⁷

It is assumed that the heater is surrounded by a pool of boiling oil. Thus, the boiling heat transfer of the surrounding oil plays a significant role in determining the overall heat transfer coefficient. Figure 3.6 shows the regimes of boiling water where the heat flux data are plotted against temperature excess, $T_w - T_{sat}$. It starts from natural convection (Region I) and then bubbles begin to form on the surface of the heater, break away, and dissipate in the liquid (Region II). As the temperature further increases, bubbles form more rapidly (Region III) and eventually form a vapor film, which blankets the heater surface. The thermal resistance of the film reduces the heat flux (Region IV). Information on the oil boiling regime was not available, so it was assumed that the oil shows the same boiling behavior as water. To obtain maximum heat transfer and to prevent the heater surface from being overheated, the boiling should remain in the nucleation boiling regime (III).

Rohsenow⁹ proposed an experimental correlation for nucleate pool boiling:

$$\frac{C_l \Delta T_x}{h_{fg} Pr_l^s} = C_{sf} \left[\frac{q/A}{\mu_l h_{fg}} \sqrt{\frac{g_c \delta}{g(\rho_l - \rho_v)}} \right]^{0.33} \quad (3-22)$$

where

C_l : Specific heat of saturated liquid, $\frac{BTU}{lb_m \cdot ^\circ F}$ or $\frac{J}{kg \cdot ^\circ C}$

ΔT_x : Temperature excess = $T_w - T_s$, $^\circ F$ or $^\circ C$

h_{fg} : Enthalpy of vaporization, $\frac{BTU}{lb_m}$ or $\frac{J}{kg}$

Pr_l : Prandtl number of saturated liquid

q/A : Heat flux per unit area, $\frac{BTU}{ft^2 \cdot h}$ or $\frac{W}{m^2 \cdot ^\circ C}$

μ_l : Liquid viscosity, $\frac{lb_m}{ft \cdot h}$ or $\frac{Kg}{m \cdot s}$

σ : Surface tension of liquid-vapor interface, $\frac{lb_f}{ft}$ or $\frac{N}{m}$

g : Gravitational acceleration, $\frac{ft}{s^2}$ or $\frac{m}{s^2}$

ρ_l : Density of saturated liquid, $\frac{lb_m}{ft^3}$ or $\frac{Kg}{m^3}$

ρ_v : Density of saturated vapor, $\frac{lb_m}{ft^3}$ or $\frac{Kg}{m^3}$

C_{sf} : Constant, determined from experimental data (equal to 0.0154 for n-pentane in contact with emery- polished copper⁷)

s : 1.0 for water and 1.7 for other liquids

Using the Rohsenow correlation, we determined the temperature excess, the temperature difference between the heater surface and the boiling oil. The physical properties of boiling oil were calculated using Aspen HYSYS software at 64 bar and 650

K. The boiling oil composition was assumed similar to heavy crude oil. Physical properties of the oil were calculated with Aspen HYSYS V8.8. The VLE calculation was performed with PVTsim software on the heavy crude oil composition. The detailed calculations are presented in Appendix D. The results of the Aspen HYSYS calculation are given below. Note that the estimated physical properties of oil were used in the calculation even though the correlations used were initially developed for boiling water, not oil.

$$C_l: 3.594 * 10^3 \frac{J}{kg \cdot ^\circ C}$$

$$h_{fg}: 1326 * 10^3 \frac{J}{kg}$$

$$\mu_l: 6.783 * 10^{-5} \frac{Kg}{m \cdot s}$$

$$\sigma: 1.766 * 10^{-3} \frac{N}{m}$$

$$g: 10 \frac{m}{s^2}$$

$$g_c = 1.0 \frac{kg \cdot m}{N \cdot s^2}$$

$$\rho_l: 304.5 \frac{Kg}{m^3}$$

$$\rho_v: 85.06 \frac{Kg}{m^3}$$

$$K_l = 4.628 * 10^{-2} \frac{W}{m \cdot K}$$

$$Pr = \frac{\mu_l C_l}{K_l} = \frac{(6.783 * 10^{-5}) * (3.594 * 10^3)}{4.628 * 10^{-2}} = 5.27$$

It is also assumed that there is $1 \frac{kW}{ft}$ heat transfer from the surface of the heater to the pool of oil. This number was defined by AMSO based on their desired heating rates. This is the minimum desired amount of heat that should be transferred from the downhole heater

to the boiling pool of oil.

$$\frac{q}{A} = \frac{\frac{q}{L}}{\pi(OD_{annulus})} = \frac{1 \frac{Kw}{ft} * \frac{1 ft}{0.3048 m}}{\pi * 10.75 in * \frac{0.0254 m}{1 in}} = 3.83 * 10^3 \frac{W}{m^2}$$

Substituting all the calculated data in Equation (3-23), we determined ΔT_x , which is the temperature difference between the surface of the heater and the boiling pool.

$$\frac{3.594 * 10^3 \Delta T_x}{1326 * 10^3 * 5.27^{1.7}} = 0.0154 \left[\frac{3.83 * 10^3}{6.783 * 10^{-5} * 1326 * 10^3} \sqrt{\frac{1.766 * 10^{-3}}{10 * (304.5 - 8 * .06)}} \right]^{0.33}$$

$$\rightarrow \Delta T_x = 32.6 \text{ } ^\circ\text{C}$$

Thus, the temperature difference between the surface of the heater and the boiling pool is about 32.6 °C. Having obtained the excess temperature, the heat transfer coefficient is given by

$$(h)_{boiling} = \frac{\frac{q}{A}}{\Delta T_x} = 117.25 \text{ W/m}^2 \cdot \text{ } ^\circ\text{C}$$

3.3.7. Calculation of metals thermal conductivities

We also need to estimate the thermal conductivities of the walls of the chamber and annulus to determine the overall heat transfer coefficient. For temperature ranges from 200 to 2000 K, the thermal conductivity of stainless steel can be calculated with Equation (3-25).¹⁰ We use this equation to estimate the conduction heat transfer coefficient; however, it is possible that stainless steel may not be used to construct the downhole heater.

$$K_{ss} \left(\frac{W}{m.K} \right) = 9.0109 + 1.5298 * 10^{-2} T_{ss} (K) \quad (3-23)$$

where T_{ss} is the temperature of the surface of the pipe. As calculated before, the temperature

of the heater surface, which is in contact with the boiling oil pool, has to be approximately 32.6 degrees hotter than the temperature of the boiling pool (650K). Thus, the temperature of the surface of the heater, T_w , would be equal to

$$T_w = T_{oil} + \Delta T_x = 650 + 32.6 = 683 \text{ K}$$

Therefore, the thermal conductivity of the outer shell of the annulus is approximately equal to

$$K_{annulus} = 9.0109 + 1.5298 * 10^{-2} * 683 = 19.45 \left(\frac{W}{m \cdot K} \right)$$

3.3.8. Calculating the overall heat transfer coefficient of the heater

Now that the convection, conduction, and boiling heat transfer coefficients are estimated, it is possible to determine the overall heat transfer coefficients and the required operating temperature at each zone inside the heater. The pipe dimensions and heat transfer areas follow.

$$ID_{chamb} = 7.981 \text{ in} \rightarrow r_{in-chamber} = 3.99 \text{ in}$$

$$OD_{chambe} = 8.625 \text{ in} \rightarrow r_{out-chamber} = 4.31 \text{ in}$$

$$ID_{outer pipe} = 10.02 \text{ in} \rightarrow r_{in-annulus} = 5.01 \text{ in}$$

$$OD_{outer pipe} = 10.75 \text{ in} \rightarrow r_{out-annulus} = 5.38 \text{ in}$$

$$A_{in-aouter pipe} = 0.79 \text{ m}^2$$

$$A_{out-outer pipe} = 0.86 \text{ m}^2$$

$$A_{in-cinne pipe} = 0.637 \text{ m}^2$$

$$A_{out-cinne pipe} = 0.688 \text{ m}^2$$

Note that since the reaction chamber is perforated, the hot flue gas in the reaction chamber will totally escape into the outer annulus. And, we can assume that the average gas temperature in the outer annulus is equal to the average gas temperature inside the reaction chamber. However, we need to calculate the overall heat transfer coefficient of the reaction chamber to determine the operating conditions (initial T, P, and level of diluent) of the heater. The latest will be discussed in more detailed in Chapter 5.

3.3.9. Determining the overall heat transfer coefficient of the annulus

First, the overall heat transfer coefficient for the outer wall of the annulus is calculated. Then, the temperature of the flue gas is estimated based on the overall heat transfer coefficient and the required amount of the heat, 1 kW/ft.

$$U_{annulus} = \frac{1}{\frac{1}{h_{annulus}} + \frac{A_{in-annulus} \ln\left(\frac{r_{out-annulus}}{r_{in-annulus}}\right)}{2\pi L K_{annulus}} + \frac{1}{h_{boiling}}} \quad (3-24)$$

$$\rightarrow (U_{annulus})_{Turbulent} = \frac{1}{\frac{1}{84.6} + \frac{0.79 \ln\left(\frac{5.38}{5.01}\right)}{2\pi * 19.45 * 1} + \frac{1}{117.25}} = 48 \left(\frac{W}{m^2 \cdot K}\right)$$

$$\frac{q}{A} = (U_{annulus})_{Turbulent} ((T_{gas})_{Turbulent} - T_w)$$

$$\rightarrow 3.83 * 10^3 = 48 ((T_{gas})_{Turbulent} - 683)$$

$$\rightarrow (T_{gas})_{Turbulent} = 763 K$$

The calculations were conducted for a 1-meter section in the middle of the heater where the flow regime in the annulus is turbulent, and the heat transfer coefficient is relatively high. The minimum heat transfer coefficient would be at the end section of the heater where the flow regime is laminar, $(Re_{annulus})_{laminar} = 37.2$. The convective heat transfer

coefficient in the laminar region of the annulus is:

$$(Nu_{annulus})_{laminar} = 3.66 + \frac{0.0668 \left(\frac{D_{h-annulus}}{L_{annulus}} \right) (Re_{annulus})_{laminar} Pr}{1 + 0.04 \left[\left(\frac{D_{h-annulus}}{L_{annulus}} \right) (Re_{annulus})_{laminar} Pr \right]^{\frac{2}{3}}}$$

$$(Nu_{annulus})_{laminar} = 3.66 + \frac{0.0668 \left(\frac{0.035}{1} \right) 37.2 * 1.84}{1 + 0.04 \left[\left(\frac{0.035}{1} \right) 37.2 * 1.84 \right]^{\frac{2}{3}}} = 3.8$$

$$(h_{annulus})_{laminar} = \frac{K_{ave}}{D_{h-annulus}} (Nu_{annulus})_{laminar} = \frac{62.69 * 10^{-3}}{0.035} * 3.8$$

$$= 6.7 \frac{W}{m^2.K}$$

The overall heat transfer coefficient in the laminar section of the annulus is:

$$\rightarrow (U_{annulus})_{Laminar} = \frac{1}{\frac{1}{6.7} + \frac{0.79 \ln \left(\frac{5.38}{5.01} \right)}{2\pi * 19.45 * 1} + \frac{1}{117.3}} = 6.4 \left(\frac{W}{m^2.K} \right)$$

$$\frac{q}{A} = (U_{annulus})_{laminar} * ((T_{gas})_{laminar} - T_w)$$

$$\rightarrow 3.83 * 10^3 = 6.4 ((T_{gas})_{laminar} - 683) \rightarrow (T_{gas})_{laminar} = 1285K$$

$$\rightarrow (T_{gas})_{laminar} = 1285K \text{ For}$$

$$T_{gas} = \frac{(T_{gas})_{Turbulent} + (T_{gas})_{laminar}}{2} = \frac{763 + 1285}{2} = 1023.6K$$

This temperature is the required average flue gas temperature so that the oil pool temperature is maintained at 650 K. Finally, the average overall heat transfer coefficient of the annulus is calculated as:

$$\frac{q}{A} = U(T_{gas} - T_w) \rightarrow 3.83 * 10^3 = U (1023.6 - 683) \rightarrow U = 11.2 \frac{W}{m^2.K}$$

Since each section of the reaction chamber is perforated and the flue gas is assumed to

entirely escape into the annulus, the calculated gas temperature, T_{gas} , is the temperature of the gas produced in the reaction chamber that escape into the annulus. Note that radiation was not taken into account in these calculations.

3.3.10. Determining the overall heat transfer coefficient in the reaction chamber

In Chapter 5, a 1-meter section of the reaction chamber is modeled with CHEMKIN software. That calculation requires an overall heat transfer coefficient from the chamber to the surroundings as boundary conditions for further CHEMKIN calculation. The overall heat transfer coefficient in the reaction chamber is calculated here.

First, the thermal conductivity of the chamber walls was calculated with Equation (3-25), while $T_{gas} = 1023.6 K$, which is the calculated gas temperature in the previous section.

$$(K_w)_{chamber} = 9.0109 + 1.5298 * 10^{-2} * 1023.6 = 24.7 \left(\frac{w}{m.K} \right)$$

As explained before, the zones in the reaction chamber are assumed isolated from each other, and the flow regime is laminar in each section. However, the flow regimes and the heat transfer coefficient in the outer annulus change along the length of the reactor. The overall heat transfer of the chamber was calculated for two cases: first, when the flow in the annulus is turbulent, and second, when the flow in the annulus is laminar. Then, the average number was reported as the overall heat transfer coefficient in the chamber.

$$(U_{chamber})_{turbulent} = \frac{1}{\frac{1}{h_{chamb}} + \frac{A_{in-chamber} \ln\left(\frac{r_{out-chamber}}{r_{in-chambe}}\right)}{2\pi L(K_w)_{chamber}} + \frac{1}{(h_{annulus})_{Turbulent}}} =$$

$$\frac{1}{\frac{1}{3.8} + \frac{0.637 * \ln(\frac{4.31}{3.99})}{2\pi * 1 * 24.4} + \frac{1}{84.6}} = 3.6 \left(\frac{W}{m^2.K} \right)$$

$$\begin{aligned} (U_{chamb})_{laminar} &= \frac{1}{\frac{1}{h_{chamber}} + \frac{A_{in-chambe} \ln(\frac{r_{out-chamber}}{r_{in-chamber}})}{2\pi L (K_w)_{chamber}} + \frac{1}{(h_{annulus})_{laminar}}} \\ &= \frac{1}{\frac{1}{3.8} + \frac{0.637 * \ln(\frac{4.31}{3.99})}{2\pi * 1 * 24.4} + \frac{1}{6.7}} = 2.4 \left(\frac{W}{m^2.K} \right) \end{aligned}$$

The average of the above is

$$\rightarrow (U_{chamb})_{average} = \frac{3.6 + 2.4}{2} = 3.01 \left(\frac{W}{m^2.K} \right)$$

Now that we determined the average gas temperature inside the heater is about 1024 K, we repeated the heat transfer calculation with the gas properties at T=1024 K. Appendix C shows the detailed gas property estimations. The average overall heat transfer coefficients of the outer annulus and the reaction chamber are estimated as 15 W/(m².K) and 3.5 W/(m².K). With this information, the average flue gas temperature was determined to be equal to 939 K.

3.3.11. Summary

The primary objective of Section II was to determine the overall heat transfer coefficient in the heater. First, the convection heat transfer coefficients of the annulus and the reaction chamber were calculated. Second, the conductive resistances of the walls were determined, and third, the boiling heat transfer coefficient of the surrounding boiling oil was estimated. Finally, the overall heat transfer coefficient of the system and the required

flue gas temperature were calculated. It was assumed that 1 kW/ft heat is transferring from the heater to the surrounding oil, based on the design specification provided by AMSO.

The average overall heat transfer coefficients of the outer annulus and the reaction chamber were estimated as 15 W/(m².K) and 3.5 W/(m².K). Then, the average flue gas temperature was determined to be equal to 939 K. This temperature is the average gas temperature that has to be reached inside the heater so that the temperature of the surrounding oil is maintained at 650 K.

3.4. References

- (1) Dow, W. M. *J. Appl. Mech.* **1950**, *17*, 431–438.
- (2) Zinjen, V. der H. B. . *Appl. Sci. Res.* **1951**, *A3*, 144.
- (3) Miller, D. In *Internal Flow Systems*; **1990**; 51–105.
- (4) Miller, D. In *Internal Flow Systems*; **1990**; 303–360.
- (5) Perry. *Perry's Chem. Eng. Handb.* **1934**, *35* (6), 35-3079-35–3079.
- (6) Dow, W. M. *J. Appl. Mech.* **1950**, 431–438.
- (7) Holman. J.P. In *Heat Transfer*; Mc Graw-Hill Publishing Company, **1981**; 415.
- (8) Anil K. M, Nashaat N.; Nassar, A. S. K. *Educ. Chem. Eng.* **2012**, *7*, 210–218.
- (9) Rohsenow, W. M. *Trans. ASME* **1952**, *74*, 969–976.
- (10) Arnoult, G.; Belmonte, T.; Kosior, F.; Dossot, M.; Henrion, G. *J. Phys. D. Appl. Phys.* **2011**, *44* (17), 174022.

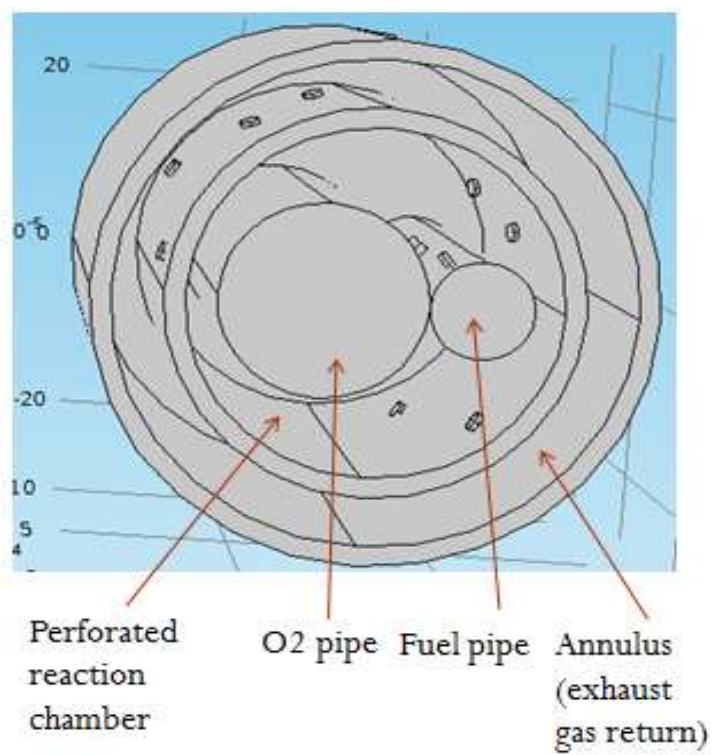


Figure 3.1: Heater configuration based on the homogeneous reaction concept

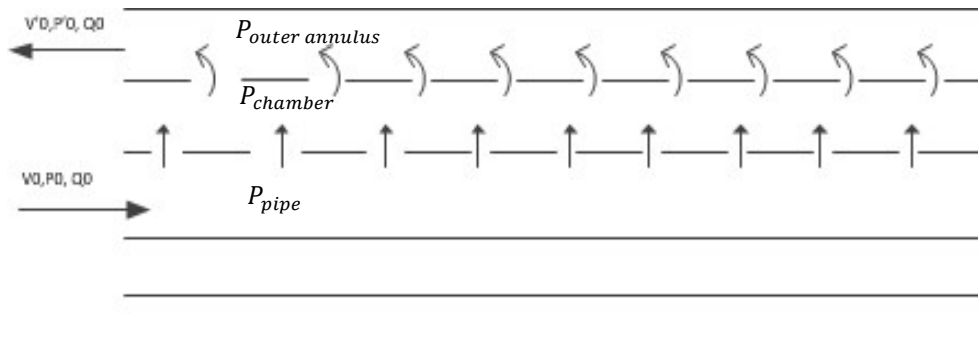
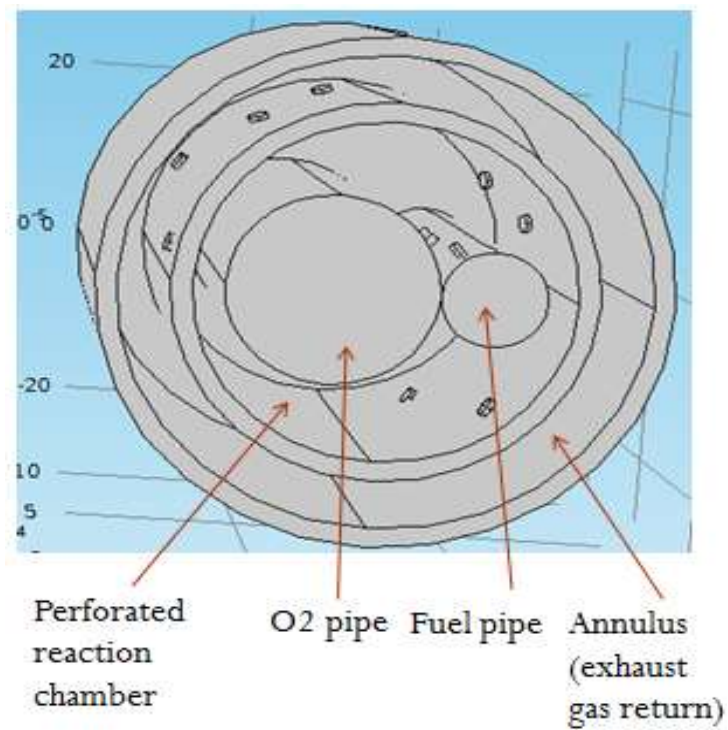


Figure 3.2: Two different views of a perforated pipe within a perforated chamber

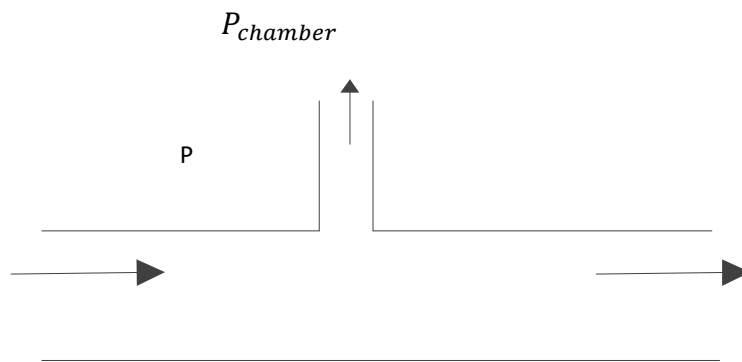


Figure 3.3: Schematic a section of a perforated pipe with one hole on it

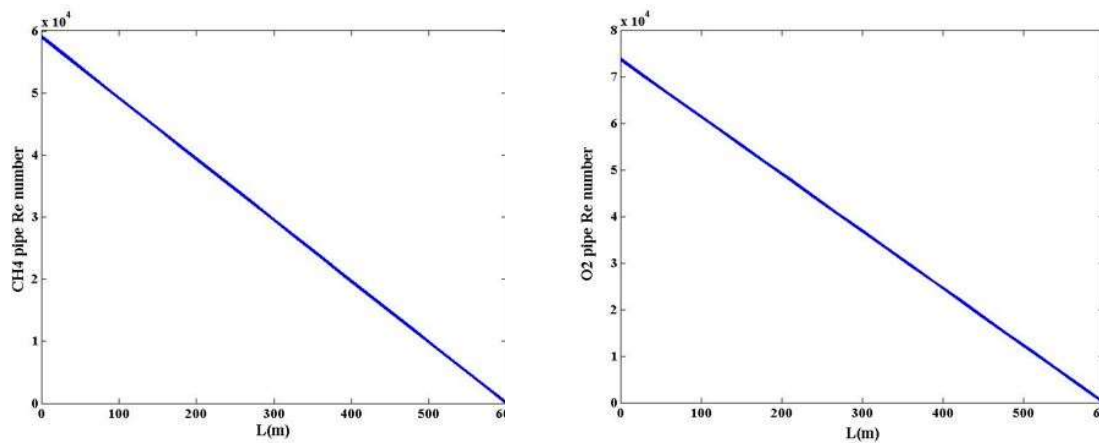


Figure 3.4: Reynold's number in each feeder pipe as a function of length

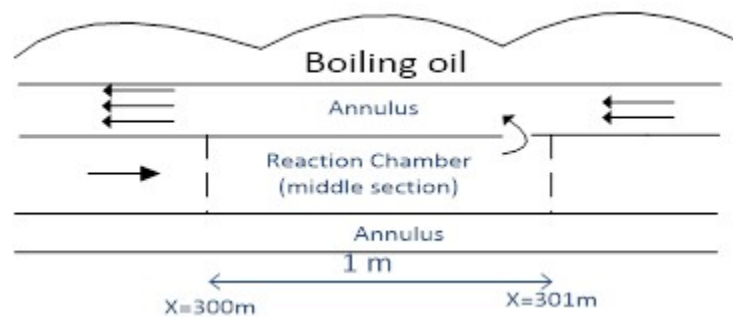


Figure 3.5: Schematic of the system considered for the heat transfer calculation

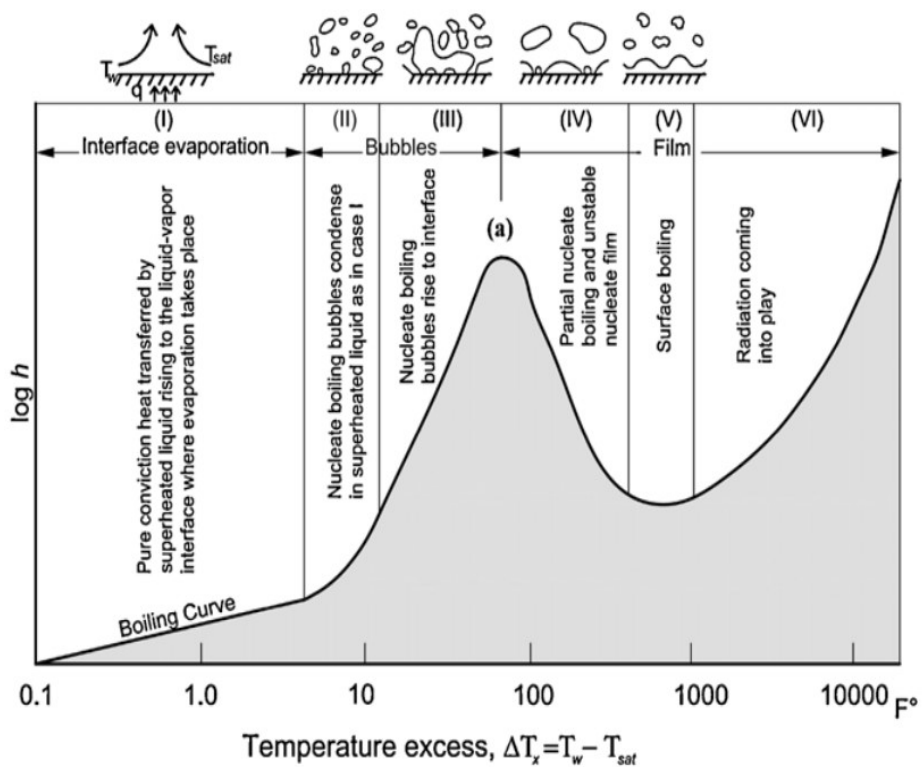


Figure 3.6: Different regimes of boiling water⁸

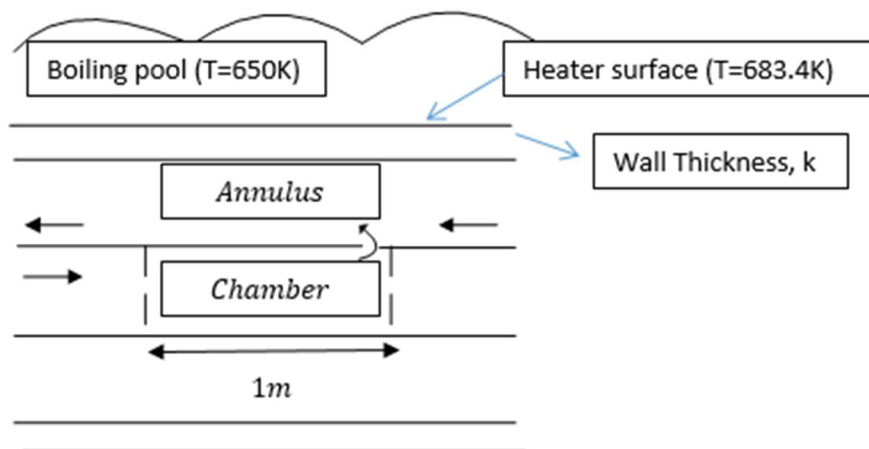


Figure 3.7: A 1-meter section of the system surrounded by the boiling oil

Table 3.1: Outer diameter, inner diameter, and the nominal sizes of the pipes based on Schedule 40 wall thickness

	Nominal sizes	OD (in)	ID (in)
Feeder pipes	3	3.5	3.068
Reaction chamber	8	8.625	7.98
Outer pipe	10	10.75	10.02

CHAPTER 4

EXPERIMENTAL WORK

4.1. Overview

Chapter 4 is a summary of experimental work performed during this project. It consists of two sections: (I) tests to explore the catalytic activity of metals used in heater construction, and (II) cold-flow studies to determine the effect of the nozzle orientation and spacing on the mixing of gases.

Section I describes experiments using stainless steels, Hastelloy-X, and a Pd-Alumina catalyst, and associated CHEMKIN modeling of methane oxidation under homogeneous flameless combustion conditions. The results show that the metals, as compared to the conventional Pd-Alumina catalyst, do not significantly catalyze methane oxidation.

Section II summarizes a cold-flow experimental study of the new heater configuration shown in Figure 1.5. A cold-flow study was performed to investigate the effect of nozzle spacing and orientation on the mixing behavior inside the heater. The experiments showed that the circumferential orientation has a significant impact on mixing of gases, whereas the axial location does not. Finally, uncertainty analysis is performed on the data from the cold-flow experiment. Some actions taken to reduce the uncertainty are also discussed.

4.2. Section I - Experimental and modeling study of catalytic oxidation of methane on several materials

This section discusses the results of testing performed to determine the catalytic activity of different metals for methane oxidation. It has both experimental and modeling components. In the experimental part, methane oxidation under flameless combustion conditions is evaluated on different stainless steels and Hastelloy-X. The results are compared with homogenous methane oxidation, as well as a conventional oxidation catalyst. In the modeling part, CHEMKIN chemical kinetics software is used to model homogenous methane oxidation under different conditions representative of our experimental work. Comparison between experimental and modeling results illustrates that the extent of methane oxidation over stainless steels and Hastelloy-X for the conditions studied can be explained by homogenous gas phase oxidation rather than a catalytic effect of these materials.

In addition, CHEMKIN¹ is used to model the methane oxidation experiments performed by Western Research Institute (WRI)² in previous research performed for AMSO. These results demonstrate that the WRI experimental data can also be explained by homogenous methane oxidation. Thus, our conclusion is that metal used in heater construction does not provide any appreciable catalytic benefit relative to homogeneous (nuncatalytic) methane oxidation for the conditions studied (500-750 °C). Preliminary trials with a conventional (Pd-based) oxidation catalyst exhibited substantial catalytic effects and facilitated complete methane oxidation at temperatures as low as 300 °C, which would be too low for use in the downhole heater.

4.2.1. Introduction

Different stainless steel alloys and Hastelloy-X were considered as potential catalysts for use in a gas-fired burner concept developed by AMSO that would serve as an underground heater for in-situ oil shale production. The materials were evaluated for their catalytic effect on methane oxidation under flameless combustion conditions in a laboratory-scale fixed-bed reactor built specifically for this purpose. Methane oxidation results for these materials were compared with homogenous methane oxidation, as well as methane oxidation by a conventional oxidation catalyst, using the same experimental setup. Commercial CHEMKIN chemical kinetics software was used to model homogenous methane oxidation under a range of conditions to compare with the experimental results obtained at the University of Utah (UofU), as well as to compare with experimental results obtained at Western Research Institute (WRI).

The following sections provide details on the experimental setup, test procedures, as well as results and discussion.

4.2.2. Experimental setup

4.2.2.1. Bench-scale apparatus

A schematic and photos of the experimental setup are shown in Figure 4.1 to Figure 4.5. The quartz tube that serves as the reaction chamber is placed vertically in an electrically-heated tube furnace (Lindberg Blue M, by Thermo Scientific), and is heated by radiation from the surrounding furnace walls. A ceramic honeycomb material is used as a support for the different catalyst beds tested in the reactor, and this ceramic support rests on dimples in the wall of the quartz tube. The furnace has its own temperature controller

and its maximum operating temperature is 1100° C. Two type-K Omega thermocouples ($\frac{1}{16}$ inch diameter) are placed inside the quartz reactor; one of them is placed into the bed of catalyst material and monitors the bed temperature, and the other is inserted from the bottom of the reactor and passes through one of the holes of the ceramic honeycomb to measure the gas temperature immediately after the bed. A data acquisition system is used to record the temperature readings every second.

A differential pressure gauge is used to measure the pressure drop across the reactor. Mass flow controllers are used to feed air and methane (Brooks 5850E for air and Cole Parmer for methane). The gases are premixed before entering the reactor at a total flowrate of 500 mL/min (methane concentration 1.5% by volume). The air-methane mixture can either bypass the reactor (for measurement of initial concentrations) or be fed into the top of the reactor.

The gas leaving the reactor is passed through a Mak 10-1 chiller (by Air Gas Thermotechnik) in order to condense any water vapor present in the stream, and through a Teflon filter (0.2 micron pore size) to remove particles before being sent to the gas analyzer (Varian CP4900 micro GC). The micro GC is used to detect species such as CH₄, H₂, CO, CO₂, O₂, N₂, and C₂ hydrocarbons; the detection limit of the instrument is around 10 ppm. The micro GC has its own pump and takes a small sample (few μ L) every 3 minutes. Figure 4.1 to Figure 4.5 provide more detailed information about the bed and the quartz reactor. The reactor consists of a quartz tube, 2 ft in length, 2.5 cm OD, and 2.2 cm ID, and has dimples in the center of the tube to support the fixed bed. Quartz is used. Due to the high temperatures of these tests, as well as to provide an inert surface for the reactor walls. Additional support for the catalyst beds is provided by a ceramic honeycomb (2.5 cm thick)

and a piece of quartz wool that is compressed to a height of 0.5 cm, both of which are placed directly on top of the dimples. The bed consisted of short pieces of wire (length of each piece is roughly 1 cm), and different bed depths are tested.

4.2.3. Experimental parameters and operating conditions

4.2.3.1. Fixed parameters

The experiments evaluated methane oxidation under flameless combustion conditions. The gas flowrate through the reactor was constant at 500 ± 5 mL/min and the methane concentration was constant at $1.4 \pm 0.1\%$ (volume) for all tests.

4.2.3.2. Materials tested

Different metals were chosen to evaluate their catalytic effect on methane oxidation. The metals evaluated include 316 SS, 304 SS, 410 SS, 420 SS, and Hastelloy-X. Chemical composition of each of these materials is reported in Appendix F. All were in the form of wire (1 mm diameter). A long roll of each metal was purchased and cut in short pieces of length 1 cm (approx.). Short lengths of wire were used as the primary bed material due to difficulty in procuring small balls of all of the different materials of interest. Balls of 316 SS were also tested to compare the effect of surface area.

Several blank tests were run for the quartz reactor itself and for the quartz reactor + ceramic honeycomb + quartz wool, in order to make sure that the results of methane oxidation were only due to the metal activity.

Ceramic balls of 3 mm diameter and a conventional oxidation catalyst (BASF PuriStar R0-20/47, Pd 0.5% in weight, supported on gamma-alumina beads) were evaluated as well.

The gamma alumina-catalyst beads have a diameter between 2 - 4 mm. Properties of the alumina - Pd catalyst beads are provided in Appendix F.

4.2.3.3. Bed depth and residence time

The bed depth of the wire metals varied between 1 and 9.5 cm and the residence times varied from 0.05 s to 2.55 s. In experiments with the Pd catalyst, the bed depth varied between 0.3 and 9.5 cm and the residence times varied from 0.09 s to 2.8 s.

4.2.3.4. Pressure

The pressure drop through the bed reactor was negligible; all the tests were conducted at atmospheric pressure of about 0.85 atm.

4.2.3.5. Furnace temperatures

The experiments were conducted at different furnace set point temperatures, ranging from 100 °C to 775 °C, and reactor temperature profiles were measured for these different furnace set point temperatures. Figure 4.6 shows the reactor temperature profiles measured at different furnace set points and Table 4.1 shows the detailed information about experimental parameters for each material.

4.2.4. *Experimental procedure*

4.2.4.1. Micro GC calibration

A calibration gas (cal-gas) containing 4.5% CO, 6.0% CO₂, 7.5% H₂, 15% CH₄, 1.5% C₂H₄, 6.0% C₂H₆, balance N₂, was used periodically to calibrate the micro GC. The cal-gas was passed through the by-pass line of the system to verify that all the species at their corresponding concentrations were detected by the micro GC. Then, the by-pass line was closed and the cal-gas was passed through the empty reactor (only the quartz tube) to also verify that the same concentrations were detected. The calibration was done at room temperature.

Prior to each test, the quartz tube was cleaned with ethanol and dried with air. The short pieces of wire were cleaned with acetone and dried with air before putting them in the reactor. Gloves were worn all the time for glassware and wire manipulation to avoid introducing any oil and/or other impurities.

Once all the parts of the system (quartz reactor, ceramic honeycomb, quartz wool, wires, thermocouples, fittings, tubing) were put together, a leak test was conducted. A digital flow meter was used to measure the gas flowrate. A certain flowrate of air was sent through the by-pass line and checked with a digital flow meter, then the gas was switched from the by-pass to the reactor and the flowrate was checked again to make sure the reactor had no leaks. With no leaks in the system, the gas-methane mixture was passed through the by-pass until the micro GC read the methane concentration that was fed.

Finally, the reactor temperature controller was set to the desired value, the gas was passed through the reactor, and the data acquisition system for temperature recording was started.

4.2.4.2. Measurement of temperature profiles

The presence of dimples in the quartz tube made it impossible to use only one thermocouple to get the temperature profile through the quartz tube; two $\frac{1}{16}$ inch type-K thermocouples were used. The top and bottom thermocouples were centered inside the reactor (they don't touch the walls of the quartz tube) and they were pulled up and down to obtain the temperature readings at different heights. This procedure was followed for each furnace set point temperature. The gas mixture was passed through the reactor while the temperatures were measured. The measured temperature was corrected for radiation loss base on reference 3.

4.2.5. *Results and discussion*

4.2.5.1. Experimental results

Different blank tests were run to consider any possible effect of the thermocouples, the ceramic honeycomb, and the quartz wool (which support the metal materials in the reactor) on methane oxidation. Figure 4.7 shows the results of the different blank tests. Each data point represents a separate, steady-state test carried out at a particular temperature. For blank test 1, the ceramic honeycomb, quartz wool, and the thermocouples were in the reactor. Then, the thermocouples were removed but the honeycomb and the quartz wool were left in place (blank test 2). Finally, the honeycomb and quartz wool were also removed and the gas mixture was passed through the empty reactor (blank test 3). The results show that for the empty reactor, methane oxidation starts and ends at a slightly lower temperature than at the other conditions. However, the difference is not significant. So, for all the tests with metals in the bed, we put thermocouples in the reactor and used ceramic honeycomb

and quartz wool in the system. Detailed results for the blank tests are included in Appendix F. Figure 4.8 shows a comparison of methane oxidation on different materials. For these tests, the bed depth was about 9.5 cm. As before, each data point represents a separate, steady state, approximately isothermal test at each temperature for each material. Thus, the curves generated represent the extent of methane oxidation at steady state as a function of temperature for the residence time within the bed. The metals (different stainless steels alloys and Hastelloy-X) show similar results for methane oxidation, and are similar to the ones obtained for the blank tests. The difference between the blank test and the tests involving a bed of material (where higher furnace set points were required to initiate onset of oxidation) are attributed to heat transfer and residence time differences. Oxidation for experiments that included a bed of metal wire starts at a furnace set point temperature around 725 °C and completes at a furnace set point temperature around 775 °C. The results suggest that the observed methane oxidation on the stainless steels and Hastelloy-X can be explained by homogeneous (noncatalytic) oxidation. For comparison, the experiment with a Pd catalyst promoted the initiation of methane oxidation at temperatures as low as 200 °C, for a bed depth of 9.5 cm, and complete oxidation occurred at a furnace set point around 300 °C. More detailed results are included in Appendix F. Note that the furnace set point temperature is not exactly equal to the bed temperature. To find the temperature at each point within the bed, refer to Figure 4.6 and Table 4.1.

The activity of the Pd catalyst was also investigated by using beds of different depth, yielding different residence times, and then comparing the temperature at which oxidation began and ended. Figure 4.9 shows the results of methane oxidation for bed depths of 9.5 cm, 1.3 cm, and 0.3 cm. The results are compared with a blank test when the gas mixture

is passed through an empty reactor. In the blank test, there is no methane conversion at furnace set point temperatures over the range 100 - 500 °C. However, methane oxidation on Pd-coated alumina starts at temperatures around 200 - 250 °C, and as the depth of the bed decreases (and residence time decreases), the oxidation ends at a higher temperature. All the previous experiments for catalytic activity of the metal samples were performed starting from lower furnace temperatures and increasing to higher temperatures. For example, for 304 SS, the test starts at 500 °C and the furnace temperature was increased gradually until oxidation started. However, one test was run starting at 775 °C, and then the temperature was gradually decreased to 500 °C. Figure 4.10 shows a comparison of methane oxidation on 304SS when the test was run from low to high temperature and vice versa. No significant difference is observed.

The activity of 304 SS was also examined by exposing the metal to the gas mixture at a furnace set point of 600 °C for about 8 hr, to determine if there was any difference in activity of the metal due to extended exposure to the reacting mixture and potential oxidation or fouling. As is shown in Figure 4.11, no significant changes in methane concentration were seen over time for the conditions studied.

4.2.5.2. CHEMKIN modeling results

CHEMKIN chemical kinetic software (available commercially from Reaction Design¹) was used to model the homogeneous oxidation of methane in the reactor at the UofU for experimental conditions and furnace temperatures of 450 °C to 750 °C. The temperature profile at each furnace setpoint temperature was measured experimentally and corrected for radiation loss.³ Since the experimental results indicated that the observed methane

oxidation can be explained by homogeneous (noncatalytic) oxidation, a series of simulations were performed to determine if this finding was supported by calculations. Appendix F provides detailed information on the modeling. Four different mechanisms, nominally described as GRI-Mech 3.0, WF, ABF, and CRECK, were used to provide transport, thermodynamic, and kinetic data. A brief description of each mechanism is given and an example modeling procedure and detailed comparisons between the results of each mechanism are also presented in Appendix F. For each furnace set point, the reactor temperature profile was obtained from the experimental data presented in Figure 4.6. A Plug-flow Reactor (PFR) assumption was used to model the experiments. Figure 4.12 shows a comparison between experimental data and a CHEMKIN prediction of methane homogenous oxidation (blank test 3— an empty reactor with no ceramic honeycomb or quartz wool). The results show that the predicted trends are in good agreement with the data. The minor differences are likely due to approximations such as use of a PFR model, as well as experimental bias error in the temperature profile measurements and assumptions in the radiation loss corrections.

The same procedure was used to model some of the experimental data obtained by Western Research Institute (WRI).² That data were previously provided under contract to AMSO, who shared the resulting data with the University of Utah. Two assumptions were used to model the WRI data. At first, it was assumed that the reactor temperature was fixed and equal to the average bed temperature reported by WRI. In a second approach, we assumed a temperature profile that was based on the average bed temperature reported by WRI and the trend in temperature observed by the University of Utah, similar to that in Figure 4.6. The detailed results of these simulations are provided in Appendix F. The

results suggest that the observed methane oxidation in the WRI tests can be explained by homogeneous oxidation rather than catalytic effects of the stainless steel or Hastelloy-X tested in their reactor.

4.2.6. Summary

Experimental and modeling studies were performed to investigate the catalytic activity of metals and catalysts that could potentially be used in heater construction and operation. Both experimental and modeling results show that the observed methane oxidation over stainless steels and Hastelloy-X can be explained by homogeneous oxidation rather than by any catalytic effect of these materials. On the other hand, Pd-coated alumina catalyst promoted complete methane oxidation at temperatures as low as 300 °C. CHEMKIN results suggest that the experimental results previously reported by WRI on the catalytic activity of stainless steel and Hastelloy-X can also be explained by homogenous methane oxidation.

4.3. Section II: Cold-flow mixing study

As discussed in Chapter 1, the homogeneous heater concept consists of two perforated pipes that inject the fuel and oxidizer into a perforated reaction chamber. The reactant mixing would be controlled by the relative locations and orientations of the nozzles in the feeder pipes. The mixing of reactants plays an important role in producing a dilute combustion environment and in controlling peak temperatures. Thus, it is critical to design a system so that the fuel and oxidizer mix appropriately along the length of the reaction chamber. A cold-flow experimental mixing study was conducted to investigate the mixing of fuel and oxidizer jets and to determine the optimum positions and orientations of the

nozzles. This section summarizes the experimental setup for this purpose and the results obtained for different cases. The latter includes uncertainty analysis.

4.3.1. Experimental setup

4.3.1.1. Bench-scale apparatus

Figure 4.13 shows the schematic and a photo of the cold-flow apparatus. It consists of two PVC pipes inside a larger, clear acrylic pipe that simulates the reaction chamber of the underground heater. The PVC pipes have holes to permit injection of either fuel or oxidizer into the reaction zone. Table 4.2 summarizes the sizes of the pipes and the holes. The pipe sizes were chosen so that the apparatus would be representative of a 1-meter section of the actual downhole heater. The hole size was estimated by the method explained in Chapter 3, Case 1, first approach. The gases are injected to the PVC pipes, pass through the holes, mix in the chamber, and escape through the exhaust. There are eight sampling probes installed at different locations in the chamber. The probes had the capability to get samples from various locations/orientations of the mixing chamber. The samples were analyzed with a micro GC to determine the gas composition. The system was designed to allow the inner pipes to move in order to change the axial and tangential orientations of the holes. The length of the apparatus was 120 cm, with one hole on each of the injection pipes.

4.3.1.2. Experimental parameters and operating conditions

The primary objective of the experiment is to study gas mixing in the chamber and determine the optimum position and orientation of holes relative to each other. The parameters for the cold-flow studies are summarized in Table 4.3.

4.3.1.3. Gas flowrates

Due to safety concerns, carbon dioxide and nitrogen were used instead of methane and oxygen. The density of nitrogen and oxygen are close to each other ($\frac{\rho_{N_2}}{\rho_{O_2}} \sim 0.9$); however, carbon dioxide is heavier than methane ($\frac{\rho_{CO_2}}{\rho_{CH_4}} \sim 2.8$), which may influence the mixing results and makes a deviation from the actual case where methane and oxygen are injected to the system. The experiment was run at atmospheric pressure even though the pressure of the actual equipment will be high (10-30 atm). Because of the difference in pressure, the mass flowrates in the cold-flow study are different from the expected operating conditions. However, the cold-flow gas flowrates were chosen so that the chamber Reynolds number would be approximately the same for the cold flow study and the actual heater for a 1-meter section of a chamber. Table 4.2 to Table 4.4 summarize the resulting dimensions and flowrates. Note that reaction was not considered in the calculation.

Two mass flow controllers metered the carbon dioxide and nitrogen from the cylinders to the system. For the nitrogen, a Brooks mass flow controller (model 5850E) was used. A Smart Trak mass flow controller (series 100) was used for the CO₂.

4.3.2. *Experimental procedure*

4.3.2.1. Orientations and positions of holes

Three cases studied are shown in Figure 4.14. In Cases 1 and 2, the holes on the PVC pipes delivered gases in adjacent or different axial locations, but had the same circumferential orientation. In Case 3, the holes were at the same axial position, but were directed away from each other. The top nozzle carried the N₂ and the bottom nozzle carried

CO₂ gas. In Case 1 and 3, the nozzles were 25 cm from the gas inlet, and in Case 2 the position of one nozzle was 25 cm, and the other was 50 cm from the gas inlet. Table 4.5 lists the injection locations for the N₂ and CO₂.

4.3.2.2. Mixing measurement methodology

There are several methods available to determine the mixing behavior of gases inside the chamber. Some of these include high-speed infrared imaging, particle image velocimetry, visualization based on acid-base reactions using an indicator, or measuring gas mixture composition with a gas chromatograph. The last method was employed in this study. A Varian micro gas chromatograph (model CP4900) was used to analyze the mixture composition at different locations inside the chamber. In the mixing chamber, the gases mix and eventually escape from a vent. The pressure in the vessel was controlled by a valve on the exhaust vent. The valve was adjusted to maintain the minimum pressure difference, ~ 690 Pa, required for the gas samples to flow to the micro GC. A manometer monitored the pressure difference between the chamber and the ambient pressure. Figure 4.15 and 4.16 show the exhaust valve and the manometer installed on the mixing chamber.

Figure 4.17 shows the location of the sampling probes in the chamber. Eight probes, four on the top and four on the side of the chamber, were installed. Each was ruled in centimeters so that their positions could be recorded. Table 4.6 summarizes their positions. The X and Z orientations of the top probes were fixed; however, they were moved along the Y-axis to sample from different Y locations. There were also four side probes for which the Y and the Z positions were fixed. They were moved along the X-axis. The fittings on the probes were chosen so that they could be easily positioned. Figure 4.18 shows one

sampling probe with a closer view of the fittings. The probes were connected to a manifold, which conveyed the gas samples to the GC. The sampling manifold is shown in Figure 4.19.

4.3.2.3. GC calibration

The GC was calibrated with five calibration gases. Table 4.7 lists the composition of each. Figure 4.20 and 4.21 show the calibration curves for CO₂ and N₂. The symbols are the average peak area obtained from the GC, and the line is a polynomial fit. The error bars are the analytic errors reported for each calibration gas. Calibration using the gas from each cylinder was repeated several times. The standard deviations and the confidence intervals (considering 95 % confidence level) for the calibrations are shown in Table 4.6.

4.3.2.4. Calibration of mass flow controllers

Both flow controllers were calibrated over the range of the desired flowrates. Each was calibrated with two separate flow meters: a 1000-milliliter graduated tubular flowmeter and a digital flow meter (gilibrator). The confidence intervals for the CO₂ and N₂ mass flow controllers were 0.01 and 0.05 lit/min, respectively, for the targeted flowrates (N₂ inlet flowrate= 4.7+/- 0.05 lit/min and CO₂ inlet flowrate= 2.3+/- 0.01 lit/min). The confidence intervals were determined considering a 95% confidence level.

4.3.3. *Results and discussion*

The CO₂ and N₂ concentrations were measured at 65 locations inside the chamber in Case 1. In Case 2 and Case 3, the concentrations were measured at 54 and 56 locations,

respectively. Sampling at each point was repeated several times to confirm repeatability.

Based on the data obtained from the top probes, a contour of the CO₂ mole fraction was generated at the $x = 0$ surface, which passes through the middle of the chamber between the two PVC pipe. Figure 4.22 shows the location of the $x=0$ surface. Figure 4.23 shows the CO₂ mole fraction at plane $x = 0$ for the three cases. Complete mixing corresponds to a CO₂ mole fraction of 33%. In Case 1 and Case 2, the two streams are well mixed. In Case 3, the higher density CO₂ tends to flow along the bottom of the chamber, where the CO₂ nozzle was oriented. Note that in the actual case, it is more likely that less scarification happens because methane density is lower than density of carbon dioxide. In addition, in the actual heater, methane will be injected to the bottom and oxygen will be injected to the top. Since the density of methane is lower than oxygen, it helps the gas mixing in the chamber. The results show that the radial orientations of the nozzles have a more significant role in the mixing behavior than the axial positions of the nozzles and that the higher density of CO₂ can lead to stratification. Case 3, where the circumferential positions of the nozzles are opposed, shows less mixing than Cases 1 and 2. Figure 4.22 and Figure 4.23 show the CO₂ mole fraction inside the mixing chamber at different locations. The samples were taken from four side-probes and they were moved in the x -direction to obtain a profile. The CO₂ mole fractions in Cases 1 and 2 are similar at all sampling locations and are about 33 mole %, which indicates complete mixing. In Case 3, the CO₂ mole fraction is high in the lower portion of the chamber and lower in the upper region. This result is consistent with injecting the higher-density CO₂ gas in the bottom of the chamber.

All cases could be suitable for heater applications depending on the purpose of the design, the desired level of mixing, and the desired temperature. Case 3 may be more

appropriate for dilute combustion. It somehow delays mixing so that we have an opportunity to mix combustion products in with the fuel and oxidizer, to thus control temperature and NO_x formation.

4.3.4. *Uncertainty analysis*

Uncertainty analysis was performed to find the possible sources of error in the experiments and to find ways to eliminate or reduce them. In the following, some of the sources of the error are listed. The strategies taken to address some of the errors are also explained.

There are different possible sources of errors in the current experiment: the apparatus, the procedure, or data analysis. In the following, several sources of uncertainty and ways to reduce them are discussed.

4.3.4.1. Sealing of the system

There is a chance of gas leakage in some parts of the apparatus. For example, there may be leakage from certain regions of the system such as the caps on the pipes and the chamber, connections of the manometer to the chamber, connection of the outlet valve to the chamber and the locations where probes are installed (especially the side-probes). Also, leakage occurs while adjusting the probe positions during each sampling interval. To minimize leakage, connections were tested for leakage before each run. A certain flowrate of air was sent to the system and all the outlets were closed. The pressure inside the chamber increased slightly above the ambient pressure. Then all connections were checked. There were two indicators for the leakage: (1) pressure inside the chamber dropped when the air flowrate

stopped; (2) Bubbles showed up in the leaking area when using soap solution.

4.3.4.2. Uncertainty of the inlet flows

The sources of uncertainty in the gas inlet flowrates are listed below.

4.3.4.2.1. Flow controller calibrations. As explained before, one flow controller was calibrated by a digital gilibrator; the other was calibrated with a bubble meter. A list of possible sources of errors in the flow controller calibrations is presented below:

- Error associated with the calibration of the digital gilibrator
- Error in connecting the gas inlet to the digital and nondigital calibrators (there may be a leakage at the inlet, and all the gases may not enter the flow meters)
- Error in measuring the time when using the nondigital flow calibrator (a stopwatch is used to measure the time the gas needs to pass the 1000 milliliter graduated tube, and human bias error can be introduced)
- Error in the data interpolation and generation of the flow calibration curve

In addition, the tolerance in the inlet pressure of the mass flow controllers could be another source of error. The data obtained from the same locations, performed a couple of times on different days, show that the uncertainty in the inlet pressure of the mass flow controller is negligible.

4.3.4.3. Uncertainty in sampling and data collection

The sources of uncertainty due to sampling and data collection are listed below.

4.3.4.3.1. Placement of the probe (uncertainty on the probe location). The sampling probes shafts were marked/scaled in centimeters. Sampling was repeated twice at the same

locations to help assess bias errors.

4.3.4.3.2. Having a manifold between the probe and the GC. There is a manifold between the sampling probes and the GC. In changing sampling locations, there is a chance that the previous gas mixture is not completely purged from the manifold and downstream tubing. To eliminate this problem, samples were drawn for 10 to 20 minutes, which is approximately equivalent to 8 to 16 manifold volumes.

4.3.4.3.3. Error in reading the pressure difference from the manometer. A manometer was installed in the mixing chamber to monitor the pressure difference between the inside of the chamber and ambient pressure. There may be a human bias error associated with the reading of the pressure from the manometer.

4.3.4.4. Uncertainty in data analysis

Uncertainty associated with the GC measurements and their interpretation is explained below.

4.3.4.4.1. Error of the GC calibration. The GC was calibrated before starting measurements. To have enough data points to generate reliable calibration curves, five calibration cylinders with different species compositions were used. The calibration data were interpolated with a polynomial curve fit. The detailed calibration procedure is explained in section.

4.3.4.4.2. The amount of the gas pulled out at each sampling intervals. The other important parameter, which may cause uncertainty in the data, is the amount of the gas pulled out at each sampling location. It is an indicator of whether a sample is representative of a particular point in the reactor, or a mixing-cup average of a larger volume. The

sampling procedure should be done so that it minimizes disturbance of the gas composition at the sampling location. The average volumetric flowrate of the gas pulled out of the system was 181.4 ml/min, which was about 2.6 % of the total gas inlet flowrate (N_2 inlet flowrate= 4.7+- 0.05 lit/min and CO_2 inlet flowrate= 2.3+- 0.01 lit/min). The ratio of the volumetric flowrate of the gas pulled out from the system to the total gas flowrate inside the chamber is small. Therefore, we can conclude that at each sampling period, a small volume of gases around the probe was pulled out and sampling did not disturb the flow pattern inside the chamber.

4.3.5. Summary

A cold-flow experimental mixing study was conducted to investigate the mixing of fuel and oxidizer jets and to determine the optimum position/orientation of the jets relative to each other.

Three cases were studied. In Cases 1 and 2, the holes on the PVC pipes were delivering gases in adjacent or different axial locations, respectively, but had the same circumferential orientation. In Case 3, the holes were at the same axial position but were directed away from each other. In Cases 1 and 3, the nozzles were 25 cm from the gas inlet, and in Case 2, the position of one nozzle was 25 cm, and the other was 50 cm, from the gas inlet. The gas compositions at different locations inside the chamber were measured with a micro GC. The results showed that in Case 1 and Case 2, the two streams were well mixed in the mixing chamber. In Case 3, there were two distinct regions, a volume where the concentration of CO_2 was high (N_2 is low) and a second where the concentration of N_2 was high. We concluded from the results that the radial orientations of the nozzles had a more

significant role in the mixing behavior than the axial positions of the nozzles. Case 3, where the circumferential positions of the nozzles were different, showed less mixing than cases 1 and 2.

An uncertainty analysis was performed and some possible sources of experimental errors were discussed. We also explained the attempts to minimize these errors in our experimental work. Finally, the volumetric flowrate of the sampling gas pulled out of the system was measured and compared with the total gas flowrate inside the chamber to make sure that the sampling procedure did not significantly disturb the flow inside the chamber.

4.4. References

- (1) Reaction Design. In *CHEMKIN-PRO 15131*; San Diego, **2013**.
- (2) Western Research Institute. *American Shale Oil Catalytic Material Tests (Private Report)*; Laramie, WY, **2009**.
- (3) Shaddix, C. R. In *Proc. Natl. Heat Transfer Conf., 33rd*; American Society of Mechanical Engineers, **1999**; 597–606.

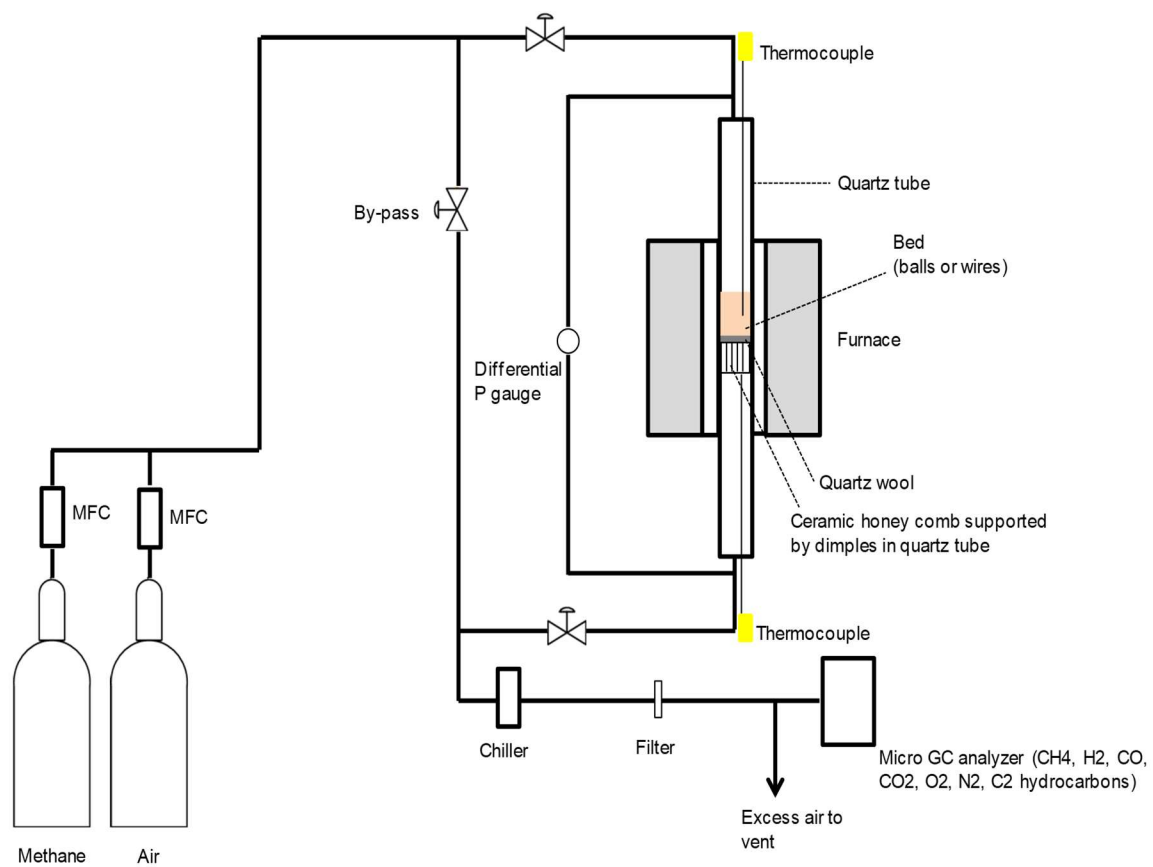


Figure 4.1: Schematic of experimental setup (fixed-bed reactor)

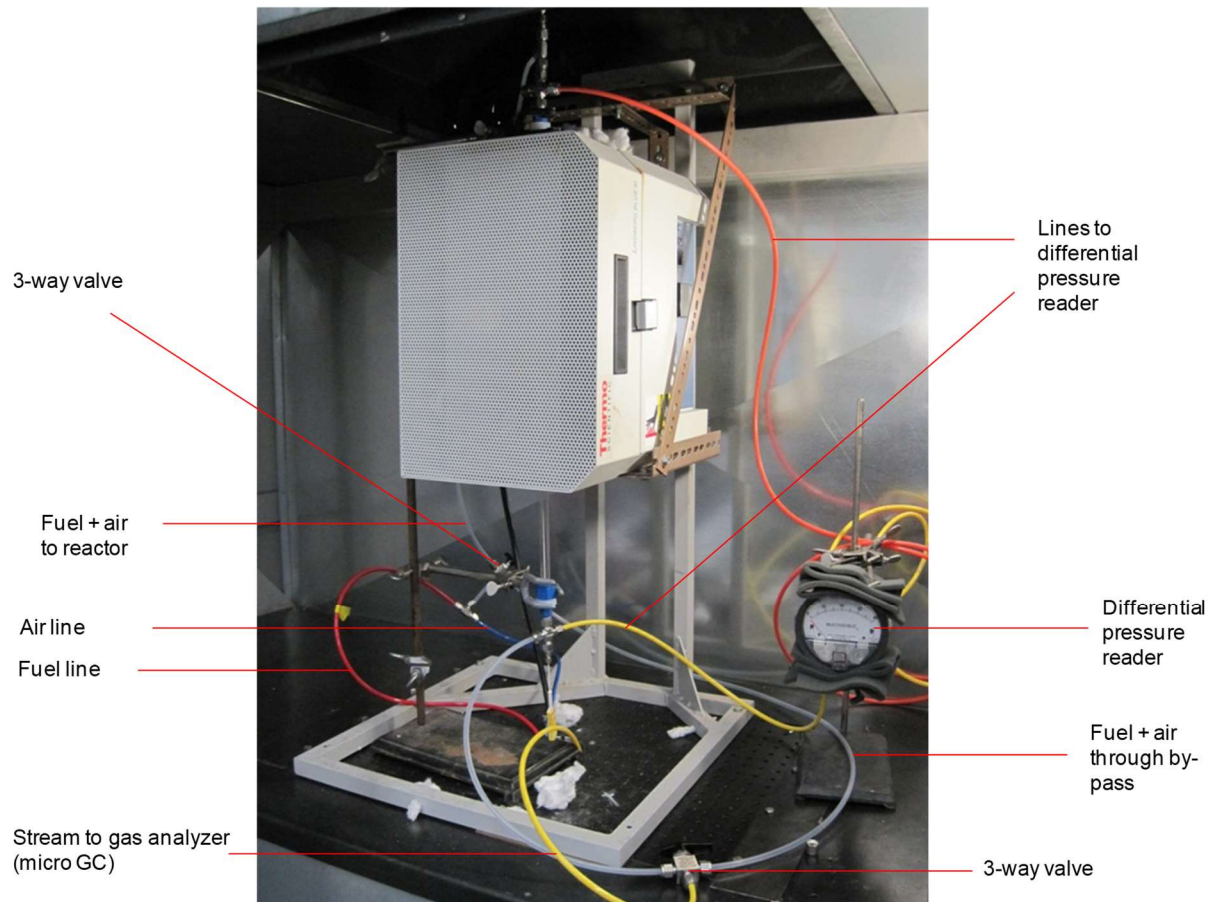


Figure 4.2: Photo of experimental system

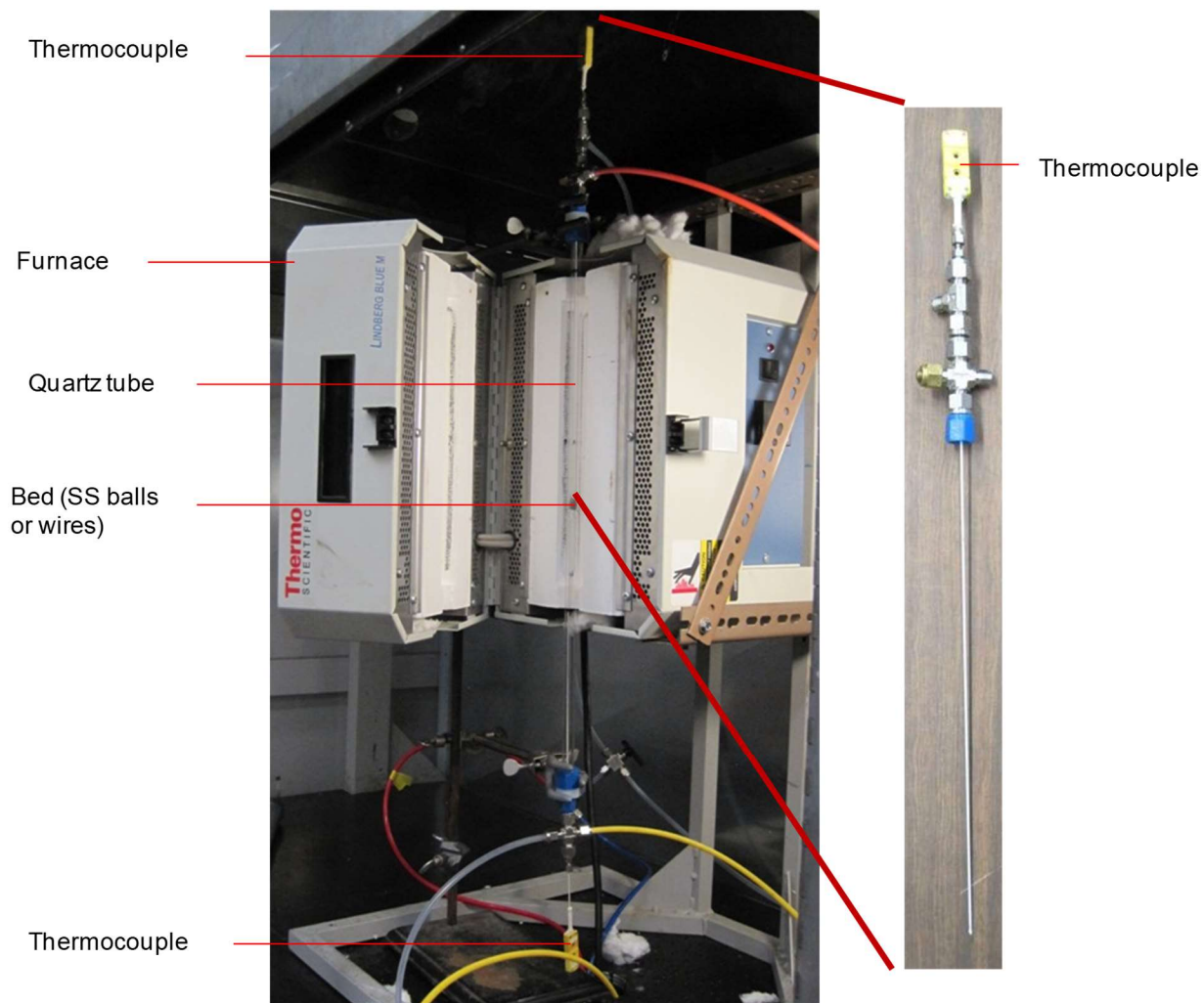


Figure 4.3: Photo of furnace

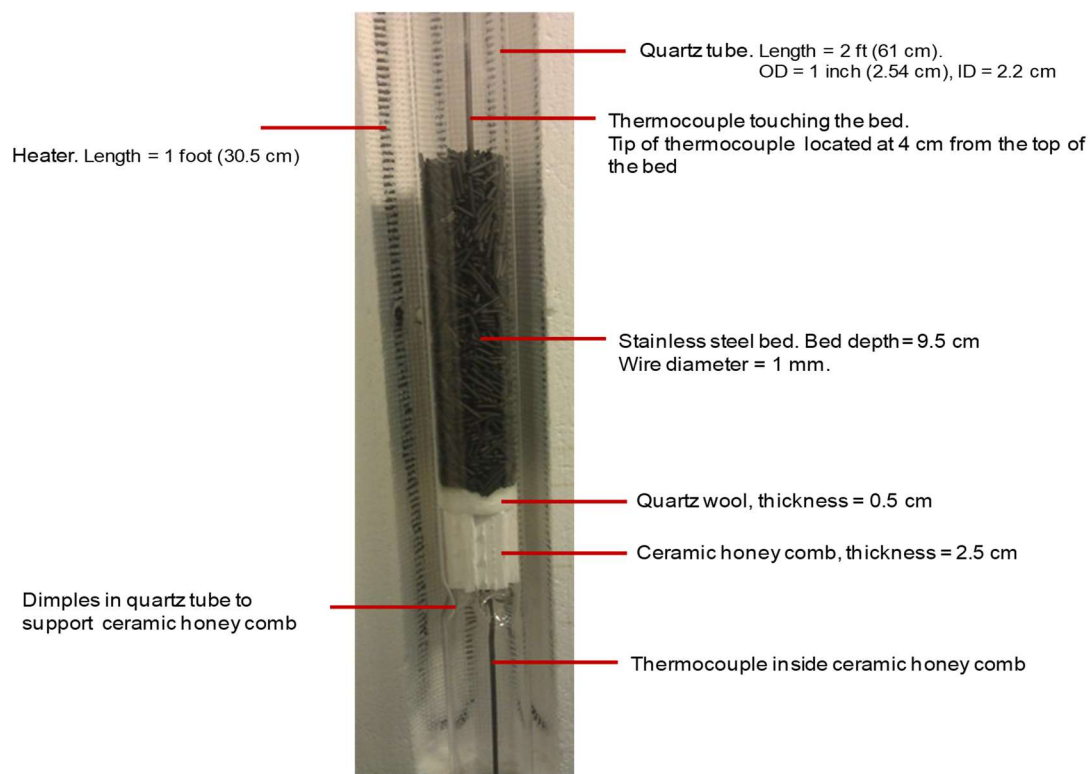


Figure 4.4: Fixed bed components

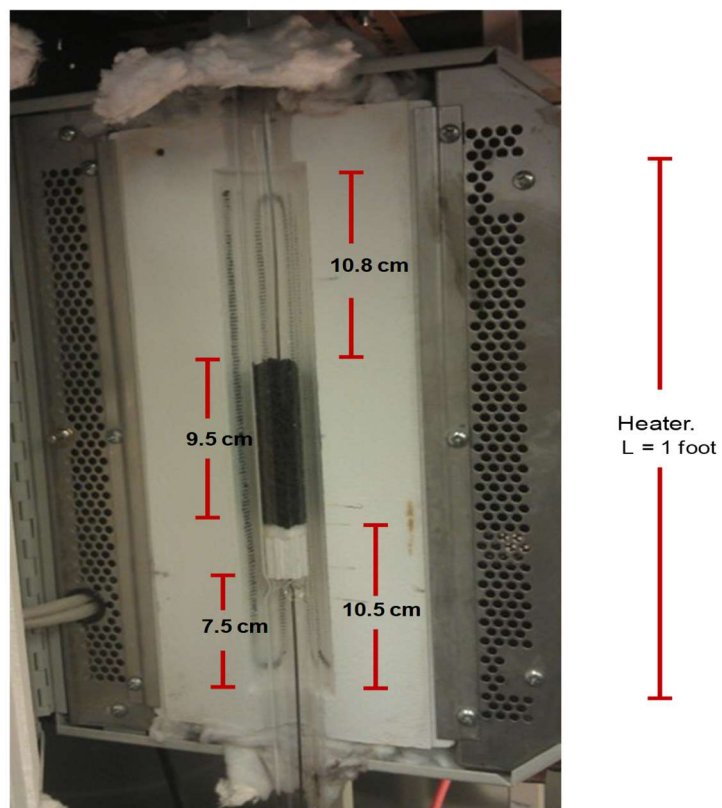


Figure 4.5: Fixed bed dimensions

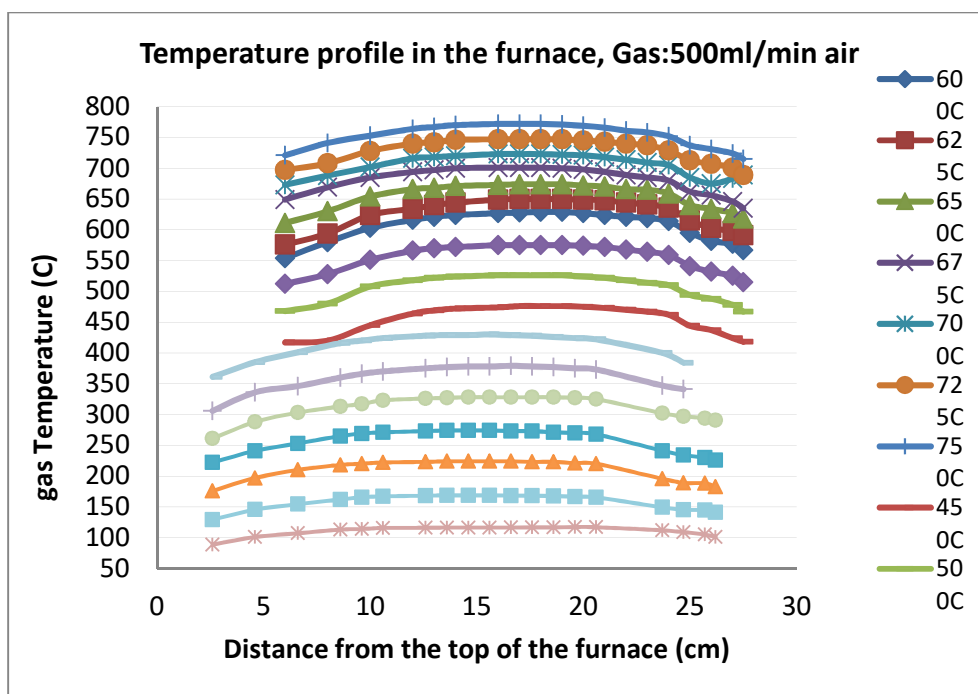


Figure 4.6: Temperature profile in the quartz tube reactor at different furnace set point temperatures (gas flowrate: 500ml/min)

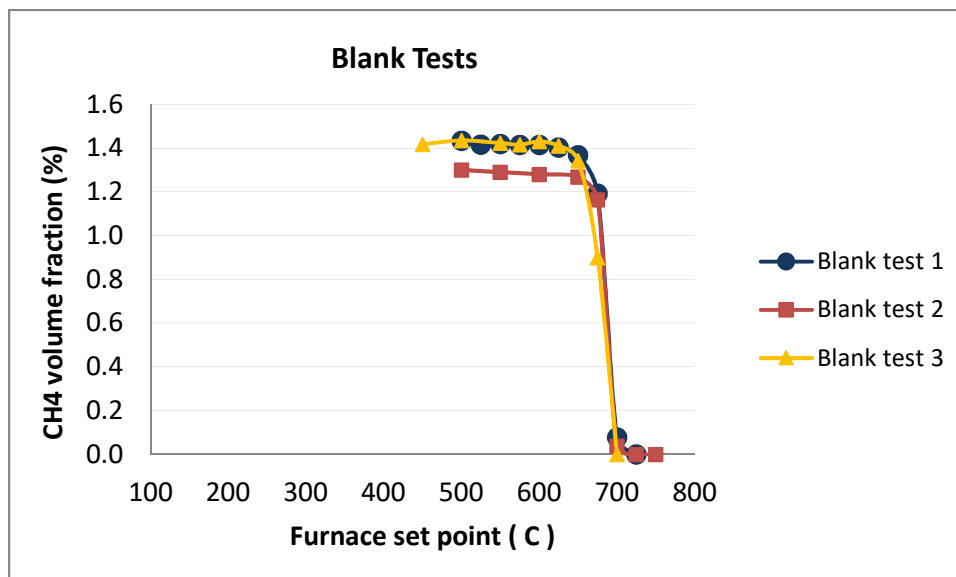


Figure 4.7: Effect of thermocouples, ceramic honeycomb, and quartz wool on methane oxidation (gas flowrate:500ml/min)

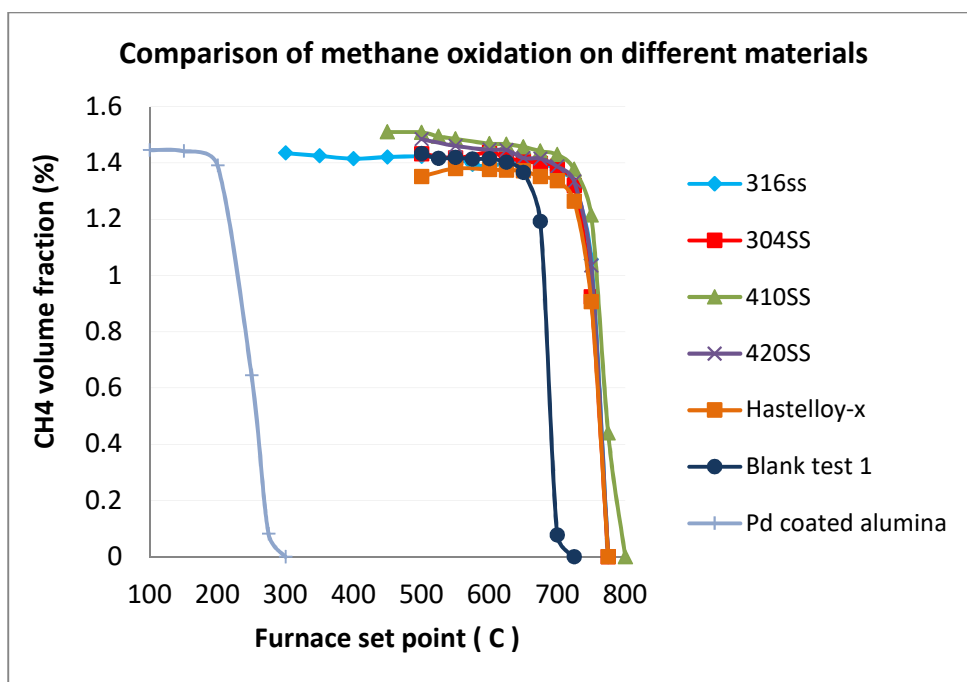


Figure 4.8: Methane oxidation on different materials (gas flowrate:500ml/min)

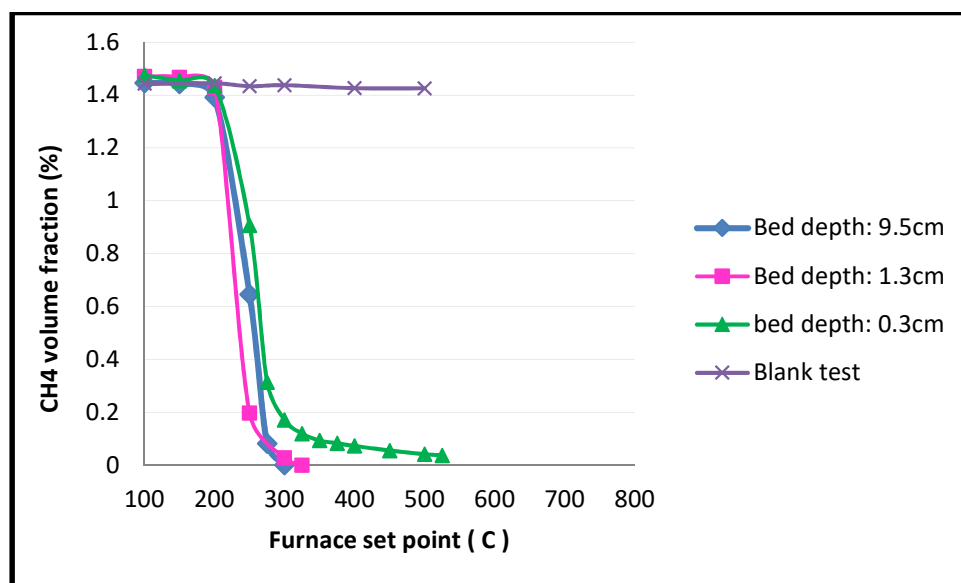


Figure 4.9: Comparison of methane oxidation on different bed depths with Pd catalyst (gas flowrate: 500 mL/min)

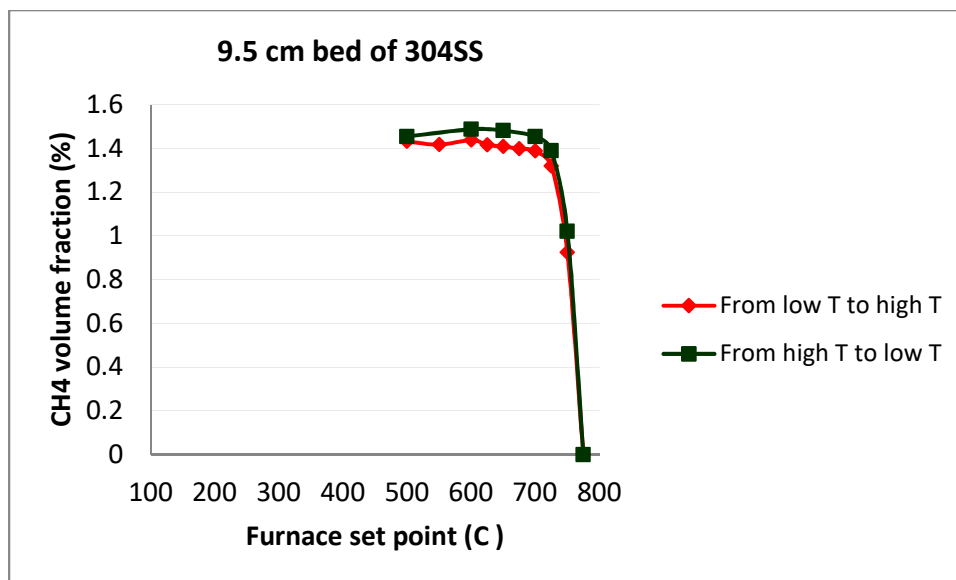


Figure 4.10: Methane oxidation on 304SS, furnace setpoint from low T to high and vice versa

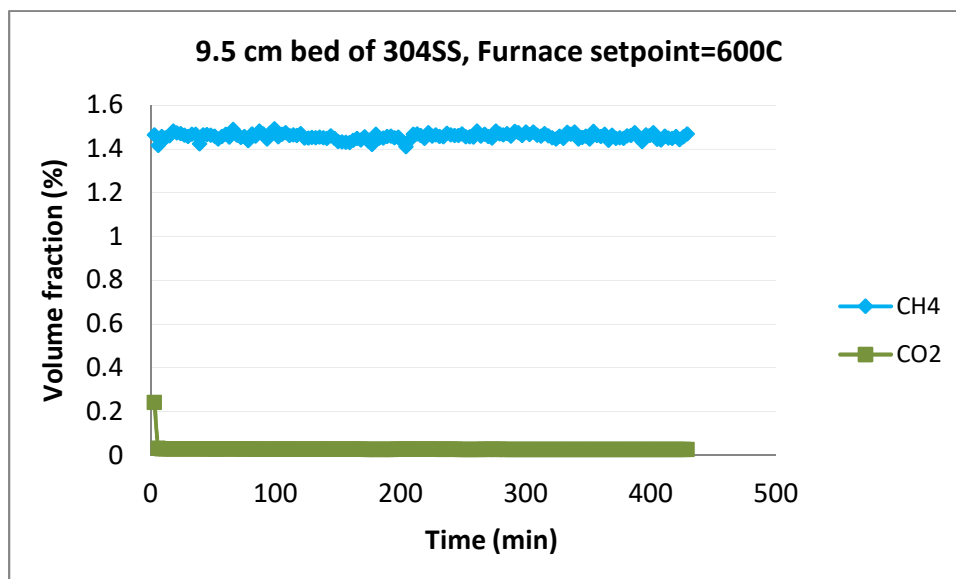


Figure 4.11: Methane oxidation on 304SS over 8 hours at furnace set point equal to 600 °C.

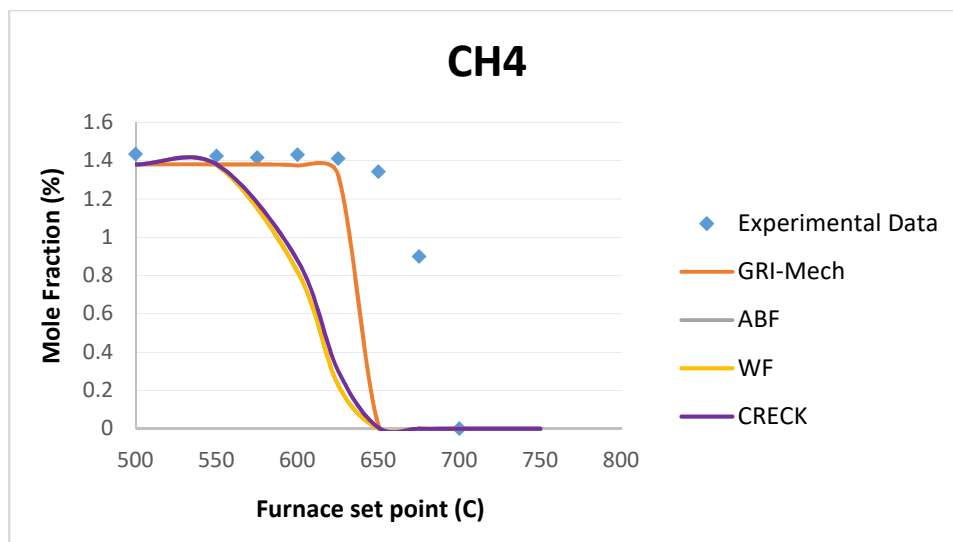


Figure 4.12: Comparison between experimental data (blank test 3) and CHEMKIN prediction of methane homogenous oxidation

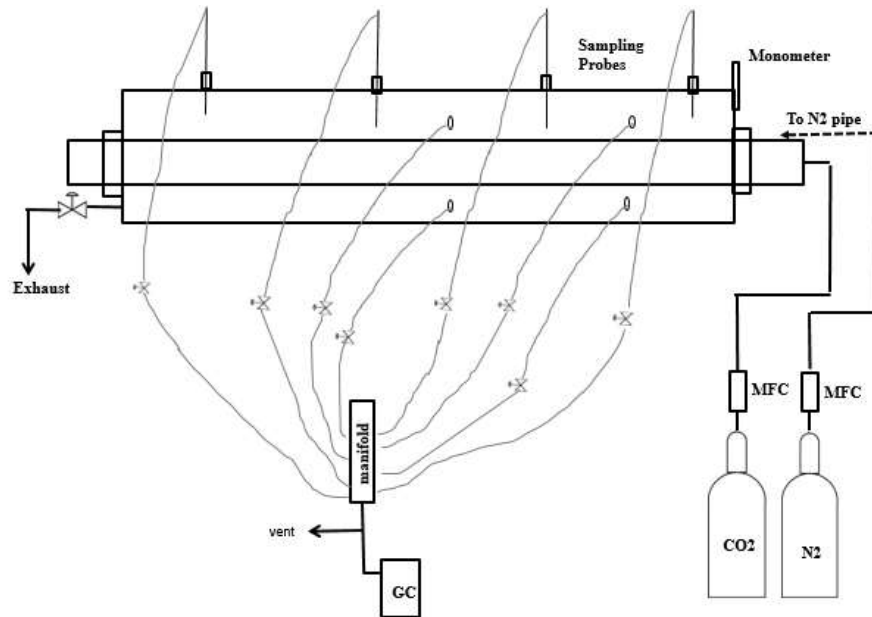


Figure 4.13: Cold-flow experimental setup

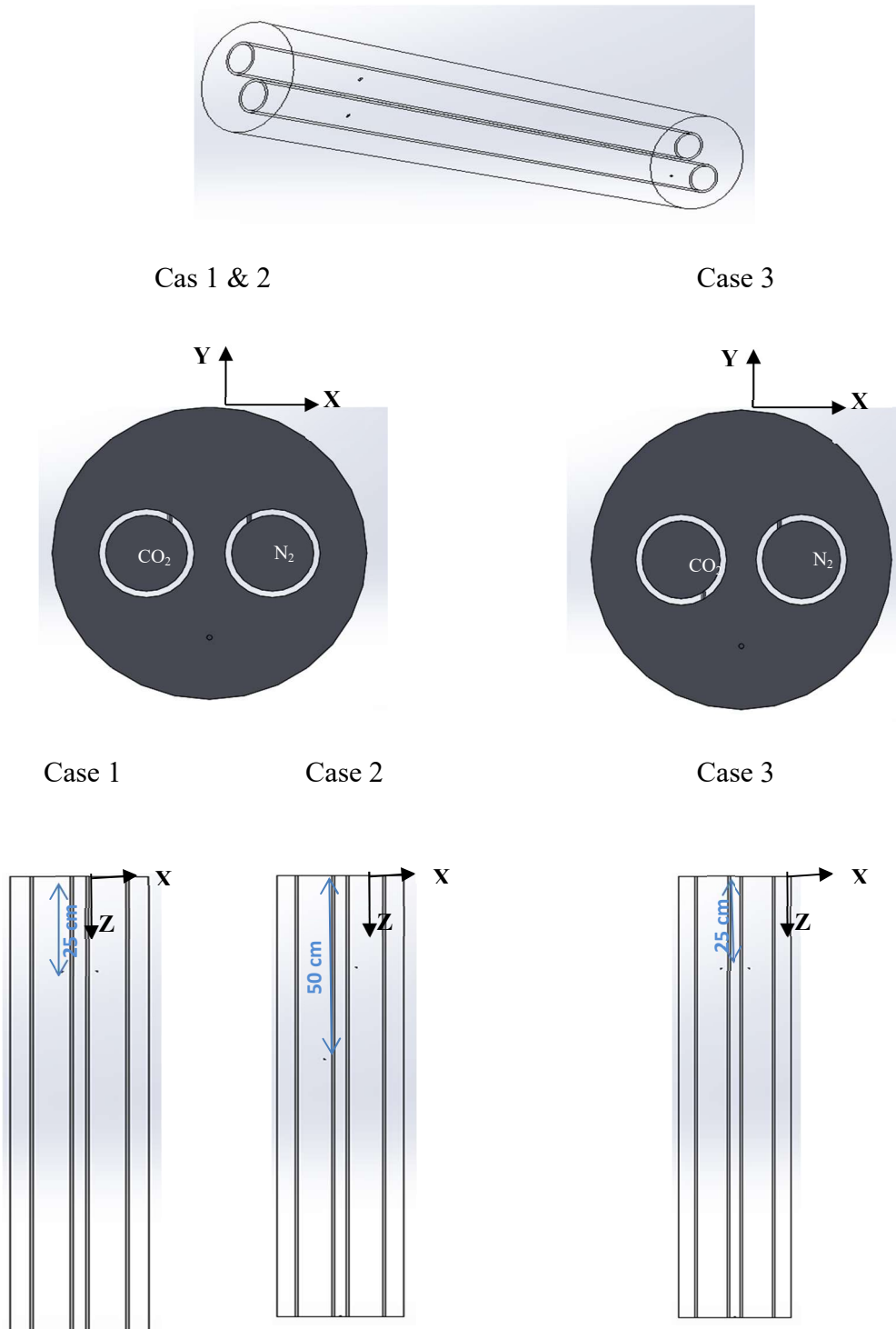


Figure 4.14: Schematics of the nozzle positions and orientations in the three studied cases

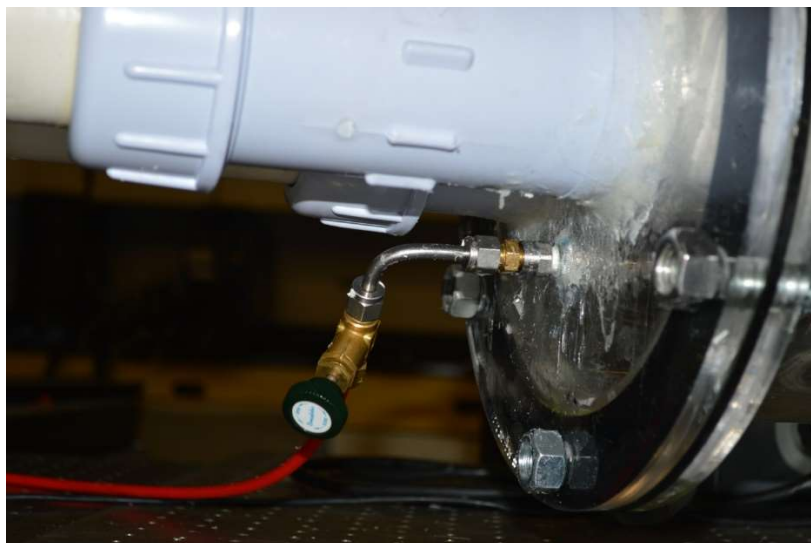


Figure 4. 15: Gas outlet

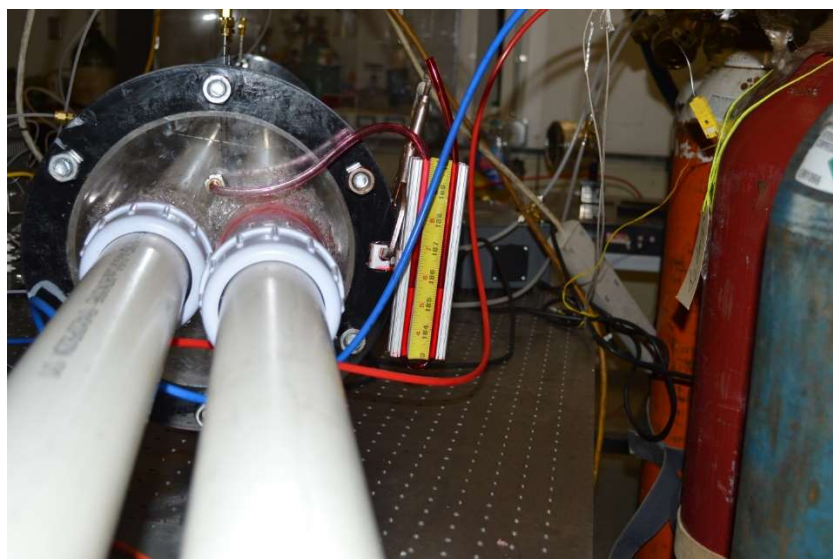


Figure 4.16: Manometer installed on the mixing chamber

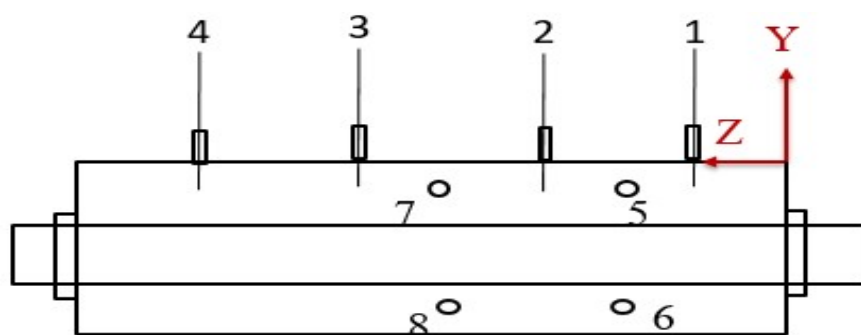


Figure 4.17: Axial locations of the sampling probes on the mixing chamber, side view of the chamber

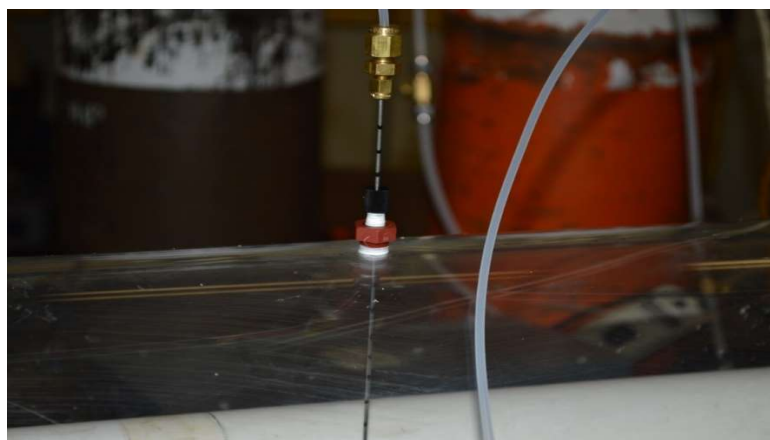
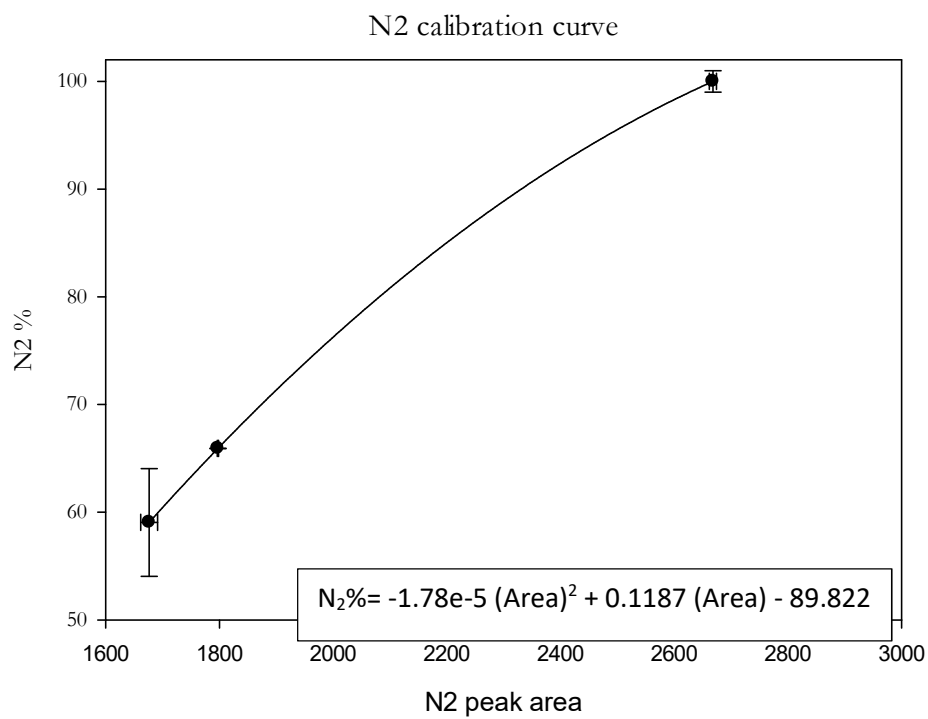
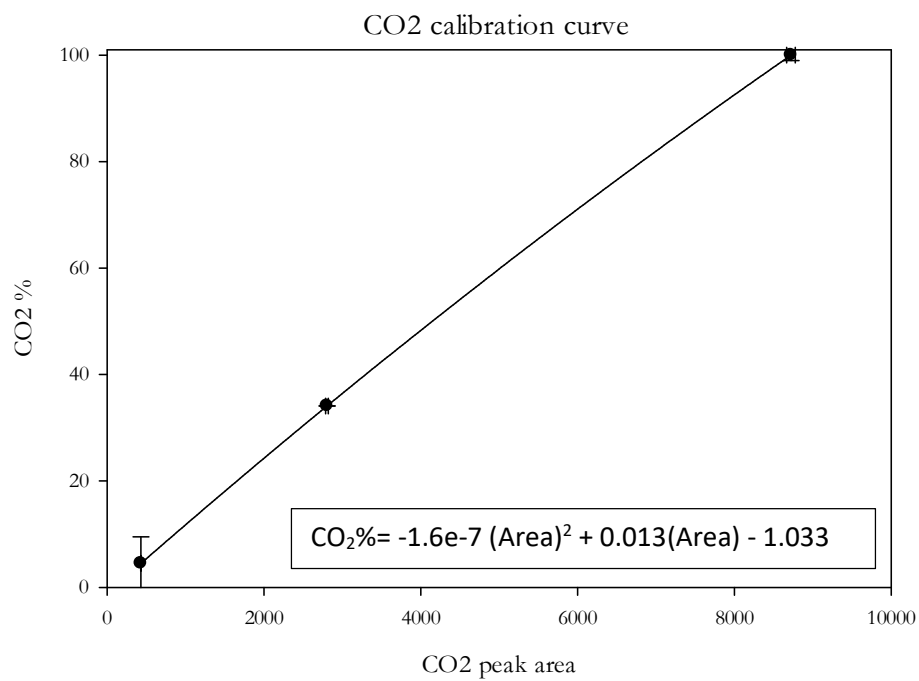


Figure 4.18: Closer view of a sampling probe and its fittings



Figure 4.19: Sampling manifold

Figure 4.20: N₂ calibration curveFigure 4.21: CO₂ calibration curve

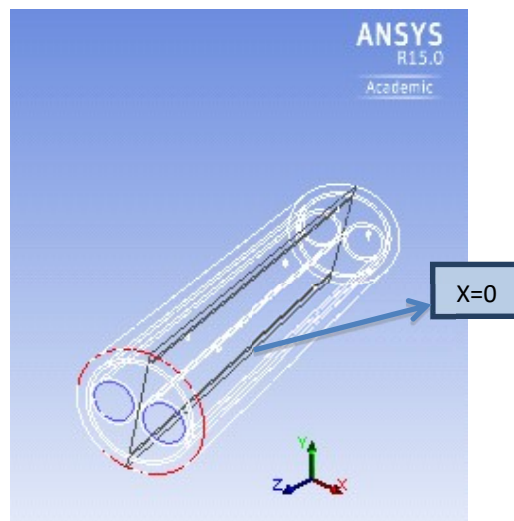


Figure 4.22: Location of planar surface at $x=0$ inside the mixing chamber

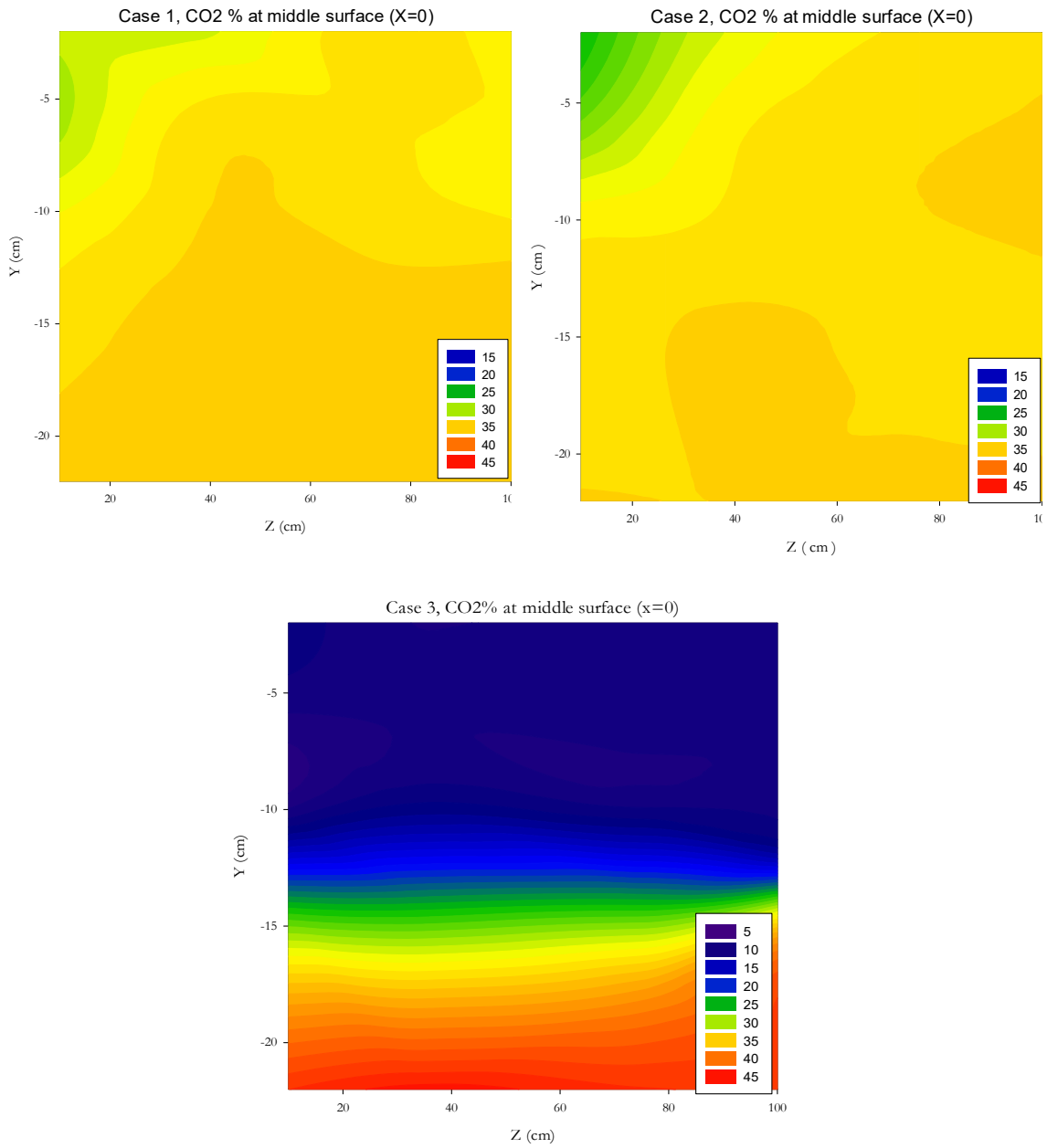


Figure 4.23: CO₂ mole fraction (%), at iso-surface x=0

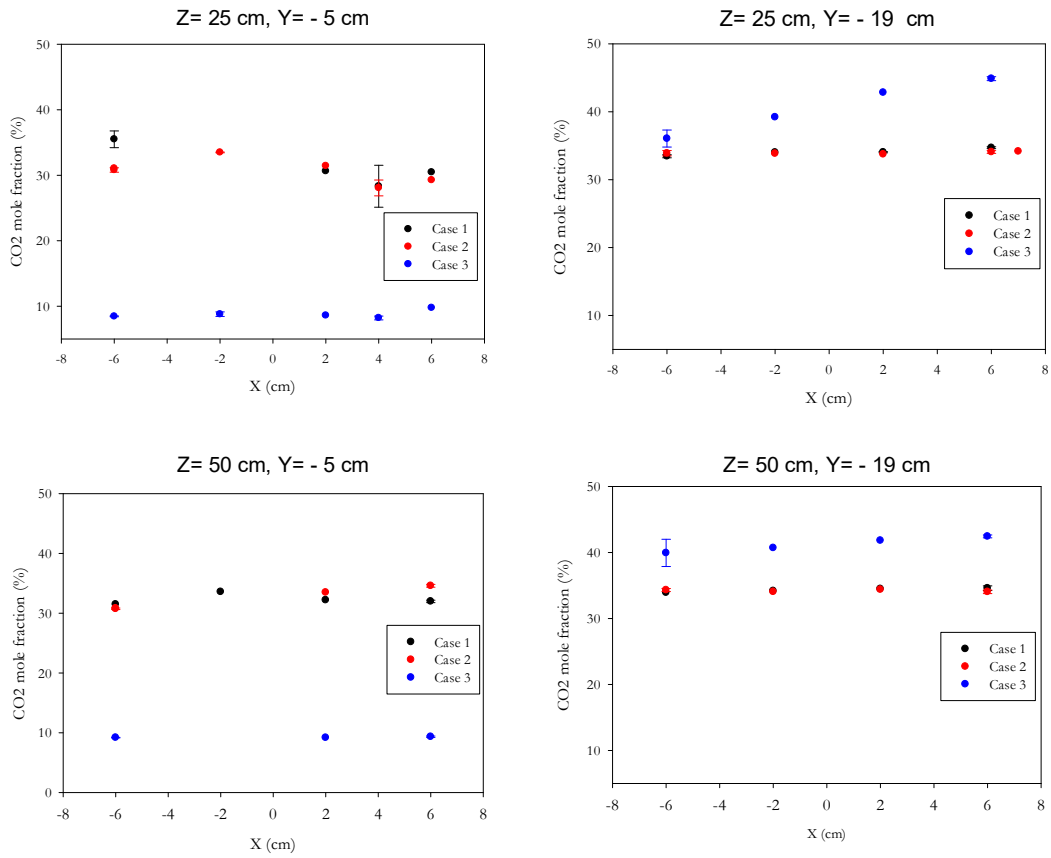


Figure 4.24: CO₂ mole fraction at different nozzle orientations

Table 4.1: Summary of tests performed

Material	Number of tests	Furnace set point T (°C)	Avg. bed T (°C)	Bed depth (cm)	Surface area (cm ² /gr)	Est. void fraction	Est. bed Volume (cm ³)	Residence time through bed (s)	Conversion
Blank test <i>(homogeneous oxidation)</i>	34	100-750	430 - 790	-	-	-	-	-	starts at set point 650°C, completes at 700°C
Ceramic balls 3 mm diameter	11	500-775	515 - 780	9.5	2.13	0.40	21.65	1.75	starts at set point 700°C, completes at 775°C
316 SS wires 1mm diameter	16	300-775	318 - 774	9.5	4.76	0.59	14.80	2.55	starts at set point 725°C, completes at 775°C
304 SS wires 1mm diameter	19	500-775	520-800	9.5	4.76	0.59	14.80	2.55	starts at set point 725°C, completes at 775°C
410 SS wires 1mm diameter	14	450-800	484-825	9.5	4.76	0.59	14.80	2.55	starts at set point 725°C, completes at 800°C

Table 4.1: Continued

Material	Number of tests	Furnace set point T (°C)	Avg. bed T (°C)	Bed depth (cm)	Surface area (cm ² /gr)	Est. void fraction	Est. bed Volume (cm ³)	Residence time through bed (s)	Conversion
420 SS wires 1mm diameter	11	500-775	531-800	9.5	4.76	0.59	14.80	2.55	starts at set point 725°C, completes at 775°C
Hastelloy-X wires 1mm diameter	11	500-775	529 - 800	9.5	4.76	0.59	14.80	2.55	starts at set point 725°C, completes at 775°C
Alumina balls coated with Pd (104 mg Pd, 2-4mm diameter)	9	100– 300	105 - 330	9.5	104.9	0.65	12.63	2.8	starts at set point 200°C, completes at 300°C
Alumina balls coated with Pd (13.6 mg Pd, 2-4mm diameter)	7	100– 325	110 - 403	1.3	13.6	0.65	1.73	0.39	starts at set point 200°C, completes at 325°C
Alumina balls coated with Pd (4.07 mg Pd, 2-4mm diameter)	15	100– 525	111 - 563	0.3	4.07	0.65	0.40	0.09	starts at set point 250°C, completes at 525°C

Table 4.2: Summary of the pipes and holes sizes

	ID (in)	Wall Thickness (in)
PVC pipes	2.469	0.203
Acrylic pipe	9.5	0.25
Holes on the PVC pipes	1/8	

Table 4.3: List of the fixed and variable parameters in the cold-flow experiment

Fixed parameters	Variable parameters
Gases: CO ₂ , N ₂	Hole positions
T=298 K, P=1 atm	Hole orientations
Number of holes: one hole on each of the N ₂ and CO ₂ pipes	
Size of the holes: 1/8 in	
Gas flowrates	

Table 4.4: Summary of the pipe sizing, gas flowrates, and Re numbers in the cold-flow experiments

	N ₂ pipe	CO ₂ pipe
Pipe length, L (m)	1.2	1.2
Number of holes, n	1	1
Hole diameter (in)	1/8	1/8
Total pipe inlet flowrate (L/min)	4.7+-0.05	2.3+-0.01

Table 4.5: XYZ location and orientation of N₂ and CO₂ holes (in centimeters) for the different cases

Case number	N ₂	CO ₂
Case 1	(4 cm, -9cm, 25 cm), up	(-4 cm, -9 cm, 25 cm), up
Case 2	(4 cm, -9cm, 25 cm), up	(-4 cm, -9 cm, 50 cm), up
Case 3	(4 cm, -9cm, 25 cm), up	(-4 cm, -9 cm, 25 cm), down

Table 4.6: Positions of the eight sampling probes

		X (cm)	Y(cm)	Z(cm)
Top probes	Probe #1	0	Moves from -2 cm to -22 cm	10
	Probe #2	0	Moves from -2 cm to -22 cm	35
	Probe #3	0	Moves from -2 cm to -22 cm	75
	Probe #4	0	Moves from -2 cm to -22 cm	100
Side Probes	Probe #5	Moves from -6 cm to +6 cm	-5	25
	Probe #6	Moves from -6 cm to +6 cm	-19	25
	Probe #7	Moves from -6 cm to +6 cm	-5	50
	Probe #8	Moves from -6 cm to +6 cm	-19	50

Table 4.7: Gas composition in each calibration gas cylinders

Calibration gas cylinder	N ₂ fraction (%)	CO ₂ fraction (%)	Other gases fraction (%)	Analytical error (%)
Cal-gas # 1	59.053	4.515	36.432	+ - 5
Cal-gas # 2	65.92	34.08		+ - 0.02
Cal-gas # 3	99		1	+ - 2
Cal-gas #4	100			
Cal-gas #5		100		

Table 4.8: Average peak areas, standard deviations, and confidence intervals for the GC calibration gas measurements

N ₂ %	Average Peak Area	Standard Deviation	Confidence Interval (95 % confidence level)
59.053	1676.33	14.89	16.86
65.92	1797.24	1.11	0.97
100	2668.25	6.26	6.13
CO ₂ %	Average Peak Area	Standard Deviation	Confidence Interval (95 % confidence level)
4.515	429.73	3.15	3.56
34.08	2802.26	17.44	15.29
100	8722.65	55.05	53.95

CHAPTER 5

MODELING

5.1. Overview

Chapter 5 has two sections. In Section I, the effect of diluents such as N_2 , CO_2 , and H_2O on the methane oxidation was investigated. The chemical and thermodynamic effects of diluents on the reactor temperature, ignition-delay, and flame stability were studied. To demonstrate the effect of the thermodynamic properties of diluents on model predictions, we conducted CHEMKIN calculations with an imaginary, inert version of each diluent. It has the same thermodynamic and transport properties as the noninert species, but does not participate as a reactant in any chemical reactions.

A sensitivity analysis was also performed to demonstrate the effect of chemical kinetic properties of diluents on model predictions. We looked at the reactions that were influenced by diluent concentrations and found the reactions that were the most sensitive to ignition-delay time within the desired operating conditions, to determine which of the reactions inhibit reactivity and which ones promote it. In all calculations, it was assumed that the reactor was adiabatic. However, in a downhole heater, there would be heat transfer from the reaction chamber to the surroundings and this issue was addressed in subsequent simulations, as noted below. The average heat transfer coefficients of the reaction chamber and the outer annulus were determined previously and discussed in Chapter 3.

In Section II, the heat transfer from the reaction chamber to the surroundings was considered in the calculations. CHEMKIN calculations were performed for a 1-meter section of the reaction chamber using nonadiabatic boundary conditions. The calculation was performed for fuel/oxidizer mixtures with varying levels of dilution over a range of temperatures to determine the bounds of homogenous ignition. A mixture of 67 mole percent CO₂ and 33 mole percent H₂O was defined as a diluent. Two canonical models, a plug-flow reactor (PFR) and a perfectly-stirred reactor (PSR), were investigated as two limiting cases. The predictions of each model were compared, and the amount of diluent required to reach the desired reactor temperature ($T \sim 939\text{K}$) was estimated.

5.2. Section I: Calculated impacts of diluents on flame temperature, ignition-delay, and flame speed of methane-oxygen mixtures at high pressure and low to moderate temperatures

5.2.1. Overview

Oxy-fuel combustion is one method to produce concentrated streams of carbon dioxide for subsequent sequestration. An additional benefit of oxy-firing is a reduction in NO_x formation. The high combustion temperatures resulting from oxy-firing are typically controlled by exhaust gas recirculation. In this work, we performed chemical kinetic (CHEMKIN) calculations using a mechanism validated for these conditions to study the effects of dilution by either carbon dioxide or water vapor on methane oxy-combustion, and to compare the results with methane air-combustion (N₂ as the diluent). The study was performed under adiabatic conditions at $P=30$ atm, $\phi=1$, and initial temperatures of $T=800$ -

1200K, which mimic the inlet conditions of many gas turbines and flameless combustors. The calculations show that H₂O addition at low initial temperatures and high pressure leads to considerable reduction in the ignition-delay time. This result is mainly due to changes in the radical pool and competition between the elementary reactions for the hydroxyl (OH), methyl-peroxyl (CH₃OO), and methoxy (CH₃O) radicals at low temperatures. On the other hand, carbon dioxide leads to lower adiabatic flame temperatures and flame speeds at elevated pressure. One reason for this effect of CO₂ is its higher specific heat capacity and lower thermal diffusivity, as compared to N₂ and H₂O. In addition, carbon dioxide dilution decreases the rate of the main chain branching reaction (R2: H + O₂ ↔ O + OH) due to increasing competition between this reaction and the reverse of (R29: CO + OH ↔ CO₂ + H) for H radicals, and thus results in reductions in flame propagation and flame speed.

5.2.2. Introduction

Oxy-fuel combustion is one method to produce concentrated streams of carbon dioxide for subsequent sequestration. An additional benefit of oxy-firing is a reduction in NO_x formation.¹⁻³ In this technique, oxygen (often with some diluents) is used as an oxidizer instead of air. Exhaust gas recirculation can be used to control the temperature and to reduce the pollutant emissions in oxy-fuel combustion systems, flameless combustors, internal combustion engines, gas turbines, and downhole heaters.⁴⁻¹⁰ Since providing oxygen is energy-intensive and expensive, oxy-fired systems usually operate near the stoichiometric ratio, and the temperature is controlled by the amount of diluent in the system.¹⁻³ However, adding diluents to the fuel/oxidizer mixture affects the flame

reactivity and combustion stability. Therefore, it is crucial to understand the effect of such diluents on the oxidation kinetics.

The diluent can alter the physical properties of the mixture (such as heat capacity or mass/thermal diffusivity) or participate in the elementary reactions. Previous work has been centered on the effect of nitrogen and carbon dioxide on the combustion of methane and natural gas.^{11–17} Some studies also investigate the effects of water vapor.^{18–22} However, few studies have performed reaction pathway and sensitivity analysis at low to moderate inlet temperatures and high pressure, which mimics the inlet condition of many gas turbines, flameless combustors, and downhole heaters. In this paper, we are trying to understand the influence of diluents on the fundamental properties of adiabatic oxy-fuel combustion at initial temperatures ranging from 800K to 1400K and pressure equal to 30 atm, by employing detailed chemical kinetics calculations. The primary objective is to determine the effects of diluents on methane oxidation; or in other words, how do the chemical and physical properties of diluents affect reactivity, ignition-delay, and flame speed of methane/oxygen mixtures for the conditions of interest.

First, we describe the computational models and chemical kinetic mechanisms used in these calculations. We also provide some validation for the mechanisms over a range of temperatures and pressures. Then, the effect of diluents on the adiabatic flame temperature, the ignition-delay time, and the flame speed is discussed. The kinetic effects, as well as the physical effects of the diluents on the methane/oxygen oxidation behavior, are investigated. Finally, we discuss some practical implications of the results for an oxy-fuel combustor working at high pressure and low-to-moderate initial temperatures within an environment using either carbon dioxide or water vapor as a diluent.

5.2.3. Chemical kinetic models, mechanisms, and validation

All of the adiabatic flame temperature and ignition-delay time calculations were conducted with the 0-D reactor package in CHEMKIN Pro, which is a homogeneous reactor model operating with constant pressure.²³ The flame speed analyzer was used for the flame speed calculations. The thermal diffusion of species (the Soret effect) was considered in flame calculations.

The chemical reaction mechanism employed in this study was published by Glarborg & co-workers.^{24,25} The mechanism was developed for light hydrocarbon (CH₄ and C₂H₆) oxidation at low-to-intermediate temperatures (500-1100 K) and high pressures (up to 100 atm), and considers the reactions and species involved at these conditions such as alkylperoxy species and their radical derivatives. The overall mechanism consists of 45 species and 316 reactions. It has been validated for oxy-fuel combustion with flow reactor experimental data at 600-900K, 50-100 atm, and stoichiometric ratios ranging from lean to fuel rich. It is also validated with RCM experimental data at 800-1250 K and 15-80atm. Glarborg et al. also evaluated their chemical mechanism against the shock tube data (1100-1700K, 7-456 atm) from the literature.^{24,26} Besides the validation efforts provided by Glarborg et al., we also performed validation of the mechanism for the conditions of this work.

Figure 5.1 compares the ignition-delay time predicted by three different mechanisms^{24,25,27,28} with experimental data at low inlet temperatures ($T < 1000$ K). The symbols represent experimental data obtained by V.G. McDonell et al. in a flow reactor.²⁹ The mechanism also provides good agreement with their data at higher temperatures; however, since oxidation with high inlet temperatures is not the focus of this paper, the

validation results are not shown here. Figure 5.1 illustrates that the ignition-delay predicted by the Glarborg mechanism is in good agreement with the experimental data, especially in the desired ranges of temperature ($T < 900\text{K}$).

Methane flame speed has been measured by many researchers³⁰⁻³⁷; however, most of the data are at pressures up to 20 atm and gas inlet temperatures of around 300 K, which is lower than the focus of this paper. Glarborg et al.²⁴ validated their mechanism for predicting flame speeds at 1, 5, and 10 atm and initial temperatures of around 300 K. We performed additional validation at temperatures up to 617 K, pressures up to 20 atm, and equivalence ratios from 0.8 to 1.2. Figure 5.2.a compares the flame speeds predicted by the Glarborg mechanism and those measured by G.L. Dugger³⁸ at atmospheric pressure, $\varphi = 1.22$ and initial $T = 367\text{-}617\text{ K}$.

Figure 5.2.b compares the flame speeds predicted by the Glarborg mechanism with experimental data at higher pressure ($P = 20\text{ atm}$, $T = 400\text{-}600\text{ K}$, $\varphi = 1$). The experimental data at $P = 20\text{ atm}$ are the same data used to validate GRI mech 2.1 and GRI mech 3.0.^{28,39}

In all cases, the model predictions are in a good agreement with the experimental data. Therefore, we can use the Glarborg mechanism to perform calculations in the desired range of operating condition with confidence.

5.2.4. Results and Discussion

5.2.4.1. The effect of diluents on adiabatic flame temperature

This section uses the mechanism and computational tools validated above to investigate how the properties of diluents affect the adiabatic flame temperature. The calculations are performed at constant pressure, $P = 30\text{ atm}$. The equivalence ratio is 1.0 and the oxidizer

is composed of 21 mole % oxygen and 79 mole % diluent (the nitrogen in the air is replaced by carbon dioxide or water vapor). The pressure is considered constant because that is typical of gas turbine combustors.⁴⁰ The equivalence ratio is unity because oxy-fuel combustors usually operate near stoichiometric conditions to save energy and avoid excess fuel or oxidizer.^{2,3,41}

Figure 5.3 shows a comparison of adiabatic flame temperature of different methane - oxidizer mixtures at gas inlet temperatures ranging from 800 to 2000 K. The adiabatic temperature is highest when nitrogen is the diluent and lowest when carbon dioxide is the diluent. Interestingly, the difference between T_{ad,N_2} , T_{ad,H_2O} , and T_{ad,CO_2} , is almost constant as the inlet temperature increases.

To quantify the physical and chemical effects of diluents on the adiabatic flame temperature calculation, two imaginary species, iH_2O and iCO_2 , are defined. The imaginary species have the same thermodynamic and transport properties as those of H_2O and CO_2 , but they do not participate in any reactions. This approach has been used by many researchers to distinguish the physical and chemical effects of different species.^{1,7,42-46} The physical effect can be highlighted by comparing the results obtained with N_2 dilution (air as the oxidizer) and the results of the imaginary diluents. The chemical effects of the diluents can then be identified by comparing the results of real diluents and imaginary diluents.

At low temperature, the chemical effect of diluents is almost negligible; the difference in adiabatic temperatures is mainly due to the difference between the heat capacities. Carbon dioxide has the highest C_p and shows the lowest flame temperature, while nitrogen, which has the lowest C_p , has the highest flame temperature. As the initial temperature

increases, the chemical effects of diluents become more important and cannot be neglected.

To summarize, adding CO₂ or H₂O as diluents to the system is beneficial to the control of reaction temperature. The physical effect of diluents, which is mostly due to different heat capacities, outweighs the chemical effects at temperature ranging from 800 K to 1200 K. Therefore, in most flameless combustion systems, gas turbines combustors, and downhole heaters where the gas initial temperature is usually 800-1200 K, the physical effect of diluents on the flame temperature is dominant and the chemical effect can be neglected. Adding a diluent with higher heat capacity (such as CO₂) is helpful in lowering the reaction temperature.

5.2.4.2. The effect of diluents on ignition-delay time

The ignition-delay time is one of the most important parameters in describing the oxidation characteristics of a mixture. It also influences flame stability and propagation.⁴⁷⁻⁴⁹ In gas turbines and many other combustors, the ignition-delay time is a crucial parameter to avoid auto ignition and possible damage to the system.⁴⁰ On the other hand, in flameless combustors and some downhole heaters, it is an important parameter to allow better mixing between the fuel/oxidizer and diluent⁵⁰ and a more uniform temperature profile. In either case, the ignition-delay time is a critical parameter and an understanding of the effect of diluents on ignition-delay time is crucial.

In this section, the effects of various diluents on the ignition-delay time of methane-oxygen-diluent mixtures are discussed, and the reasons behind each observation are investigated. For all calculations, the values of initial conditions were chosen to be in the ranges typical of gas turbines: 30 atm, gas inlet temperatures varying from 800 K to 1400 K, and an equivalence ratio of unity. Preliminary calculations over a wide range of

conditions (1 to 30 atm and 300 K - 2000 K) displayed the same qualitative trends as our more focused calculations.

Figure 5.4 shows the ignition-delay time of a methane/oxygen mixture diluted with different species as a function of gas inlet temperature. The mole fraction of oxygen in the oxidizer is 21% and the balance is diluent. Figure 5.4 demonstrates that the ignition-delay time decreases as the inlet gas temperature increases. The results are in agreement with the observations of Donohoe et al.⁵¹ Figure 5.4 also illustrates that at inlet temperatures above 1000 K, there is no significant difference between the delays seen with CO₂, H₂O, and N₂ as diluents. At lower temperatures, water vapor addition decreases the ignition-delay time quite significantly, while carbon dioxide causes a slight increase in ignition-delay. The same trend has been observed by other researchers.⁴¹ One reason why carbon dioxide may provide an increase in ignition-delay could be its relatively high heat capacity. As the heat capacity increases, the reaction temperature drops and thus the ignition-delay time increases. There are also some kinetic considerations that may affect the ignition-delay. Sensitivity and reaction pathway analyses were performed to understand why water vapor leads to the lowest ignition-delay time, as compared to the two other diluents.

In general, a temperature sensitivity analysis is an indicator to determine how much a particular elementary reaction contributes to temperature change when a mixture ignites. Therefore, it is possible to determine the reactions that contribute most to the ignition. Such an analysis is usually performed by perturbing the pre-exponential factor of each individual reaction rate (basically perturbing the rate constant) with a small constant and monitoring the effect of these perturbations on temperature.⁵² Figure 5.5 shows the temperature sensitivity of the elementary reactions (listed in Table 5.1) during the ignition of a methane

- oxygen mixture in the presence of different diluents at initial $T=800$ K, 30 atm, and $\phi = 1$. The oxidizer consists of 21 mole % O_2 and 79 mole % diluent. The reaction that shows higher temperature sensitivity plays a more important role in the ignition behavior. The positive sensitivity coefficient means increasing the rate of the reaction leads to higher temperature (more heat production), while the negative coefficient means increasing the rate of the reaction leads to a lower temperature (less heat production).

Based on the sensitivity and the reaction pathway analysis, we can identify three main reasons why the water vapor addition promotes methane oxidation and reduces the ignition-delay time at low temperature.

First, at low temperature, R120 is dominant, and methane is mostly consumed by methyl-peroxyl radical (CH_3OO) to produce methyl radical (CH_3). Reactions R123 and R118 are important elementary reactions that consume methyl-peroxyl radical (CH_3OO) and thus compete with R120. Figure 5.6 shows the rate of consumption of CH_3OO by R118 and R123. Note that the negative rates mean that the CH_3OO radicals are consumed by the forward reactions of R118 and R123. The comparison in Figure 5.6 is between N_2 and water vapor as diluents. Figure 5.6 illustrates that the rate of consumption of CH_3OO is higher (R123) in the absence of water vapor. Therefore, at low T , in the absence of water vapor, there is more competition between R120 and R123 for CH_3OO radical, which yields a slower consumption of methane. Thus, the ignition-delay time decreases when water vapor is the diluent. Second, the other critical elementary reaction at low temperature is R102 whereby methane consumes methoxy radicals (CH_3O) to produce methyl radicals (CH_3).

R92 also competes with R102 for methoxy radical (CH_3O). Figure 5.7 shows that in

the absence of water vapor, the rate of consumption of methoxy radical (CH_3O) by R92 is higher. Hence, there is more competition between R102 and R92 when nitrogen is the diluent, leading to slower consumption of methane and an increase in ignition-delay time.

Third, in the presence of water vapor, the rate of production of OH radicals by reaction R25 significantly increases from 6.72×10^{-4} to 1.36×10^{-1} mole/cm³-sec. There are two reasons for this increase: first and most important, the third-body efficiency of water is much higher than for other species in R25 (efficiencies shown in Table 5.1); second, as shown in Figure 5.8, the rate of production of H_2O_2 (R23) slightly increases when water vapor is the diluent. The increased concentration of OH radicals in the presence of water vapor favors methane oxidation by R47 and lowers the ignition-delay time. Because of these three reasons, having water vapor in methane combustion processes operating at high pressure and low temperature helps the oxidation and decreases the ignition-delay time.

Finally, the effect of the pressure and diluent mole fraction was investigated. Figure 5.9 shows the ignition-delay time of a constant methane-oxygen mixture with increasing levels of dilution by N_2 , CO_2 or H_2O . The ignition-delay time was calculated at 800 K, $\phi=1$, and $P=10$ atm and 30 atm. As shown in the figure, the ignition-delay time increases as the diluent mole fraction increases, regardless of the diluent, and decreases as the pressure increases. As discussed before, adding water vapor as a diluent promotes methane oxidation and reduces the ignition-delay time. This effect is more significant at lower pressure and higher diluent mole fraction.

Please note that Figure 5.9 presents the effect of N_2 and CO_2 in the absence of H_2O . However, in actual combustion situations, water vapor exists as either a byproduct of combustion or humidity in the fuel/oxidizer streams. Thus, it is certainly of great interest

to investigate the ignition behavior of methane in the presence of varying levels of humidity. Figure 5.10, shows the ignition-delay time of a constant methane- oxygen-diluent mixture with increasing H₂O mole fraction. The ignition-delay time of methane was calculated at an inlet temperature of 800 K, P=30 atm, and $\phi=1$, while the total concentration of diluent was fixed (oxidizer consisted of 21 mole % O₂ and 79 mole % diluent). The diluent is a mixture of "CO₂+H₂O" or "N₂+H₂O" and the level of H₂O mole fractions in N₂ and CO₂ changes. As explained before, CO₂ addition to methane-oxygen mixtures increases the ignition-delay time more than N₂ addition. Thus, as shown in Figure 5.10, the ignition-delay of "CO₂+H₂O" case is higher than "N₂+H₂O" case. It also shows that H₂O addition to the CO₂ or N₂ diluents (even with low H₂O mole fraction) reduces the ignition-delay time in these adiabatic calculations. The ignition-delay drops as the H₂O mole fraction increases. The slope of the graphs is sharper at lower H₂O mole fraction (less than 10 %), which demonstrates that the presence of even small percentages of humidity affects the ignition behavior of methane, and reduces the ignition-delay time.

The trends for "N₂+H₂O" and "CO₂+H₂O" cases are the same, especially at low H₂O mole fractions; however, as the H₂O mole fraction increases, the effect of H₂O becomes more significant for the "CO₂+H₂O" case.

5.2.4.3. The effect of diluents on flame speed

When a diluent is added to a mixture, the concentration of fuel and oxidizer drops, which leads to a lower net reaction rate and lower flame speed. In addition, each diluent changes the thermal and mass diffusivities and heat capacity of the mixture, which also affect the flame speed. Finally, some noninert diluents participate in chemical reaction

pathways and affect the flame speed.⁴³

The objective of this section is to better understand the effect of the diluents, N_2 , CO_2 , and H_2O , on the flame speed of methane-oxygen mixtures at high pressure and low to intermediate inlet temperatures. Figure 5.11 illustrates the effect of different diluents on the flame speed for a methane-oxygen mixture at $P=30$ atm, inlet $T=800$ K, and $\phi = 1$. The flame speed decreases as the diluent mole fraction increases; however, carbon dioxide reduces the flame speed more significantly than the other diluents. Similar results have been reported by other researchers¹⁴⁻¹⁷ for methane-air mixtures.

Unlike carbon dioxide, both nitrogen and water vapor addition decrease the flame speed almost linearly. This observation is consistent with experiments performed at atmospheric pressure and inlet temperatures of 300-400 K.^{7,14,46}

The sensitivity of flame speed to carbon dioxide may be due to its higher specific heat capacity and lower thermal diffusivity relative to N_2 and H_2O .⁴¹ Kinetic effects may also be significant. Ghoniem et al.¹ investigated the effects of CO_2 , H_2O , and N_2 dilution on flame speed of methane-oxygen mixtures. They showed that nitrogen dilution has no kinetic effect on the flame speed of methane-air mixture. Thus, we focus here on quantifying the physical and kinetic effects (including the third-body efficiency and the chemical effects) of CO_2 and H_2O dilution.

The relative contribution of the third-body efficiency, the physical and the chemical properties can be determined by defining four imaginary species as follows:

iCO₂: Species has the same thermodynamic and transport properties and third-body efficiency as CO_2 , but does not participate chemically in any reaction.

iCO_{2_n}: Species has the same thermodynamic and transport properties as CO_2 but does not

participate in any reaction, either as a reactant or as a third-body species.

iH₂O: has the same thermodynamic, transport properties and third-body efficiency as H₂O, but does not participate chemically in any reaction.

iH₂O_n: has the same thermodynamic and transport properties of H₂O, but does not participate in any reaction, either as a reactant or as a third-body species.

N₂ is taken as a reference case. At a given diluent mole fraction, the relative decrease due to the physical, chemical and third-body efficiency effects are determined by calculating the following ratios:^{7,14}

$$\text{Physical effect}_{(\text{CO}_2 \text{ or } \text{H}_2\text{O})} = \frac{\text{flame speed}_{(\text{N}_2)} - \text{flame speed}_{(\text{iCO}_{2,\text{n}} \text{ or } \text{iH}_2\text{O}_{,\text{n}})}}{\text{flame speed}_{(\text{N}_2)} - \text{flame speed}_{(\text{CO}_2 \text{ or } \text{H}_2\text{O})}}$$

$$\text{Chemical effect}_{(\text{CO}_2 \text{ or } \text{H}_2\text{O})} = \frac{\text{flame speed}_{(\text{iCO}_2 \text{ or } \text{iH}_2\text{O})} - \text{flame speed}_{(\text{CO}_2 \text{ or } \text{H}_2\text{O})}}{\text{flame speed}_{(\text{N}_2)} - \text{flame speed}_{(\text{CO}_2 \text{ or } \text{H}_2\text{O})}}$$

Third – body efficiency effect_(CO₂ or H₂O)

$$= \frac{\text{flame speed}_{(\text{iCO}_{2,\text{n}} \text{ or } \text{iH}_2\text{O}_{,\text{n}})} - \text{flame speed}_{(\text{iCO}_2 \text{ or } \text{iH}_2\text{O})}}{\text{flame speed}_{(\text{N}_2)} - \text{flame speed}_{(\text{CO}_2 \text{ or } \text{H}_2\text{O})}}$$

Figure 5.12 quantifies the effects of third-body efficiency and physical and chemical characteristics of H₂O and CO₂ dilution on the flame speed for a fixed methane/oxygen mixture at P=30 atm, T=800K, and φ=1. It demonstrates that as the diluent mole fraction increases, the chemical effect becomes less important, and diluent transport properties or physical effects become dominant. Many researchers^{1,43,44} observe that the primary effect of carbon dioxide is not on the kinetic or diffusive transport properties, but on the thermal properties of the mixture. As shown in the previous section, adding carbon dioxide increases the specific heat of the mixture and drops the flame temperature, and thus the flame speed.

We also investigated the chemical effect of diluents in more detail and determined the reactions that play a significant role in controlling the flame speed at the desired operating condition. Since at a diluent mole fraction equal to 0.3 ($X_{\text{diluent}}=0.3$), the percentage of the kinetic and the physical effects of diluents on the flame speed are roughly similar in magnitude, further sensitivity analysis is performed at $X_{\text{diluent}}=0.3$.

A sensitivity analysis was performed to identify the important elementary reactions affecting flame speed. The built-in function of CHEMKIN Pro²³ was used to calculate the mass flow rate sensitivity, which is indicative of the sensitivity of flame speed to reaction rate constants. This approach has also been used by other researchers to identify the reactions controlling flame speed.^{25,30,53} Figure 5.13 shows the results of the analysis for a stoichiometric methane/oxygen/diluent mixture at $P=30$ atm and inlet $T=800$ K. The mole fraction of the diluents was 0.3. Figure 5.13 illustrates that reaction R2, the main chain-branching reaction, is the most critical reaction in the prediction of flame speed and controls the prediction of the methane flame speed to a great extent.

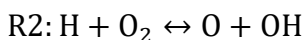
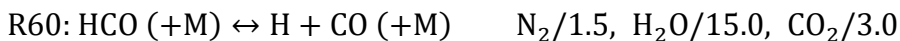


Figure 5.14 compares the net rate of production of OH radicals by R2 in the presence of different diluents. The reaction rate of R2 is highest in the presence of nitrogen and lowest in the presence of carbon dioxide. This observation indicates that adding H_2O and CO_2 as diluents, as opposed to N_2 , inhibits the reaction R2 and decreases the flame speed. There are other reactions that affect the flame speed, but to a lesser extent. For example, the terminating reaction (R68), which competes for H radicals with the main chain branching reaction (R2), exhibits negative sensitivities and slows down the flame speed.



The third-body efficiency of water vapor is equal to 10.0, while the carbon dioxide and nitrogen values are 4.0 and 1.4, respectively. Therefore, there is stronger inhibition due to the higher third-body efficiency of H₂O in R68. However, the inhibiting effect of H₂O is partially offset by the hydrogen production of R60, where again the third-body efficiency of H₂O is higher than that of CO₂ and N₂.



Glarborg et al.²⁴ argue that R60, a decomposition reaction for HCO, increases the flame speed; however, the reactions of HCO with H, OH, and O₂ terminate the radical chains and slow down flame propagation. They also indicate that the oxidation of CO by OH (R29) is among the reactions controlling the flame speed. This finding is in agreement with other studies^{7,17,41,43,54,26,55-58} that indicate that CO₂ actively participates in the reverse of R29, which competes with R2 for H radicals and reduces the flame speed.



5.2.5. Summary

The effects of the diluents N₂, CO₂, and H₂O on the oxidation behavior of methane-oxygen mixtures at low to moderate reactor inlet temperatures (T=800-1400 K) and high pressure (P=30 atm) were studied. The physical and the kinetic effects of the diluents were quantified and the following conclusions were reached. At low gas inlet temperature, the flame temperature is mainly controlled by the thermal properties of the diluents, and the chemical effect of the diluents is almost negligible. The diluents decrease the flame temperature in the order of their molar isobaric heat capacities ($C_{P(\text{CO}_2)} > C_{P(\text{H}_2\text{O})} > C_{P(\text{N}_2)}$) with CO₂ causing the largest decrease and N₂ the smallest. The physical properties

of the diluents also alter the ignition-delay time and the flame speed of the mixture. As the heat capacity of the mixture increases, the reaction temperature and the flame speed drop and the ignition-delay time increases.

Adding diluents to a mixture also affects the radical pool and changes the elementary reaction rates and pathways. Water vapor addition at low initial temperature (800-900 K) promotes methane oxidation and decreases the ignition-delay time. In the absence of water vapor, there is more competition between reactions R120, R123, and R118 for methylperoxy radical (CH_3OO) and between R102 and R92 for methoxy radical (CH_3O). These competitions lead to a slower consumption of methane and a higher ignition-delay time in the absence of water vapor.

Finally, a flow sensitivity analysis was performed to determine the elementary reactions which control the flame speed. The main chain-branching reaction (R2) is the most critical reaction in controlling the flame speed. In the presence of carbon dioxide, there is more competition between reverse R29 and R2 for H radical, which leads to lower flame speed.

Based on these observations, some recommendations can be made for the practical implication of CO_2 or H_2O dilution in an oxy-fuel combustor operating at high pressure ($P=30$ atm), and low inlet temperature ($T=800$ K). Carbon dioxide delays the ignition, slows the combustion reactions, and lowers the temperature rise, compared to the two other diluents (N_2 and H_2O). Therefore, CO_2 dilution seems promising in a MILD (moderate or intense low oxygen dilution) combustion system where having a delayed oxidation and lower reaction temperature is desired. In addition, CO_2 dilution increases the ignition-delay time, drops the flame temperature, and thus reduces the risk of explosion in gas turbines

where there is a concern regarding the autoignition of a gas mixture in the premixed duct. However, carbon dioxide leads to the lowest flame speed, as compared to the two other diluents, which may have implications for flame stabilization. Since H₂O leads to better flame stability as compared to CO₂, and reduces the ignition-delay time, it may be a good option for a downhole heater where faster oxidation initiation and a more stable flame is required. These general recommendations are based on validated kinetic model predictions; however, more detailed simulations and experimental validation of a particular device or application would be required for implementation.

5.3. Section II: Determination of ignition bounds when including heat transfer considerations

5.3.1. Introduction

In Section I, the walls of the chamber were assumed adiabatic. However, in a downhole heater, there is a heat transfer from the chamber to the surroundings. An overall heat transfer coefficient of 3.5 W/m²K was calculated in Chapter 3, Section II, and the average gas temperature in the outer annulus surrounding the chamber was determined to be 939K.

The primary objective of this section is to find the temperature and compositional ranges that permit ignition of methane-oxygen mixtures in the heater when there are heat losses to the surroundings.

5.3.2. Modeling

The nonadiabatic CHEMKIN calculations are performed for a 1-meter-long chamber with hydraulic diameter of 3.3 inches. Two separate models, a plug flow reactor model

(PFR) and a perfectly stirred reactor model (PSR), are considered. In the downhole heater, a reaction chamber is neither a PFR nor a PSR reactor. However, these two models are considered as two limiting cases.

The volume of the reactor in both models is 5518 cm^3 . The Glarborg mechanism is used for methane oxidation. Please refer to Section I for more detailed information on the mechanism.

The effects of the initial gas temperature and diluent mole fraction on the average reactor temperature were evaluated. In Section I, the effects of H_2O and CO_2 on methane oxidation were studied separately. However, in reality, part of the flue gas (mixture of CO_2 and H_2O) may be recirculated to the chamber to control the oxidation. Therefore, in this section, the diluent is a mixture of 67 mole % CO_2 and 33 mole % H_2O , which is a representative flue gas composition.

A stoichiometric methane- oxygen mixture at 10 atm was injected to the reactors, and the effect of the inlet gas temperature and the dilution by flue gas on the reactor temperature was investigated. We seek the optimum conditions in which the average reactor temperature reaches the required temperature, 939 K. In all cases, the inlet CH_4 and O_2 molar flowrate was constant. Flue gas, mixtures of CO_2 and H_2O , was added to the system (mole fraction varied from 0-90% flue gas) as a diluent, and the inlet mass flowrate was defined correspondingly. In the PSR model, two of the three parameters (residence time, inlet flow rate and the reactor volume) must be defined. We therefore fixed the inlet mass flow rate and the PSR reactor volume, which are equal to the inlet flow rate and the reactor volume in the PFR model. The heat transfer surface area for both models was 2633 cm^2 . The gas residence times in the PFR model and the PSR model are different because, as

shown below, their gas temperatures are different.

5.3.3. Results and discussion

Figure 5.15 shows the reactor temperature as a function of diluent (flue gas) mole fraction, and the inlet gas temperature and reactor type are compared. The curves are generated based on data points obtained from separate calculations at a certain initial temperature and flue gas mole fraction. The dashed lines are the PSR temperatures, while the solid lines are the average temperatures along the 1-meter PFR.

In most cases, especially when the inlet temperature is less than 700K, the reactor temperatures predicted by the fully-mixed PSR are higher than those for the PFR. Consequently, as shown in Figure 5.16, the gas residence time in the PSR is generally less than that for the PFR. As a result, the gas in the PSR has less time to transfer heat than in the PFR, which can also lead to higher temperatures in the PSR. Note that in both models, a consistent external heat transfer coefficient, $U = 3.12 \text{ W/m}^2\cdot\text{K}$, is used since both reactors would be exposed to the same external environment. The heat transfer coefficient is approximately equal to the heat transfer coefficient calculated in Chapter 3, Section II. Figure 5.16 also shows that the PFR is more sensitive to variations in the gas inlet temperature than the PSR model. For both models, as the inlet temperature increases, the reactor temperature increases, and the residence time drops. The heat transfer calculations in Chapter 3 show that the average combustion gas temperature inside the chamber should be around 939 K to provide the desired amount of heat to the surrounding oil. At any inlet temperature, the PSR model shows that the diluent (flue gas) mole fraction in the gas mixture should be at least 0.85 in order for the reactor temperature to reach 939 K, with

higher inlet temperatures requiring greater flue gas dilution. However, depending on the gas inlet temperature, we can have a diluent mole fraction as low as 0.4 and still reach an average reactor temperature of 939 K in a PFR. For example, when the gas inlet temperature is 500K, the PFR model shows that 55% dilution is required to reach an average temperature of 939 K inside the chamber. In reality, the downhole heater is neither a PFR nor a PSR reactor. The actual operation will be between these two limiting cases. Since the length to diameter ratio of the reactor is 12 ($L/D > 10$), the PFR model would generally be considered a more reasonable approximation; thus, we would anticipate that actual downhole heater operation will tend more towards the PFR model predictions than the PSR predictions.

5.4. References

- (1) Bongartz, D.; Ghoniem, A. F. *Combust. Flame*, **2015**, *162* (7), 2749–2757.
- (2) M.B.Toftegaard; J.Brix; P.A.Jensen; P.Glarborg, A. D. J. *Prog. Energy Combust. Sci.* **2010**, *36*, 581–625.
- (3) H.M.Kvamsdal; K.Jordal, O. B. *Energy*, **2007**, *32*, 10–24.
- (4) A.K. Burnham; H. Wallman; J. Mcconaghy; R. Day. Heater and Method for Recovering Hydrocarbons from Underground Deposits. WO 2010/053876 A2, **2010**.
- (5) Cavaliere, A.; Joannon, M. De. *Mild Combustion*, **2004**, *30*(4), 329-366.
- (6) Cong, L.; Dagaut, P. *Energy & Fuels*, **2009**, *23* (2), 725–734.
- (7) Galmiche, B.; Halter, F.; Foucher, F.; Dagaut, P. *Energy & Fuels*, **2011**, *25* (3), 948–954.
- (8) De Jager, B.; Kok, J. B. W.; Skevis, G. *Proc. Combust. Inst.* **2007**, *31 II* (x), 3123–3130.
- (9) Jonsson, M.; Yan, J. *Energy*, **2005**, *30*, 1013–1078.
- (10) Skevis, G.; Chrissanthopoulos, A.; Goussis, D. A.; Mastorakos, E. .; Derksen, M. A.

- F.; Kok, J. B. W. *Appl. Therm. Eng.* **2004**, *24*, 1607–1618.
- (11) Dagaut, P.; Nicolle, A. *Combust. Flame*, **2005**, *140*, 161–171.
- (12) Dagaut, P.; Mathieu, O.; Nicolle, A.; Dayma, G. *Combust. Sci. Technol.* **2005**, *177*, 1767–1791.
- (13) Nicolle, A.; Dagaut, P. *Fuel*, **2006**, *85*, 2469–2478.
- (14) Halter, F.; Foucher, F.; Landry, L.; Mounaïm-Rousselle, C. *Combust. Sci. Technol.* **2009**, *181*, 813–827.
- (15) Tanoue, K. In *SAE Paper No. 2003-01-1774*; **2003**.
- (16) Zhu, D. L.; Egolfopoulos, F. N.; Law, C. K. In *Proc. Combust. Inst.* **1988**, 1537–1545.
- (17) Khan, A. R.; Anbusaravanan, S.; Kalathi, L.; Velamati, R.; Prathap, C. *Fuel*, **2017**, *196*, 225–232.
- (18) Mazas, A. N.; Fiorina, B.; Lacoste, D. A.; Schuller, T. *Combust. Flame*, **2011**, *158* (12), 2428–2440.
- (19) Le Cong, T.; Dagaut, P. *Energy & Fuels*, **2009**, *23* (2), 725–734.
- (20) Seiser, R.; Seshadri, K. *Proc. Combust. Inst.* **2005**, *30* (Pt.1), 407–414.
- (21) Richards, G. A.; Casleton, K. H.; Chorpening, B. T. *Proc. Inst. Mech. Eng. Part A J. Power Energy*, **2005**, *219* (A2), 121–126.
- (22) C. J. Goy, A. J. M. and G. O. T. *ASME*, **2001**, *2*, 1–7.
- (23) Reaction Design. In *CHEMKIN-PRO 15131*; San Diego, **2013**.
- (24) Hashemi, H.; Christensen, J. M.; Gersen, S.; Levinsky, H.; Klippenstein, S. J.; Glarborg, P. *Combust. Flame*, **2016**, *172*, 349–364.
- (25) C. Rasmussen, J. G. Jakobsen, P. G. *Int. J. Chem. Kinet.* **2008**, *40* (12), 778–807.
- (26) Glarborg, P.; Bentzen, L. L. B. *Energy & Fuels*, **2008**, *22* (20), 291–296.
- (27) The San Diego Mechanism, [http:// web. eng. ucsd. edu / mae/ groups/ combustion/ mechanism. html](http://web.eng.ucsd.edu/mae/groups/combustion/mechanism.html).
- (28) Smith, G. P.; Golden, D. M.; Frenklach, M.; Moriarty, N. W.; Eiteneer, B.; Goldenberg, M.; Bowman, C. T.; Hanson, R. K.; Song, S.; William C. Gardiner, J.; Lissianski, V. V.; Qin, Z. GRI-Mech 3.0 http://www.me.berkeley.edu/gri_mech/.
- (29) Beerer, D. J.; Mcdonell, V. G. *Proc. Combust. Inst.* **2011**, *33* (1), 301–307.

- (30) Hashemi, H.; Christensen, J. M.; Gersen, S.; Levinsky, H.; Klippenstein, S. J.; Glarborg, P. *Combust. Flame*, **2016**, *172*, 349–364.
- (31) X.J. Gu; M.Z. Haq; M. Lawes, R. W. *Combust. Flame*, **2000**, *121*, 41–58.
- (32) P. Dirrenberger, H. Le Gall; R. Bounaceur; O. Herbinet; P.A. Glaude; A. Konnov, F. B.L. *Energy Fuels*, **2011**, *25* (9), 3875–3884.
- (33) G. Rozenchan; D.L. Zhu; C.K. Law; S.D. Tse, O. propagation. *Proc. Combust. Inst.* **2002**, *29* (2), 1461–1470.
- (34) E. Varea; V. Modica; A. Vandel, B. R. *Combust. Flame*, **2012**, *159* (2), 577–590.
- (35) M. Goswami; S.C.R. Derks; K. Coumans; W.J. Slikker; M.H. de Andrade Oliveira; R.J.M. Bastiaans; C.C.M. Luijten; L.P.H. de Goey, A. K. *Combust. Flame*, **2013**, *160* (9), 1627–1635.
- (36) T. Tahtouh; F. Halter, C. M.R. *Combust. Flame*, **2009**, *156* (9), 1735–1743.
- (37) W. Lowry; J. de Vries; M. Krejci; E. Petersen; Z. Serinyel; W. Metcalfe; H. Curran, G. B. *J. Eng. Gas Turbines Power*, **2011**, *133* (9), 91501.
- (38) Dugger, G. L. **1958**, <https://digital.library.unt.edu/ark:/67531/metadc59848/>.
- (39) *Just, Th. (1994) Private communication.*; **1994**, http://www.me.berkeley.edu/gri_mech/.
- (40) M. Boyce. *Gas Turbine Engineering Handbook*, 4th ed.; Butterworth-Heinemann, Waltham, **2002**.
- (41) Bongartz, D.; Ghoniem, A. F. *Combust. Flame*, **2015**, *162* (7), 2749–2757.
- (42) Zhang, J.; Mi, J.; Li, P.; Wang, F.; Dally, B. B. *Energy and Fuels*, **2015**, *29* (7), 4576–4585.
- (43) Chan, Y. L.; Zhu, M. M.; Zhang, Z. Z.; Liu, P. F.; Zhang, D. K. *Energy Procedia*. **2015**, *75*, 3048–3053.
- (44) Di Benedetto, A.; Di Sarli, V.; Salzano, E.; Cammarota, F.; Russo, G. *Int. J. Hydrogen Energy*, **2009**, *34* (16), 6970–6978.
- (45) Li, S. C.; Williams, F. A. *J. Eng. Gas Turbines Power*, **2002**, *124* (3), 471.
- (46) Mazas, A. N.; Fiorina, B.; Lacoste, D. A.; Schuller, T. *Combust. Flame*, **2011**, *158* (12), 2428–2440.
- (47) Yin, C.; Yan, J. *Appl. Energy*, **2016**, *162*, 742–762.
- (48) Suda, T.; Masuko, K.; Sato, J.; Yamamoto, A.; Okazaki, K. *Fuel*, **2007**, *86* (12–13), 2008–2015.

- (49) Normann, F.; Andersson, K.; Leckner, B.; Johnsson, F. *Prog. Energy Combust. Sci.* **2009**, *35* (5), 385–397.
- (50) Oijen, J. A. Van. *Proc. Combust. Inst.* **2013**, *34* (1), 1163–1171.
- (51) Donohoe, N.; Heufer, K. A.; Aul, C. J.; Petersen, E. L.; Bourque, G.; Gordon, R.; Curran, H. J. *Combust. Flame*, **2015**, *162* (4), 1126–1135.
- (52) Zhao, Z.; Juan, L. I.; Kazakov, A.; Dryer, F. L. *Int. J. Chem. Kinet.* **2005**, *37* (5), 282–295.
- (53) Kochar, Y.; Bloomer, D.; Clay, M.; Lieuwen, T.; Seitzman, J. *U.S. Natl. Combust. Meet.* **2011**, No. 7.
- (54) Liu, F.; Guo, H.; Smallwood, G. J. *Combust. Flame*, **2003**, *133*, 495–497.
- (55) Liu, F.; Guo, H.; Smallwood, G. J.; Gulder, O. L. *Combust. Flame*, **2001**, *125*, 778–787.
- (56) Masri, A. R.; Dibble, R. W.; Barlow, R. S. *Combust. Flame*, **1992**, *91*, 285–309.
- (57) Zhang, C.; Atreya, A.; Lee, K. *Symp. Combust. Proceedings*, **1992**, *24th*, 1049–1057.
- (58) Zhang, C.; Atreya, A.; Lee, K. In *Proc. Combust. Inst.* **1992**; 1049.

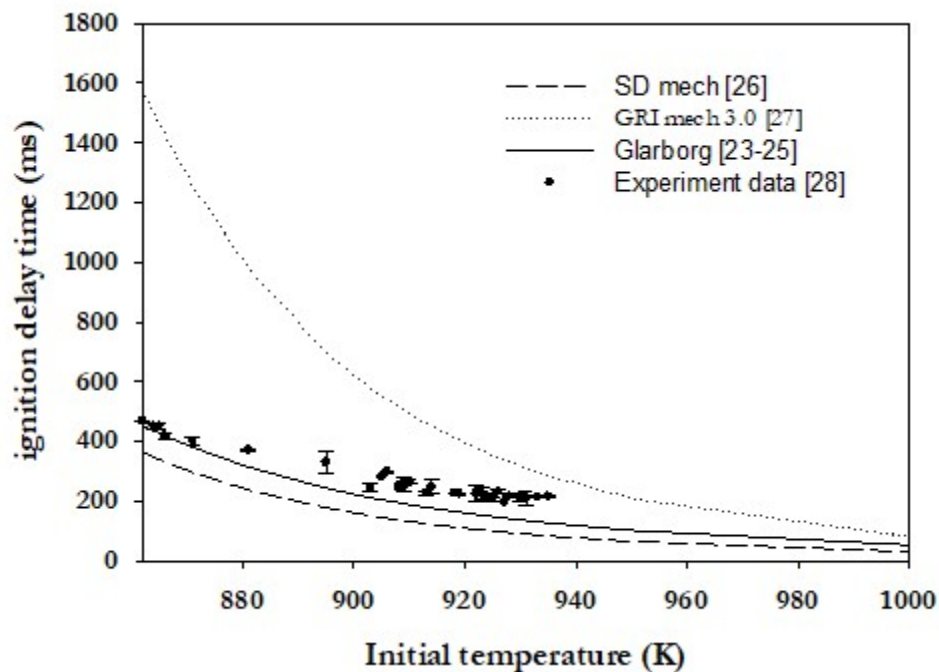


Figure 5.1: Ignition-delay time of methane-air mixtures at $P=9$ atm and $\phi=0.6$, comparison between the experimental data and predictions using different chemical mechanisms. Symbols are experimental data from V.G. McDonnell et al²⁹.

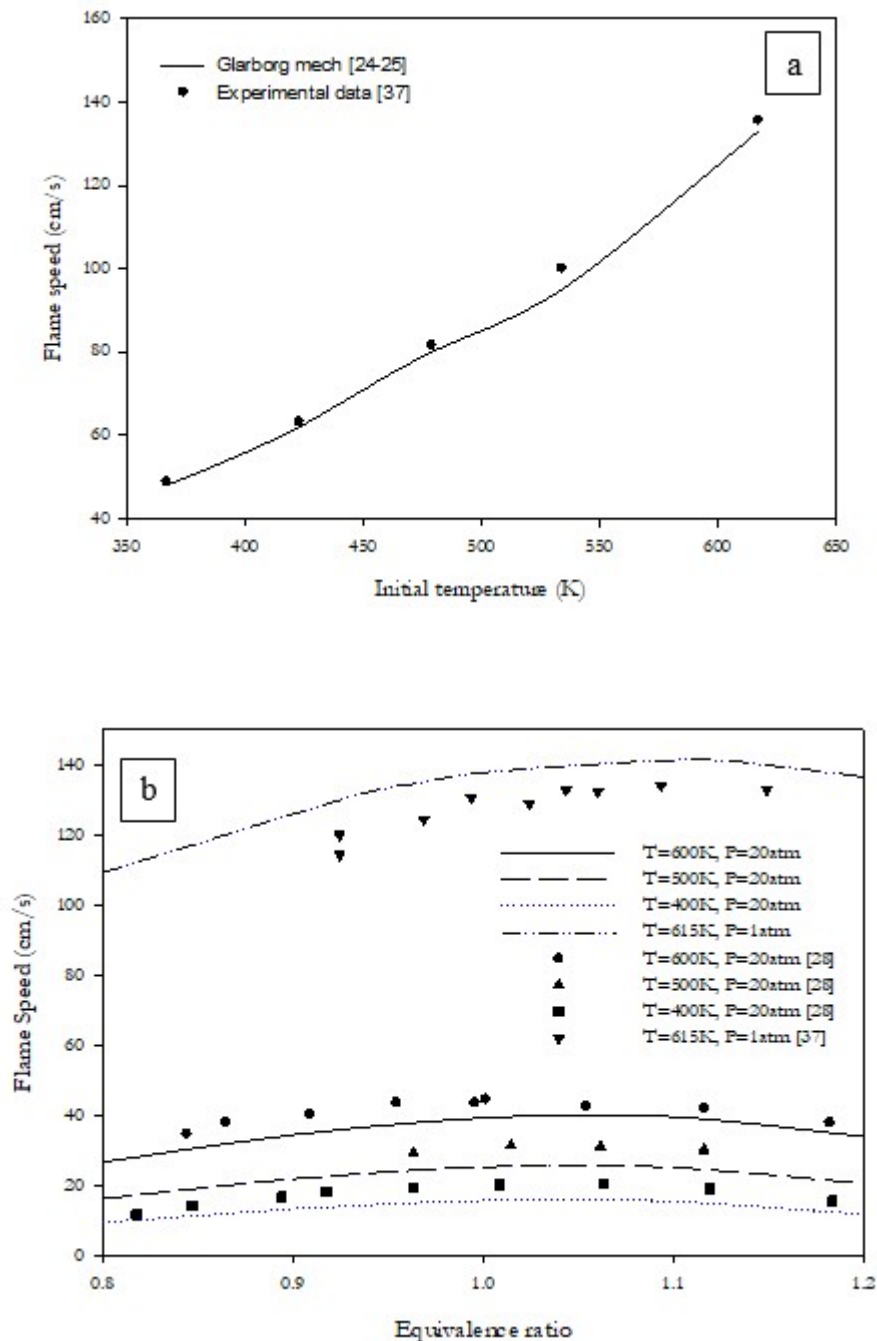


Figure 5.2: Flame speed validation, a) Comparison between experimental data³⁸ and the Glarborg mechanism²⁴, for a methane - air mixture, $P=1 \text{ atm}$, $\phi=1.22$. b) Comparison between experimental data^{28,38} and the Glarborg mechanism²⁴, for a stoichiometric methane - air mixture. Symbols are the experimental data

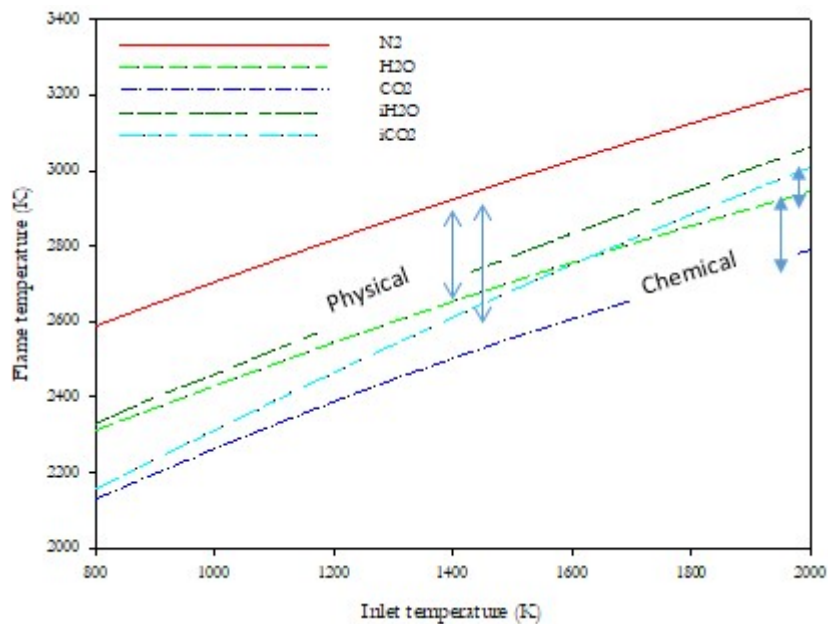


Figure 5.3: Adiabatic temperature vs. gas initial temperature, quantifying the physical and chemical effects of the diluents

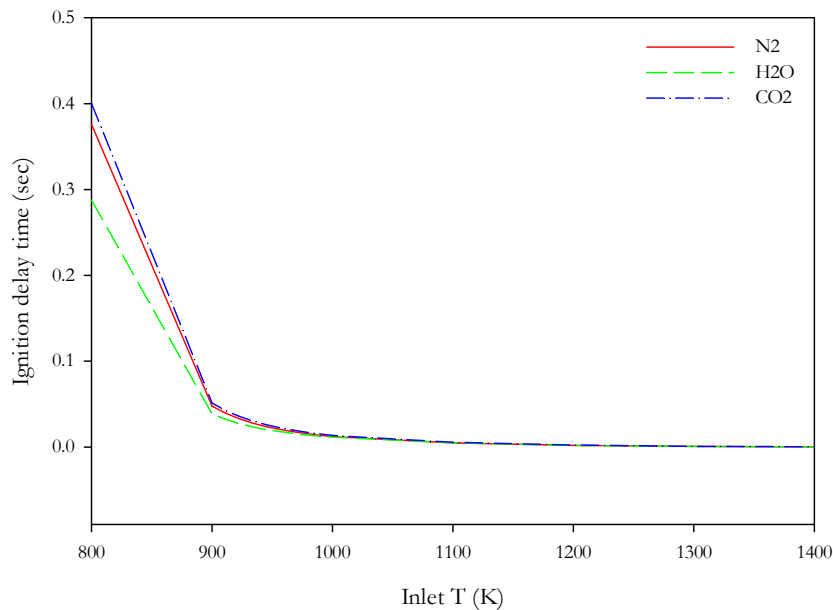


Figure 5.4: Comparison of ignition-delay time of a methane/oxygen mixture diluted with different diluents (21% O₂+79% diluent), P=30 atm, $\phi=1$

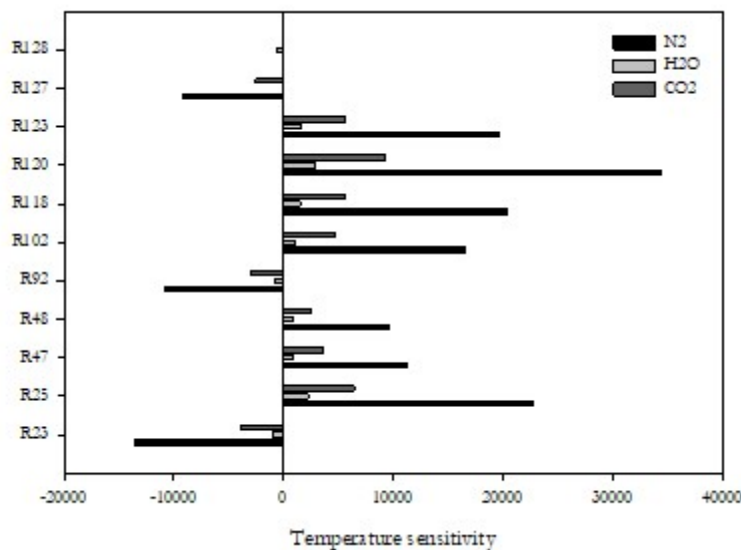


Figure 5.5: Temperature sensitivity to the pre-exponential factors of elementary reaction rates during the ignition of methane/oxygen mixture diluted with several species. Initial $T=800$ K, $P=30$ atm, $\phi=1$

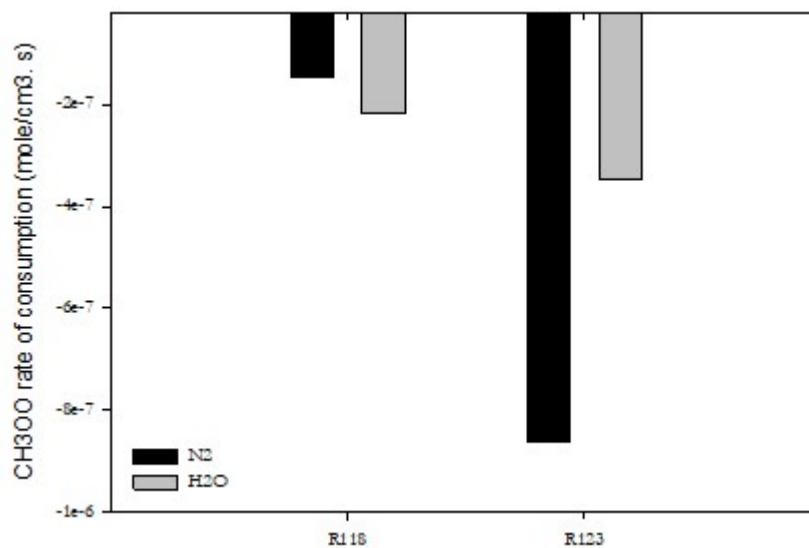


Figure 5.6: Comparison of the rate of consumption of CH_3OO radical in the presence and absence of water vapor by R118 and 123 (initial $T=800$ K, $P=30$ atm, $\phi=1$, diluent mole fraction=0.79)

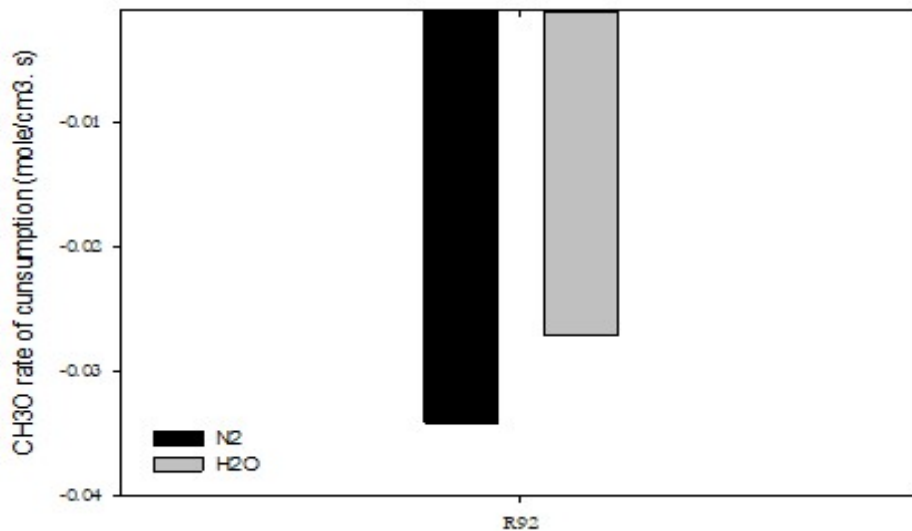


Figure 5.7: Comparison of the rate of production of CH₃O radical in the presence and absence of water vapor by R92. (initial T=800 K, P=30 atm, $\phi=1$, diluent mole fraction=0.79)

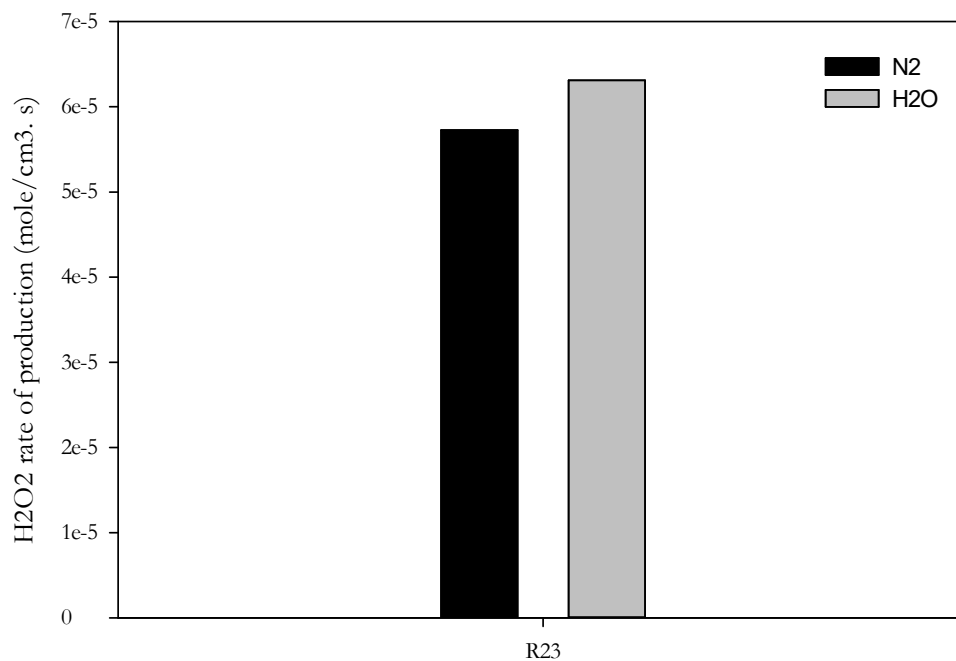


Figure 5.8: Comparison of the rate of production of H₂O₂ radical in the presence and absence of water vapor by R23 (initial T=800 K, P=30 atm, $\phi=1$, diluent mole fraction=0.79)

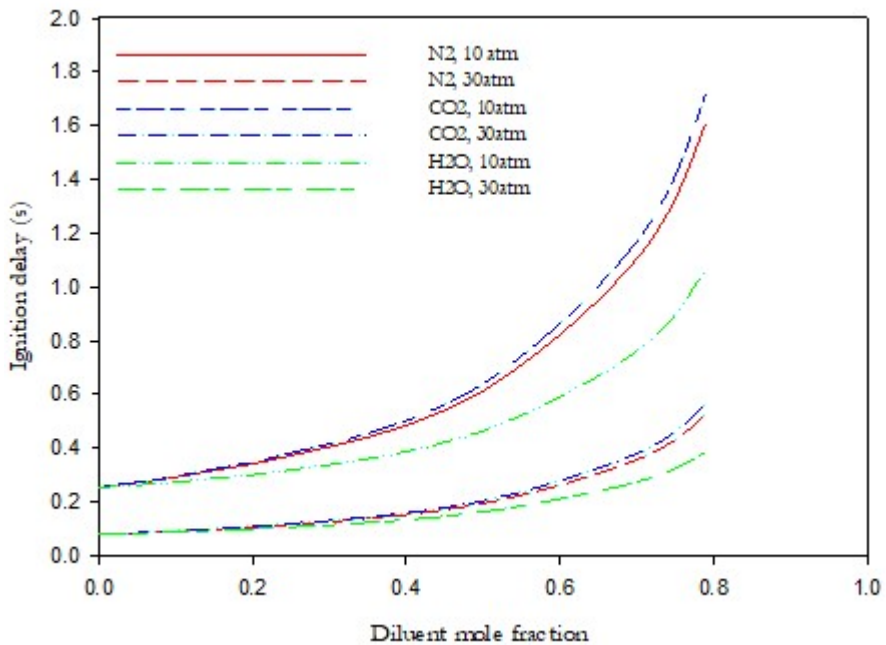


Figure 5.9: Effect of pressure and diluent mole fraction on the ignition-delay time of $\text{CH}_4/\text{O}_2/\text{diluent}$ mixture, inlet $T=800\text{ K}$, $\varphi=1$

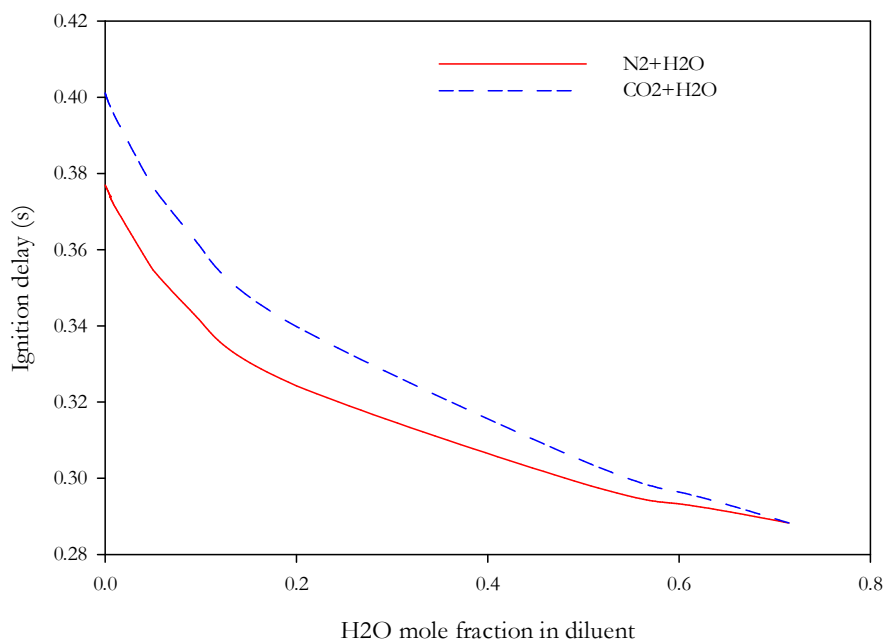


Figure 5.10: Effect of water vapor on the ignition-delay time of $\text{CH}_4/\text{oxidizer}$ mixtures, (oxidizer consists of 21 mole % O_2 and 79 mole % diluent), inlet $T=800\text{ K}$, $\varphi=1$

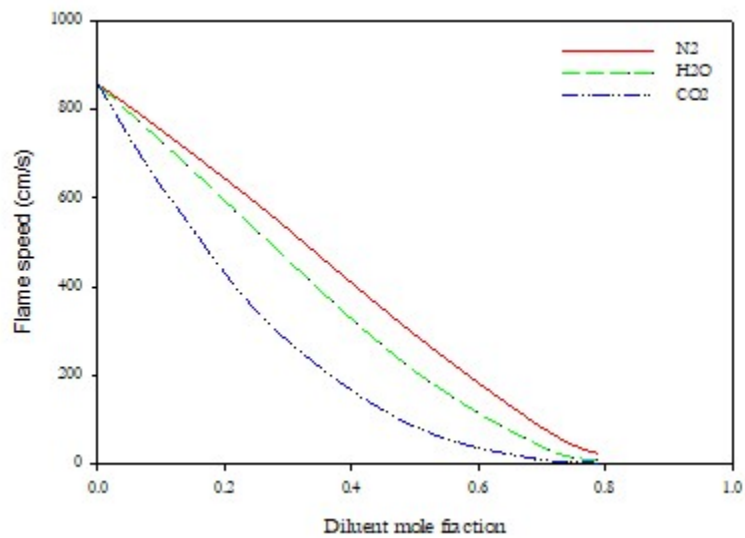


Figure 5.11: Comparison of the effect of different diluents on flame speed for a methane/oxygen mixture, $P=30$ atm, inlet $T=800$ K, $\varphi = 1$

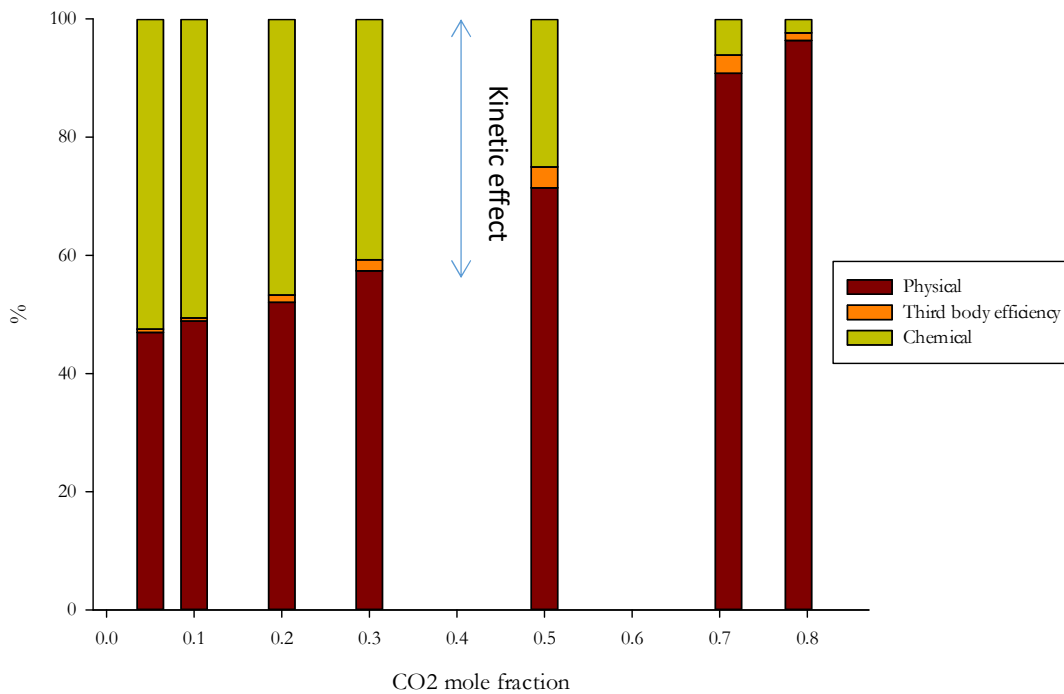
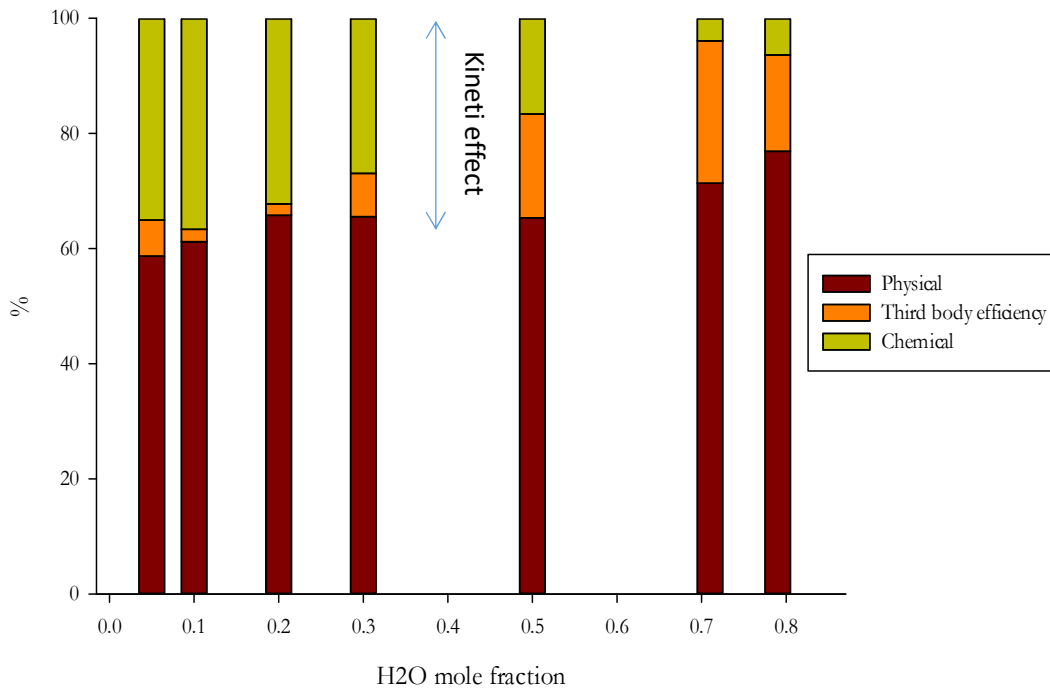


Figure 5.12: Effects of third-body efficiency, physical and chemical properties of H₂O and CO₂ on flame speed for a methane/oxygen mixture. P=30 atm, inlet T=800 K, $\phi=1$

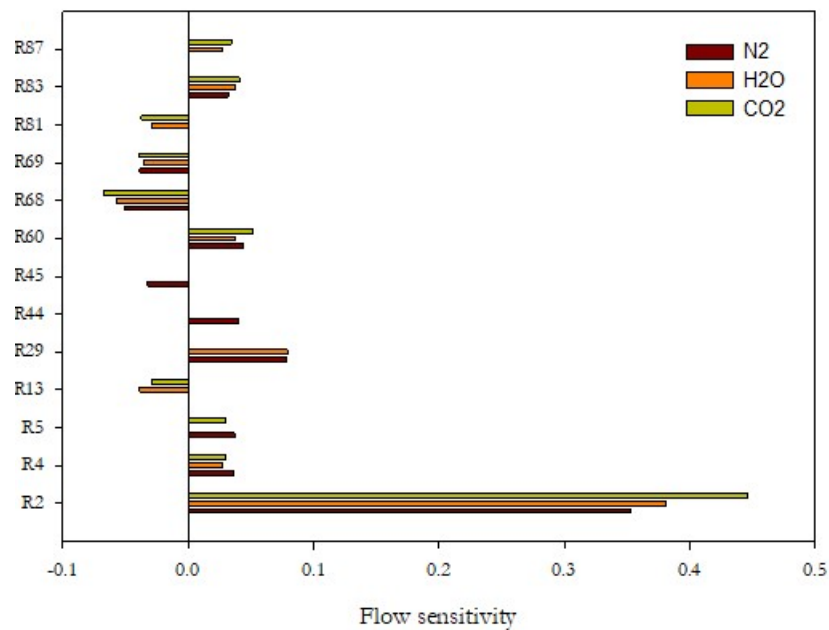


Figure 5.13: Flow sensitivity for methane/oxygen mixture at $P=30$ atm, inlet $T=800$ K, $\varphi=1$, $X_{\text{diluent}}=0.3$

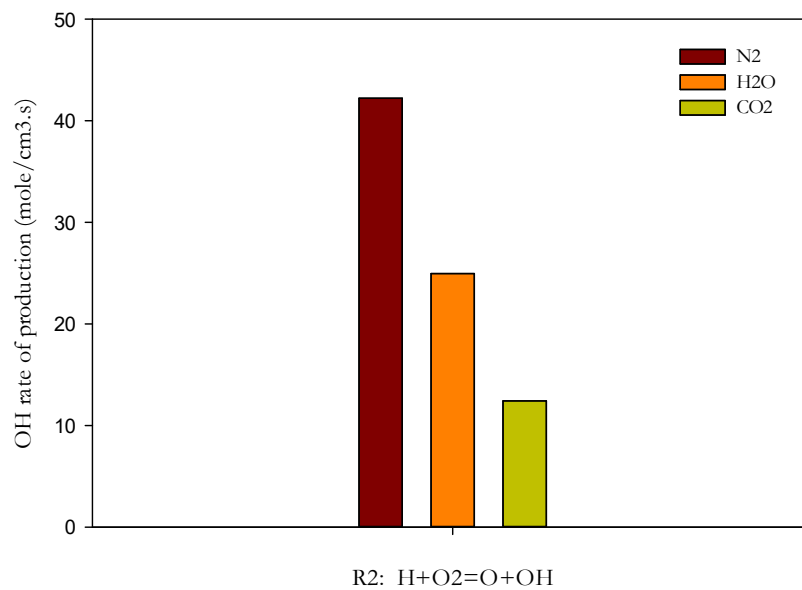


Figure 5.14: Comparison of rate of production of OH radical from reaction R2 for different diluents at $P=30$ atm, inlet $T=800$ K, $\varphi=1$, $X_{\text{diluent}}=0.3$

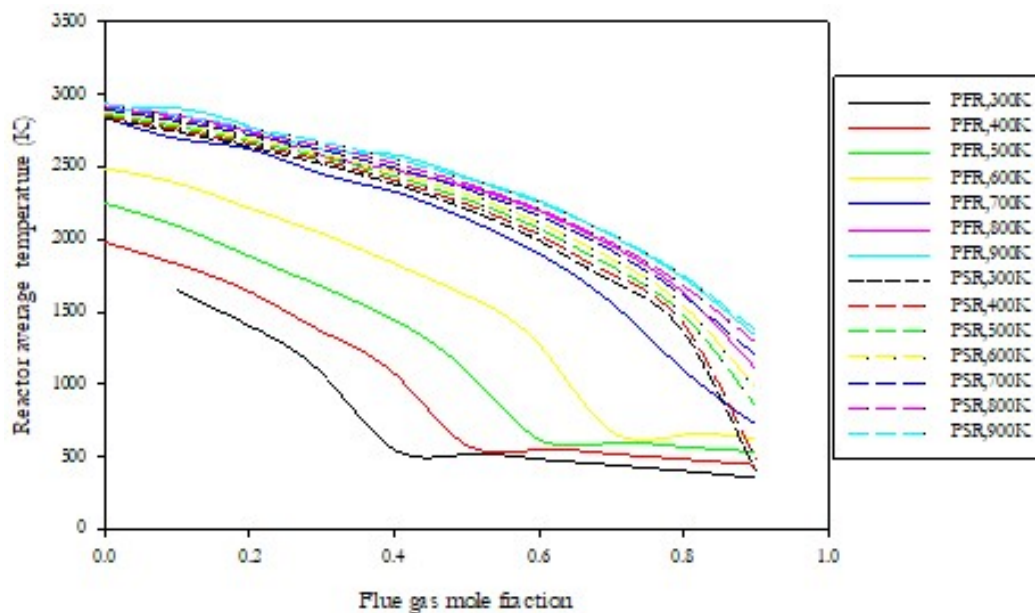


Figure 5.15: Reactor temperature as a function of the diluent mole fraction and gas inlet temperature for PFR and PSR models at 10 atm

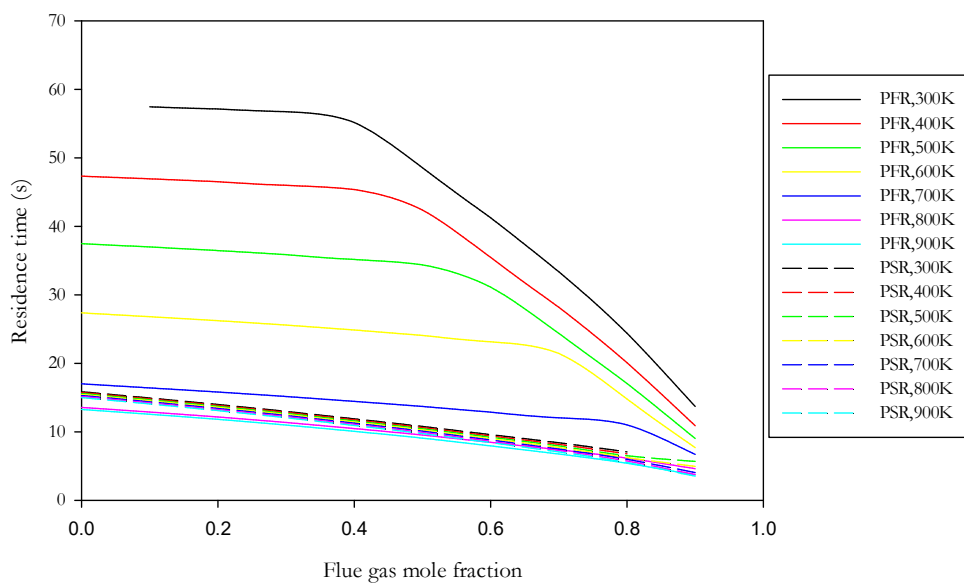


Figure 5.16: Residence time as a function of the diluent mole fraction and gas inlet temperature; comparison of PFR and PSR models at 10 atm

Table 5.1: List of elementary reactions during the ignition of methane/oxygen mixture, initial T=800 K, P=30 atm, $\varphi=1$

R120: $\text{H}_3\text{OO}+\text{CH}_4\rightleftharpoons\text{CH}_3\text{OOH}+\text{CH}_3$	
R118: $\text{CH}_3\text{OO}+\text{HO}_2\rightleftharpoons\text{CH}_3\text{OOH}+\text{O}_2$	
R123: $\text{CH}_3\text{OO}+\text{CH}_2\text{O}\rightleftharpoons\text{CH}_3\text{OOH}+\text{HCO}$	
R102: $\text{CH}_3\text{O}+\text{CH}_4\rightleftharpoons\text{CH}_3\text{OH}+\text{CH}_3$	
R92: $\text{CH}_3\text{O}(\text{+M})\rightleftharpoons\text{CH}_2\text{O}+\text{H}(\text{+M})$	
R47: $\text{CH}_4+\text{OH}\rightleftharpoons\text{CH}_3+\text{H}_2\text{O}$	
R25: $\text{H}_2\text{O}_2(\text{+M})\rightleftharpoons 2\text{OH}(\text{+M})$	$\text{H}_2\text{O}/12 \quad \text{AR}/ 0.64 \quad \text{He}/ 2.5$
R23: $2\text{HO}_2\rightleftharpoons\text{H}_2\text{O}_2+\text{O}_2$	
R48: $\text{CH}_4+\text{HO}_2\rightleftharpoons\text{CH}_3+\text{H}_2\text{O}_2$	
R23: $2\text{HO}_2\rightleftharpoons\text{H}_2\text{O}_2+\text{O}_2$	
R127: $2\text{CH}_3\text{OO}\rightleftharpoons 2\text{CH}_3\text{O}+\text{O}_2$	
R128: $2\text{CH}_3\text{OO}\rightleftharpoons\text{CH}_3\text{OH}+\text{CH}_2\text{O}+\text{O}_2$	

CHAPTER 6

SUMMARY AND CONCLUSION

6.1. Overview

This chapter includes a brief introduction, key conclusions, and recommendations for future work.

6.2. Introduction

The primary objective of this project was to develop a downhole heater to raise oil shale to a specified temperature in situ, and to recover energy-rich liquids and gas. The project had two main phases. Phase I was a preliminary study investigating several different burner concepts for generating heat at great depth and over significant horizontal lengths. That preliminary study included engineering calculations to examine overall energy balances, heat transfer, and pressure drop considerations. Then, two burner concepts, homogeneous oxidation and catalytic oxidation, were investigated. In Phase II, a unique configuration of a downhole heater was proposed which eliminates some of the issues regarding previously-considered configurations. The feasibility and applicability of the proposed heater have been investigated by looking at key issues that have not been completely addressed in the literature by other researchers. The issues addressed in Phase II were:

- 1- Do some of the inexpensive and widely-available metals have reasonable catalytic activity and durability such that they can be considered as a catalyst for methane oxidation in our application?
- 2- How to design the fuel/oxidizer nozzles along the length of 2000 ft of the heater so that the fuel/oxidizer distribution, and thus heat release, remains uniform.
- 3- How does nozzle orientation and position in the heater affect the fuel and oxidizer mixing behavior?
- 4- How does the presence of exhaust gas in the heater affect the oxidation behavior?
- 5- How do the chemical and thermodynamic properties of diluents, CO₂, N₂, and H₂O, affect the ignition delay time of methane?
- 6- Which specific reactions inhibit or promote methane oxidation in the presence of diluents?

6.3. Summary and conclusions

The dissertation consists of six chapters: (1) Introduction, (2) Literature review, (3) Engineering calculations, (4) Experimental work, (5) Modeling and reaction analysis, and (6) Summary and future work.

Chapter 1 introduces the project. It includes the motivations and objectives, as well as a brief summary.

Chapter 2 is the literature review. It consists of two sections. The focus of Section I is to review the combustion behavior of natural gas and oxygen mixtures at high pressures and low initial temperatures ($P \sim 10\text{-}30$ atm and $T \sim 700\text{-}1000$ K). The effects of pressure, temperature, and diluent concentration on flammability, ignition, and stability were also

summarized.

The literature shows that both temperature and pressure have a notable effect on flammability limits, such that it is not possible to use flammability data at ambient conditions for heater calculations. It is also shown that pressure has a more significant effect on UFL than LFL.

Research shows that although the presence of higher hydrocarbons and hydrogen can accelerate methane ignition at high initial temperatures (1200-2000 K), it doesn't have any significant effect on methane ignition at lower initial temperatures ($T \sim 800\text{K}$). Please note that those studies were done mostly at high pressure ($P \sim 20\text{ atm}$), and the effect of pressure was also considered in the results. The conclusion is that there would be a minor effect of higher hydrocarbons and hydrogen on ignition properties of methane at the desired operating conditions.

There are several factors, such as pressure, nozzle diameter, gas exit velocity, O_2 concentration, and flue gas species concentration, that affect flame stability. The data show that the presence of flue gas species such as CO_2 decrease flame stability. On the other hand, increasing the pressure or O_2 concentration helps to improve flame stability.

Section II focuses on finding suitable catalyst for methane oxidation. Methane oxidation catalysts are divided into two categories, noble metal catalysts and transition metal catalysts. Fast Engineering Ltd. has claimed¹ that they developed a transition-metal-type catalyst for hydrocarbon oxidation that worked for 4-5 years at temperatures in the range of 1300–1600 K. This catalyst consists of an alumina carrier coated with nickel oxide, NiO. Some specifications of this catalyst are provided in Chapter 4. No additional information has been found for this catalyst to date.

Chapter 3 summarizes preliminary engineering calculations to support the design of a new heater configuration. It consists of two sections. In Section I, calculations were performed to determine appropriate sizes for feeder pipes and nozzles, as well as the pressure distributions in different sections of the heater. The main objective of Section I was to design a system so that a uniform flow distribution is maintained along the 2000 ft of the heater. Two different cases were considered:

Case 1: the fuel and oxidant pipe sizes are constant, and the hole sizes change

Case 2: the hole sizes are constant, and the fuel and oxidant pipe sizes change

In both cases, the gas inlet temperature and pressure in the feeder pipes were 900 K and 10 atm. It was assumed that there was no reaction occurring in the chamber and that the gas properties were constant along the system.

Three different approaches were evaluated in Case 1. In the first two approaches, it was assumed that the gases were injected into a chamber, which had a constant pressure. In the third approach, the axial pressure distribution in the chamber was also taken into account. In Case 2, it was assumed the hole diameters and the hole spacing were constant and uniform along the length of the pipe. The cross-sectional area of the feeder pipe changes along the length of the system. Note that all the calculations were based on the assumption that the fuel was pure methane and the oxidizer was pure oxygen. However, in the downhole heater, natural gas probably will be used as the fuel, and there may be some diluents such as N_2 , CO_2 , or H_2O present in the O_2 stream in the oxidizer pipe. Thus, the results may change based on the gas composition and properties. In Section II, overall energy balance and heat transfer calculations were used to determine the overall heat transfer coefficient in the heater and the required gas mixture temperature to meet design

specifications. The results of this chapter were the inputs for future calculations. The average overall heat transfer coefficients of the outer annulus and the reaction chamber were estimated as $15 \text{ W}/(\text{m}^2 \cdot \text{K})$ and $3.5 \text{ W}/(\text{m}^2 \cdot \text{K})$, respectively. The average flue gas temperature was determined to be equal to 939 K. This temperature is the average gas temperature that has to be reached inside the heater so that the temperature of the surrounding oil is maintained at 650 K.

Chapter 4 is a summary of experimental work performed during this project. It consists of two sections. In Section I, experimental and CHEMKIN² modeling studies were performed to investigate the catalytic activity of metals and catalysts that could potentially be used in heater construction and operation. Both experimental and modeling results show that the observed methane oxidation over stainless steels and Hastelloy-X can be explained by homogeneous oxidation rather than by any catalytic effect of these materials. On the other hand, Pd-coated alumina catalyst promoted complete methane oxidation at temperatures as low as 600 K. In addition, CHEMKIN was used to model the methane oxidation experiments performed by Western Research Institute (WRI)³ in previous research for AMSO. These results demonstrated that the WRI experimental data can also be explained by homogenous methane oxidation. Thus, our conclusion is that typical metals that would be used in heater construction do not provide any appreciable catalytic benefit relative to homogeneous (noncatalytic) methane oxidation for the conditions studied (Initial $T \sim 500\text{-}1100 \text{ K}$).

Section II summarizes a cold-flow experimental study of the new heater configuration. A cold-flow study was performed to investigate the effect of nozzle spacing and orientation on the mixing behavior inside the heater. Three cases were studied. In Cases 1 and 2, the

holes on the feeder pipes were delivering gases in adjacent or different axial locations, respectively, but had the same circumferential orientation. In Case 3, the holes were at the same axial position but were directed away from each other. In Cases 1 and 3, the nozzles were 25 cm from the gas inlet, and in Case 2, the position of one nozzle was 25 cm, and the other was 50 cm, from the gas inlet. The gas compositions at different locations inside the chamber were measured with a micro GC. The results showed that in Cases 1 and 2, the two streams were well mixed in the mixing chamber. In Case 3, there were two distinct regions, a volume where the concentration of CO₂ was high (N₂ is low) and a second where the concentration of N₂ was high. The conclusion is that the radial orientations of the nozzles had a more significant role in the mixing behavior than the axial positions of the nozzles. Case 3, where the circumferential positions of the nozzles were different, showed less mixing than Cases 1 and 2.

Chapter 5 consists of the modeling studies and reaction analysis using CHEMKIN. This chapter has two sections. In Section I, the effects of the diluents N₂, CO₂, and H₂O on the oxidation behavior of methane-oxygen mixtures at low-to-moderate reactor inlet temperatures (T=800-1400 K) and high pressure (P=30 atm) were studied. The physical and kinetic effects of the diluents were quantified and the following conclusions were reached.

At low gas inlet temperatures, the flame temperature was mainly controlled by the thermal properties of the diluents, and the chemical effect of the diluents was almost negligible. The diluents decreased the flame temperature in the order of their molar isobaric heat capacities ($C_{P(\text{CO}_2)} > C_{P(\text{H}_2\text{O})} > C_{P(\text{N}_2)}$), with CO₂ causing the largest decrease and N₂ the smallest. The physical properties of the diluents also alter the ignition delay time

and the flame speed of the mixture. As the heat capacity of the mixture increases, the reaction temperature and the flame speed drop, while the ignition delay time increases. Adding diluents to a mixture also affects the radical pool and changes the elementary reaction rates and pathways. Water vapor addition at a low initial temperature (800-900 K) promotes methane oxidation and decreases the ignition delay time.

Note that in Section I, it was assumed that the reactor was adiabatic. However, in a downhole heater, there would be heat transfer from the reaction chamber to the surroundings, and this issue was addressed in Section II. In Section II, CHEMKIN calculations were performed for a 1-meter section of the reaction chamber using non-adiabatic boundary conditions. Two separate models, a plug flow reactor model (PFR) and a perfectly-stirred reactor model (PSR), were considered. The calculation was performed for fuel/oxidizer mixtures with varying levels of dilution (0 to 90 mole %) over a range of initial temperatures (300-900 K) to determine the bounds of homogeneous ignition. A mixture of 67 mole % CO₂ and 33 mole % H₂O was defined as a diluent. The heat transfer calculations in Chapter 3 show that the average combustion gas temperature inside the chamber should be around 939 K to provide the desired amount of heat to the surrounding oil. Results showed that at any inlet temperature, with the PSR model, the diluent (flue gas) mole fraction in the gas mixture should be at least 0.85 in order for the reactor temperature to reach 939 K, with higher inlet temperatures requiring greater flue gas dilution. However, depending on the gas inlet temperature, we can have a diluent mole fraction as low as 0.4 and still reach an average reactor temperature of 939 K in a PFR. In reality, the downhole heater is neither a PFR nor a PSR reactor. Since the length-to-diameter ratio of the reactor is 12 ($L/D > 10$), the PFR model would generally be considered a more reasonable

approximation; thus, the actual downhole heater operation will tend more towards the PFR model predictions than the PSR predictions.

6.4. Recommendations for future work

Some recommendations for future work are listed below:

- 1- In the cold-flow experiment, a 1-meter section of the reaction chamber was considered. The experimental setup consisted of two PVC pipes inside an acrylic tube. There was a hole on each PVC pipe serving as a nozzle to inject the gas into the chamber. A longer section of the heater with more holes on each feeder pipe is recommended. This configuration will aid in understanding the effect of the presence of adjacent holes on flow distributions on each feeder pipe, and will allow investigation of the effect of nozzle spacing on gas mixing behavior.
- 2- In Chapter 4, the gas mixing experiment was conducted at room temperature and atmospheric pressure with CO₂ and N₂. Experimental tests are needed at realistic temperature and pressures with natural gas and oxygen as the fuel and oxidizer.
- 3- In Chapter 5, the effect of diluents on oxidation behavior of methane/oxygen mixtures was investigated using CHEMKIN. However, in the actual heater, natural gas will be used as the fuel. For future work, natural gas/oxygen mixtures should be studied to investigate the effect of higher hydrocarbons and hydrogen on the oxidation behavior.
- 4- Although many experimental studies have been conducted on the effect of diluents, especially CO₂, on methane oxidation behavior, there is still little experimental data available on the effect of diluents at low-to-moderate initial temperatures (T=800-

1100 K) and high pressure, with diluent mole fractions greater than 30 %. Experiments are needed to study the effect of diluents, such as carbon dioxide, water vapor, or even a mixture of these two as a representation of flue gas, at the above-mentioned conditions.

- 5- Pilot-scale tests are needed at operating conditions of the downhole heater (P~10-30atm, inlet T~400-800K), with natural gas/oxygen/diluent mixtures.

6.5. References

- (1) D. L. Astanovsky; L. Z. Astanovsky, P. V. K. *Catal. Ind.* **2013**, 5, 148–155.
- (2) Reaction Design. In *CHEMKIN-PRO 15131*; San Diego, **2013**.
- (3) Western Research Institute. *American Shale Oil Catalytic Material Tests (Private Report)*; Laramie, WY, **2009**.

APPENDIX A

CHEMKIN CALCULATION TO FIND GAS PROPERTIES

The diagram view and all the steps of CHEMKIN calculation are shown in Figures A.1 to A.7. O₂, CH₄, and CO₂ streams are mixed in a physical mixer and then injected into the plug flow reactor.¹ The summary of the model, reactor information, operating, and flow conditions are listed in Table A.1.

Table A. 1: Model summary and the boundary conditions

Reaction mechanism	Glarborg mechanism (Low T, high P oxidation)
Operating condition of mixer	T=800K, P=10 bar
Operating condition of the plug flow reactor	T=800K, P=10 bar
Dimension of the plug flow reactor	D=3.3 in, L=1m
Heat flux through the wall of the reactor	0.022 kJ/cm.s
CH ₄ inlet condition 0.00467	$\dot{m} = 7.48 * 10^{-5} \frac{kg}{s}, T = 800K$
O ₂ inlet condition 0.0094	$\dot{m} = 2.99 * 10^{-4} \frac{kg}{s}, T = 800K$
CO ₂ inlet condition 0.014	$\dot{m} = 6.17 * 10^{-4} \frac{kg}{s}, T = 800K$

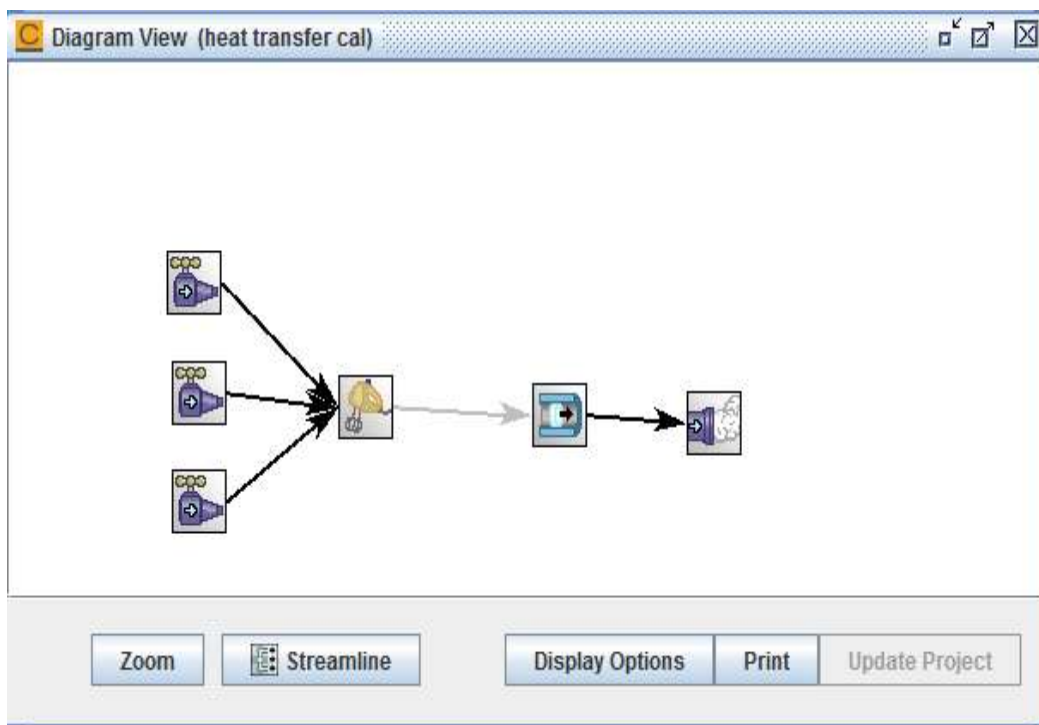


Figure A.1: CHEMKIN calculation, Diagram view

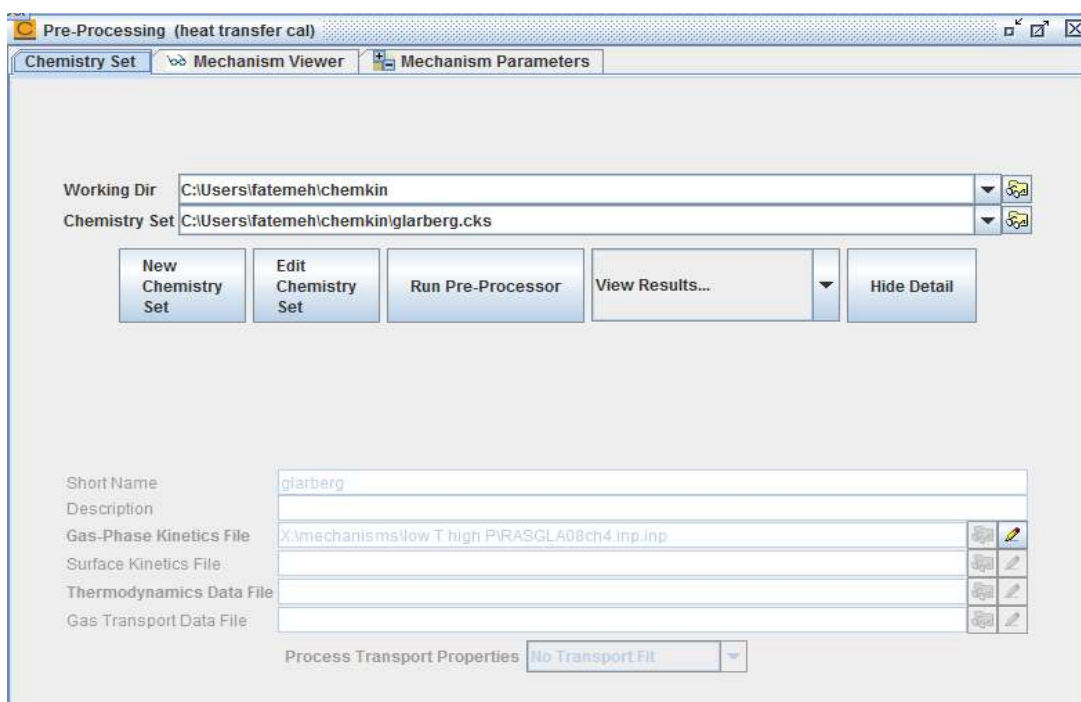


Figure A.2: CHEMKIN calculation, Glarborg oxidation chemistry

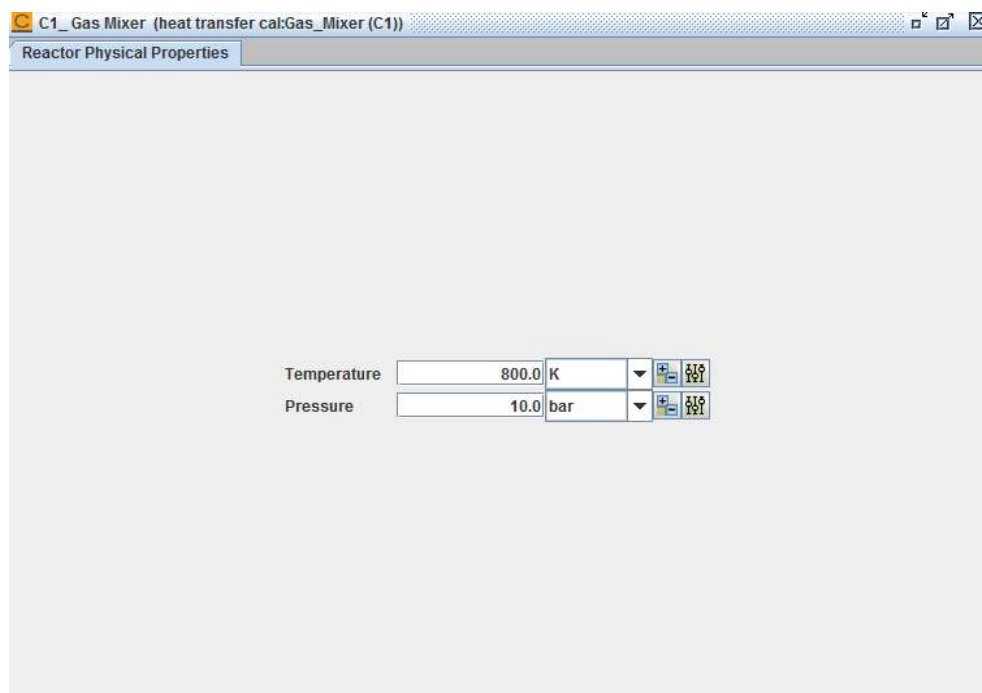
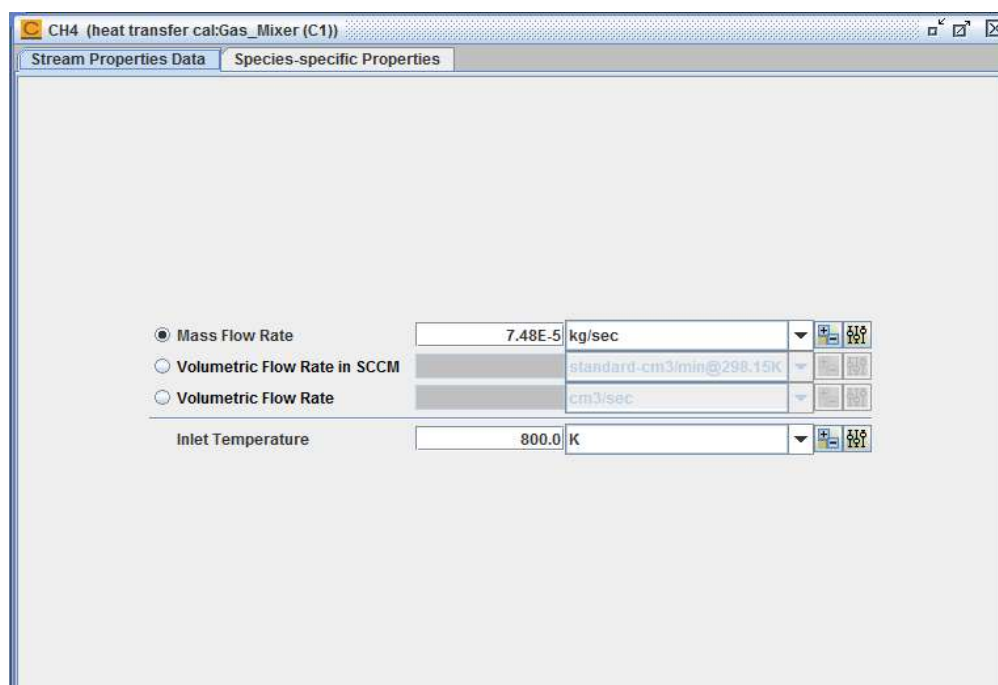
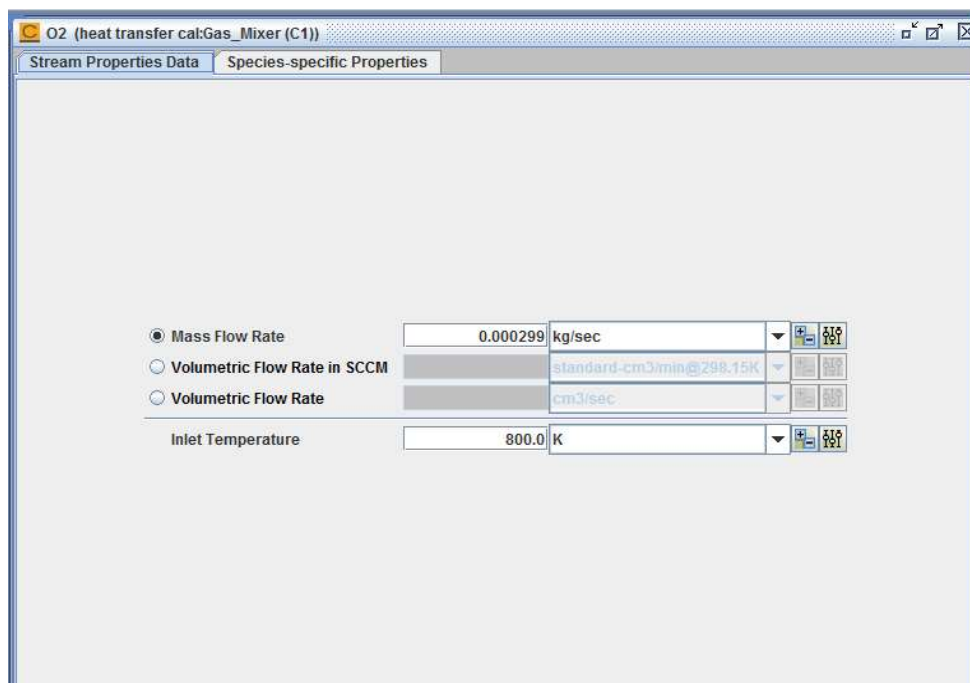
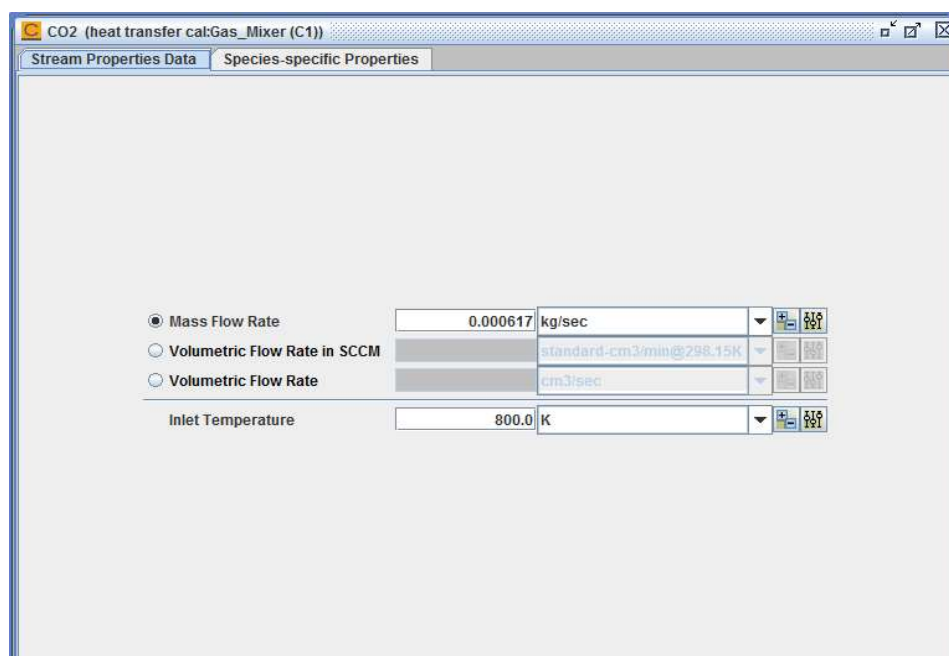


Figure A.3: CHEMKIN calculation, mixer operating condition

Figure A.4: CHEMKIN calculation, CH₄ stream flowrate

Figure A.5: CHEMKIN calculation, O₂ stream flowrateFigure A.6: CHEMKIN calculation, CO₂ stream flowrate

C2_PFR (heat transfer cal:PFR (C2))

Reactor Physical Properties

Problem Type: Solve Gas Energy Equation

Turn on Momentum Equation
 Turn off Momentum Equation

Turn on Residence Time Calculation
 Turn off Residence Time Calculation

Starting Axial Position: 0.0 cm

Ending Axial Position: 1.0 m

Diameter: 3.3 inch, Constant
 Cross-sectional Area: cm², Constant
 Axial Velocity Profile: cm/sec, Select Profile...

Internal Surface Area Per Unit Length: cm, Constant

External Surface Area Per Unit Length: cm, Constant

Temperature: 800.0 K

Pressure: 10.0 bar, Constant

Heat Flux Per Unit Length: 0.022 kJ/cm-sec, Constant
 Heat Transfer Coefficient: cal/cm²-K-sec

Ambient Temperature: K

Figure A.7: CHEMKIN calculation, plug flow model

APPENDIX B

DETERMINING THE EXHAUST GAS INITIAL PROPERTIES

The Aspen Hysys modeling is performed to determine the initial values for the exhaust gas properties.² Figure B.1 to Figure B.5 show the steps of the calculation.

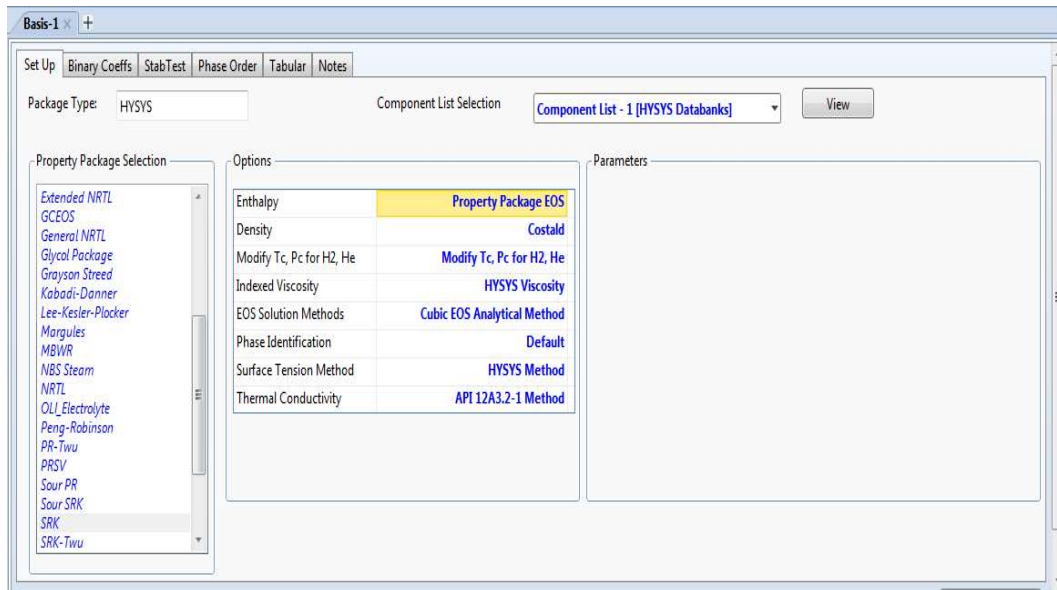


Figure B.1: Aspen HYSYS, Fluid Package Selection, SRK equation of state

Material Stream: 1

Worksheet Attachments Dynamics

Worksheet

Stream Name	1	Vapour Phase
Vapour / Phase Fraction	1.0000	1.0000
Temperature [C]	1827	1827
Pressure [kPa]	1000	1000
Molar Flow [kgmole/h]	2.855e-005	2.855e-005
Mass Flow [kg/h]	9.910e-004	9.910e-004
Std Ideal Liq Vol Flow [m3/h]	1.176e-006	1.176e-006
Molar Enthalpy [kJ/kgmole]	-2.176e+005	-2.176e+005
Molar Entropy [kJ/kgmole-C]	250.8	250.8
Heat Flow [kJ/h]	-6.213	-6.213
Liq Vol Flow @Std Cond [m3/h]	1.092e-006	1.092e-006
Fluid Package	Basis-1	
Utility Type		

OK

Delete Define from Stream... View Assay

Figure B.2: Aspen HYSYS, Gas condition input

Material Stream: 1

Worksheet Attachments Dynamics

Worksheet

	Mole Fractions	Vapour Phase
CO2	0.5980	0.5980
H2O	0.2763	0.2763
Hydrogen	0.0041	0.0041
Oxygen	0.0638	0.0638
CO	0.0367	0.0367
Methane	0.0210	0.0210

Total 1.00000

Edit... View Properties... Basis...

OK

Delete Define from Stream... View Assay

Figure B.3: Aspen HYSYS, gas composition input

Material Stream: 1

Worksheet Attachments Dynamics

Worksheet	Stream Name	1	Vapour Phase
Conditions	Molecular Weight	34.71	34.71
Properties	Molar Density [kgmole/m3]	5.720e-002	5.720e-002
Composition	Mass Density [kg/m3]	1.986	1.986
Oil & Gas Feed	Act. Volume Flow [m3/h]	4.991e-004	4.991e-004
Petroleum Assay	Mass Enthalpy [kJ/kg]	-6270	-6270
K Value	Mass Entropy [kJ/kg-C]	7.225	7.225
User Variables	Heat Capacity [kJ/kgmole-C]	62.97	62.97
Notes	Mass Heat Capacity [kJ/kg-C]	1.814	1.814
Cost Parameters	LHV Molar Basis (Std) [kJ/kgmole]	2.823e+004	2.823e+004
Normalized Yields	HHV Molar Basis (Std) [kJ/kgmole]	4.145e+004	4.145e+004
	HHV Mass Basis (Std) [kJ/kg]	1194	1194
	CO2 Loading	<empty>	<empty>
	CO2 Apparent Mole Conc. [kgmole/m3]	<empty>	<empty>
	CO2 Apparent Wt. Conc. [kgmol/kg]	<empty>	<empty>
	LHV Mass Basis (Std) [kJ/kg]	813.1	813.1
	Phase Fraction [Vol. Basis]	1.000	1.000
	Phase Fraction [Mass Basis]	1.000	1.000
	Phase Fraction [Act. Vol. Basis]	1.000	1.000
	Mass Exergy [kJ/kg]	2017	<empty>
	Partial Pressure of CO2 [kPa]	598.0	<empty>
	Cost Based on Flow [Cost/s]	0.0000	0.0000
	Act. Gas Flow [ACT_m3/h]	4.991e-004	4.991e-004
	Avg. Liq. Density [kgmole/m3]	24.27	24.27
	Specific Heat [kJ/kgmole-C]	62.97	62.97

Property Correlation Controls

Preference Option: Active

OK

Delete Define from Stream... View Assay

Figure B.4: Aspen Hysys, Gas properties output 1

Material Stream: 1

Worksheet Attachments Dynamics

Worksheet	Property	Value	Unit
Conditions	Partial Pressure of H2S [kPa]	0.0000	<empty>
Properties	Cp/(Cp - R)	1.152	1.152
Properties	Cp/Cv	1.152	1.152
Composition	Heat of Vap. [kJ/kgmole]	4.169e-004	<empty>
Oil & Gas Feed	Kinematic Viscosity [cSt]	36.05	36.05
Petroleum Assay	Liq. Mass Density (Std. Cond) [kg/m ³]	907.3	907.3
K Value	Liq. Vol. Flow (Std. Cond) [m ³ /h]	1.092e-006	1.092e-006
User Variables	Liquid Fraction	0.0000	0.0000
Notes	Molar Volume [m ³ /kgmole]	17.48	17.48
Cost Parameters	Mass Heat of Vap. [kJ/kg]	1201	<empty>
Normalized Yields	Phase Fraction [Molar Basis]	1.0000	1.0000
	Surface Tension [dyne/cm]	<empty>	<empty>
	Thermal Conductivity [W/m-K]	6.269e-002	6.269e-002
	Viscosity [cP]	7.157e-002	7.157e-002
	Cv (Semi-Ideal) [kJ/kgmole-C]	54.65	54.65
	Mass Cv (Semi-Ideal) [kJ/kg-C]	1.574	1.574
	Cv [kJ/kgmole-C]	54.66	54.66
	Mass Cv [kJ/kg-C]	1.575	1.575
	Cv (Ent. Method) [kJ/kgmole-C]	<empty>	<empty>
	Mass Cv (Ent. Method) [kJ/kg-C]	<empty>	<empty>
	Cp/Cv (Ent. Method)	<empty>	<empty>
	Reid VP at 37.8 C [kPa]	<empty>	<empty>
	True VP at 37.8 C [kPa]	1.658e+004	1.658e+004
	Liq. Vol. Flow - Sum(Std. Cond) [m ³ /h]	1.092e-006	1.092e-006
	Viscosity Index	8.219	<empty>

Property Correlation Controls

Preference Option: Active

OK

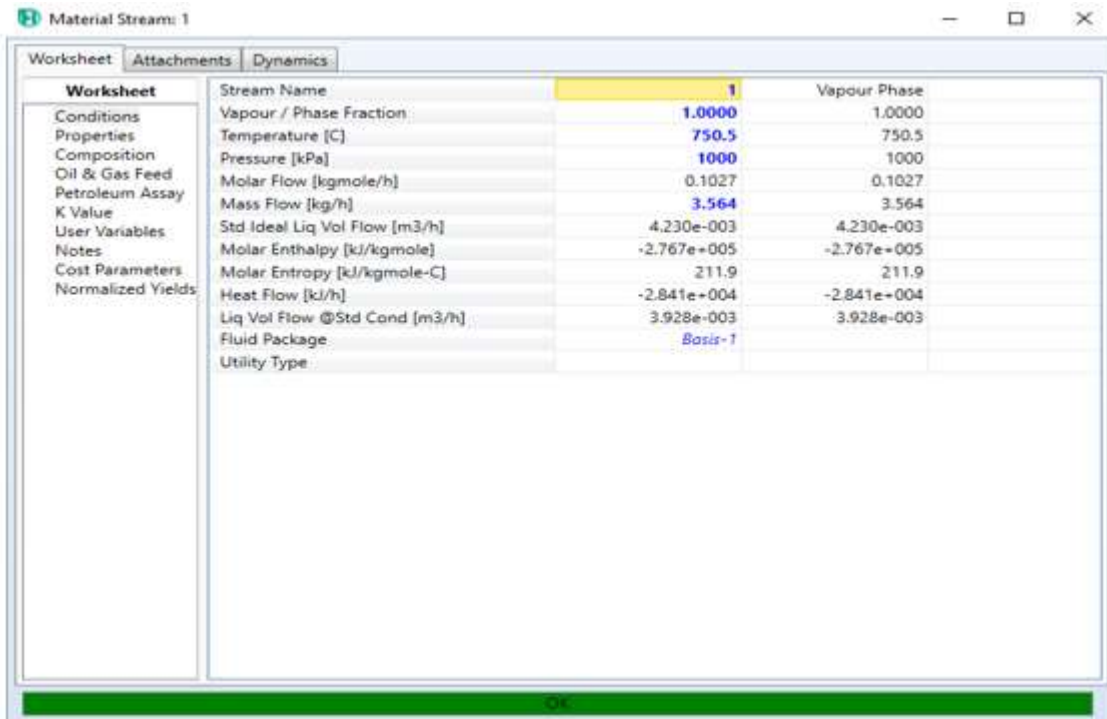
Delete Define from Stream... View Assay

Figure B.5: Aspen HYSYS, Gas properties output 2

APPENDIX C

DETERMINING THE EXHAUST GAS FINAL PROPERTIES

The Aspen Hysys modeling is performed to determine the final values for the exhaust gas properties. Figure C.1 to Figure C.4 show the steps of the calculation.



The screenshot shows the 'Material Stream: 1' dialog box in Aspen HYSYS. The 'Worksheet' tab is active, displaying a table of properties for the stream. The 'Stream Name' is '1' and the 'Vapour Phase' is selected. The 'Vapour / Phase Fraction' is 1.0000. The temperature is 750.5 C, pressure is 1000 kPa, molar flow is 0.1027 kgmole/h, and mass flow is 3.564 kg/h. The fluid package is 'Basis-1'.

Worksheet	Stream Name	1	Vapour Phase
Conditions	Vapour / Phase Fraction	1.0000	1.0000
Properties	Temperature [C]	750.5	750.5
Composition	Pressure [kPa]	1000	1000
Oil & Gas Feed	Molar Flow [kgmole/h]	0.1027	0.1027
Petroleum Assay	Mass Flow [kg/h]	3.564	3.564
K Value	Std Ideal Liq Vol Flow [m3/h]	4.230e-003	4.230e-003
User Variables	Molar Enthalpy [kJ/kgmole]	-2.767e+005	-2.767e+005
Notes	Molar Entropy [kJ/kgmole-C]	211.9	211.9
Cost Parameters	Heat Flow [kJ/h]	-2.841e+004	-2.841e+004
Normalized Yields	Liq Vol Flow @Std Cond [m3/h]	3.928e-003	3.928e-003
	Fluid Package	Basis-1	
	Utility Type		

Figure C.1: Aspen HYSYS, gas condition input

Material Stream: 1

Worksheet Attachments Dynamics

Worksheet

	Mole Fractions	Vapour Phase
Methane	0.0210	0.0210
CO2	0.5981	0.5981
CO	0.0367	0.0367
H2O	0.2763	0.2763
Hydrogen	0.0041	0.0041
Oxygen	0.0638	0.0638

Total: 1.00000

Buttons: Edit... View Properties... Basis... OK

Figure C.2: Aspen HYSYS, gas composition input

Material Stream: 1

Worksheet Attachments Dynamics

Worksheet

Property Name	Value	Vapour Phase
Stream Name	1	
Molecular Weight	34.71	34.71
Molar Density [kgmole/m3]	0.1173	0.1173
Mass Density [kg/m3]	4.070	4.070
Act. Volume Flow [m3/h]	0.8756	0.8756
Mass Enthalpy [kJ/kg]	-7971	-7971
Mass Entropy [kJ/kg-C]	6.104	6.104
Heat Capacity [kJ/kgmole-C]	49.12	49.12
Mass Heat Capacity [kJ/kg-C]	1.415	1.415
LHV Molar Basis (Std) [kJ/kgmole]	2.824e+004	2.824e+004
HHV Molar Basis (Std) [kJ/kgmole]	4.146e+004	4.146e+004
HHV Mass Basis (Std) [kJ/kg]	1194	1194
CO2 Loading	<empty>	<empty>
CO2 Apparent Mole Conc. [kgmole/m3]	<empty>	<empty>
CO2 Apparent Wt. Conc. [kgmol/kg]	<empty>	<empty>
LHV Mass Basis (Std) [kJ/kg]	813.4	813.4
Phase Fraction [Vol. Basis]	1.000	1.000
Phase Fraction [Mass Basis]	1.000	1.000
Phase Fraction [Act. Vol. Basis]	1.000	1.000
Mass Exergy [kJ/kg]	650.2	<empty>
Partial Pressure of CO2 [kPa]	598.1	<empty>

Property Correlation Controls

Preference Option: Active

OK

Figure C.3: Aspen HYSYS, Gas properties output 1

Material Stream: 1

Worksheet Attachments Dynamics

Worksheet			
Conditions	Kinematic Viscosity [cSt]	10.05	10.05
Properties	Liq. Mass Density (Std. Cond) [kg/m3]	907.3	907.3
Composition	Liq. Vol. Flow (Std. Cond) [m3/h]	3.928e-003	3.928e-003
Oil & Gas Feed	Liquid Fraction	0.0000	0.0000
Petroleum Assay	Molar Volume [m3/kgmole]	8.528	8.528
K Value	Mass Heat of Vap. [kJ/kg]	1201	<empty>
User Variables	Phase Fraction [Molar Basis]	1.0000	1.0000
Notes	Surface Tension [dyne/cm]	<empty>	<empty>
Cost Parameters	Thermal Conductivity [W/m-K]	7.627e-002	7.627e-002
Normalized Yields	Viscosity [cP]	4.089e-002	4.089e-002
	Cv (Semi-Ideal) [kJ/kgmole-C]	40.81	40.81
	Mass Cv (Semi-Ideal) [kJ/kg-C]	1.176	1.176
	Cv [kJ/kgmole-C]	40.74	40.74
	Mass Cv [kJ/kg-C]	1.174	1.174
	Cv (Ent. Method) [kJ/kgmole-C]	<empty>	<empty>
	Mass Cv (Ent. Method) [kJ/kg-C]	<empty>	<empty>
	Cp/Cv (Ent. Method)	<empty>	<empty>
	Reid VP at 37.8 C [kPa]	<empty>	<empty>
	True VP at 37.8 C [kPa]	1.658e+004	1.658e+004
	Liq. Vol. Flow - Sum(Std. Cond) [m3/h]	3.928e-003	3.928e-003
	Viscosity Index	-2.071	<empty>

Property Correlation Controls

Preference Option: Active

Figure C.4: Aspen HYSYS, Gas properties output 2

APPENDIX D

DETERMINING THE PROPERTIES OF THE BOILING OIL

Physical properties of the oil are calculated with Aspen HYSYS V8.8.^{2,3} The temperature of the oil is assumed to be 650K. The formation pressure increases with depth and is estimated according to the hydrostatic pressure gradient, which is approximately 0.465(psi/ft).

$$P_{formation} = 0.465 \left(\frac{Psi}{ft} \right) * 2000 (ft) = 930 psi$$

Please note that formation pressure in impermeable rocks such as shale is higher. Since the real data of formation pressure for AMSO's wells bores are not available, 930 psi is considered as the reservoir pressure. The VLE calculation is performed with PVTsim software on the heavy crude oil composition. Table D.1 shows the approximate composition of the heavy crude oil. The C10+ Specific Gravity and molar weight are assumed to be 0.875 and 240 gr/mole. Figure D.1 is the approximate PT diagram of the oil. Figure D.2 to Figure D.4 show the steps of the Hysys modeling.

Table D.1: Approximate composition of the heavy crude oil

Components	Mole (%)	Mole fraction
N ₂	0.103	0.00103
CO ₂	0.528	0.00528
C1	39.200	0.392
C2	5.018	0.05018
C3	2.804	0.02804
iC4	0.641	0.00641
nC4	1.107	0.01107
iC5	0.507	0.00507
nC5	0.538	0.00538
nC6	0.766	0.00766
nC7	4.790	0.0479
nC8	4.645	0.04645
nC9	4.076	0.04076
C10+	35.277	0.35277

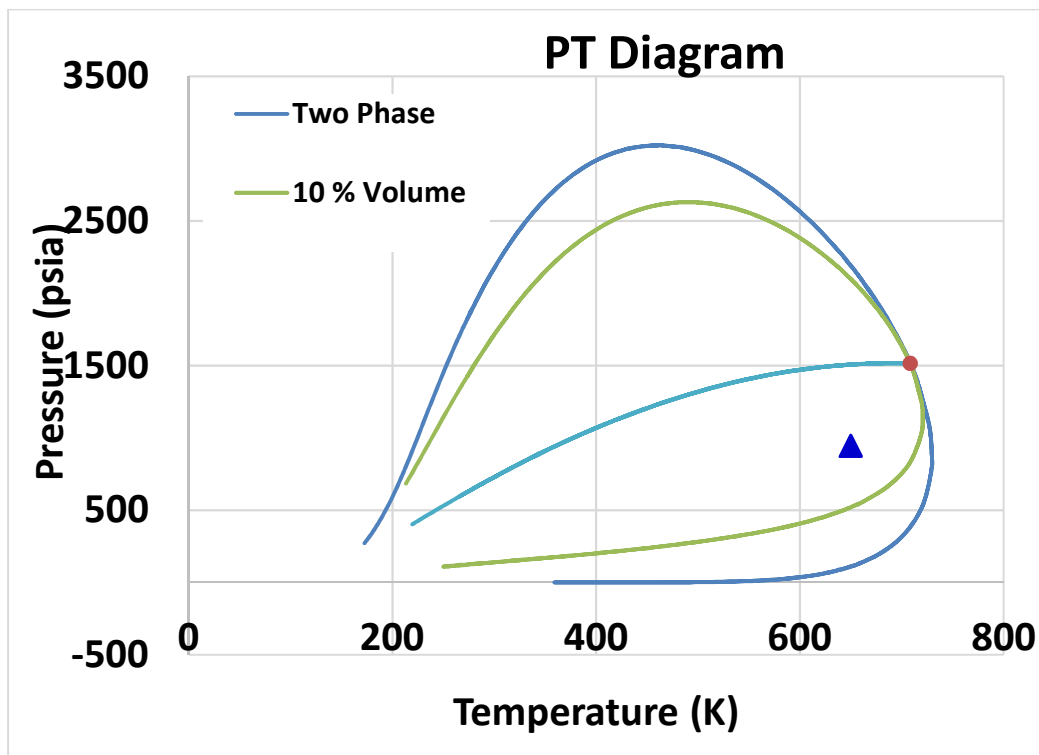


Figure D.1: Approximate PT diagram of the oil

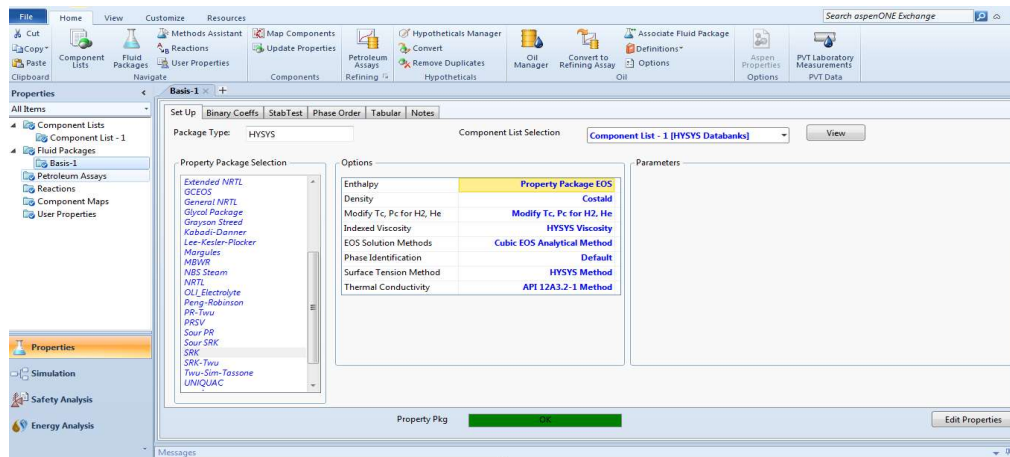


Figure D.2: Aspen HYSYS calculation, property package selection

Material Stream: oil

Worksheet Attachments Dynamics

Worksheet	Stream Name	oil	Vapour Phase	Liquid Phase
Conditions	Vapour / Phase Fraction	0.4578	0.4578	0.5422
Properties	Temperature [C]	376.9	376.9	376.9
Composition	Pressure [kPa]	6412	6412	6412
Oil & Gas Feed	Molar Flow [kgmole/h]	100.0	45.78	54.22
Petroleum Assay	Mass Flow [kg/h]	1.119e+004	3039	8150
K Value	Std Ideal Liq Vol Flow [m3/h]	16.25	5.084	11.16
User Variables	Molar Enthalpy [kJ/kgmole-C]	-1.316e+005	-9.337e+004	-1.639e+005
Notes	Molar Entropy [kJ/kgmole-C]	481.0	337.0	602.6
Cost Parameters	Heat Flow [kJ/h]	-1.316e+007	-4.275e+006	-8.888e+006
Normalized Yields	Liq Vol Flow @Std Cond [m3/h]	15.66	5.095	10.83
	Fluid Package	Basis-1		
	Utility Type			

OK

Delete Define from Stream... View Assay

Figure D.3: Aspen HYSYS calculation, oil conditions

Material Stream: oil

Worksheet Attachments Dynamics

Worksheet	Mole Fractions	Vapour Phase	Liquid Phase
Conditions	Nitrogen	0.0016	0.0006
Properties	CO2	0.0053	0.0034
Composition	Methane	0.3920	0.2421
Oil & Gas Feed	Ethane	0.0502	0.0349
Petroleum Assay	Propane	0.0280	0.0213
K Value	i-Butane	0.0064	0.0052
User Variables	n-Butane	0.0111	0.0091
Notes	i-Pentane	0.0051	0.0045
Cost Parameters	n-Pentane	0.0054	0.0048
Normalized Yields	n-Hexane	0.0077	0.0073
	n-Heptane	0.0479	0.0485
	n-Octane	0.0464	0.0497
	n-Nonane	0.0426	0.0459
	n-C17	0.3528	0.5229

Total 1.00000

Edit... View Properties... Basis...

OK

Delete Define from Stream... View Assay

Figure D.4: Aspen HYSYS calculation, oil composition

APPENDIX E

DETERMINING THE GAS PHYSICAL PROPERTIES

Physical properties of the oil are calculated with Aspen HYSYS V8.8. Figure E.1 to Figure E.6 show the steps of the calculation and the physical properties of the CH₄ properties. Figure E.7 to Figure E.12 show the steps of the calculation and the physical properties of O₂.

E.1. Determining the CH₄ properties

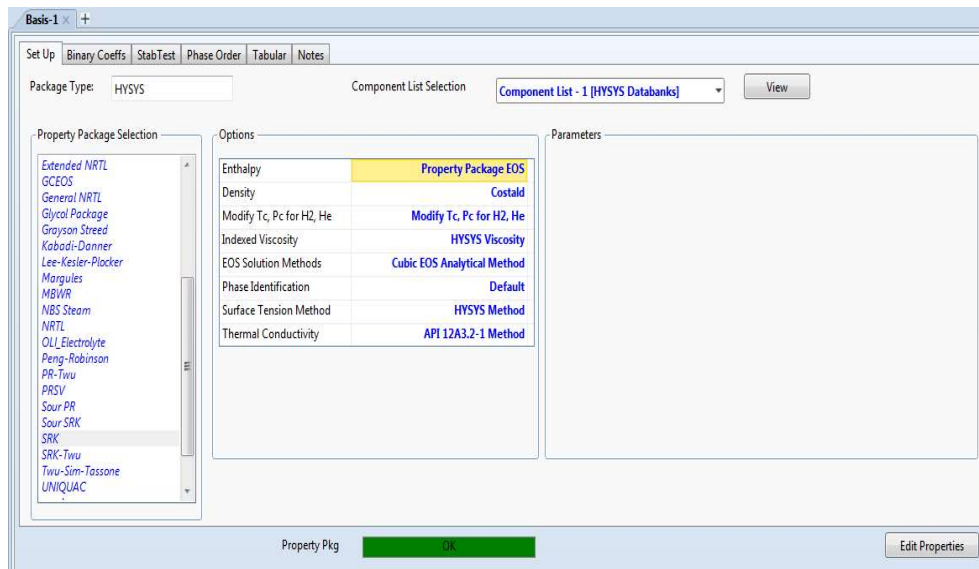


Figure E.1: Aspen HYSYS, fluid package selection, SRK equation of state

Material Stream: CH4

Worksheet Attachments Dynamics

Worksheet	Stream Name	CH4	Vapour Phase
Conditions	Vapour / Phase Fraction	1.0000	1.0000
Properties	Temperature [C]	526.9	526.9
Composition	Pressure [kPa]	1000	1000
Oil & Gas Feed	Molar Flow [kgmole/h]	100.0	100.0
Petroleum Assay	Mass Flow [kg/h]	1604	1604
K Value	Std Ideal Liq Vol Flow [m3/h]	5.358	5.358
User Variables	Molar Enthalpy [kJ/kgmole]	-5.013e+004	-5.013e+004
Notes	Molar Entropy [kJ/kgmole-C]	210.9	210.9
Cost Parameters	Heat Flow [kJ/h]	-5.013e+006	-5.013e+006
Normalized Yields	Liq Vol Flow @Std Cond [m3/h]	2360	2360
	Fluid Package	Basis-1	
	Utility Type		

OK

Delete Define from Stream... View Assay

Figure E.2: Aspen HYSYS, gas condition input

Material Stream: CH4

Worksheet Attachments Dynamics

Worksheet	Methane	Mole Fractions	Vapour Phase
Conditions		1.0000	1.0000

Total 1.00000

Edit... View Properties... Basis...

OK

Delete Define from Stream... View Assay

Figure E.3: Aspen HYSYS, gas composition input

Material Stream: CH4

Worksheet Attachments Dynamics

Worksheet	Stream Name	CH4	Vapour Phase
Conditions	Molecular Weight	16.04	16.04
Properties	Molar Density [kgmole/m3]	0.1499	0.1499
Composition	Mass Density [kg/m3]	2.404	2.404
Oil & Gas Feed	Act. Volume Flow [m3/h]	667.3	667.3
Petroleum Assay	Mass Enthalpy [kJ/kg]	-3125	-3125
K Value	Mass Entropy [kJ/kg-C]	13.15	13.15
User Variables	Heat Capacity [kJ/kgmole-C]	63.59	63.59
Notes	Mass Heat Capacity [kJ/kg-C]	3.964	3.964
Cost Parameters	LHV Molar Basis (Std) [kJ/kgmole]	8.027e+005	8.027e+005
Normalized Yields	HHV Molar Basis (Std) [kJ/kgmole]	8.847e+005	8.847e+005
	HHV Mass Basis (Std) [kJ/kg]	5.515e+004	5.515e+004
	CO2 Loading	<empty>	<empty>
	CO2 Apparent Mole Conc. [kgmole/m3]	<empty>	<empty>
	CO2 Apparent Wt. Conc. [kgmol/kg]	<empty>	<empty>
	LHV Mass Basis (Std) [kJ/kg]	5.003e+004	5.003e+004
	Phase Fraction [Vol. Basis]	1.000	1.000

Property Correlation Controls

Preference Option: Active

OK

Delete Define from Stream... View Assay

Figure E.4: Aspen HYSYS, gas properties outputs, part 1

Material Stream: CH4

Worksheet Attachments Dynamics

Worksheet	Phase Fraction [Mass Basis]	1.000	1.000
Conditions	Phase Fraction [Act. Vol. Basis]	1.000	1.000
Properties	Mass Exergy [kJ/kg]	1035	<empty>
Composition	Partial Pressure of CO2 [kPa]	0.0000	<empty>
Oil & Gas Feed	Cost Based on Flow [Cost/s]	0.0000	0.0000
Petroleum Assay	Act. Gas Flow [ACT_m3/h]	667.3	667.3
K Value	Avg. Liq. Density [kgmole/m3]	18.66	18.66
User Variables	Specific Heat [kJ/kgmole-C]	63.59	63.59
Notes	Std. Gas Flow [STD_m3/h]	2364	2364
Cost Parameters	Std. Ideal Liq. Mass Density [kg/m3]	299.4	299.4
Normalized Yields	Act. Liq. Flow [m3/s]	<empty>	<empty>
	Z Factor	1.003	1.003
	Watson K	19.52	19.52
	User Property	<empty>	<empty>
	Partial Pressure of H2S [kPa]	0.0000	<empty>
	Cp/(Cp - R)	1.150	1.150
	Cp/Cv	1.152	1.152

Property Correlation Controls

Preference Option: Active

OK

Delete Define from Stream... View Assay

Figure E.5: Aspen HYSYS, gas properties outputs, part 2

Material Stream: CH4

Worksheet Attachments Dynamics

Worksheet	Property	Value	Unit
Conditions	Heat of Vap. [kJ/kgmole]	6766	<empty>
Properties	Kinematic Viscosity [cSt]	9.927	9.927
Composition	Liq. Mass Density (Std. Cond) [kg/m3]	0.6798	0.6798
Oil & Gas Feed	Liq. Vol. Flow (Std. Cond) [m3/h]	2360	2360
Petroleum Assay	Liquid Fraction	0.0000	0.0000
K Value	Molar Volume [m3/kgmole]	6.673	6.673
User Variables	Mass Heat of Vap. [kJ/kg]	421.8	<empty>
Notes	Phase Fraction [Molar Basis]	1.0000	1.0000
Cost Parameters	Surface Tension [dyne/cm]	<empty>	<empty>
Normalized Yields	Thermal Conductivity [W/m-K]	0.1252	0.1252
	Viscosity [cP]	2.387e-002	2.387e-002
	Cv (Semi-Ideal) [kJ/kgmole-C]	55.28	55.28
	Mass Cv (Semi-Ideal) [kJ/kg-C]	3.446	3.446
	Cv [kJ/kgmole-C]	55.22	55.22
	Mass Cv [kJ/kg-C]	3.442	3.442
	Cv (Ent. Method) [kJ/kgmole-C]	<empty>	<empty>
	Mass Cv (Ent. Method) [kJ/kg-C]	<empty>	<empty>
	Cp/Cv (Ent. Method)	<empty>	<empty>
	Reid VP at 37.8 C [kPa]	<empty>	<empty>
	True VP at 37.8 C [kPa]	<empty>	<empty>
	Liq. Vol. Flow - Sum(Std. Cond) [m3/h]	2360	2360
	Viscosity Index	1.034e-002	<empty>

Property Correlation Controls

Preference Option: Active

Delete Define from Stream... View Assay

Figure E.6: Aspen HYSYS, gas properties outputs, part 3

E.2. Determining the O₂ properties

Basis-1

Set Up Binary Coeffs Stab Test Phase Order Tabular Notes

Package Type: HYSYS Component List Selection: Component List - 1 [HYSYS Databanks]

Property Package Selection:

- <none>
- Acid Gas
- Acid Gas - Physical Solvents
- Antoine
- ASME Steam
- Braun K10
- BWRS
- Chao Seader
- Chien Null
- Clean Fuels Pkg
- CPA
- Eso Tabular
- Extended NRTL
- GCEOS
- General NRTL
- Glycol Package
- Grayson Streed
- Kabadi-Danner
- Lee-Kesler-Plöcker
- Margules
- MBWR

Dense Phase Tuning Specification:

Dense Phase Tuning: Default

Default Dense Phase Tuning Factor: 1.0

The DPT can be used to control/alter the predicted liquid and vapor phase boundaries in supercritical region. DPT > 1 enlarges the vapor region. DPT < 1 narrows the vapor region. DPT cannot be smaller than 0.5 or greater than 2. DPT should be used with care and should not be applied when not in the supercritical region.

BWRS Component Parameters:

	B0	A0	C0	gamma
Methane	4.515e-02	2.021e+05	2.248e+09	5.793e-03
Oxygen	3.264e-02	1.193e+05	8.772e+08	2.893e-03

Property Pkg OK Edit Properties

Figure E.7: Aspen HYSYS, fluid package selection, BWRS equation of state

Material Stream: O2

Worksheet Attachments Dynamics

Worksheet

Worksheet	Stream Name	O2	Vapour Phase
Conditions	Vapour / Phase Fraction	1.0000	1.0000
Properties	Temperature [C]	526.9	526.9
Composition	Pressure [kPa]	1000	1000
Oil & Gas Feed	Molar Flow [kgmole/h]	100.0	100.0
Petroleum Assay	Mass Flow [kg/h]	3200	3200
K Value	Std Ideal Liq Vol Flow [m3/h]	2.813	2.813
User Variables	Molar Enthalpy [kJ/kgmole]	1.582e+004	1.582e+004
Notes	Molar Entropy [kJ/kgmole-C]	195.1	195.1
Cost Parameters	Heat Flow [kJ/h]	1.582e+006	1.582e+006
Normalized Yields	Liq Vol Flow @Std Cond [m3/h]	2362	2362
	Fluid Package	Basis-1	
	Utility Type		

OK

Delete Define from Stream... View Assay

Figure E.8: Aspen HYSYS, gas condition input

Material Stream: O2

Worksheet Attachments Dynamics

Worksheet

Worksheet	Mole Fractions	Vapour Phase
Conditions	Methane	0.0000
Properties	Oxygen	1.0000
Composition		
Oil & Gas Feed		
Petroleum Assay		
K Value		
User Variables		
Notes		
Cost Parameters		
Normalized Yields		

Total 1.00000

Edit... View Properties... Basis...

OK

Delete Define from Stream... View Assay

Figure E.9: Aspen HYSYS, gas composition input

Material Stream: O2

Worksheet Attachments Dynamics

Worksheet	Stream Name	O2	Vapour Phase
Conditions	Molecular Weight	32.00	32.00
Properties	Molar Density [kgmole/m3]	0.1500	0.1500
Composition	Mass Density [kg/m3]	4.800	4.800
Oil & Gas Feed	Act. Volume Flow [m3/h]	666.6	666.6
Petroleum Assay	Mass Enthalpy [kJ/kg]	494.4	494.4
K Value	Mass Entropy [kJ/kg-C]	6.097	6.097
User Variables	Heat Capacity [kJ/kgmole-C]	33.68	33.68
Notes	Mass Heat Capacity [kJ/kg-C]	1.053	1.053
Cost Parameters	LHV Molar Basis (Std) [kJ/kgmole]	0.0000	0.0000
Normalized Yields	HHV Molar Basis (Std) [kJ/kgmole]	0.0000	0.0000
	HHV Mass Basis (Std) [kJ/kg]	0.0000	0.0000
	CO2 Loading	<empty>	<empty>
	CO2 Apparent Mole Conc. [kgmole/m3]	<empty>	<empty>
	CO2 Apparent Wt. Conc. [kgmol/kg]	<empty>	<empty>
	LHV Mass Basis (Std) [kJ/kg]	0.0000	0.0000
	Phase Fraction [Vol. Basis]	1.000	1.000
	Phase Fraction [Mass Basis]	1.000	1.000
	Phase Fraction [Act. Vol. Basis]	1.000	1.000
	Mass Exergy [kJ/kg]	385.4	<empty>
	Partial Pressure of CO2 [kPa]	0.0000	<empty>
	Cost Based on Flow [Cost/\$]	0.0000	0.0000
	Act. Gas Flow [ACT_m3/h]	666.6	666.6
	Avg. Liq. Density [kgmole/m3]	35.55	35.55
	Specific Heat [kJ/kgmole-C]	33.68	33.68

Property Correlation Controls

Preference Option: Active

OK

Delete Define from Stream... View Assay

Figure E.10: Aspen HYSYS, gas properties output, part 1

Material Stream: O2

Worksheet Attachments Dynamics

Worksheet	Std. Gas Flow [STD_m3/h]	2364	2364
Conditions	Std. Ideal Liq. Mass Density [kg/m3]	1138	1138
Properties	Act. Liq. Flow [m3/s]	<empty>	<empty>
Composition	Z Factor	1.002	1.002
Oil & Gas Feed	Watson K	4.786	4.786
Petroleum Assay	User Property	<empty>	<empty>
K Value	Partial Pressure of H2S [kPa]	0.0000	<empty>
User Variables	Cp/(Cp - R)	1.328	1.328
Notes	Cp/Cv	1.330	1.330
Cost Parameters	Heat of Vap. [kJ/kgmole]	5513	<empty>
Normalized Yields	Kinematic Viscosity [cSt]	9.117	9.117
	Liq. Mass Density (Std. Cond) [kg/m3]	1.355	1.355
	Liq. Vol. Flow (Std. Cond) [m3/h]	2362	2362
	Liquid Fraction	0.0000	0.0000
	Molar Volume [m3/kgmole]	6.666	6.666
	Mass Heat of Vap. [kJ/kg]	172.3	<empty>
	Phase Fraction [Molar Basis]	1.0000	1.0000
	Surface Tension [dyne/cm]	<empty>	<empty>
	Thermal Conductivity [W/m-K]	6.076e-002	6.076e-002
	Viscosity [cP]	4.376e-002	4.376e-002
	Cv (Semi-Ideal) [kJ/kgmole-C]	25.37	25.37
	Mass Cv (Semi-Ideal) [kJ/kg-C]	0.7928	0.7928
	Cv [kJ/kgmole-C]	25.32	25.32
	Mass Cv [kJ/kg-C]	0.7913	0.7913
	Cv (Ent. Method) [kJ/kgmole-C]	<empty>	<empty>

Property Correlation Controls

Preference Option: Active

OK

Delete Define from Stream... View Assay

Figure E.11: Aspen HYSYS, gas properties output, part 2

Material Stream: O2

Worksheet Attachments Dynamics

Worksheet	Property	Value 1	Value 2
Conditions	Cp/(Cp - R)	1.328	1.328
Conditions	Cp/Cv	1.330	1.330
Properties	Heat of Vap. [kJ/kgmole]	5513	<empty>
Composition	Kinematic Viscosity [cSt]	9.117	9.117
Oil & Gas Feed	Liq. Mass Density (Std. Cond) [kg/m ³]	1.355	1.355
Petroleum Assay	Liq. Vol. Flow (Std. Cond) [m ³ /h]	2362	2362
K Value	Liquid Fraction	0.0000	0.0000
User Variables	Molar Volume [m ³ /kgmole]	6.666	6.666
Notes	Mass Heat of Vap. [kJ/kg]	172.3	<empty>
Cost Parameters	Phase Fraction [Molar Basis]	1.0000	1.0000
Normalized Yields	Surface Tension [dyne/cm]	<empty>	<empty>
	Thermal Conductivity [W/m-K]	6.076e-002	6.076e-002
	Viscosity [cP]	4.376e-002	4.376e-002
	Cv (Semi-Ideal) [kJ/kgmole-C]	25.37	25.37
	Mass Cv (Semi-Ideal) [kJ/kg-C]	0.7928	0.7928
	Cv [kJ/kgmole-C]	25.32	25.32
	Mass Cv [kJ/kg-C]	0.7913	0.7913
	Cv (Ent. Method) [kJ/kgmole-C]	<empty>	<empty>
	Mass Cv (Ent. Method) [kJ/kg-C]	<empty>	<empty>
	Cp/Cv (Ent. Method)	<empty>	<empty>
	Reid VP at 37.8 C [kPa]	<empty>	<empty>
	True VP at 37.8 C [kPa]	<empty>	<empty>
	Liq. Vol. Flow - Sum(Std. Cond) [m ³ /h]	2362	2362
	Viscosity Index	-5.607	<empty>

Property Correlation Controls

Preference Option: Active

OK

Delete Define from Stream... View Assay

Figure E.12: Aspen HYSYS, gas properties output, part 3

APPENDIX F

CATALYTIC EXPERIMENTAL STUDY CATALYTIC MATERIALS PROPERTIES

Table F.1: Chemical composition of materials tested as catalyst

	C	Mn	Cr	Mo	Ni	Fe	Si	P	S	Pd	Alumina	Others
SS 304	0.08	2	18 - 20	-	8 - 10.5	Balance	1	0.45	0.03	-	-	-
SS 316	0.08	2	16 - 18	2 - 3	10 - 14	Balance	1	0.45	0.03	-	-	-
SS 410	0.15	1	11.5 - 13.5	-	-	Balance	1	0.45	0.03	-	-	-
SS 420	0.15	1	12 - 14	-	-	Balance	1	0.4	0.03	-	-	-
Hastelloy X	0.1	1 max	22	9	Balance	18	1 max	-	-	-	-	Co = 1.5 W = 0.6 B = 0.008 max
Pd coated Alumina	-	-	-	-	-	-	-	-	-	0.5	Balance	

Table F.2: Properties of Pd coated Alumina catalyst

Particle size/shape	2-4 mm / Beads
Sock-load density	750 kg/m ³
Max. Temperature	600 °C
Surface area	250 - 300 m ² /g
Price	\$ 250/ 500gr

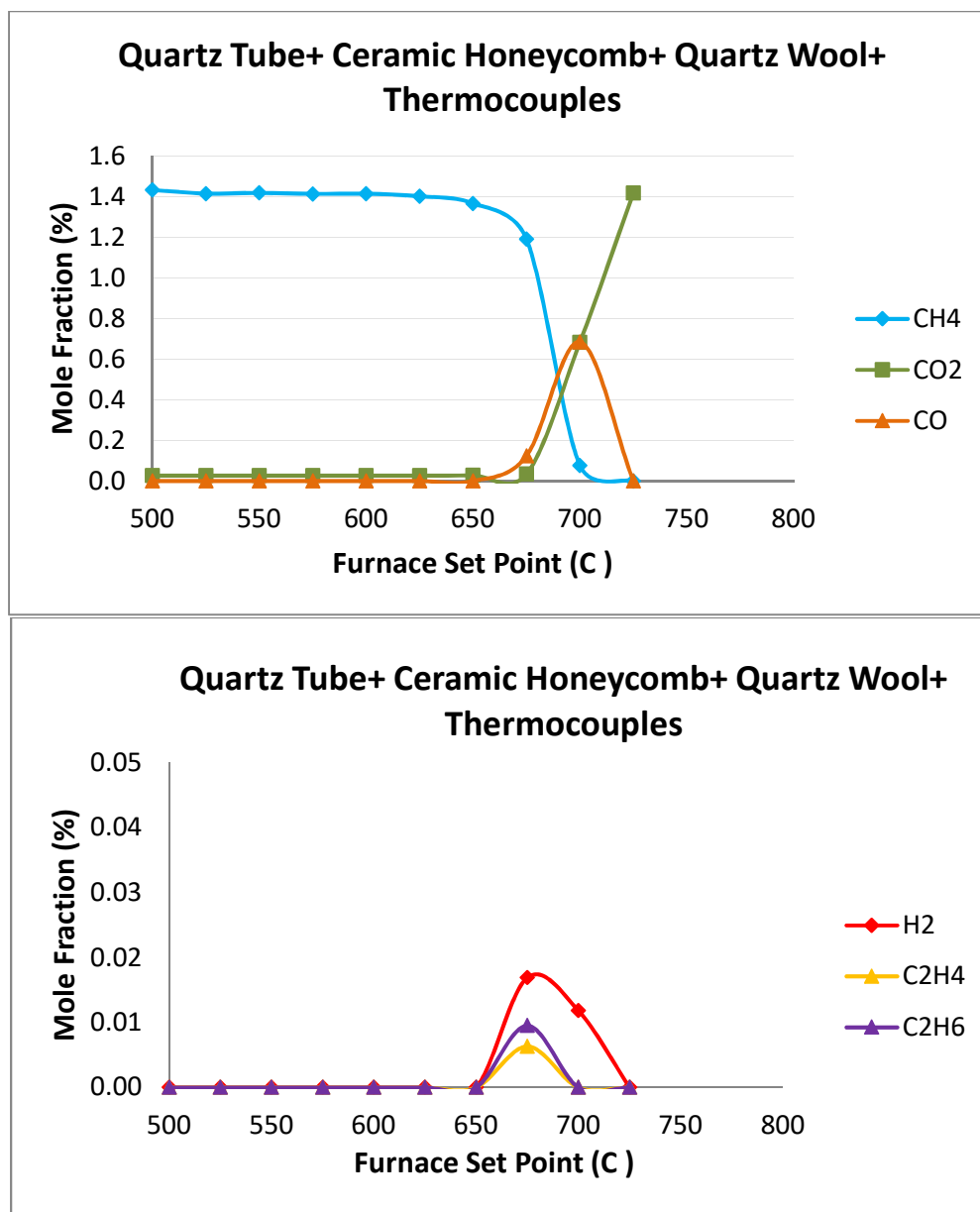


Figure F.1: Experimental results of blank test 1

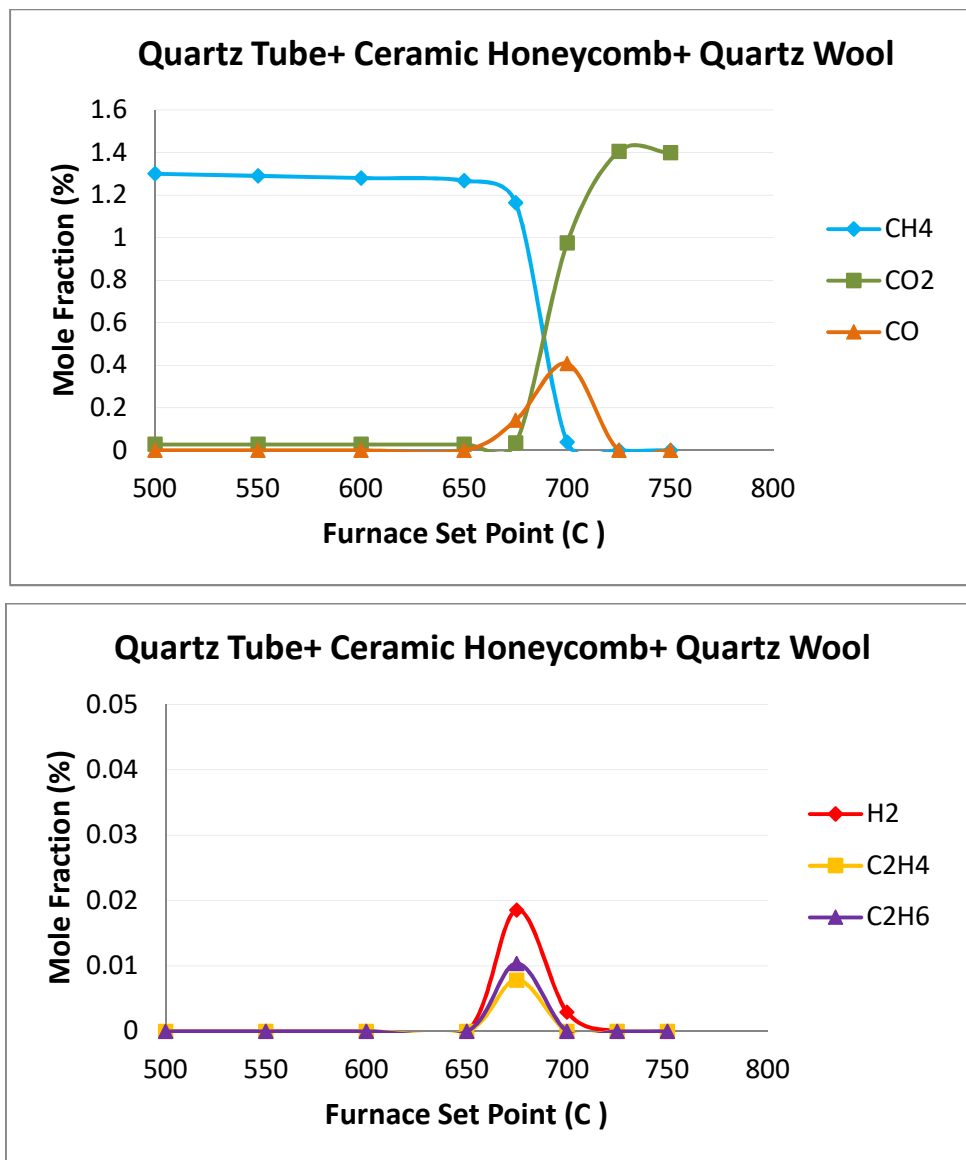


Figure F.2: Experimental results of blank test2

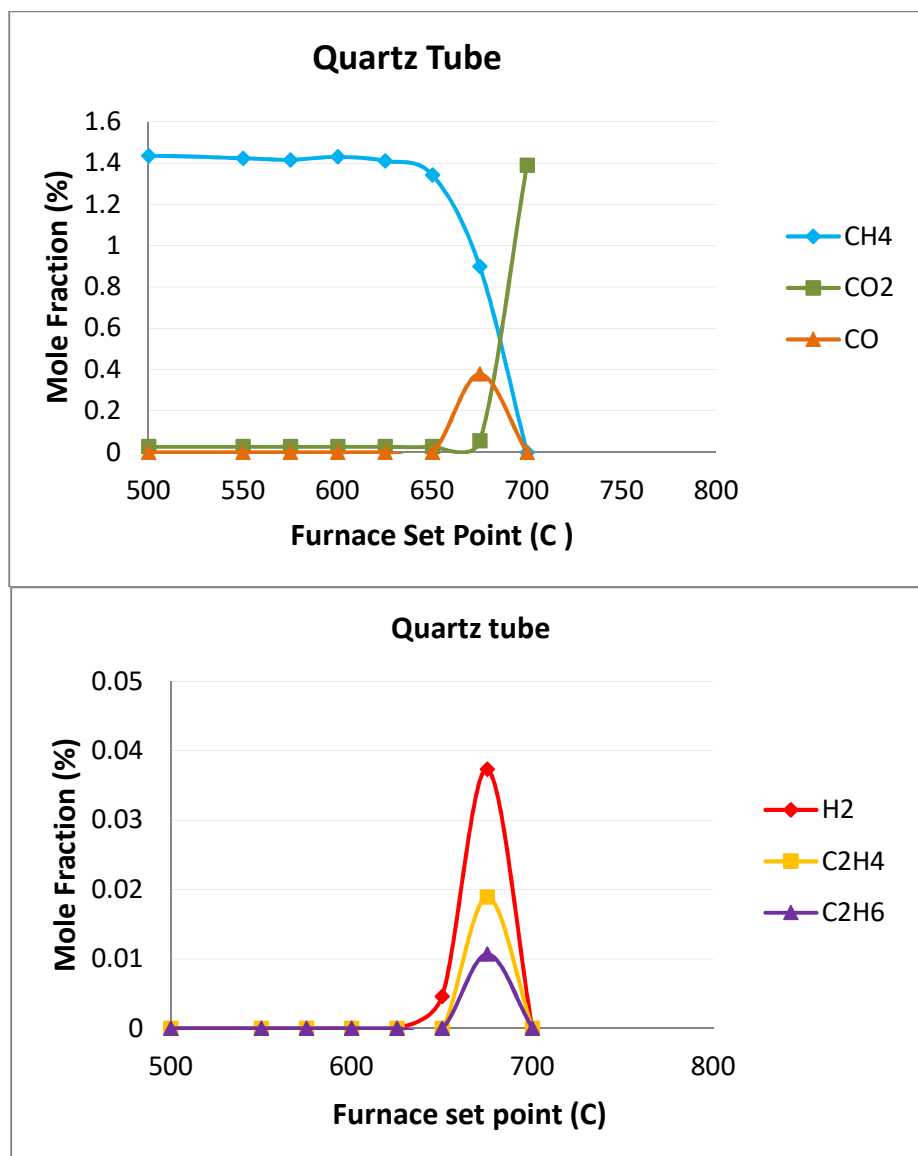


Figure F.3: Experimental results of blank test3

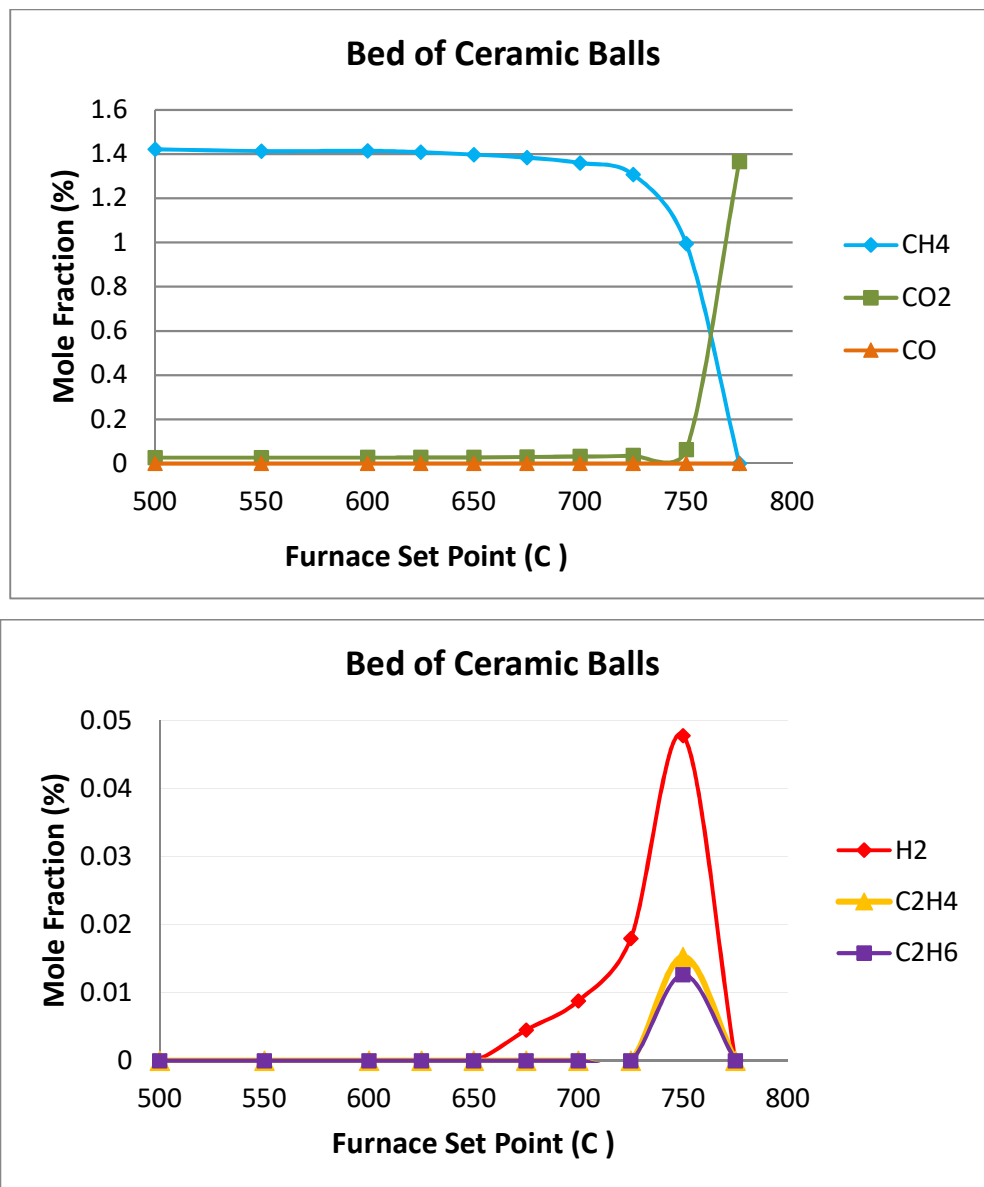


Figure F.4: Experimental results of methane oxidation on 9.5cm bed of ceramic balls

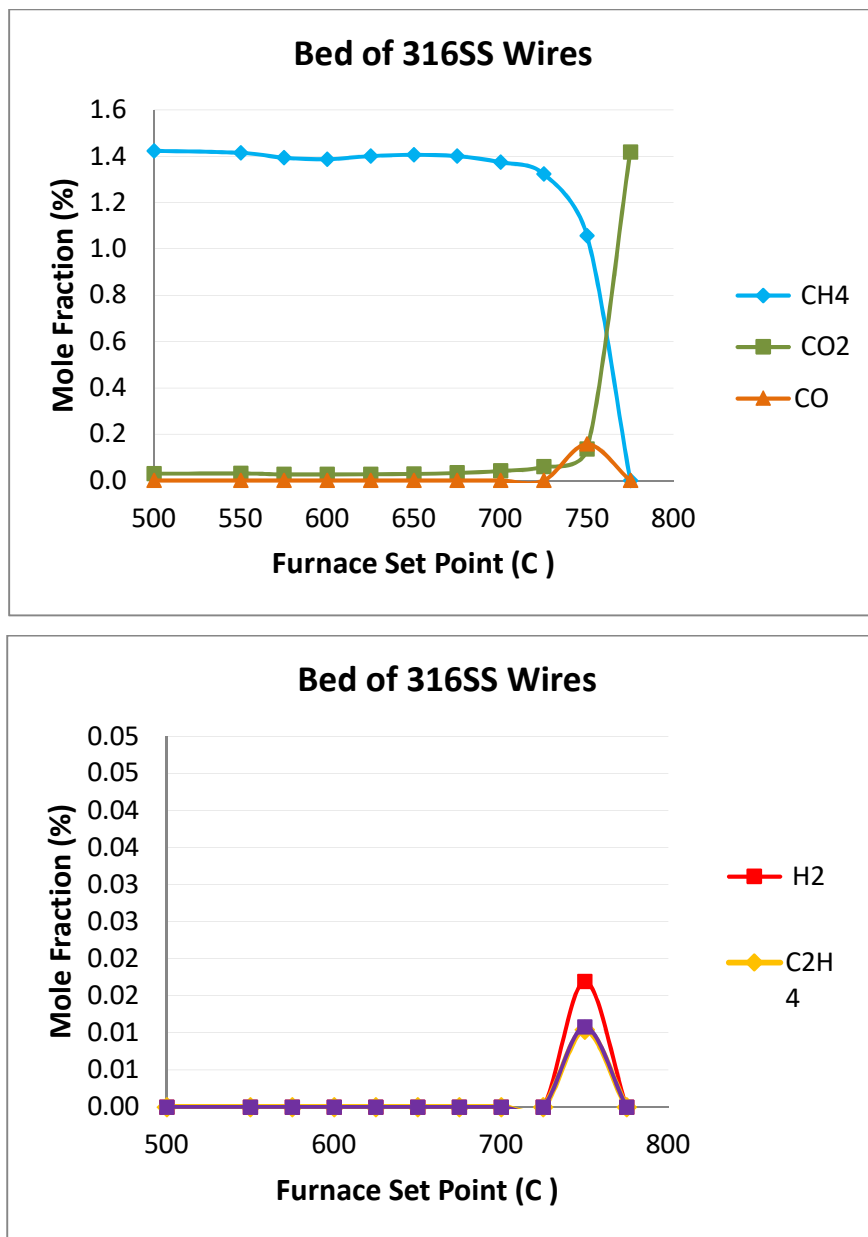


Figure F.5: Experimental results of methane oxidation on 9.5cm bed of 316SS

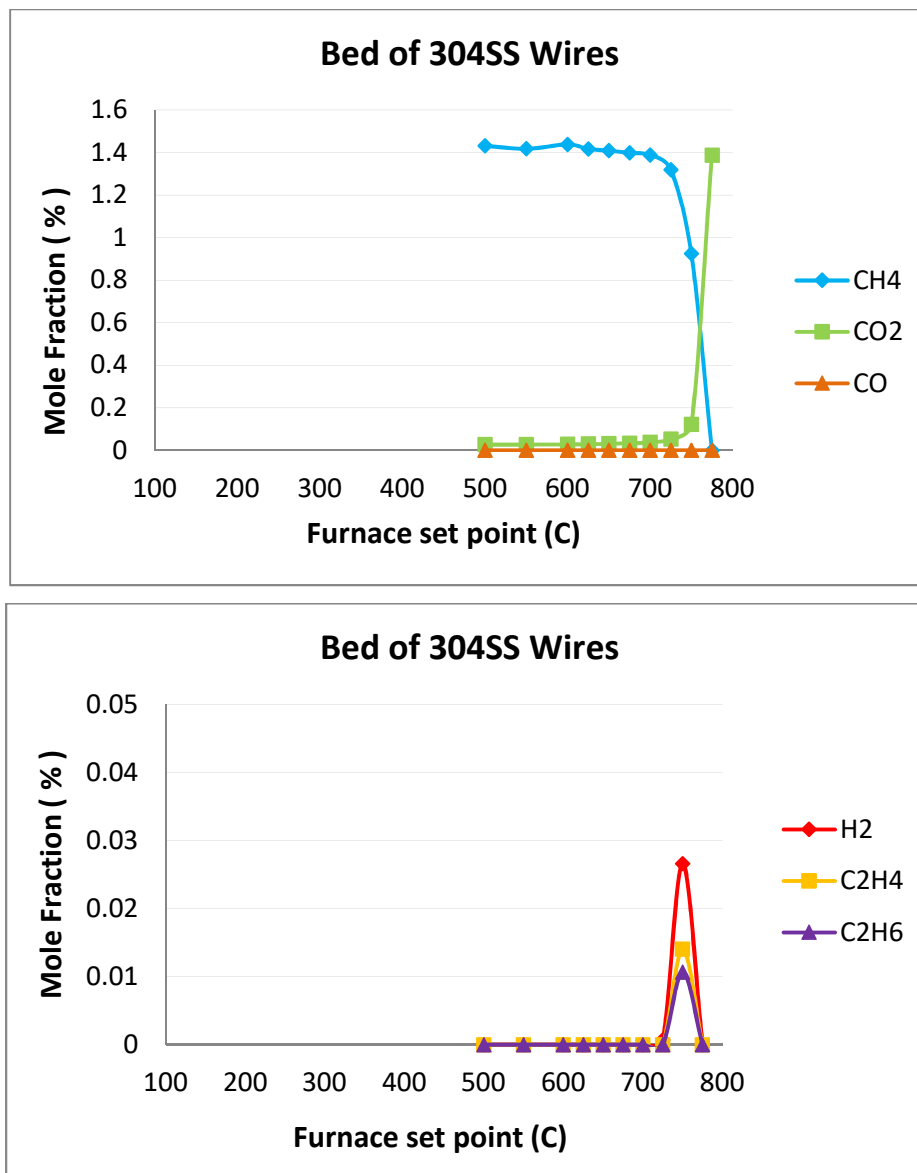


Figure F.6: Experimental results of methane oxidation on 9.5cm bed of 304SS

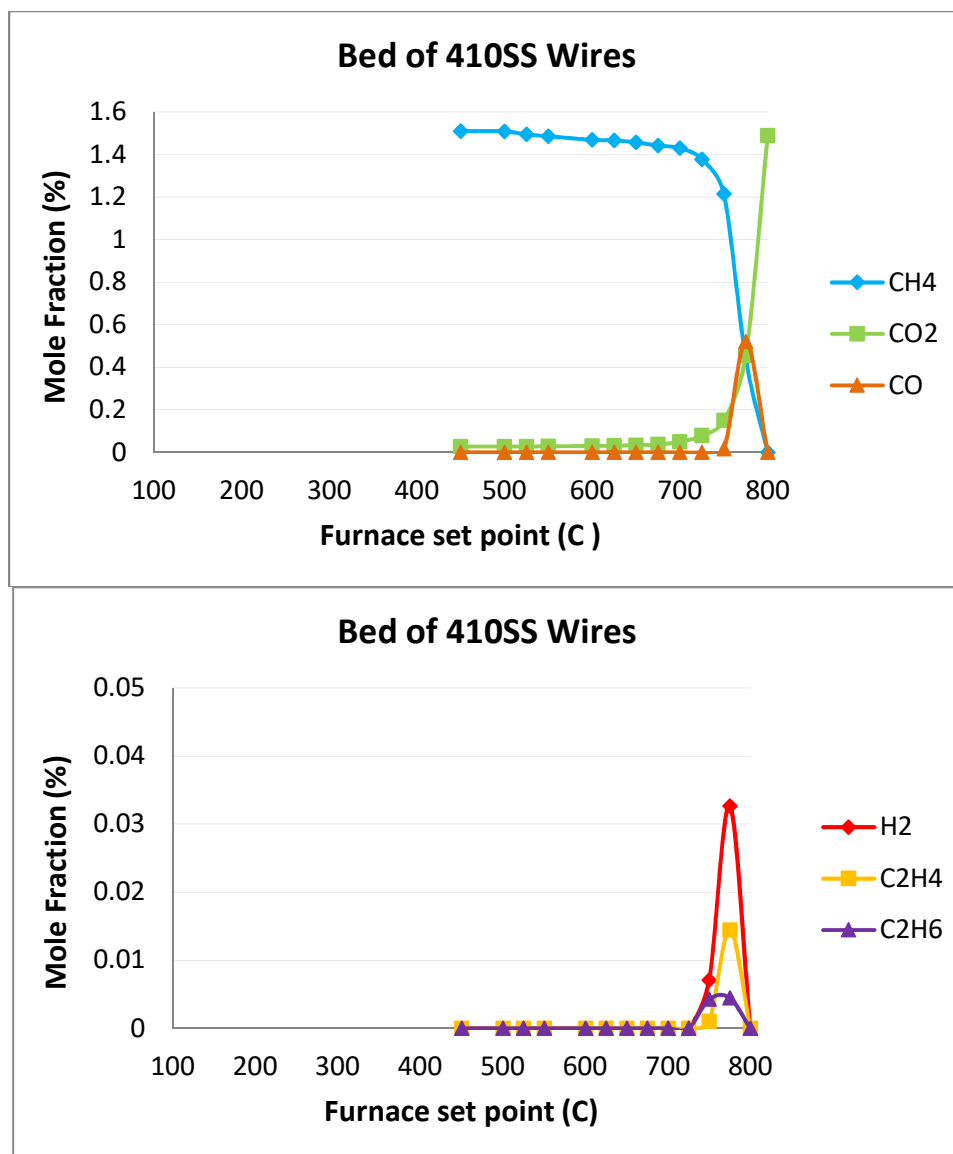


Figure F.7: Experimental results of methane oxidation on 9.5cm bed of 410SS

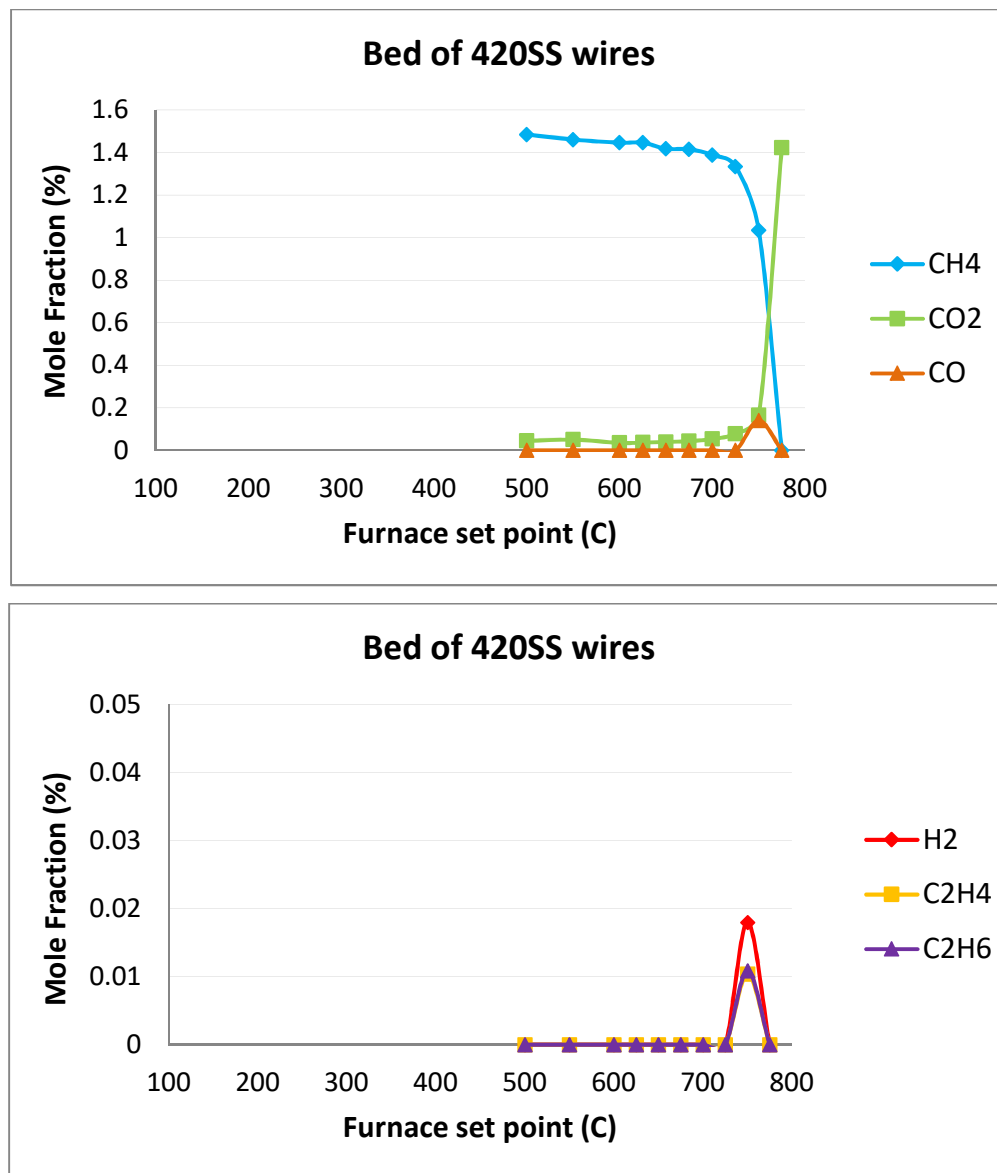


Figure F.8: Experimental results of methane oxidation on 9.5cm bed of 420SS

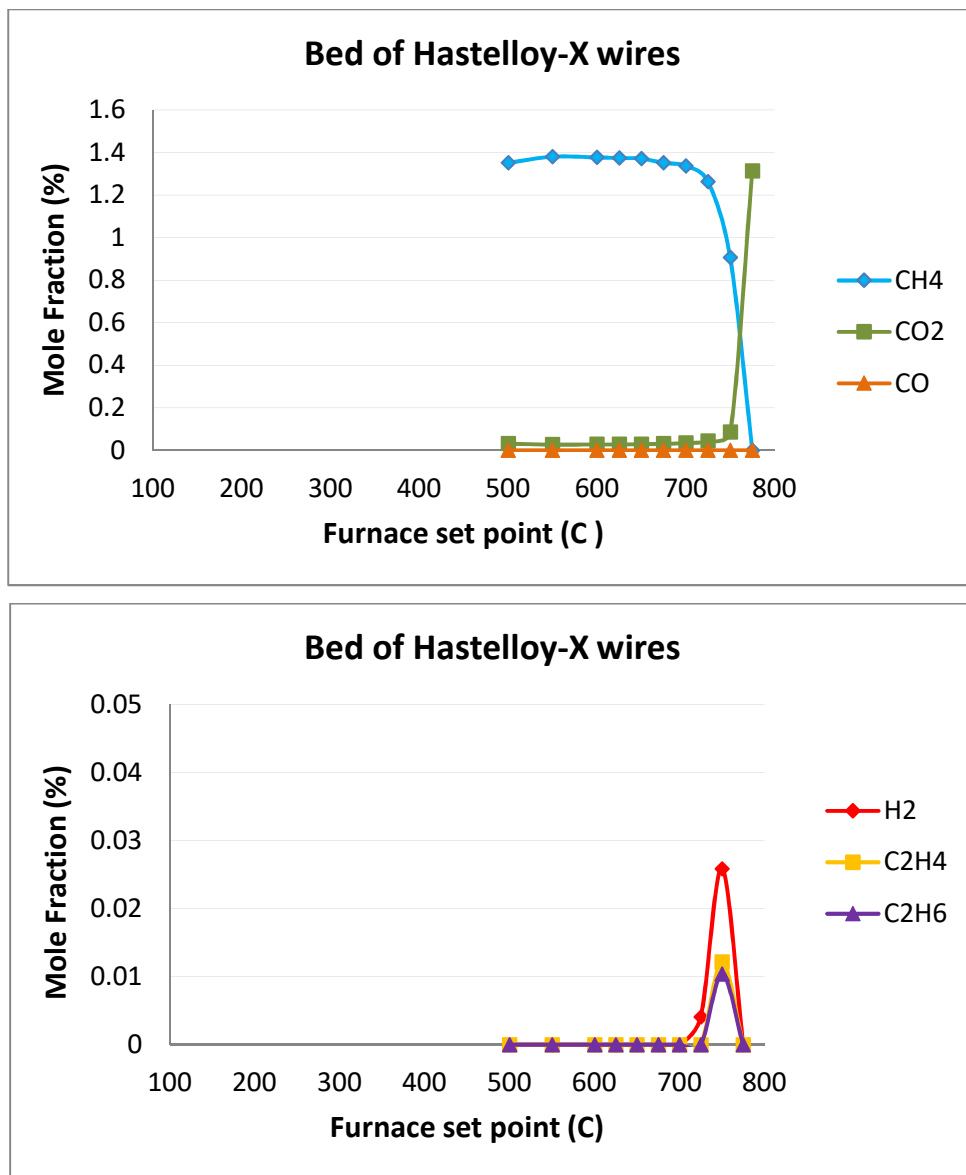


Figure F.9: Experimental results of methane oxidation on 9.5cm bed of Hastelloy-X

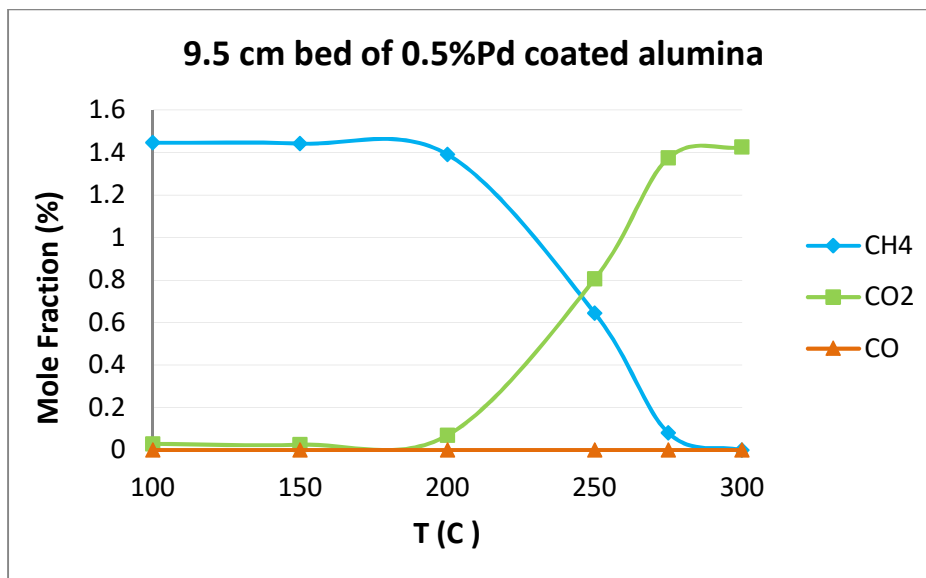


Figure F.10: Experimental results of methane oxidation on 9.5cm bed of Pd coated alumina beads

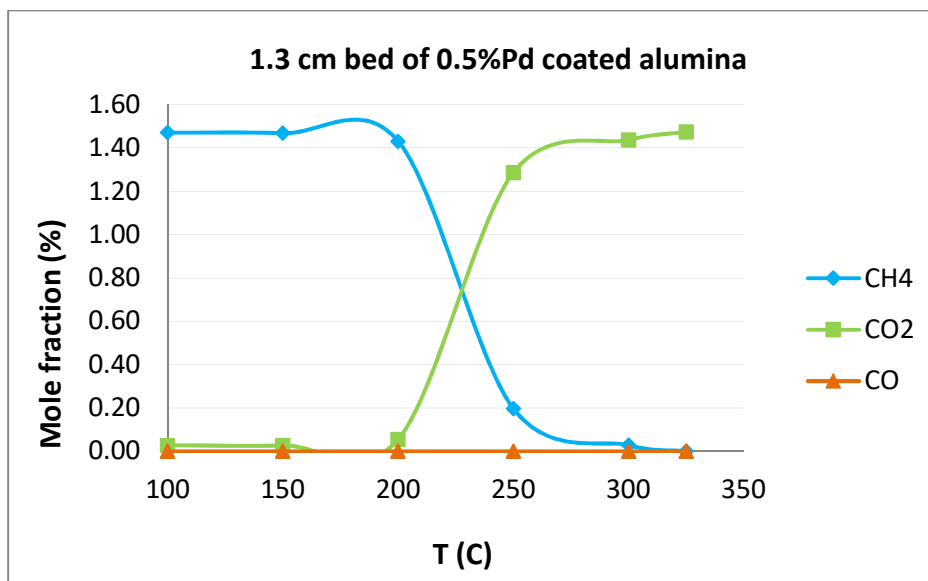


Figure F.11: Experimental results of methane oxidation on 1.3cm bed of Pd coated alumina beads

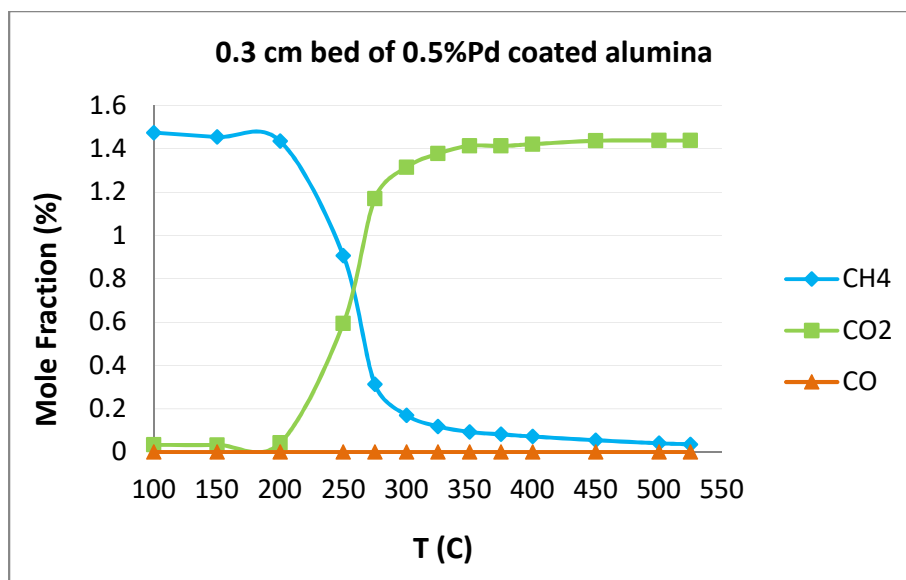


Figure F.12: Experimental results of methane oxidation on 0.3cm bed of Pd coated alumina beads

F.1. CHEMKIN modeling

Four different mechanisms were used in CHEMKIN to model methane oxidation based on the UofU and the WRI experimental conditions. Table F.3 shows a basic comparison between the mechanisms.

Table F.3: different models used to predict the methane combustion⁴⁻⁷

Model	Number of reactions	Number of species	Year	Developers
GRI- Mech 3.0	325	53	2000	Frenklach, et al.
WF	527	99	1997	Frenklach, et al.
ABF	543	101	2000	Frenklach, et al.
CRECK	13532	435	2012	Ranzi, et al.

F.2. GRI mechanism⁶

GRI-Mech is a mechanism designed to model natural gas combustion, including NO formation and reburn chemistry. The model is a product of computational and experimental

research sponsored by the Gas Research Institute and carried out at The University of California at Berkeley, Stanford University, The University of Texas at Austin, and SRI International.

GRI-Mech is a compilation of elementary chemical reactions and associated rate constant expressions. Most of the rate constant parameters have been obtained with direct laboratory measurements. All reactions are assumed reversible even though negligible reversible reactions occur in many of them. An optimization process is used to obtain kinetics which have reasonable predictability of basic combustion properties. Some details of the optimization procedure are provided in reference 6.

GRI-Mech 3.0 is the successor to version 2.11. The changes include adding 4 species, recomputing the methanol decomposition / chemical activation, adding Acetaldehyde and Vinyloxy chemistry to better describe ethylene oxidation, adding a minimal set of propane kinetics to model the propane and higher hydrocarbons in natural gas as minor constituents, and adding new expressions for the $\text{H} + \text{O}_2$ reactions, $\text{CH}_3 + \text{O}_2$, $\text{CH}_2\text{O} + \text{H}$, and CH_2O decomposition, and to $\text{CH}_3 + \text{O}$ and $\text{CH}_2 + \text{O}_2$ branching paths,

GRI-Mech contains some species and reactions which are not important for natural gas combustion kinetic. However, they could be important in other cases such as modeling flame radiation or ionization where elementary reactions becoming very important.

F.3. WF and ABF mechanisms^{4,5}

The WF reaction mechanism was developed by Wang and Frenklach in 1997⁵ to use for oxidation of methane, ethane, ethylene, and acetylene at flame temperatures. It is based on GRI-Mech1.2. Aromatic chemistry is included up to the formation of pyrene in this

mechanism. The WF mechanism predicts well the major, minor, and small-aromatic species but underpredicts two-, three-, and four-ring aromatics. So, the ABF mechanism is developed to address these issues. It includes modifications of gas-phase reactions and aromatic species which make the ABF mechanism predict well the major, minor, and aromatic species up to pyrene in laminar premixed flames of ethane, ethylene, and acetylene fuels.

F.4. CRECK model⁷

The Chemical Reaction Engineering and Chemical Kinetics (CRECK) group are developing detailed and semidetailed kinetic mechanisms of the pyrolysis, oxidation, and combustion of gas, liquid, and solids. One of these mechanisms is the CRECK Complete Mechanism: Low and High temperature which contains wide range mechanism of pyrolysis, partial oxidation, and combustion of hydrocarbon fuels, up to 16 C atoms, including alcohols, esters, and reference components of surrogates of real fuels. CRECK is continuously updating and the last version was released on Nov 2013; however, the present results are based on 2012 version.

Figures F.13 to F.17 show the implementation of the ABF mechanism in CHEMKIN to model homogenous oxidation of methane at furnace set point equal to 550 °C. Figures F.18 to F.20 shows the comparison of CHEMKIN results with different mechanisms and the UofU experimental data.

**F.5. CHEMKIN modeling procedure for homogenous
oxidation of methane at furnace set point
equal to 550°C**

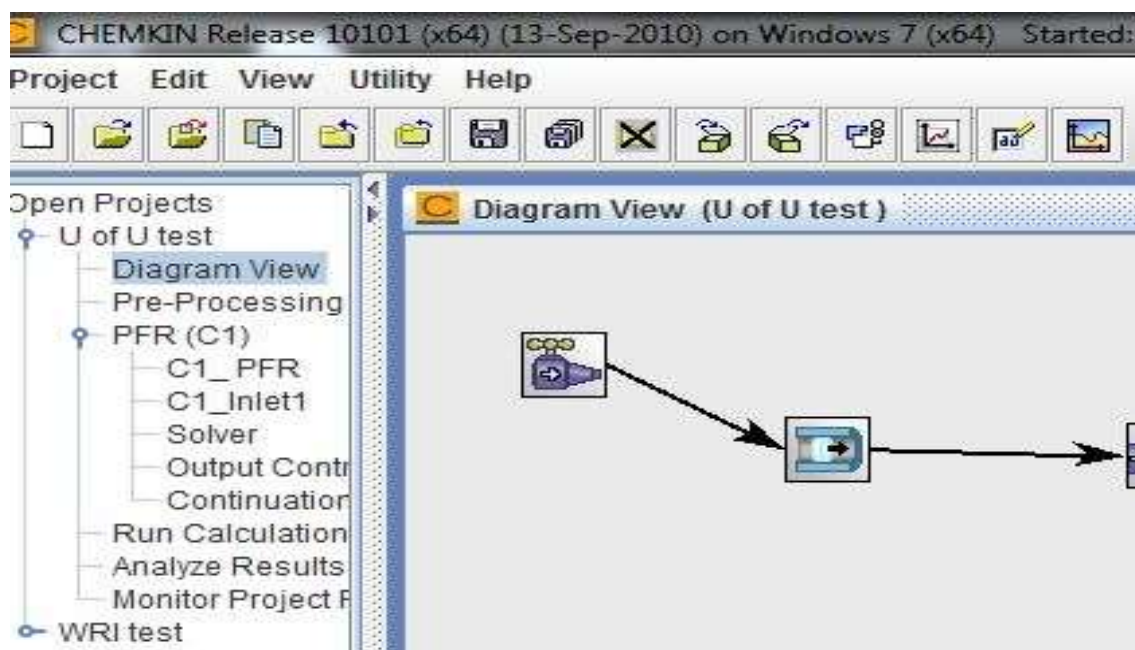


Figure F.13: CHEMKIN capture: Diagram View

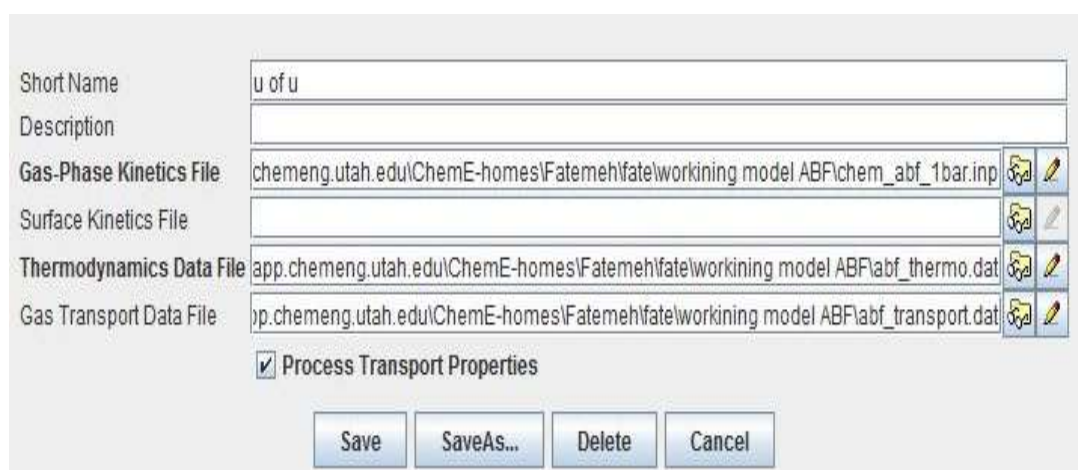


Figure F.14: CHEMKIN capture: Pre-Processing

Axial Velocity
 Mass Flow Rate
 Volumetric Flow Rate in SCCM
 Volumetric Flow Rate

Inlet Temperature Profile

		cm/sec		
		g/sec		Constant
500.0	standard-cm3/min@298.15K			Constant
		cm3/sec		Constant
		K		Select Profile..

Figure F.15: CHEMKIN capture: Steam Property

Species	Reactant Fraction
CH4	0.013803031
CO2	0.000266201
N2	0.778885307
O2	0.207045461

Figure F.16: CHEMKIN capture: Species Specific Properties

Problem Type: Fix Gas Temperature

Turn on Momentum Equation
 Turn off Momentum Equation

Turn on Residence Time Calculation
 Turn off Residence Time Calculation

Starting Axial Position: 0.0 ft
 Ending Axial Position: 1.0 ft

Diameter: 2.2 cm
 Cross-sectional Area: cm²
 Axial Velocity Profile: cm/sec

Internal Surface Area Per Unit Length: cm
 External Surface Area Per Unit Length: cm

Temperature: 550C
 Pressure: 0.85 atm

Surface Temperature Same as Gas Temperature
 Surface Temperature: K

Mixture Viscosity: 0.0 g/cm-sec
 Gas Reaction Rate Multiplier: 1.0

Figure F.17: CHEMKIN capture: Inlet

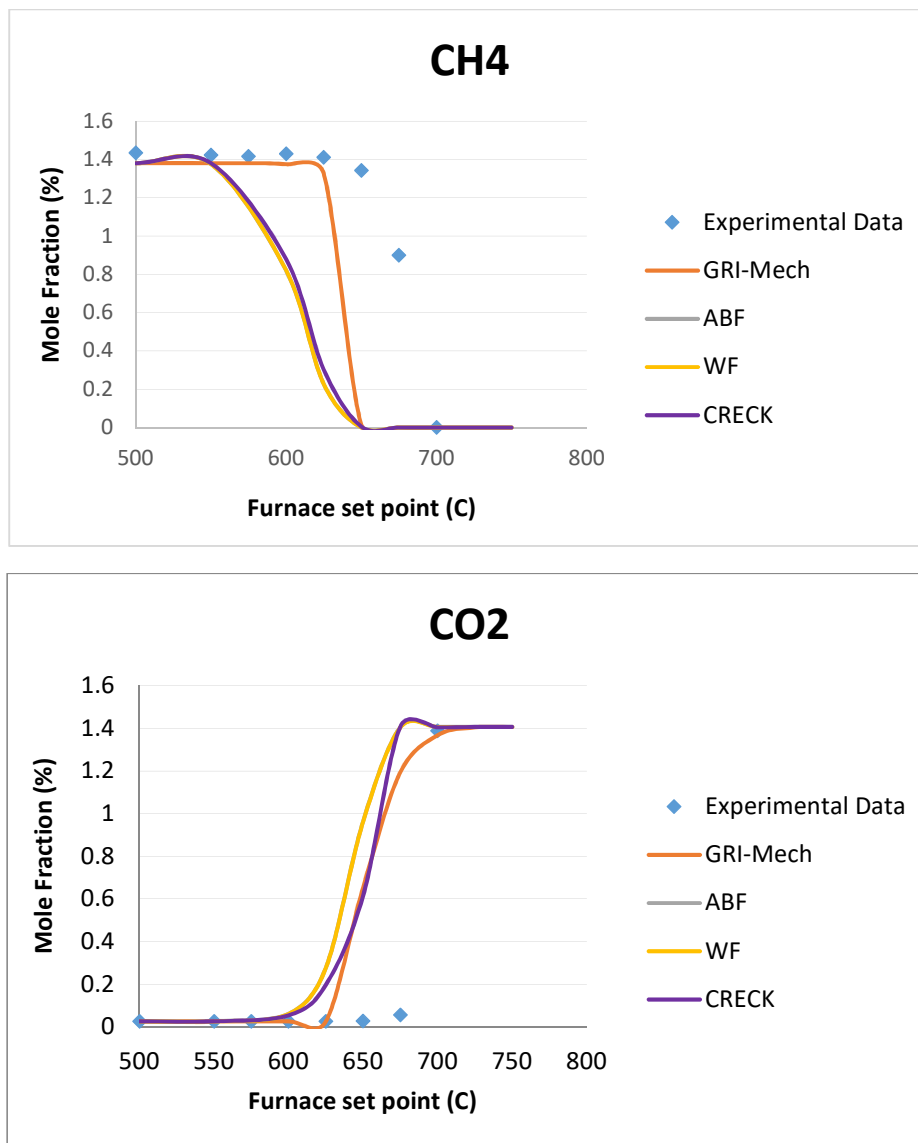


Figure F.18: Comparison of CHEMKIN modeling prediction based on four different mechanisms and the UofU experimental data, CH₄ and CO₂ mole fraction

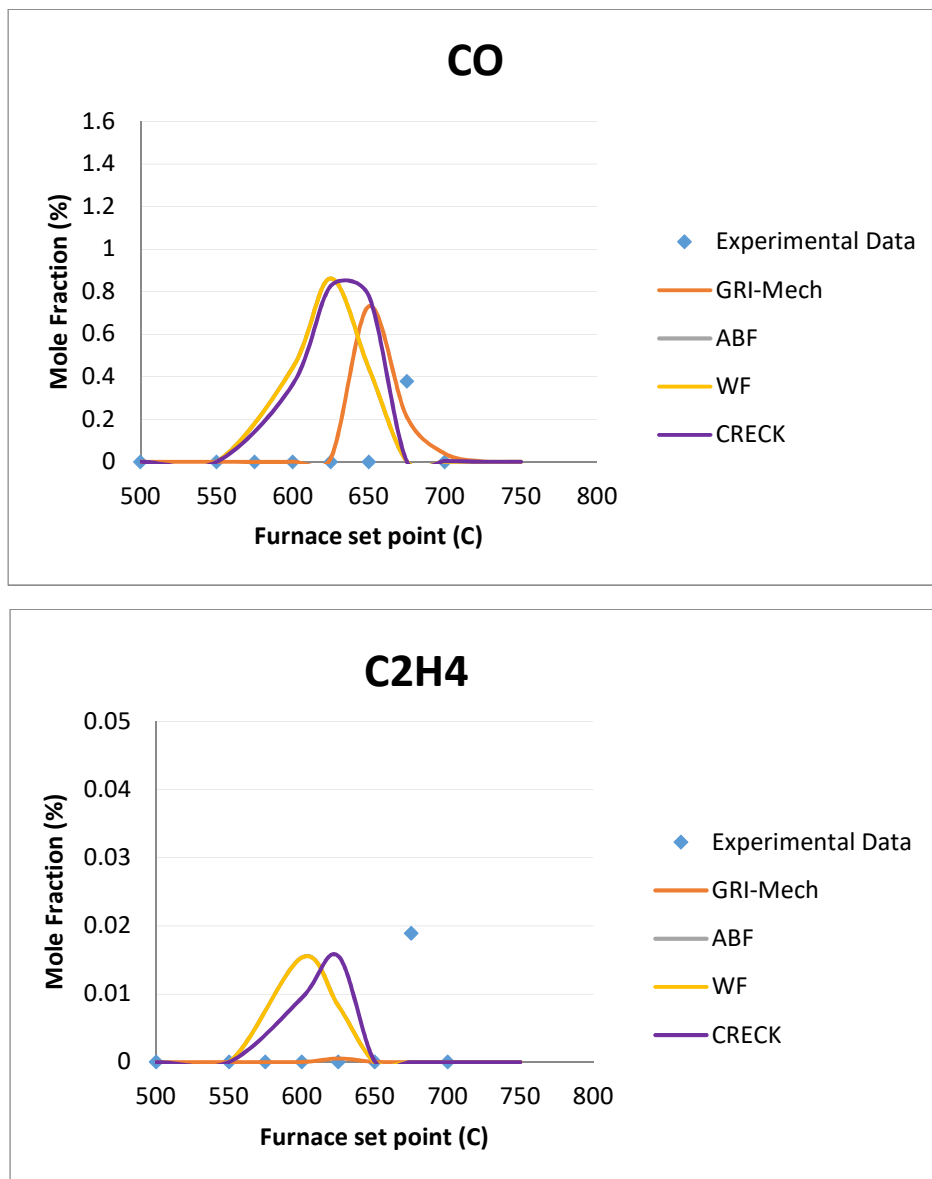


Figure F.19: Comparison of CHEMKIN modeling prediction based on four different mechanisms and the UofU experimental data, CO and C₂H₄ mole fraction

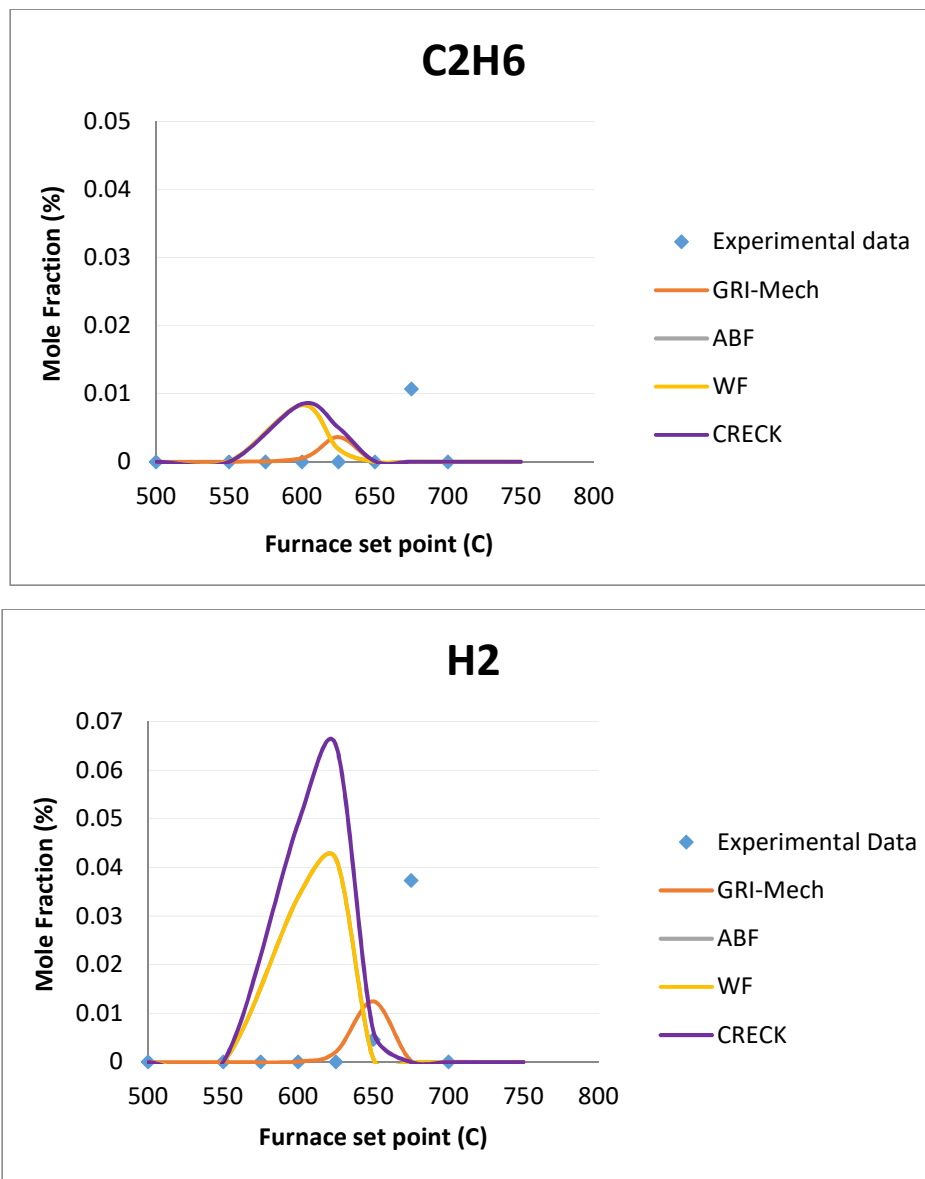


Figure F.20: Comparison of CHEMKIN modeling prediction based on four different mechanisms and the UofU experimental data, C₂H₆ and H₂ mole fraction

Figure F.18 illustrates that the modeling results are in good agreement with the experimental data. All the mechanisms are showing similar prediction for methane oxidation. However, the light-off temperatures predicted by modeling with different mechanisms are lower than those observed in the experimental data. This difference is probably because of the assumptions made in the modeling and the experimental errors.

GRI-Mech is predicting light-off temperatures which are nearer to the experimental results. CH₄ and CO concentrations predicted by GRI-Mech are also in better agreement with the experimental data. For CO₂ concentration, all mechanisms predict pretty similar results. CRECK, ABF, and WF mechanisms have better prediction for H₂, C₂H₄, and C₂H₆ concentration than GRI-Mech.

F.6. CHEMKIN results based on WRI experimental conditions

Some of the experimental data obtained by Western Research Institute (WRI)⁸ were modeled with CHEMKIN. Two different assumptions were used to model the WRI experimental data. At first, it was assumed that the reactor temperature was fixed and equal to the average bed temperature reported by WRI. In a second approach, we assumed a temperature profile that was based on the average bed temperature reported by WRI and the trend of temperature profile observed by the University of Utah. Transport, thermodynamic, and kinetic data were obtained from the GRI-Mech 3.0, WF, and ABF mechanism at first. Figures F.21 to F.24 show the modeling results.

F.7. Comparison of experimental data and CHEMKIN

prediction of methane conversion at bed

average temperature: 420 °C

Table F.4: WRI experimental result, Material: 316SS, Average bed temperature: 420 °C

Test number	Disc material	Control temperature (°C)	Disc average temperature (°C)	Nominal flow (SLPM)	Inlet gas composition	Reactor pressure (Psig)	Pressure drop (psid)	Methane conversion (%)
1	316 SS	475	420	2	9.95% O ₂ 89.55% N ₂ 0.49% CH ₄	140	9.0	3.9

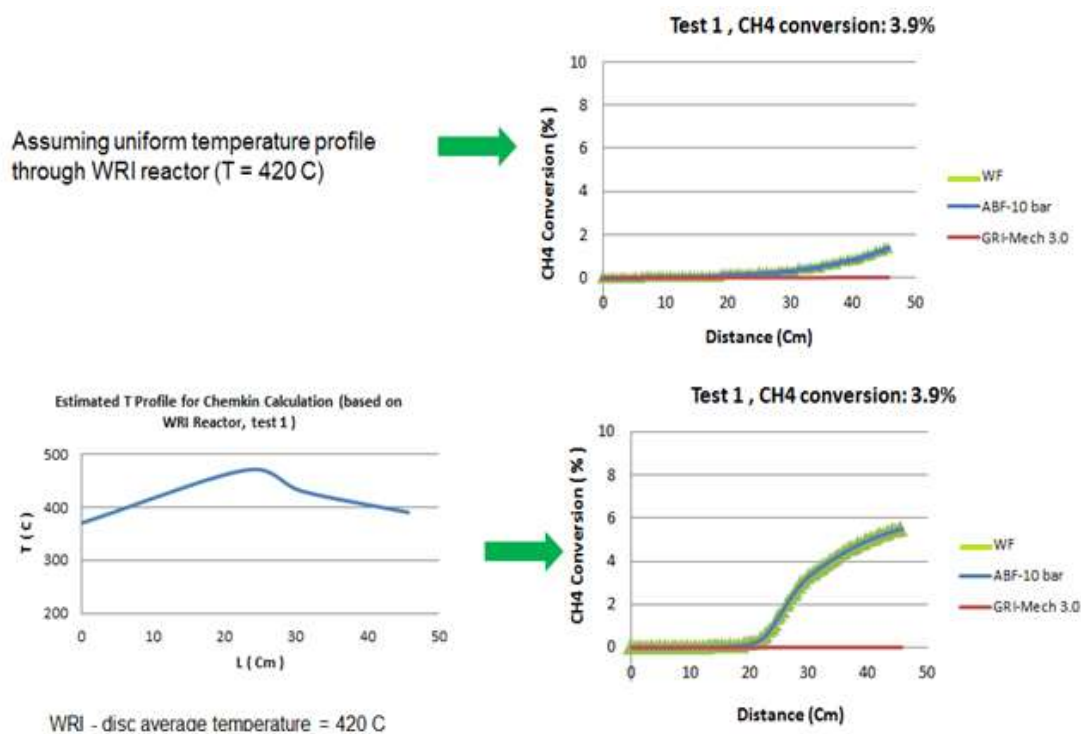


Figure F.21: Methane conversion predicted by CHEMKIN based on WF, ABF, and GRI-Mech3.0 mechanisms (bed average temperature: 420 °C)

F.8. Comparison of experimental data and CHEMKIN

prediction of methane conversion at bed

average temperature: 450 °C

Table F.5: WRI experimental result, Material: 304SS, Average bed temperature: 450 °C

Test number	Disc material	Control temperature (°C)	Disc average temperature (°C)	Nominal flow (SLPM)	Inlet gas composition	Reactor pressure (Psig)	Pressure drop (psid)	Methane conversion (%)
8	304 SS	475	450	1	9.95% O ₂ 89.55% N ₂ 0.49% CH ₄	150	< 2.75	11.0

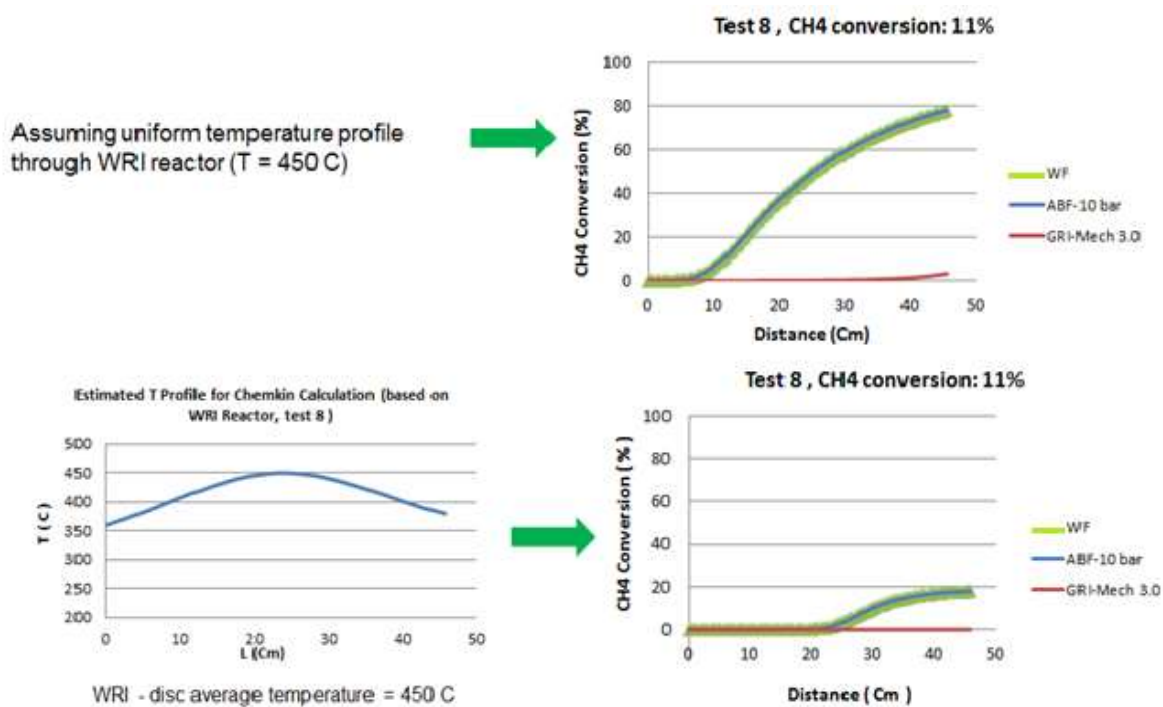


Figure F.22: Methane conversion predicted by CHEMKIN based on WF, ABF, and GRI-Mech3.0 (bed average temperature: 450 °C)

F.9. Comparison of experimental data and CHEMKIN

prediction of methane conversion at bed

average temperature: 510 °C

Table F.6: WRI experimental result, Material: 316SS, Average bed temperature: 510 °C

Test number	Disc material	Control temperature (°C)	Disc average temperature (°C)	Nominal flow (SLPM)	Inlet gas composition	Reactor pressure (Psig)	Pressure drop (psid)	Methane conversion (%)
9	304 SS	550	510	2	9.95% O ₂ 89.55% N ₂ 0.49% CH ₄	150	<2.75	46.25

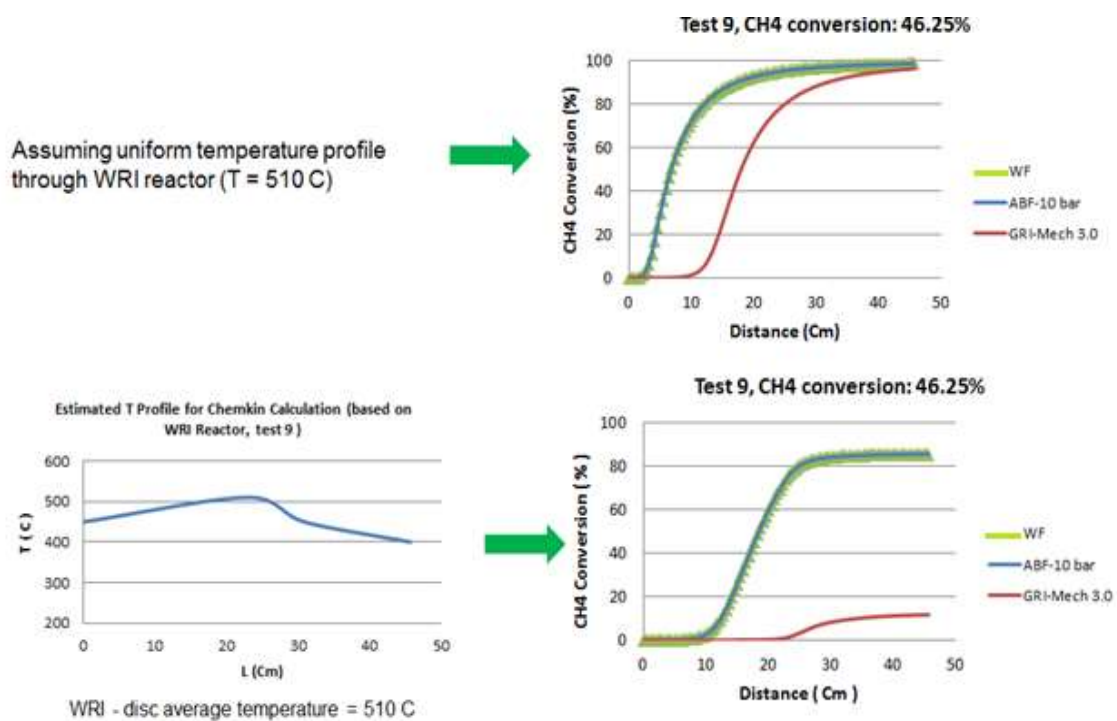


Figure F.23: Methane conversion predicted by CHEMKIN based on WF, ABF, and GRI-Mech3.0 (bed average temperature: 510 °C)

F.10. Comparison of experimental data and CHEMKIN

prediction of methane conversion at bed

average temperature: 625 °C

Table F.7: WRI experimental result, Material: Hastelloy-X, Average bed temperature: 650 °C

Test number	Disc material	Control temperature (°C)	Disc average temperature (°C)	Nominal flow (SLPM)	Inlet gas composition	Reactor pressure (Psig)	Pressure drop (psid)	Methane conversion (%)
18	Hastelloy-X	650	625	4	9.95% O ₂ 89.55% N ₂ 0.49% CH ₄	140	9.5	96.9

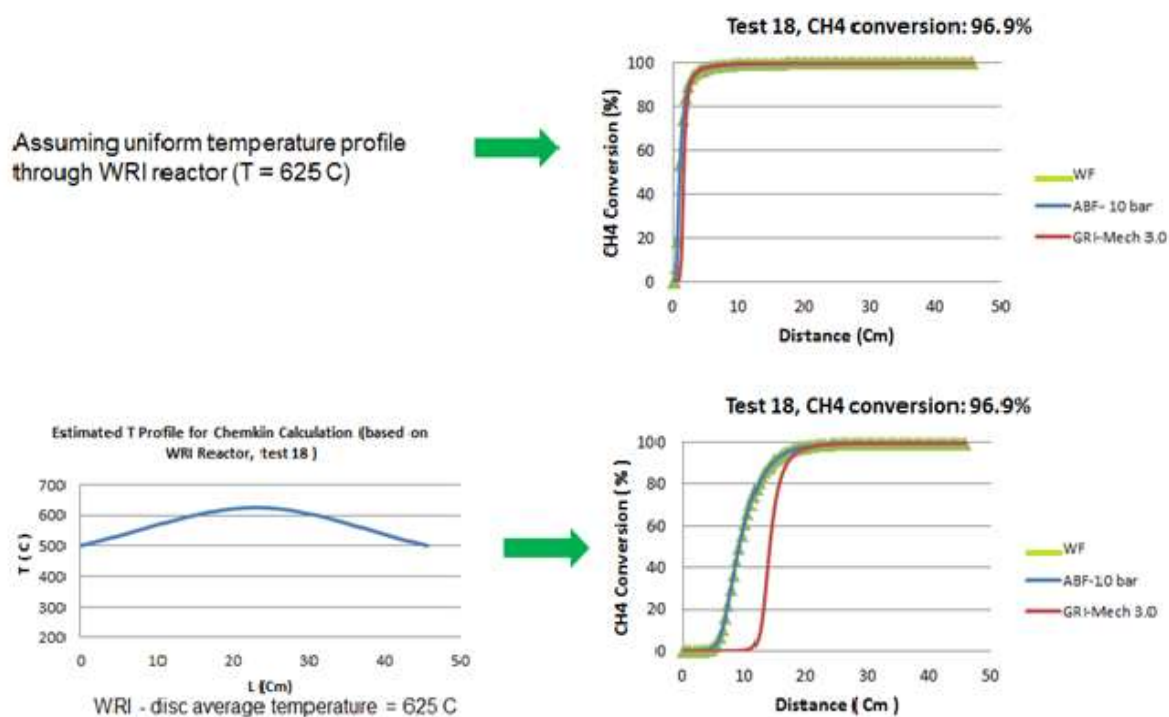


Figure F.24: Methane conversion predicted by CHEMKIN based on WF, ABF, and GRI-Mech3.0 (bed average temperature: 625 °C)

F.11. References

- (1) Reaction Design. In *CHEMKIN-PRO 15131*; San Diego, **2013**.
- (2) Aspen Hysys www.hyprotech.com.
- (3) PVTsim <https://www.pvtsimnova.com>.
- (4) ABF Modeling <http://combustion.berkeley.edu/soot/mechanisms/abf.html>.
- (5) WF Modeling <http://combustion.berkeley.edu/soot/mechanisms/wf.html>.
- (6) Smith, G. P.; Golden, D. M.; Frenklach, M.; Moriarty, N. W.; Eiteneer, B.; Goldenberg, M.; Bowman, C. T.; Hanson, R. K.; Song, S.; William C. Gardiner, J.; Lissianski, V. V.; Qin, Z. GRI-Mech 3.0 http://www.me.berkeley.edu/gri_mech/.
- (7) CRECK Modeling <http://creckmodeling.chem.polimi.it>.
- (8) Western Research Institute. *American Shale Oil Catalytic Material Tests (Private Report)*; Laramie, WY, **2009**.